SYNTHESIS AND CHARACTERIZATION OF MOLYBDENUM-BASED NANOCOMPOSITES FILM FOR WATER SPLITTING APPLICATIONS

CHOONG ZHENG LIN

FACULTY OF SCIENCE

UNIVERSITI MALAYA

KUALA LUMPUR

2022

Universiti Malaya

SYNTHESIS AND CHARACTERIZATION OF MOLYBDENUM-BASED NANOCOMPOSITES FILM FOR WATER SPLITTING APPLICATIONS

CHOONG ZHENG LIN

DISSERTATION SUBMITTED IN FULFILLMENT OF THE REQUIREMENTS FOR THE DEGREE OF MASTER OF SCIENCE

DEPARTMENT OF CHEMISTRY
FACULTY OF SCIENCE
UNIVERSITI MALAYA
KUALA LUMPUR

2022

Universiti Malaya

UNIVERSITI MALAYA

ORIGINAL LITERARY WORK DECLARATION

Name of Candidate**: CHOONG ZHENG LIN**

Matric No: **SMA170028 (17028521/2)**

Name of Degree: **MASTER OF SCIENCE**

Title of Dissertation ("this work"):

SYNTHESIS AND CHARACTERIZATION OF MOLYBDENUM-BASED NANOCOMPOSITES FILM FOR WATER SPLITTING APPLICATIONS

Field of Study:

INORGANIC CHEMISTRY (ORGANOMETALLIC AND THIN SOLID FILMS)

I do solemnly and sincerely declare that:

(1) I am the sole author/writer of this Work;
(2) This Work is original;
(3) Any use of any work in which copyright exists was done by way of fair dealing and for permitted purposes and any excerpt or extract from, or reference to or reproduction of any copyright work has been disclosed expressly and sufficiently and the title of the Work and its authorship have been acknowledged in this Work;
(4) I do not have any actual knowledge nor do I ought reasonably to know that the making of this work constitutes an infringement of any copyright work;
(5) I hereby assign all and every rights in the copyright to this Work to the University of Malaya ("UM"), who henceforth shall be owner of the copyright in this Work and that any reproduction or use in any form or by any means whatsoever is prohibited without the written consent of UM having been first had and obtained;
(6) I am fully aware that if in the course of making this Work I have infringed any copyright whether intentionally or otherwise, I may be subject to legal action or any other action as may be determined by UM.

Candidate's Signature Date: 28th August 2022

Subscribed and solemnly declared before,

Witness's Signature Date: 28th August 2022

Name:

Designation:

University of Malaya

SYNTHESIS AND CHARACTERIZATION OF MOLYBDENUM-BASED NANOCOMPOSITES FILM FOR WATER SPLITTING APPLICATIONS

ABSTRACT

The molybdenum-based nanocomposite films in the form of Mo_2S_3/MoP_2 composite were prepared by using AACVD method with the single source precursor of $[CpMo(CO)_2(S_2P(SPhMe)_2)]$ **(1)** ($Cp = C_5H_5$) in THF at 0.01 M under argon gas flow in different deposition conditions inclusive of different deposition temperatures (450 °C, 550 °C, 650 °C), duration of deposition time (20 mins, 30 mins and 40 mins), different volume of precursor solution (10, 15, 20 and 25 mL) and carrier gas flow rate (0.3 and 0.5 SCFH). The bandgap energy values obtained in the visible light spectrum were close to the literature values for Mo_2S_3 and MoP_2 at ~2.3 eV and ~2.8 eV, respectively. The deposition conditions had no significant effect on the band gap of the films. Among all the films synthesized for this study, the 20 ml/30 mins film fabricated at 550 °C with carrier gas flow rate of 0.3 SCFH generated the best current density of 10 mA/cm^2 at 250 mV due to wide distribution of MoP_2 grains across the film, which promoted significant interaction between Mo_2S_3 and MoP_2 particles in the heterojunctions that provide sufficient amount of active sites for catalysing hydrogen evolution reaction (HER). With a favourable surface roughness, R_q of 106.4 nm resulted from suitable mean particle size of 1000-3000 nm coupled with film thickness of 968 nm had provided the film with abundance of active sites, which have the propensity to undergo HER reaction in 0.25 M H_2SO_4 acidic media (pH 0.95) owing to a low electron transport resistance of 0.715 kΩ. Based on the Tafel slopes, the approximate overall extracted values of 120 mV/dec for all the fabricated films indicated that Volmer reaction was the rate determining step in HER. Films fabricated at 450 °C with different volumes of precursor solution and deposition times were chosen as a study model for electrochemical studies in alkaline media prepared by mixing 0.25 M of Na_2S and 0.35M of Na_2SO_3 (pH 11.71). It was found

Universiti Malaya

that oxygen evolution reaction (OER) was more significant than HER in alkaline media. However, the 20 mL/20 mins film fabricated at 450 °C with the carrier gas flow rate of 0.5 SCFH exhibited a large Tafel slope of 190 mV/dec and a very large onset potential of 1.14 V in OER. Therefore, Mo_2S_3/MoP_2 composite material may not be a suitable electrocatalyst for OER activity in alkaline media. The electrochemical studies from fabrication of films under different synthesis conditions mentioned above via AACVD could be applied to determine an appropriate morphology that is suitable as electrocatalysts for water splitting application.

Keywords: MoS_2/MoP_2 composite material, AACVD, HER, films, water splitting.

Universiti Malaya

SINTESIS DAN CIRI-CIRI FILEM NANOKOMPOSIT BERASASKAN MOLIBDENUM UNTUK APLIKASI PEMECAHAN AIR

ABSTRAK

Filem nanokomposit berasaskan molibdenum dalam bentuk komposit Mo_2S_3/MoP_2 telah disediakan dengan menggunakan kaedah AACVD dengan prekursor sumber tunggal $[CpMo(CO)_2(S_2P(SPhMe)_2)]$ (1) ($Cp = C_5H_5$) dalam THF pada 0.01 M di bawah aliran gas argon dalam keadaan pemendapan berbeza termasuk suhu pemendapan berbeza (450 °C, 550 °C, 650 °C), tempoh masa pemendapan (20 minit, 30 minit dan 40 minit), isipadu larutan prekursor yang berbeza (10, 15, 20 dan 25 mL) dan kadar aliran gas pembawa (0.3 dan 0.5 SCFH). Nilai tenaga celah jalur yang diperolehi dalam spektrum cahaya kelihatan adalah hampir dengan nilai literatur untuk Mo_2S_3 dan MoP_2 pada ~2.3 eV dan ~2.8 eV, masing-masing. Keadaan pemendapan tidak mempunyai kesan yang ketara ke atas jurang jalur filem. Di antara semua filem yang disintesis untuk kajian ini, filem 20 ml/30 minit yang difabrikasi pada 550 °C dengan kadar aliran gas pembawa 0.3 SCFH menghasilkan ketumpatan arus terbaik 10 mA/cm^2 pada 250 mV disebabkan pengedaran luas butiran MoP_2 merentasi filem itu yang menggalakkan interaksi ketara antara zarah Mo_2S_3 dan MoP_2 yang menyediakan jumlah tapak aktif yang mencukupi untuk memangkinkan tindak balas evolusi hidrogen (HER). Dengan kekasaran permukaan yang menggalakkan (Rq = 106.4 nm) terhasil daripada saiz zarah min yang sesuai 1000-3000 nm ditambah dengan ketebalan filem 968 nm telah menyediakan filem dengan banyak tapak aktif, yang mempunyai kecenderungan untuk menjalani tindak balas HER dalam 0.25 M H_2SO_4 media berasid (pH 0.95) disebabkan oleh rintangan pengangkutan elektron yang rendah (0.715 kΩ). Berdasarkan cerun Tafel, anggaran nilai keseluruhan yang diekstrak sebanyak 120 mV/dec untuk semua filem rekaan menunjukkan bahawa tindak balas Volmer ialah langkah penentu kadar dalam HER. Filem yang direka pada suhu 450 °C dengan isipadu larutan prekursor yang berbeza dan

Universiti Malaya

masa pemendapan telah dipilih sebagai model kajian untuk kajian elektrokimia dalam media alkali yang disediakan dengan mencampurkan 0.25 M Na_2S dan 0.35 M Na_2SO_3 (pH 11.71). Telah didapati bahawa tindak balas evolusi oksigen (OER) adalah lebih ketara daripada HER dalam media beralkali. Walau bagaimanapun, filem 20 mL/20 minit yang direka pada 450 °C dengan kadar aliran gas pembawa 0.5 SCFH mempamerkan cerun Tafel yang besar sebanyak 190 mV/dec dan potensi permulaan yang sangat besar iaitu 1.14 V dalam OER. Oleh itu, bahan komposit Mo_2S_3/MoP_2 mungkin bukan pemangkin elektro yang sesuai untuk aktiviti OER dalam media alkali. Kajian elektrokimia daripada fabrikasi filem di bawah keadaan sintesis berbeza yang dinyatakan di atas melalui AACVD boleh digunakan untuk menentukan morfologi yang sesuai yang sesuai sebagai elektromangkin untuk aplikasi pemisahan air.

Kata kunci: Bahan komposit Mo_2S_3/MoP_2, AACVD, HER, filem, pemisahan air.

Universiti Malaya

ACKNOWLEDGEMENT

First of all, I would like to thank God for His strength and resources which supported me spiritually and emotionally and I must not forget that He also provided me with help through the people to whom I must also extend my deepest gratitude. I would like to thank Professor Dr Richard Wong Chee Seng and Associate Professor Dr Tan Kong Wai who have been my important mentors and supervisors throughout my study and I am very grateful for all their invaluable advice, guidance as well as their friendly support that helped me in the Masters' journey.

I would like to thank my external co-supervisor Dr Ooi Mei Lee who is from Universiti Tunku Abdul Rahman (UTAR) in Kampar, Perak who supervised me in my experimental works and also provided me with access to the instruments in UTAR that were necessary for my research works. Besides, I would like to thank Kelvin Lau Ching, a student from UTAR who helped me a lot with characterization using AFM and SEM.

Moreover, I would like also to thank my collaborator from Physics Department in Universiti Malaya, Associate Professor Dr Goh Boon Tong who guided me in my paper writing, provided me with access to the instruments for my work and also his invaluable advice regarding the analysis of my samples.

In addition to that, I am very grateful to have loving family members who have always been my spiritual support**.** I would also like to express my greatest gratitude to my senior Lim Chu Er who had been my important tutor who taught me a lot in experimental works. I am also thankful to have my two lab mates who are also my close friends, Lee Shiaw Xian and Gan Chun Hau who taught me a lot through their approach in carrying out the lab works

Last but not least, I would like to thank the grants AUA-UAEU Joint Research Grant Project (IF016-2021) (Physics Department) and FP029-2019A (Chemistry Department) for financially supporting my research work.

Universiti Malaya

TABLE OF CONTENT

Universiti Malaya

Universiti Malaya

Universiti Malaya

Universiti Malaya

Universiti Malaya

LIST OF FIGURES

University of Malaya

Universiti Malaya

Universiti Malaya

Universiti Malaya

Universiti Malaya

Universiti Malaya

Universiti Malaya

LIST OF TABLES

Universiti Malaya

Universiti Malaya

LIST OF ABBREVIATIONS

AACVD : Aerosol-Assisted Chemical Vapor Deposition

AFM : Atomic Force Microscopy

CB : Conduction band

Cp : Cyclopentadienyl

CV : Cyclic Voltammetry

DTG : Derivative Thermogravimetry

EDX : Energy Dispersive X-ray

EIS : Electrochemical Impedance Spectroscopy

Eq. : Equation

FESEM : Field Emission Scanning Electron Microscopy

FFT : Fast Fourier Transform

Fig. : Figure

FTO : Fluorine Tin-doped Oxide

HER : Hydrogen Evolution Reaction

HRTEM : High Resolution Transmission Electron Microscopy

JCPDS : Joint Committee on Powder Diffraction Standard

LSV : Linear Sweep Voltammetry

Mo : Molybdenum

MS : Mott-Schottky

OER : Oxygen Evolution Reaction

P : Phosphorus

RHE : Reversible Hydrogen Electrode

S : Sulphur

SCFH : Standard Cubic Feet per Hour

TGA : Thermogravimetric Analysis

Universiti Malaya

THF	:	Tetrahydrofuran
VB	:	Valence band
XPS	:	X-ray Photoelectron Spectroscopy
XRD	:	X-ray Diffraction

Universiti Malaya

CHAPTER 1: INTRODUCTION

1.1 Introduction

Since the industrial revolution, the industrialization and transportation depend heavily on non-renewable energy resources such as fossil fuel, coals and petroleum but one day they will be depleted and the consumption of the hydrocarbon-based fuels is not environmentally friendly as the combustion of the fuels produce greenhouse gases like CO_2 that causes global warming (Fronzi et al., 2018). Therefore, alternative energy resources that are clean and renewable such as hydrogen fuel are highly desirable as substitutes to replace the hydrocarbon-based fuels. Hydrogen fuel when combusted in the fuel system only produces water as the product and hence does not cause environmental issues (Fan et al., 2021). Hydrogen can be utilised as clean energy source for generation of electricity without emission of greenhouse gases like CO_2 and the fuel which has high energy density with high-energy yield of 122 kJ/g which is equivalent to 2.75 times more than fossil-based fuels (Lamb et al., 2020). As of year 2020, the global hydrogen consumption has been reported to be around 400-500 Nm^3 and the rate of hydrogen consumption has gone on increasing trend at the rate of 5-10 % annually (Lamb at al., 2020).

Electrolysis of water or water splitting by electrical energy is a standard method in hydrogen production as green energy (Ariffin et al., 2015). Water splitting process has attracted wide attention for the simplicity of the method and it is also economically appealing. However, the production of hydrogen by electrolysis is still at the primary stage with only 4% of hydrogen gas being produced globally by using this technology (Pareek et al., 2020). Currently, 95 % of hydrogen is produced by steam methane reforming and coal gasification, the methods that are not environmentally friendly (Downes et al., 2018; Rabi et al., 2020). Thermal water splitting or water splitting by heat

Universiti Malaya

energy is also used for hydrogen production in which heat energy is supplied by focusing the sunlight and also by using the waste heat supplied by nuclear reactors (Ariffin et al., 2015; Fronzi et al., 2018). The disadvantage of using thermal water splitting is its low efficiency because very high temperature must be achieved for a complete reaction cycle (~2500 K) (Fronzi et al., 2018). Photoelectrochemical (PEC) water splitting is another type of water splitting process driven by solar energy with the help of photosensitive semiconductor (Ariffin et al., 2015).

In electrolysis process, water is split into hydrogen and oxygen in their respective half reactions namely hydrogen evolution reaction (HER) and oxygen evolution reaction (OER). noble metals such as platinum (Pt), palladium (Pd) and other Pt-based materials are the conventional electrocatalysts used for water splitting process or specifically HER due to its near zero overpotential. Although platinum and Pt-based electrocatalysts have highest efficiency in catalysing HER, but, due to its very expensive cost and its low natural abundancy, the commercialization of the noble metal-based catalysts is limited (Ouyang et al., 2015; Wu et al., 2017). For OER, iridium oxide (IrO_2) or ruthenium oxide (RuO_2) are the benchmark electrocatalysts (Lan et al., 2018). Other Pt group metals like ruthenium (Ru) have attracted much attention due to its relatively low cost and it possesses hydrogen binding energy that is close to Pt and therefore Ru-based electrocatalysts have been developed as well (Li et al., 2021).

Strategies have been developed at the great pace to synthesize the non-noble metal-based electrocatalysts for water splitting, such as sulphides, carbides, phosphides, oxides metal-organic frameworks (MOFs) and carbon-based metal-free materials which are more cost-effective substitutes to replace the noble metal-based electrocatalysts for hydrogen production in the large scale (Fereja et al., 2021; Tang et al., 2018). Among the non-noble electrocatalysts, transition metal chalcogenides and phosphide have proven

Universiti Malaya

high efficiency in catalysing HER (Ouyang et al., 2015). Transition metal dichalcogenides (compounds with the general formula of MX_2) have been developed at great pace for water splitting application (Wang et al., 2015). Among the dichalcogenides, molybdenum and tungsten sulphides (MoS_2 and WS_2) are most studied as electrocatalysts for HER and the materials possess the band gaps of 1.1-1.7 eV (Anantharaj et al., 2016; Hankare et al., 2009). Besides chalcogenides, nitrides, borides and phosphides of Mo and W were reported as efficient catalysts for HER (Anantharaj et al., 2016).

Transition metal chalcogenides are family of inorganic semiconductor materials that are generally used in a range of applications such as photovoltaic devices. They are good candidates for absorber layer in thin film solar cell (Hankare et al., 2009). Among the chalcogens (Group 16 elements), sulphur is widely used in production of electrocatalysts due to its large electronegativity which has the value of 2.5 and it could enhance delocalisation of electrons thus providing efficient electron transfer channel for the electron movement from metal cations to S (Su et al., 2021).

Among the transition metal dichalcogenides, MoS_2, both in amorphous and crystalline states is an attractive material for electronic and optical applications due to its high abundancy and high activity (Song et al., 2016). However, its unsatisfactory electrocatalytic performance is mainly due to its poor conductivity with limited active sites at the edges. The electrocatalytic performance of the MoS_2 is also limited by its poor electrical transport and therefore strategies were developed to change the surface structure of MoS_2 (Song et al., 2016). A stable supply of free moving electrons is highly favoured at the surface of the electrocatalyst for redox reaction and therefore, the mobility of the charge carriers like holes and electrons determines the catalytic performance of the electrocatalyst (Rajamathi et al., 2017).

Universiti Malaya

It was also reported that chemical doping could enhance the electrocatalytic performance of MoS_2 (Liu et al., 2017). Doping with electron donating element such as phosphorus was also found to improve the electrocatalytic activity of MoS_2 (Wu et al., 2017). Other phase of molybdenum sulphide such as molybdenum sesquisulphides (Mo_2S_3) are shown to be more advantageous over MoS_2 due to its structure that favours three-dimensional electron transport (Zhou et al., 2018).

Titania and silicon are used as substrates or medium to support the adhesion of the electrocatalyst onto their conducting surfaces. The materials are non-toxic, abundant in nature and environmentally friendly. However, silicon ($E_g = 1.1$ eV) and other materials with small band gap have stability issues in water splitting environment (Seger et al., 2014). The large bandgap energy value of titania ($E_g = 3.4$ eV) hinders the excitation of electrons from valence band (VB) to conduction band (CB). The band gap must be large enough for sufficient thermodynamic energy required to drive the water splitting process which has the redox potential of 1.23 V. At the same time, the bandgap energy value should be low enough to ensure sufficient kinetic overpotentials for oxygen and hydrogen evolution processes (Chen et al., 2010). Therefore, the position of VB and CB of an electrocatalyst should fit into the potential range of water reduction and oxidation potential (Kochuveedu, 2016).

Aerosol assisted chemical vapour deposition (AACVD) is an inexpensive ambient pressure CVD method which can produce thin films of metal chalcogenide semiconductors (Tedstone et al., 2017). The stoichiometry of the metal and chalcogenide element composition can be controlled by the preparation of precursor solution. AACVD enables the use of less expensive and environmentally friendly chemicals as precursors which is important for mass production (Kun et al., 2018). The final morphology and structure of the thin film on the semiconductor produced by AACVD method can be

Universiti Malaya

controlled by experiment parameters such as furnace temperature, gas flow, concentration and type of precursor (Hernández-Salcedo et al., 2015). In our study, the Mo_2S_3/MoP_2 composite films were fabricated with different parameters of fabrication process by AACVD such as gas flow, deposition time, volume of precursor solution and deposition temperature. The electrochemical property of the films was analysed to study the effect of the final morphology and topology of the films on the performance in HER activity in acidic media as well as OER in alkaline media.

1.2 Objectives

1. To synthesize Mo_2S_3/MoP_2 composite material by AACVD method with the single source precursor solution prepared by dissolving the as-synthesized organometallic complex in a volatile organic solvent (e.g., THF).

2. To characterize of the as-synthesized films by using XRD, Raman spectroscopy, XPS, TEM, AFM and SEM.

3. To determine the bandgap energy value of the as-synthesized films by UV-vis spectroscopy.

4. To investigate the electrochemical properties of the films for water splitting process.

1.3 Scope of Studies

In this study, the Mo_2S_3/MoP_2 composite films were fabricated on the fluorine tin-doped oxide glass substrate by aerosol-assisted chemical vapour deposition (AACVD) method in different synthesis conditions such as durations of deposition, volume of precursor solution and deposition temperatures. Electrochemical studies were performed

Universiti Malaya

to analyse the electronic properties of the films for water splitting process. The surface topology and morphology of the fabricated films were analysed to study the effect of the fabrication conditions on the electrocatalytic performance of the composite films. The optical property of the films was also studied to determine the bandgap energy values which were used to construct the band diagram for electron transfer mechanism during water splitting process.

Universiti Malaya

CHAPTER 2: LITERATURE REVIEW

2.1 Electrochemical water splitting

In water splitting process, water is broken down into hydrogen (hydrogen evolution reaction, HER) described as the reductive half reaction at cathode and oxygen (oxygen evolution reaction, OER) as the oxidative half reaction at anode with the help of semiconductor as an electrocatalyst. However, water splitting is thermodynamically unfavourable and hence electrocatalysts with high efficiency are required to render the process more feasible. The threshold potential for water splitting is 1.23 V ($\Delta G° = 237.2$ kJ/mol). In acidic media, HER occurs at 0 V whereas OER occurs at 1.23 V (Anantharaj et al., 2016; Li et al., 2021) whereas in alkaline media, HER occurs at -0.828 V and OER at 0.402 V (Li et al., 2021). The overall half reactions for HER and OER are shown in the following.

HER: $2H^+(aq) + 2e^- \rightarrow H_2(g)$ (2.1)

OER: $2H_2O(l) \rightarrow 4e^- + 4H^+(aq) + O_2(g)$ (2.2)

Taking 100 % as the ideal Faradaic efficiency for water splitting process, the amount of hydrogen evolved is twice the amount of oxygen produced and both half reactions depend on the total electrical charge flow in the solution (Shi et al., 2016). Fig. 2.1 illustrates the electrochemical water splitting process. Small band gap is desirable in the electrocatalyst which facilitates electron movement, charge transfer and enhances the electrical conductivity of the material (Liang et al., 2018). As a high-performance HER electrocatalyst, the bottom of the conduction band has the potential which is more negative than HER redox potential and the top edge of the valence band has the potential which is more positive than the OER redox potential (Sathish et al., 2006).

University Malaya

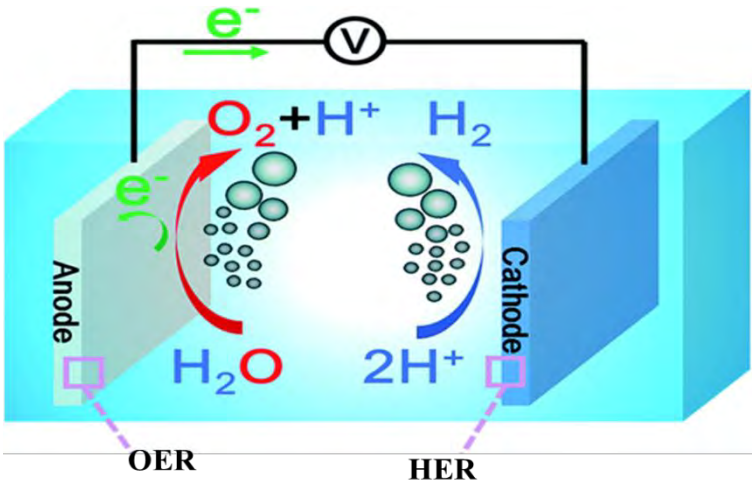

Figure 2.1: Electrochemical water splitting process with HER and OER half reactions (Figure sourced from Yan et al., 2016).

The materials with low band gap are desired for a vast array of applications such as optical, transistors, batteries, insulators, catalysts, photocatalysis, gas sensors and environmental purification (Ayal et al., 2016; Seo et al., 2015). Electrocatalytic semiconductors can be categorised as p-type, n-type and hybrid. The mechanism of water splitting catalysed by p-type, n-type and hybrid semiconductors are illustrated in Fig. 2.2. Mechanism water splitting involves the generation of hole-electron charge carrier pairs. The holes oxidise water to generate oxygen and electrons reduce H^+ to H_2 (Joy et al., 2018).

Universiti Malaya

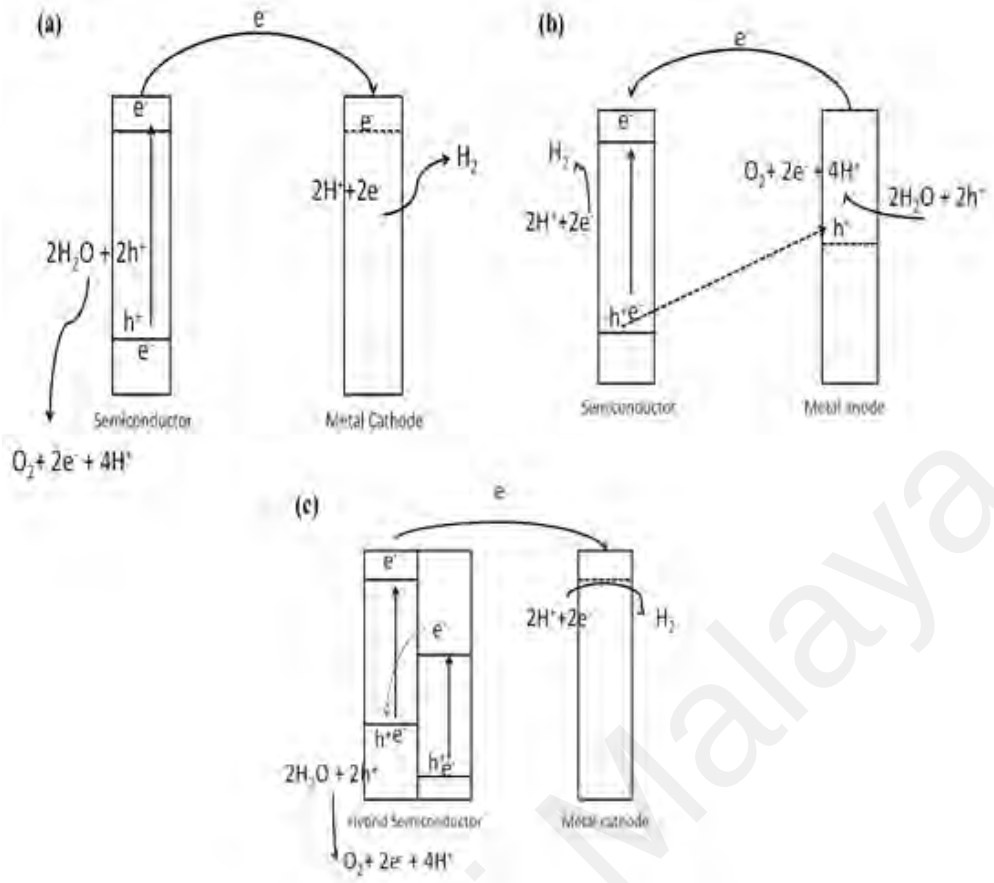

Figure 2.2: Water splitting mechanism of (a) n-type, (b) p-type and (c) hybrid semiconductor electrocatalysts (Figure sourced from Minggu et al., 2010).

In water splitting, HER involves hydrogen adsorption and desorption mechanism. The highly efficient HER electrocatalysts have the near zero value of free energy for hydrogen adsorption, ΔG_{H*} which indicates strong binding of hydrogen atoms to the surface as well as good desorption of hydrogen atoms as H_2 gas (Fronzi et al., 2018).

2.2 Transition Metal Compounds (TMCs)

Transition elements have unpaired d-orbital electrons that are available to participate in electrocatalytic activity and therefore, TMCs are widely studied to access their electrocatalytic property in water splitting application (Li et al., 2021). TMCs are also earth abundant and can be utilized in a large scale as materials to catalyse water

Universiti Malaya

splitting process. TMCs include transition metal oxides, nitrides, phosphides, carbides and sulphides (Zhang et al., 2020). The electronic properties of the transition metal cations promote the synergistic effect between the cations and heteroatoms (C, S, P etc.) in the TMCs materials (Xu et al., 2021).

Among the TMCs, transition metal sulphides are regarded as the novel 2D materials and their electronic and optical properties are tuneable for their wide applications such as transistors, batteries and catalysts (Seo et al., 2015). Compounds like transition metal chalcogenides (Group 16 elements) for instance MoS_2 and WS_2 had been used as HER catalysts. As bulk materials, both chalcogenides have the indirect band gaps of ~1.3 eV and ~1.4 eV respectively (Tedstone et al., 2017).

Transition metal phosphides (TMPs) are also fabricated as potential electrocatalysts to drive water splitting process. TMPs can be understood as highly electronegative phosphorus element being doped into the transition metals such as Fe, Co, Cu, Ni, Mo and W (Shi et al., 2016).

In TMPs, due to electronegativity of phosphorus, the presence of metal-phosphorus bonds could cause a minor stabilization of 3d orbital of the transition metals and also small charge transfer from the metal cations to phosphorus. In the phosphorus-based electrocatalyst for HER, the phosphorus atoms that are more negatively charged can effectively trap positively charged hydroxonium ions or protons in the electrolyte whereas metal cations in the TMPs act as hydride acceptors (Fereja et al., 2021). Considering this fact, HER activity can be improved by increasing the atomic percentage of phosphorus (Shi et al., 2016). In a study involving monodispersed nickel phosphide nanocrystals, a series of nickel phosphide with varied compositions of Ni and P were produced (Ni_2P, Ni_5P_4 and $Ni_{12}P_5$). Among the nickel phosphides, Ni_5P_4 which had the highest atomic percentage of P (44%) exhibited the highest catalytic performance (Xiao

Universiti Malaya

et al., 2014). However, if the material is heavily doped with more electronegative phosphorus, the material will exhibit poor conductivity due to delocalisation of electron in metal (Guruprasad et al., 2019). Therefore, the amount of P in TMPs must be optimised for good catalytic activity and good conductivity of the materials (Fereja et al., 2021).

Mo-based catalysts have shown excellent electrochemical performance with similar electrocatalytic performance as Pt-based electrocatalysts (Wu et al., 2017; Xu et al., 2021). The undoped MoS_2 showed n-type behaviour while the P-doped MoS_2 showed p-type behaviour. The donor and acceptor concentrations for undoped MoS_2 sample and P-doped MoS_2 were reported to be $\sim 2.6 \times 10^{15}\ cm^{-3}$ and $\sim 1.0 \times 10^{19}\ cm^{-3}$ respectively (Momose et al., 2018).

2.2.1 Molybdenum Disulphides

Molybdenum disulphide, MoS_2 is easily fabricated and the material could possess the 2D structure like that of the graphene (Guruprasad et al., 2019). In 2D structure, MoS_2 has similar ΔG_{H*} to Pt therefore becoming the focus of attraction in researches for developing high-performance HER catalysts (Xu et al., 2021). The material is also attractive for its high carrier mobility (Momose et al., 2018). MoS_2-based materials are cost effective, highly stable and possessing great potential in electrocatalytic hydrogen production (Liu et al., 2017). The material has also the favourable optical band gap of ~1.8 eV in the visible spectrum (Yang et al., 2015). However, bulk MoS_2 exhibits poor electrocatalytic performance in HER but when in the nanoparticle phase, MoS_2 is shown to exhibited high activity in catalysing HER (Jaramillo et al., 2007).

MoS_2 exists in many phases such as 2H, 3R, 1T, 1T'*etc*. depending on the arrangement of MoS_6 which is the building blocks of the MoS_2 structure and each phase exhibits different performances of the material in HER (Zhou et al., 2018). For instance,

Universiti Malaya

2H and 3R phases show limited HER performance due the low conductivity and their lack of active basal planes whereas 1T' phase possesses Mo-Mo chain in a zigzag structure which exhibits better HER performance however the electron transport in 1T' along c-axis is restricted by the intermolecular Van der Waals forces of attraction. (Zhou et al., 2018).

Despite many advantages MoS_2 are bestowed with, however, the unsatisfactory electrocatalytic performance is mainly due to its poor conductivity with limited active sites in the edges instead of the more exposed basal planes. The nanosheets in the bulk MoS_2 are stacked together by weak intermolecular Van der Waals force causing the accessibility of the active sites to be restricted (Guruprasad et al., 2019). The electrocatalytic performance of the MoS_2 is also limited by its poor conductivity (Song et al., 2016). 2H-MoS_2 and 1T'-MoS_2 were reported to reach 10 mA/cm^2 which is the benchmark current density for HER activity at the overpotentials (vs. RHE) of 320 and 187 mV respectively (Higgins et al., 2021). The HER activity of the MoS_2 by solely utilising the expose edge has already reached its limit until this day due to its poor inter-particle electron transport (Liu et al., 2017). Therefore, strategies to enhance the HER activity of its basal planes are greatly sought after.

The 2H-MoS_2 phase in bulk state has the reported indirect and direct band gaps of 1.2 and 1.95 eV respectively at room temperature (Frey et al., 1999).

2.2.2 Molybdenum Sesquisulphides (Mo_2S_3)

The 3D crystal structure of Mo_2S_3 is understood as molecular Mo-S chains intercalated in 1T'-MoS_2 and the resulting structure provides Mo_2S_3 with better electrical conductivity (33670 S/m at 300 K) than 2H-MoS_2 (0.005 S/m at 300 K) and 1T'-MoS_2

Universiti Malaya

(4116 S/m at 300 K) due to the zigzag chains in Mo_2S_3 being bonded to 1T' units, offering three-dimensional electron transport (Zhou et al., 2018).

Mo_2S_3 nanorods had been synthesized by solid-gas reaction at 870 °C in H_2S/Ar (Che et al., 2003). Mo_2S_3 nanoflowers had also been synthesized by using CVD at 810 °C (Zhong et al., 2012). Urchin-like Mo_2S_3 had the small onset potential of 67 mV, reaching current density of 10 mA/cm^2 at 257 mV and had the small Tafel slope of 64 mV/dec (Zhou et al., 2018). The pure monoclinic Mo_2S_3 in nanoflower structure (diameter = 0.5-2.0 μm and leaf thickness = ~10 nm) had also been successfully synthesized at low temperature of 150 °C using hydrothermal method (Nishanthi et al., 2019).

The ultrathin Mo_2S_3 nanosheets synthesized on N, S-dual-doped graphitic biocarbon spheres were also reported and the resulting structure contained rich active sites which bestowed the material with high HER kinetics (Bo et al., 2022). The rhombohedral phase change from MoS_2 to Mo_2S_3 was observed by doping with Ni cations into MoS_2 (Swathi et al., 2019). Other Ni/Mo-based material such as tubular NiS/Mo_2S_3 microspheres had also been fabricated as high-performance supercapacitors (Wu et al., 2021). Fabrication of heterostructure involving Mo_2S_3 such as Co_3S_4/Mo_2S_3 has also been reported in the PEC water splitting application (Li et al., 2022).

2.2.3 Molybdenum phosphides

Transition metal phosphides (TMPs) could exhibit favourable electrocatalytic performance in HER due to the presence of lone-pair electrons in 3p and unoccupied 3d orbitals in phosphorus which promotes local charge density as well as accommodates surface charge state (Ouyang et al., 2015).

Of the examples of TMPs, molybdenum phosphide (MoP) has been shown to be a candidate as an active HER catalyst. The advantages of molybdenum phosphides are

Universiti Malaya

high abundancy and their stability in both acidic and alkaline conditions (Wu et al., 2017). It has been studied for its catalytic property in hydro-desulfurization (HDS) (Wu et al., 2016).

The electrochemical performance of MoP and MoP_2 for HER was compared and it was found that MoP_2 had more superior catalytic activity than the MoP materials due to higher P content in MoP_2 nanoparticles, which provided more active sites than MoP nanoparticles (Wu et al., 2016). The increased activity caused by higher atomic percentage of P was shown by another study involving MoP and Mo_3P, MoP with the higher atomic percentage of P required lower overpotential than Mo_3P to achieve the same current density in the electrochemical studies (Pan et al., 2015). MoP_2 nanosheets on carbon cloth have been synthesized and the material exhibited high catalytic activity in HER and the performance is more superior than MoS_2 on carbon cloth (Zhu et al., 2016).

2.3 Properties of Electrocatalysts

2.3.1 Film Thickness

The surface property of the thin films determines the transport of the charge carriers such as electrons (Lin et al., 2016). The film thickness effect on the hydrogen absorption and desorption of palladium on gold single crystal electrodes had been reported (Kibler, 2008). Therefore, the influence of film thickness on the materials is significant and the parameter has to be considered in optimizing the performance of the as-fabricated electrocatalysts as well as photocatalysts (Downes et al., 2018). In the study carried out by Downes et al., the CoBHT (CoBHT = cobalt benzenhexathiolate) modified glassy carbon electrodes with varying film thickness were fabricated and the increasing trend in HER activity was observed with increasing film thickness (23-244 nm) but when

Universiti Malaya

the thin film thickness reached 1000 nm, the HER activity decreased showing insufficient electron migration from the surface through the thick film (Downes et al., 2018).

Lin et al. had reported the effects of thickness on the HER performance of the MoS_2 thin films on SiO_2-Si substrate and found that conductivity decreased with the increase in film thickness and as a result the higher charge transfer efficiency for the electrons to migrate from the MoS_2 surface to the protons was observed in the thin film with smaller thickness (Lin et al., 2016).

In photocatalysts, the film thickness is also an important factor which determines the material's energy conversion efficiency from solar energy to HER activity (Patil et al., 2003). The film thickness of the photocatalysts must be adjusted to reduce the hole-electron recombination process and also retaining the sufficient amount of the light harvesting material in photocatalysts (Kim et al., 2020).

The relationship between the film thickness with particle size of the photocatalysts was shown by Patil et. al by fabricating $CdS_{0.9}Te_{0.1}$ materials with varying thickness and it was found that grain size of the thin film increased with the increase in film thickness (Patil et al., 2003).

2.3.2 Particle Sizes

The performance of the electrocatalysts can be enhanced by the manipulation of the electronic structure by adjusting the particle size/shape parameter (Su et al., 2021). The particle size effects determine the catalytic activity per active site which is crucial for the electrocatalytic performance of the electrocatalysts. Reducing the particle size of the deposit can improve the performance of the electrocatalysts by increasing the surface area of the electrocatalyst and exposing more active sites of the materials (Kudo et al., 2000; Wang et al, 2018). The enhanced OER activity due to more exposure of active sites of the

Universiti Malaya

crystalline RuO_2 by particle size reduction was reported (Jirkovský et al., 2006). The electrochemical performance also showed a decreasing trend with increasing particle size of Co_3O_4 due to the decreasing number of active sites that is required for the electrocatalytic activity (Kudo et al., 2000).

It was reported that band gap increased when the particle size decreased but on the contrary, lower particle sizes and higher surface area of the material promoted higher HER rate (Sathish et al., 2006). In photocatalysts, the surface area determines the number of active sites and the particle size affects the distance the photogenerated holes and electrons take to migrate to the active sites (Kudo et al., 2000). It was also reported that increasing particle size increased the charge transfer resistance of the electrocatalysts and increased the probability of recombination of electron-hole pair which is not desirable in photocatalysts. (Kudo et al., 2000; Saha et al., 2018). Therefore, the optimization of particle size is required in fabrication of efficient electrocatalyst (Wang et al., 2015).

2.3.3 Morphology

Morphology of the fabricated catalysts is an important denominator for the reaction kinetics of catalysts in HER. In the study involving MoS_2/MoP catalysts, the porous structure shown in the SEM analysis was shown to have enhanced the diffusion of charges in the electrolyte which resulted to better electrocatalytic performance whereas the core-shell structure of the MoS_2/MoP catalyst had less interfaces between MoS_2 and MoP and therefore exhibiting poorer electrochemical performance than the catalyst with homogenous distribution of MoS_2 and MoP (Wu et al., 2018). Porous structure could provide large surface area of contact of active material with electrolyte which may result to enhanced electrocatalytic performance (Zhang et al., 2018). The S-doped MoP material had been fabricated by electrochemical anodic treatment combined with two-step chemical vapour deposition (CVD) method and the resulting porous morphology after the

Universiti Malaya

electrochemical anodic treatment was found to promote proton transport, hydrogen absorption and electron transfer (Liang et al., 2018).

Sheet-like structure also endows the electrocatalysts with outstanding electrocatalytic kinetics of the materials. The sheet-like morphology provides more active sites for water splitting activity (Wu et al., 2019). The strong interface connection between MoP nanoparticles with carbon nanotube network greatly enhanced the electrocatalytic performance of MoP/MWCTs (MWCT = multi-walled carbon nanotubes) material owing to large active surface area and enhanced electronic transport (Xiao et al., 2021). The uniform hybridization of the small MoP particles with carbon nanotubes benefited the MoP/CNTs with superior HER activity (Zhang et al., 2018). It was also reported that highly dispersive small nanoparticles of the electrocatalyst could result to enhanced diffusion rate of the electrolyte in penetrating the electrocatalyst and subsequently leading to excellent HER performance (Zhang et al., 2018).

2.3.4 Surface roughness

The performance of the electrocatalyst also depends on the surface roughness. In photocatalytic application such as photoelectrochemical (PEC) water splitting, the surface roughness plays important role in absorption of solar light. Generally, there are three main types of surface morphology namely the V-type groove, sinusoidal and random structures and the figures illustrating the surface morphology are displayed in Fig. 2.3 (Niu et al., 2019). The high surface roughness of the electrocatalyst contributes to more accessible active sites for HER activity and leads to the improvement in electrocatalytic behaviour of the materials (Abdel-Karim et al., 2012; Dai et al., 2017) . However, too much surface roughness may lead to high resistivity to electron transport due to increased scattering of electrons (Tang et al., 2012). Therefore, the surface roughness should be optimised to

Universiti Malaya

ensure low resistivity in electron transport as well as more assessable active site for electrocatalytic activity.

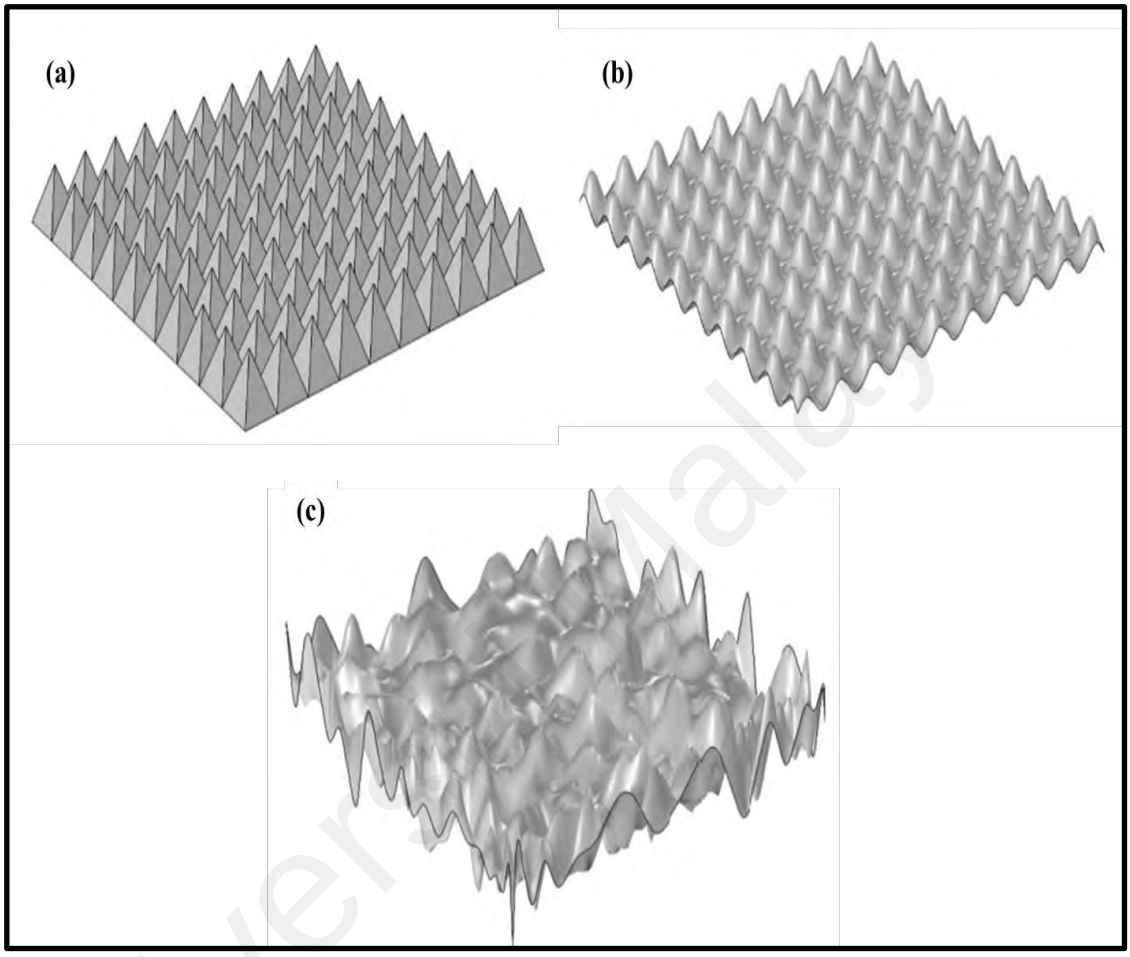

Figure 2.3: Three types of surface morphology namely (a) V-type groove, (b) sinusoidal and (c) random structures (Figure sourced from Niu et al., 2019).

2.4 Strategies to improve Electrocatalytic Properties of Molybdenum Sulphides Materials

2.4.1 Phase Transformation

To overcome the limitations that restrict the high performance of MoS_2 in HER, strategies to change the surface structure of MoS_2 had been developed and the phase transformation from less electronic conductive 2H-MoS_2 to more electronic conductive metallic 1T-MoS_2 had been performed (Song et al., 2016). Other strategies were also

developed to engineer the nanostructure of MoS_2 into hollow spheres, defective nanosheets, amorphous films, and nanoflower that exhibited enhanced electrocatalytic performance than the bulk MoS_2 (Liu et al., 2017). The reduction of stacked layers of the MoS_2 has been the main focus aimed for increasing the number of edge sites which are active in electrocatalytic performance (Song et al., 2016).

2.4.2 Chemical Doping

Chemical doping could enhance the electrocatalytic performance of MoS_2 (Liu et al., 2017). MoS_2 especially in 2H-MoS_2 phase have large number of in-plane domains that are not active for electrocatalytic activity and therefore heteroatom doping applied to the material can activate the in-plane domains causing charge transfer to the defects and promote the charge distribution and electrocatalytic activity is enhanced as a result (Li et al., 2021). Electrocatalysts with hetero-doping such as, nitrogen-sulphur co-doped graphene, metal sulphide doped with second metal, Pt-doped MoS_2, phosphorus-modified WN/graphene and oxygen-modified MoS_2 had shown improved HER performance (Ouyang et al., 2015). The doping of Pt atom in the sulphide activated the in-plane sulphur atoms to catalyse HER (Deng et al., 2015). The enhanced electrocatalytic performance is due to the changes in the charge states caused by alteration in the band gap, enhanced interaction with the dopants as well as altered surface and charge property. (Ouyang et al., 2015).

Large band gap restricts the electron flow from valence band to conduction band. This process is important to drive free moving electrons to participate in water splitting process. For metal sulphide-based material, doping with a second metal cation such as Fe, Co and Ni was found to improve the catalytic performance of the metal sulphides by decreasing the band gap between VB and CB of metal sulphides which is desirable for

Universiti Malaya

enhancing electrical conductivity, electron movement and charge transfer (Merki et al., 2012; Liang et al., 2018). Doping with heteroatom like S was shown to decrease the band gap in MoP (Liang et al., 2018). The band gap of the monolayer MoS_2 and MoP were reported to be ~2.18 and ~2.07 eV, respectively and the resulting S-doped MoP had the low band gap of 0.62 eV (Liang et al., 2018).

Doping also promotes the formation of defects which benefits the electrocatalytic performance of the material. Mo-doped Ni_2P and W-doped MoP materials exhibited better performance in HER owing to the reduction in the number of d-band electrons of Ni in Ni_2P so that it could accommodate the filling of electrons for HER and the presence of defects in MoP endowed the material with enhanced active sites for HER activity (Fereja et al., 2021).

Group V elements (N, P, As) were reported as candidates for an acceptor in MoS_2 of which, P is suitable candidate because it is nontoxic, stable in air as solid and also the element is compatible with semiconductors (Momose et al., 2018). Doping with electron donating element such as phosphorus was also found to improve the electrocatalytic activity of MoS_2 (Wu et al., 2017). However, the mechanism of P in enhancing the activity of molybdenum chalcogenides in HER was not clarified (Ye et al., 2016). It was reported that P-dopant created crystal defects in MoS_2 and subsequently enhanced its electrocatalytic property (Guruprasad et al., 2019).

Phosphorus can occupy between layered structure of MoS_2 and thus is able to reduce agglomeration of the structure causing more exposure of active sites for HER process (Guruprasad et al., 2019). P dopant was also found to enlarge the (002) interlayer spacings to 0.91 nm from 0.62 nm (pristine MoS_2) in MoS_2 which enhanced the hydrogen adsorption and release, exhibiting low overpotential of ~43 mV at 10 mA/cm^2 and possess small Tafel slope of 34 mV/dec (Liu et al., 2017).

Universiti Malaya

The difference in electronegativity of S and P (S higher than P) can tune the hydrogen adsorption free energy, ΔG_{H*} and enhance the reversible binding of hydrogen to the electrocatalyst (Wu et al., 2018). The binding energy between the hydrogen atom and substrate is related to the work that is required to fill the initial unoccupied electronic state of the substrate (Ye et al., 2016).

The ΔG_{H*} of the P dopants was calculated to be 0.04 eV and acted as the active sites for HER and also reduced the ΔG_{H*} of sulphur in the basal plane to 0.43 eV from 2.2 eV of the pristine MoS_2 (Liu et al., 2017). The HER free energy diagram is displayed in Fig. 2.4 to show the hydrogen adsorption mechanism of the P-doped MoS_2. The result had shown that the basal plane of the MoS_2 had become active for HER activity by the presence of the P dopant which facilitated faster electron transfer rate between the basal planes of MoS_2.

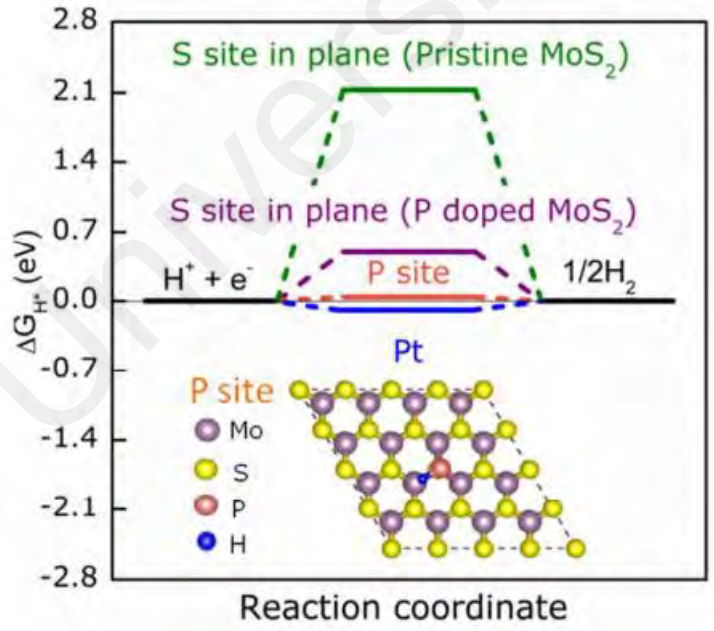

Figure 2.4: HER free energy diagrams of pristine MoS_2 and P-doped MoS_2 (Figure sourced from Liu et al., 2017).

Universiti Malaya

2.4.3 Heterostructures

The synergistic effect of dual materials (e.g., between P and S) in the electrocatalyst promotes remarkable performance. Phosphorization of MoS_2 at suitable temperature can promote the formation of MoS-MoP heterostructures, which provides active sites rich in defects and interfaces (Li et al., 2021). The similar atomic radii of S and P enables the replacement of S by P to create the heterojunction material (Wu et al., 2019).

The solid solution $MoS_{2(1-x)}P_x$ had been synthesized by annealing the MoS_2 particulate with different amounts of red phosphorus incorporated into the solid solution at 750 °C in argon/hydrogen flow with MoS_2 being transformed into MoP during the reaction (Ye et al., 2016). The results obtained from the work carried out by Ye et al. demonstrated that $MoS_{0.94}P_{0.53}$ solid solution which had larger surface area than the other solid solutions with varying S and P compositions, provided the solid solution with the best HER kinetics (Liang et al., 2018; Ye et al., 2016). The $MoS_{2(1-x)}P_x$ solid solution was found to exhibit the maximum performance with the reported overpotential of ~150 mV to generate the current density of 10 mA/cm^2 (Wu et al., 2017). Fig. 2.5 illustrates the role of P alloying in promoting greater absorption of hydrogen atom on the MoS_2 catalyst by accommodating more electrons from the adsorbed hydrogen atoms in the $MoS_{2(1-x)}P_x$ solid solution.

S doped into MoP was reported to be the promising high-performance HER catalyst due to the synergistic effect between P and S anions in the electrocatalyst (Kibsgaard et al., 2014; Liang et al., 2018). In MoP catalyst, the introduction of S into the material promoted the formation of surface phosphosulphide which provided active sites in HDS (Kibsgaard et al., 2014). S dopants can promote the electron transfer from electrocatalyst to electrolyte (Liang et al., 2018).

Universiti Malaya

In the MoS_2/MoP catalysts, the formation of heterogenous interfaces between MoS_2 and MoP create active sites for excellent HER performance and allow the migration of electrons (Wu et al., 2019; Wu et al., 2017). The hierarchical flower-like MoS_2/MoP core-shell heterojunctions had also been designed and the material had exhibited excellent electrocatalytic performance over broad pH range (Wu et al., 2016). The tuning of MoP/MoS_2 ratio can also affect the performance of the heterostructure material (Wu et al., 2019). The improved activity in the MoS_2/MoP heterostructure was attributed to the electronic interactions between MoS_2 and MoP through charge redistribution but, the actual mechanism in the enhancement of HER performance was not yet clarified (Li et al., 2021; Wu et al., 2017; Ye et al., 2016).

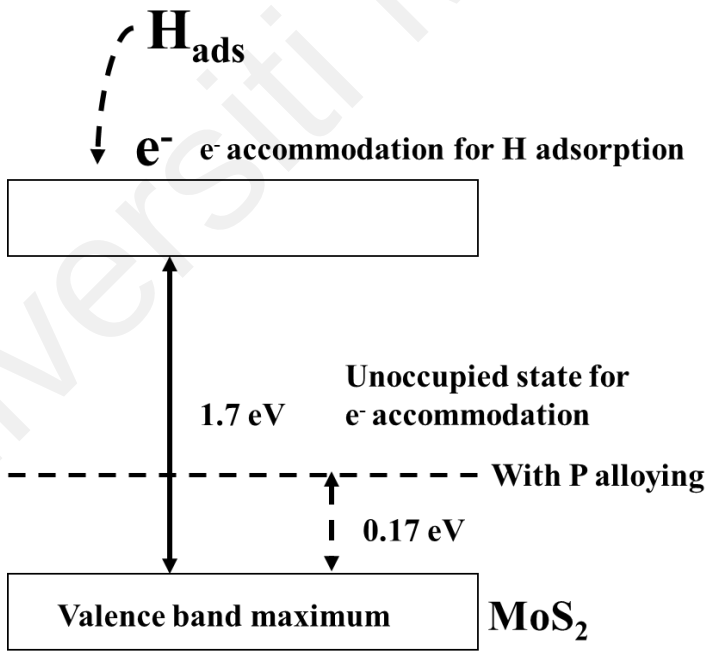

Figure 2.5: The role of P in promoting greater H adsorption on the MoS_2 catalyst in $MoS_{2(1-x)}P_x$ solid solution (Figure sourced from Ye et al., 2016).

Universiti Malaya

2.4.4 Doped Heterostructures

The HER activity of MoS_2/MoP heterostructure can be further improved by being introduced with the noble metal single atom sites (e.g., Ru) (Li et al., 2021). Li et al. had synthesized Ru-doped MoS_2/MoP heterostructure that were grown on the conductive carbon cloth and overpotentials of 45 and 114 mV were required to generate the current density of 10 mA/cm^2 and 100 mA/cm^2 respectively (Li et al., 2021). This shows the enhanced activity of the heterostructure material can be promoted by doping with foreign atom.

2.5 Factors affecting the Performance of P-doped Molybdenum Sulphide Materials

2.5.1 Matrix of Electrocatalyst

A suitable matrix for the electrocatalyst can enhance the electrocatalytic performance of the materials. The use of carbon sphere support in producing MoS_2 catalysts had improved the HER performance by reducing aggregation of the catalysts, increasing surface area for improved contact with electrolyte and reducing the resistance (Wu et al., 2017).

The use of conducting carbon matrix such as reduced graphene oxide (rGO) and porous carbon electrodes were reported to have enhanced the conductivity of the electrocatalysts and hence bestowing the materials with enhanced electrocatalytic kinetics (Higgins et al., 2021). In comparison with the HER performance of pristine MoP which exhibited the current density of 10 mA/cm^2 with overpotential of 177 mV vs. RHE, the MoP supported with carbon sphere was shown to produce the same current density with lower overpotential of 136 mV vs. RHE. 1T'-MoS_2 in carbon-based matrix was also reported to have produced 10 mA/cm^2 with lower overpotential of 180 mV vs. RHE from

Universiti Malaya

187 mV without the carbon matrix. This has shown that the presence of supporting medium such as carbon-based matrix can enhance the electrochemical performance of the catalyst in HER (Wu et al., 2016; Wu et al., 2017).

The reported use of polypyrrole provided carbon matrix to MoS_2-MoP prevented the aggregation of the catalyst during high temperature treatment and this advantage was bestowed to the composite material to exhibit more superior electrochemical performance than the same heterostructure without the carbon matrix requiring 55 mV lower overpotential than the latter to generate 10 mA/cm^2 (Wu et al., 2017). The carbon matrix also increased the interlayer distance of the heterostructure leading to enhanced electronic conductivity within the material (Wu et al., 2017).

It was reported that MoP catalyst was difficult to be fabricated on silicon substrates due to their incompatibility so a graphene interlayer was introduced between Si and MoP catalyst to effectively incorporate the two materials together (Jun et al., 2021). In photoelectrochemical applications, the graphene enhances the flow of photogenerated electrons through Mo-O-C covalent bonding which provided the bridging for MoP catalyst and thus improves HER process with its numerous active sites (Jun et al., 2021).

2.5.2 Deposition temperature

The synthesis temperature has significant effect on the electrocatalytic property of the electrocatalysts. Based on the study carried out by Wu et al., the electrocatalytic performance of the MoP-MoS_2 catalyst treated at temperature of 800, 900 and 1000 °C were displayed in Table 2.1 which showed enhanced performance from 800 to 900 °C due to increased loading of MoP but the electrocatalytic performance was poorer at 1000 °C which was caused by aggregation in the catalyst at high temperature (Wu et al., 2018).

Universiti Malaya

Table 2.1: The onset potentials and overpotentials at 10 mA/cm^2 for the MoP-MoS_2 treated at different temperature (Table sourced from Wu et al., 2018).

Temperature (°C)	Onset Potential, η_0 (mV)	Overpotential, η_{10} (mV)
800	107	176
900	64	102
1000	86	139

It was also reported that phosphating temperature could also control the MoP/MoS_2 composition of the heterostructure material shown by the lower MoP content in the material produced at lower phosphating temperature (Wu et al., 2019).

2.5.3 Amount of Dopants

The P ratio in the $MoS_{2(1-x)}P_x$ solid solution had significant effect on the electrochemical performance of the materials. The *J-V* curves obtained from LSV analysis carried out by Ye et al. for the $MoS_{2(1-x)}P_x$ solid solution with different P content are displayed in Fig. 2.6. Due to the similar atomic radii of P and S, P is introduced into MoS_2 by substitutional doping in which P replaces the S-site of MoS_2 (Momose et al., 2018; Ye et al., 2016).

Universiti Malaya

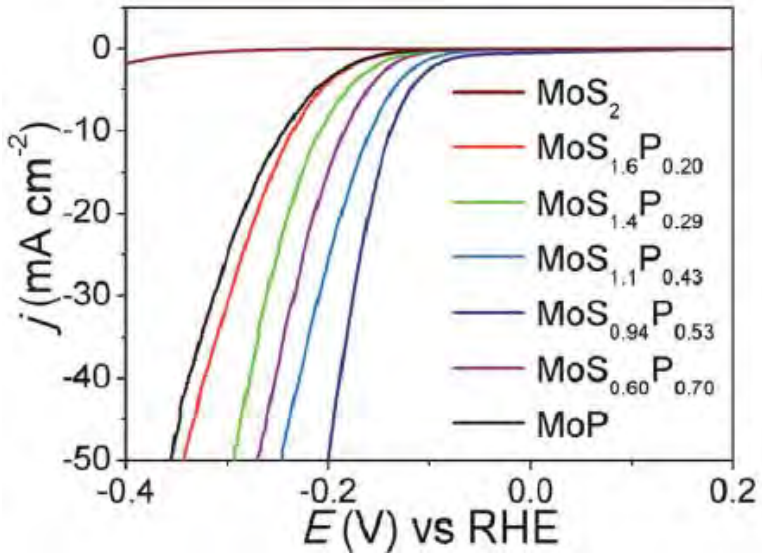

Figure 2.6: *J-V* curves of $MoS_{2(1-x)}P_x$ where x = 0-1 (Figure sourced from Ye et al., 2016).

The P-doped MoS_2 was also prepared by Liu et al. with different amount of P dopants. In the study, the *J-V* curves displayed in Fig. 2.7 obtained from LSV analysis showed that increasing amount of P-dopant into MoS_2 exhibited improved electrochemical performance of the materials (Liu et al., 2017). The Mott-Schottky (MS) plot shown in Fig. 2.8 displayed decreasing slopes (increasing charge carrier density) with increasing amount of doped P indicating that higher P content in the MoS_2 nanosheets increased the charge carrier densities of the semiconductor (Liu et al., 2017).

Universiti Malaya

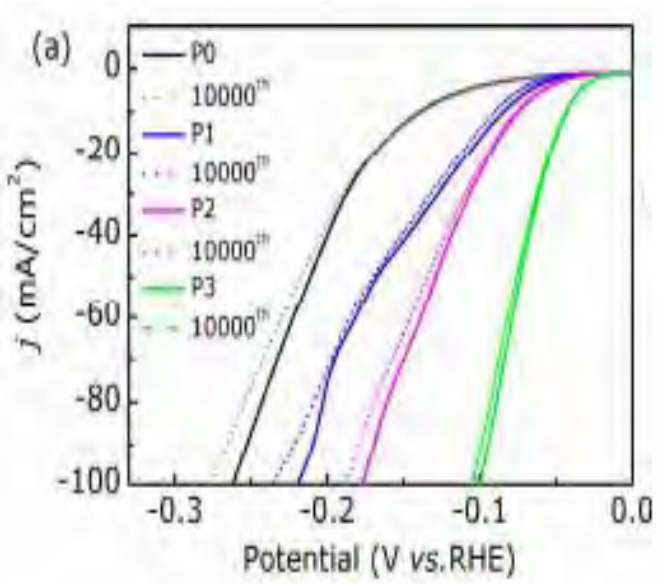

Figure 2.7: *J-V* curves of MoS|P samples where P0 is only MoS_2 and P1, P2, P3 are a series of increasing amount of P doped into MoS_2 (Figure sourced from Liu et al., 2017).

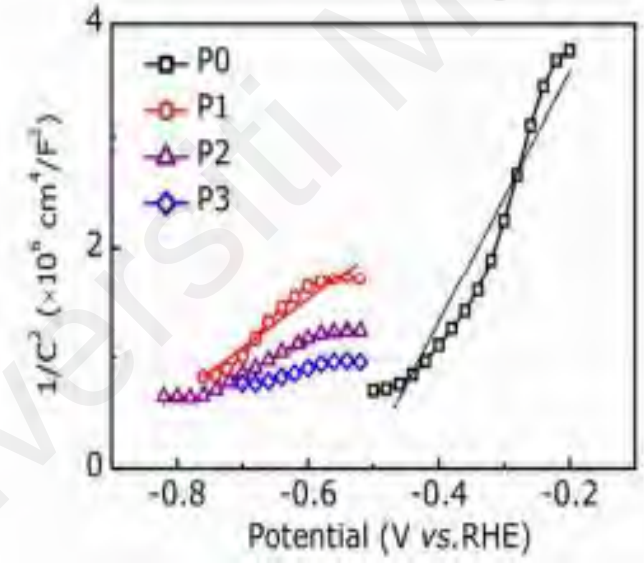

Figure 2.8: Mott-Schottky plots of MoS|P samples where P0 is only MoS_2 and P1, P2, P3 are a series of increasing amount of P doped into MoS_2 (Figure sourced from Liu et al., 2017).

Wang et al. had fabricated the hybrid black phosphorus quantum dot-MoS_2 by a method called liquid exfoliation method in which the monolayered MoS_2 was coated onto SiO_2/Si wafer followed by pipetting the absolute alcohol solution of black phosphorus onto the MoS_2 surface and dried at 40 °C on hot plate in CVD (Niu et al., 2021). The

black phosphorus quantum dots increased the material's conductivity by giving high concentration of electrons, that was ~5.39×10^{12} cm^{-2} (with 10 μL BP QD solution) (Niu et al., 2021). The study had shown that the higher the amount of phosphorus doping, the higher the charge carrier concentration would be. Based on the abovementioned studies, it is found that the amount of phosphorus doping has significant effects on the electrocatalytic performances of the transition chalcogenide thin films by increasing the electron density of the electrocatalyst.

2.5.4 Precursor Sources

The type of precursor sources also contributes to the performance of P-doped molybdenum chalcogenide materials in HER process. Ye et.al had demonstrated that the mixing of MoS_2 and MoP in the ratio of 1:1 or 1:4 did not improve HER performance synergistically although the ratios resembled that of $MoS_{0.94}P_{0.53}$ and$MoS_{0.60}P_{0.70}$ solid solutions respectively (Ye et al., 2016). This has shown that the catalyst fabricated from single source precursor may exhibit different HER performance from the catalyst which is fabricated from mixing of more than one precursor sources even though the atomic ratio of Mo, S and P are the same in single-source and dual-source precursor.

2.6 Aerosol-assisted Chemical Vapour Deposition (AACVD)

Deposition of the electrocatalyst materials on the substrates is carried out by various methods such as spray pyrolysis, sol-gel, metal-organic chemical vapour deposition (MOCVD) as well as aerosol-assisted chemical vapour deposition (AACVD) (Ketchemen et al., 2018).

Of the abovementioned deposition methods to fabricate electrocatalytic materials, AACVD is a simple technique for the one-step fabrication of the catalyst in ambient

Universiti Malaya

pressure. The advantages of using AACVD are the use of wider range of precursors without the need of only using volatile solvent, high deposition rate, high reproducibility, flexible reaction environment and synthesis of multi-component materials with precise stoichiometric control (Ariffin et al., 2015; Ehsan et al., 2012). AACVD is carried out at standard atmospheric pressure and therefore can be operated without much difficulty (Ehsan et al., 2012). Besides that, AACVD can also control the morphology and particle growth of the thin films (Wang et al., 2017). The low-cost production of the material is desired for the large-scale production and AACVD is a very attractive method because the fabrication process involves low cost and allows for easy composition control and homogeneity of the films (Ketchemen et al., 2018).

AACVD is the facile route towards fabrication of transition-metal chalcogenides thin films such as ReS_2, MoS_2, CdS, FeS_2 as well as SnS by single-source precursors (Al-Dulaimi et al., 2017). The use of single-source precursors in AACVD method is shown to be more advantageous than other deposition methods because it produces materials with better stoichiometry and with less defects (Ketchemen et al., 2018). Dual-source precursor approach in AACVD can also be employed for alloying of other transition metal cations into a pristine material. For instance, Cr was doped into MoS_2 with dual-precursor source by using AACVD method to improve the mechanical properties of MoS_2 (Tedstone et al., 2017). Re-doped MoS_2 thin films were deposited on glass substrates by AACVD method using dual-source precursor, $[Mo(S_2CNEt_2)_4]$ and $[Re(S_2CC_6H_5)(S_3CC_6H_5)_2]$ (Al-Dulaimi et al., 2017).

2.6.1 Processes involved in AACVD

AACVD process involves the delivery of the vaporizable precursor aerosol to the deposition zone (Ariffin et al., 2015). There are two decomposition pathways for the

Universiti Malaya

formation of the particles in the catalyst namely the heterogenous and homogenous processes. In heterogenous process, the aerosol is deposited on the substrate and undergoes adsorption and decomposition processes and thin film is formed as a result (Ariffin et al., 2015; Kun et al., 2018). In homogenous process, decomposition occurs in the vapour phase in which the reactive aerosol undergoes exothermic oxidation which results to the formation of temperature gradient which is a driving force towards controlling the vapour-phase decomposition for particle growth (Ariffin et al., 2015; Kun et al., 2018).

AACVD involves three key steps in the formation of thin film; (1) The formation of aerosol vapour of precursor solution, (2) transportation of the vapour by a carrier gas into the furnace and (3) the recovery process of the deposited particles (Hernández-Salcedo et al., 2015). The morphology and structure of the fabricated catalyst greatly depend on the AACVD parameters such as furnace temperature, carrier gas flow and concentration of precursor solution (Ariffin et al., 2015; Hernández-Salcedo et al., 2015).

Once the vapour enters the furnace tube, the solvent which dissolves the precursor material will undergo evaporation at high temperature and the concentration of the droplets on the surface of the substrate increases. After the droplets on the surface of the substrate reaches the critical supersaturation, nucleation occurs and the solutes will be precipitated out in the droplet and subsequently, the solid particle will grow on the surface of the substrate and grow into thin film (Hernández-Salcedo et al., 2015).

Regarding the evaporation of the solvent droplets, the droplet size reduces as it travels further through the tube and concentration increases as a result. Nucleation or formation of particles occur once the concentration reaches supersaturation and precipitation of the solutes occurs (Hernández-Salcedo et al., 2015). Hollow particles are formed when nucleation occurs at the surface when the solute concentration in the centre

Universiti Malaya

of the droplet is lower than equilibrium saturation (Hernández-Salcedo et al., 2015). If nucleation occurs when the solute concentration at centre of the droplet is higher than equilibrium saturation, the solid particles are formed (Hernández-Salcedo et al., 2015).

2.7 Parameters of Aerosol-assisted Chemical Vapour Deposition (AACVD)

The morphology of the thin films is dictated by the deposition parameters of AACVD method which is the key linking to the electrocatalytic performance of the thin films. In the following, we explore the effects of various AACVD parameters on the final morphology of the thin films.

2.7.1 Choice of Precursor

It was reported that different precursor used in AACVD process produced different types of morphology. In the study carried out by Walters et al., when zinc acetate was used as the precursor for the fabrication of zinc oxide, ZnO thin film at 450 °C, the particles were spherical in shape with the diameter of 300-400 nm along with some hexagonal shape measuring 1-2 mm (Walters et al., 2009). ZnO thin film produced by Hamid et al. by AACVD method at 350 °C possessed a different morphology than the one produced by Walters et al. by using a different precursor, the high nuclearity zinc complex, $Zn_6(OAc)_8(\mu - OH)_2(dmae)_2(dmaeH)_2$ (where OAc = acetate and dmaeH = N, N'-dimethylaminoethanol). The ZnO thin film showed compact, continuous and smooth morphology with spherical shape and clear grain boundaries (Hamid et al., 2008).

Universiti Malaya

2.7.2 Choice of Solvent

The role of solvent in AACVD reaction in the final morphology of the materials is governed by the physical properties of the solvents such as heat of combustion, boiling point, viscosity, specific heat capacity and coordinating ability of the solvent of choice (Ehsan et al., 2012; Ketchemen et al., 2018). The choice of solvent for AACVD process can also control the particle size of the deposit (Ehsan et al., 2012). In AACVD, the gas-phase nucleation process (homogenous and heterogenous reactions) is directed by the boiling point of the solvent (Ketchemen et al., 2018).

TiO_2 thin films fabricated by AACVD were found to possess either anatase or rutile phases depending on the type of solvent used. Methanol produced rutile TiO_2 while others including ethanol, hexane, dichloromethane and isopropanol produced anatase TiO_2. Interestingly, only rutile TiO_2 was produced with the mixture of ethanol and methanol even when methanol in the solvent mixture was as low as 10 % (Edusi et al., 2012).

Deposition of Bi_2S_3 thin films via AACVD carried out by Kun et al. demonstrated that different solvent produced different morphology of the thin film (Kun et al., 2018). Tris-(piperidinedithiocarbamato) bismuth (III) complex dissolved in solvent composed of mixture of chloroform/methanol at 3:1 and chloroform/ acetonitrile at 3:1 produced Bi_2S_3 thin film by AACVD with different morphologies as described in Table 2 for deposition temperature of 350, 400 and 450 °C.

Universiti Malaya

Table 2.2: Morphologies of Bi_2S_3 thin films fabricated with different solvents by AACVD (Table sourced from Kun et al., 2018).

Solvent	Temperature (°C)	Morphology
Chloroform/ Methanol (3:1)	350	Randomly arranged hexagonal plates with ribbon-like fibres.
	400	Irregularly shaped with wide size distribution.
	450	Leaf-like plates with needle-like fibres.
Chloroform/ Acetonitrile (3:1)	350	Long cylindrical fibres.
	400	Mixture of fibres and underlying plates.
	450	Long cylindrical fibres.

The thin film morphologies depend on the type of solvents used in AACVD process and the relationship is explained by difference in the heat of combustion and evaporation of the solvents which determine the growth of thin film to go through either heterogenous or homogenous process (Kun et al., 2018). Based on the study carried out by Kun et al., chloroform promotes homogenous process in deposition reaction due to its very low boiling point that facilitates the evaporation of the solvent leaving the solute particles in the vapour phase after decomposition of the precursor material whereas methanol with higher boiling point caused the decomposition to occur on the heated substrate to form Bi_2S_3 (Kun et al., 2018).

Universiti Malaya

2.7.3 Deposition Temperature

The growth temperature during AACVD process directs the nucleation of particles on the substrates by either homogenous or heterogenous reactions (Ketchemen et al., 2018). It had been reported that when deposition temperature increased, the spherical morphology of the particles produced by AACVD was lost and they were agglomerated (Hernández-Salcedo et al., 2015).

Different deposition temperature can produce different morphologies of the thin films as well as dictating the particle sizes. In the study carried out by Shahid et al., it was observed that at deposition temperature of 250 °C, the ZnO particles grown on soda glass substrate were small and poorly defined in the particle size range of 0.1- 0.3 μm but increased to 0.2-0.7 μm at deposition temperature of 475 °C whereas at deposition temperature of 325 and 400 °C the films were observed to be more smooth, more compact and the grains were homogenously distributed (Shahid et al., 2012). The SEM images showing the morphologies of the ZnO thin films fabricated at different deposition temperature are displayed in Fig. 2.9.

Universiti Malaya

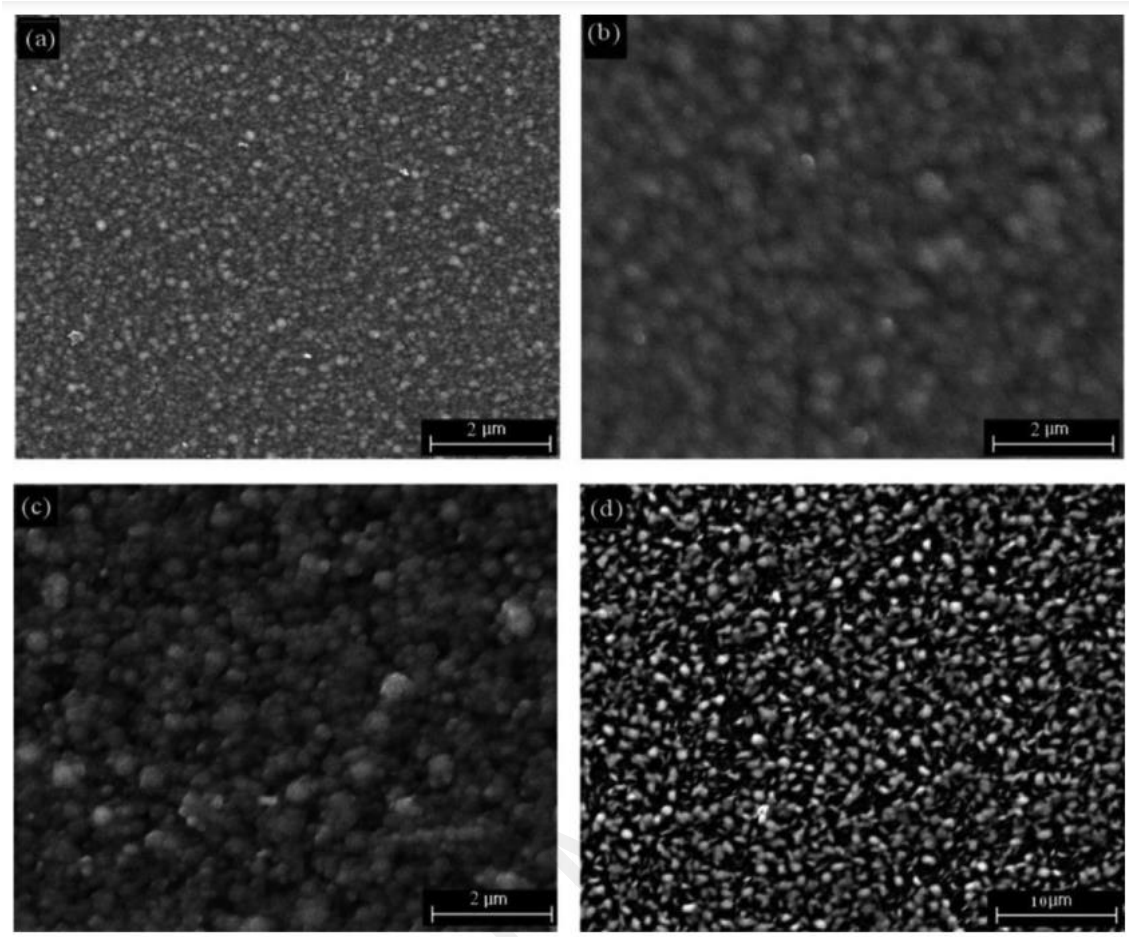

Figure 2.9: SEM images of the ZnS morphologies produced at deposition temperature of (a) 250, (b) 325, (c) 400 and (d) 475 °C (Photo sourced from Shahid et al., 2012).

2.7.4 Carrier Gas Flow Rate

The flow rate of the carrier gas in AACVD has significant effect on the crystal quality, surface structure and electrical properties of the electrocatalysts therefore, a suitable flow rate must be employed to achieve high deposition rate for the fabrication of high-quality thin films with excellent properties in electrocatalytic performance (Wang et al., 2017). Faster flow rate promotes the generation of higher vapour pressure of the precursor solution which increases the interaction of particles with the substrate during AACVD process and larger film thickness will be formed (Yu et al., 2013). The favourable film thickness and the uniformity of deposition can thus be controlled by tuning the carrier gas flow rate in AACVD process.

2.7.5 Concentration of Precursor Solution

Concentration of the precursor solution has the significant effect on the final morphology of the thin films. For instance, the ZnO thin films fabricated with varying zinc acetate precursor concentration also exhibited different morphology with closely connected particles produced from lower precursor concentration (0.05 M) and isolated particles produced from higher precursor concentration (0.175 M) (Ma, 2021). The same study also demonstrated that the highest concentration (0.25 M) resulted to the largest grain size and the particles were further isolated from each other (Ma, 2021). The deposition of gold films was carried out with varying concentration of precursor solution, $HAuCl_4$ and it was found that high precursor concentration caused spherical and rodlike particles to grow on the thin films whereas low precursor concentration led to the formation of island growth morphology (Palgrave et al., 2007).

When higher precursor concentration is used for AACVD, more precursor molecules per unit volume are transported by the carrier gas which subsequently increases the grain size as well as the film thickness (Ma, 2021). The concentration of the precursor solution also drives the mechanism of particle growth. It had been proposed that high precursor concentration favours the gas-phase nucleation process and therefore, the particles appear isolated on the film whereas low precursor concentration favours surface reaction which promotes the island growth morphology of the films (Palgrave et al., 2007).

Universiti Malaya

CHAPTER 3: METHODOLOGY

3.1 Materials and Reagents

Celite and silica gel (Mesh size 230-400 mesh ASTM) were from Fluka. Silica gel 60 F_{254} plates with aluminium sheets were from MERCK and were used for thin-layered chromatography. The celite, silica gel and TLC plates were pre-heated at 140 °C overnight prior to use. AR grade solvents used in this study were *n*-hexane, toluene, ether and THF which were from MERCK. The reagents used in this study were 2,4-bis(*p*-tolylthio)1,3-dithia-2,4-diphosphetane-2,4-disulfide (Davy's reagent) from Tokyo Chemical Industry and $Cp_2Mo_2(CO)_6$ from Strem Chemicals. The FTO glass substrates were from Sigma-Aldrich, and it was cut into sizes measuring 2 cm by 1 cm.

3.2 General procedures

All the synthetic procedures were carried out with standard Schlenk technique. Further manipulations were carried out inside the dry-box under argon gas atmosphere. All the solvents used in this study were redistilled with Na/benzophenone to remove all moisture and dissolved air prior to use. The glass substrates used for deposition process were cleansed with deionised water under sonication followed by acetone and the substrates were air dried prior to use.

3.3 Physical measurements

^{1}H, ^{13}C and ^{31}P-NMR spectra were obtained using JEOL ECX FT NMR 400 MHz Spectrometer at Faculty of Science in Universiti Tunku Abdul Rahman (UTAR). The samples were prepared in deuterated benzene-d_6. The chemical shifts were referenced to residual C_6H_6 in benzene-d_6. FT-IR spectrum was measured in Nujol mulls on KBr

Universiti Malaya

(potassium bromide) salt plate in the range of 4000-400 cm^{-1} with using Perkin-Elmer RX 1 Fourier Transform Infra-Red (FTIR) spectrometer at Faculty of Science in UTAR.

The decomposition temperature of precursor material was determined by thermogravimetric analysis (TGA) by using Perkin-Elmer TGA 4000 instrument at Department of Chemistry in University of Malaya (UM). The precursor material was heated from 29.07 to 869.35 °C at the heating rate of 10˚C/min under nitrogen purging at the flow rate of 20 mL/min. The optical property studies for the determination of band gap energy were performed by UV-vis spectrophotometry by employing UV-vis 2600 Shimadzu spectrophotometer in the range of 200-900 nm at Department of Chemistry in UM. The film thickness was measured by using surface profilometer (Bruker Dektak XT) equipped with stylus with radius of 12.5 μm in Nitride Clean Room at AMCAL in UM. The surface topology of the films was observed by atomic force microscopy (AFM) by using Park Systems XE-70 at Faculty of Science of UTAR. The surface morphology and particle size were analysed by field electron-scanning electron microscopy (FE-SEM) by employing JEOL JSM-700F Field Emission SEM in secondary electron imaging (SEI) with accelerating voltage of 2-4 kV at Faculty of Science of UTAR. The elemental mapping displaying distribution of elements over the films was studied by using energy dispersive X-ray spectroscopy (EDX) also carried out with the same SEM instrument with accelerating voltage of 20 kV with INCA detector.

The powder X-ray diffractometer patterns of the materials incorporated in the films were obtained by employing Shimadzu 6000 diffractometer in the range from 2θ = 10° to 90° with Cu K_α radiation (λ=0.154 nm) under voltage of 40 kV and current of 30 mA at room temperature at Faculty of Science in UTAR. The vibrational modes of the films were analysed by Raman spectroscopy via Renishaw model in Low Dimensional Materials Research Centre (LDMRC) at Department of Physics in UM by using 514 nm

Universiti Malaya

edge laser with 10% laser power passing through 1200 l/mm diffraction grating under 60 s of exposure time and the sample observation was performed by using 50× objective lens. The oxidation states of the elements incorporated in the films were analysed by X-ray photoelectron spectroscopy (XPS) by using NANOTEC beamline, BL 5.3 at Synchrotron Light Research Institute in Thailand with the energy source with λ=1638.4 eV. The lattice fringes of the materials grown in the films were observed by high-resolution transmission electron microscopy (HRTEM) by employing JEOL JEM-2100F field emission gun with emission accelerating voltage of 200 kV at emission current of 142 μA at Department of Physics in UM. The measurement of lattice spacing and processing of FFT images from HRTEM were carried out by using the Digital Micrograph GMS 3 software.

3.4 Preparation of [$CpMo(CO)_2(S_2P(SPhMe)_2)$](1)

The preparation of **1** was carried out following the reported procedures by Wong et al. (2010). Complex **1** was the precursor material for fabricating the films by AACVD method. In the preparation of complex **1**, $Cp_2Mo_2(CO)_4$ (400 mg) and 2,4-bis(*p*-tolylthio)1,3-dithia-2,4-diphosphetane-2,4-disulfide (Davy's reagent) (402 mg), in the ratio of 1:1 was dissolved in 25mL toluene inside the Schlenk flask. $Cp_2Mo_2(CO)_4$ was prepared by thermolysis of $Cp_2Mo_2(CO)_6$ at 120 °C for 24 h (Curtis et al., 1978). The reaction mixture was refluxed for 5 h at 70 °C. The resultant dark pinkish brown product mixture was isolated *via* column chromatography through dry loading method. The greenish brown fraction was eluted with the solvent of *n*-hexane/toluene in 2:1 with total volume of ~50 mL. The solution was pump-dried followed by recrystallization in toluene layered with *n*-hexane at -20 °C for three days to yield 160 mg (yield: ~34.5 %) of brown crystals of complex **1**. The structure of complex **1** was shown in Fig. 3.1. The purified complex **1** was authenticated with ^{1}H, ^{13}C and ^{31}P-NMR and IR (Nujol mull).

Universiti Malaya

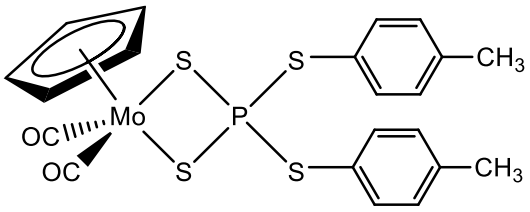

Figure 3.1: Chemical structure of complex 1.

3.5 Deposition of films by AACVD

The films were fabricated at different AACVD conditions by varying deposition time, volume of precursor solution along with deposition time and deposition temperature. In this work, the concentration of the precursor solution was prepared in 0.01 M. The precursor solution was prepared by dissolving complex **1** in THF in the two-necked round bottomed flask and, in this study, The solution was sonicated for 5 minutes before being connected to the delivery tube which was housed inside the tube furnace.

The schematic diagram illustrating the apparatus setup for AACVD process is displayed in Fig. 3.2. The flask containing the precursor solution was immersed into the water-filled piezoelectric humidifier and was connected to the delivery tube. The FTO glass substrate with area of 1 cm by 2 cm was placed inside the delivery tube 4 cm from the inlet mouth of the tube. The other end of the delivery tube was connected to the bubbler which displayed the flow rate of the passing argon gas which acted as a carrier gas. The carrier gas flow rate was controlled by gas regulator.

After the humidifier was switched on, the aerosol droplets were generated from the precursor solution. The aerosol droplets were consisted of complex **1** dissolved in THF and were carried by the argon gas to be deposited onto FTO glass substrate inside the delivery tube at the carrier gas flow rate of 0.3 SCFH (Standard cubic feet per hour) for study with different deposition time and fixed volume. All the other films were

Universiti Malaya

fabricated with the gas flow rate of 0.5 SCFH. The delivery tube was preheated by the furnace to the studied deposition temperature.

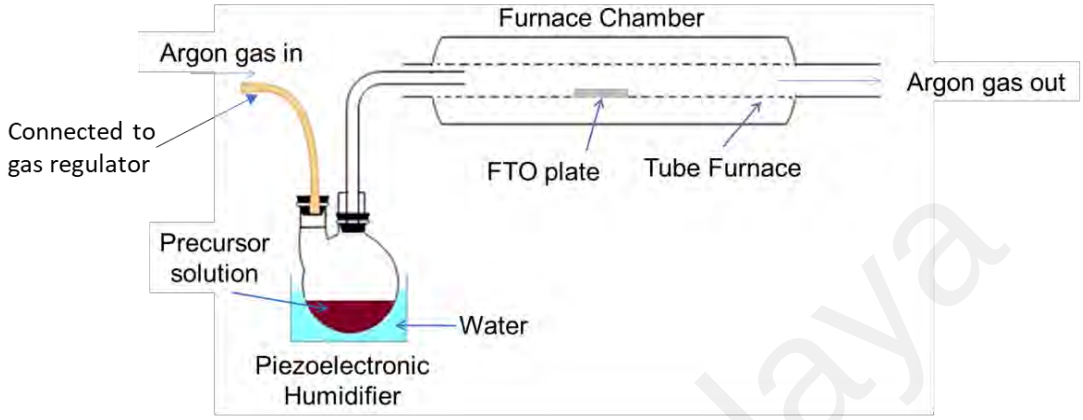

Figure 3.2: Schematic diagram of apparatus setup for AACVD.

3.6 Electrochemical Studies Measurement

In the electrochemical studies, the three-electrode configuration of Princeton Applied Research (PAR-VersaSTAT-4) workstation was used with Ag/AgCl reference electrode filled with 3M NaCl solution, platinum wire was the counter electrode and the fabricated films were the working electrodes. The electrolyte used was 0.25 M H_2SO_4 with the pH of 0.95. To study the water splitting process in alkaline media, the alkaline electrolyte was prepared by mixing 0.25 M Na_2S and 0.35M Na_2SO_3 solution with the pH of 11.71. Before electrochemical analysis was performed, the electrolyte was purged with nitrogen gas for 15 minutes with stirring. For all the fabricated films, cyclic voltammetry (CV) was scanned from -0.6 to 0.6 V vs. Ag/AgCl for 5 cycles with the scan rate of 0.1 V/s. Linear sweep voltammetry (LSV) was analysed from -0.6 to 0.6 V vs. Ag/AgCl with scan rate of 0.02 V/s. Mott-Schottky analysis was performed from -1 to 1 V vs. Ag/AgCl with amplitude of 10 mV RMS. The electrochemical impedance spectroscopy (EIS) of

Universiti Malaya

the films was analyzed within the frequency range of 0.01 Hz to 100,000 Hz by using amplitude of 25 μA RMS.

Universiti Malaya

CHAPTER 4: RESULTS AND DISCUSSION

4.1 Preparation of [$CpMo(CO)_2(S_2P(SPhMe)_2)$] (1) as Precursor for AACVD

Complex 1 was prepared by following the procedures reported by Wong et al. (2010) and was purified *via* recrystallisation with toluene/*n*-hexane. The purified complex 1 was authenticated with ^{1}H, ^{13}C and ^{31}P-NMR (Refer to Fig. 4.1- 4.3) and FTIR nujol mull (Refer to Fig. 4.4) prior to use as precursor for AACVD process to avoid any contamination on the fabricated films.

4.1.1 Nuclear Magnetic Resonance (NMR) Analyses

The ^{1}H, ^{13}C and ^{31}P-NMR chemical shifts of the authenticated complex 1 were compared with the literature (Wong et al., 2010). From the ^{1}H-NMR spectrum as displayed in Fig. 4.1, the signals at 1.92 ppm (s) and 4.50 ppm (s) were ascribed to $-CH_3$ and Cp ($-C_5H_5$), respectively. The multiplets as recorded in the range of 6.80- 7.73 ppm were ascribed to aromatic $-C_6H_4$ of the ligand. From the ^{13}C-NMR spectrum as shown in Fig. 4.2, the peaks at 21.28 and 21.56 ppm were ascribed to $-CH_3$ of the ligand. The chemical shift at 95.98 ppm was ascribed to Cp rings. The peaks in the range of 130.34-142 ppm were ascribed to aromatic carbons in $-C_6H_4$ of the ligand. Peaks at 256.42 and 256.49 ppm were ascribed to carbonyl ligands. From the ^{31}P-NMR spectrum as displayed in Fig. 4.3, a singlet peak occurred at 125.60 ppm. All these observations from the NMR analyses well agreed with the literature indicating that complex 1 was successfully prepared and purified.

Universiti Malaya

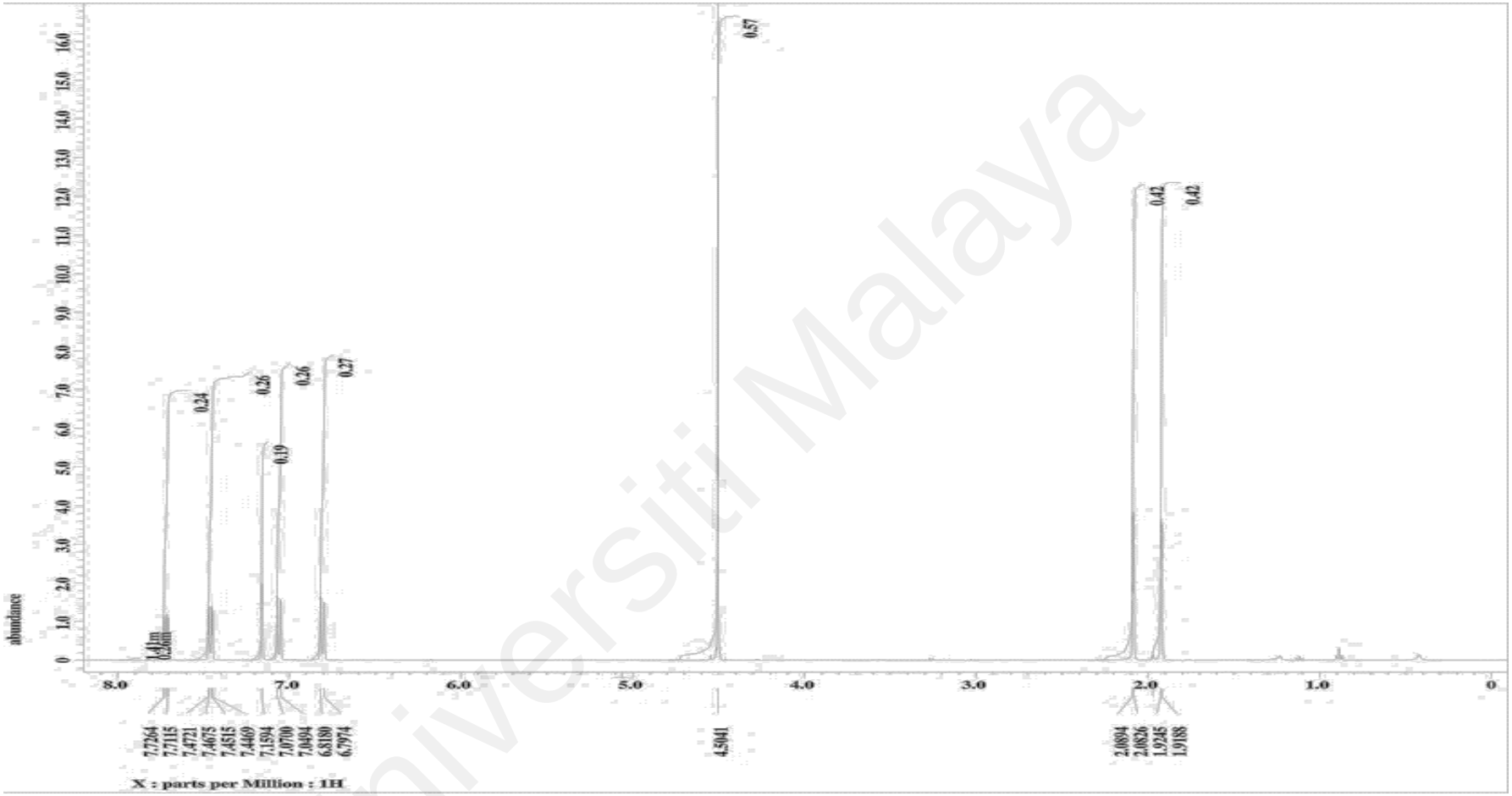

Figure 4.1: H-NMR spectrum of complex 1.

Universiti Malaya

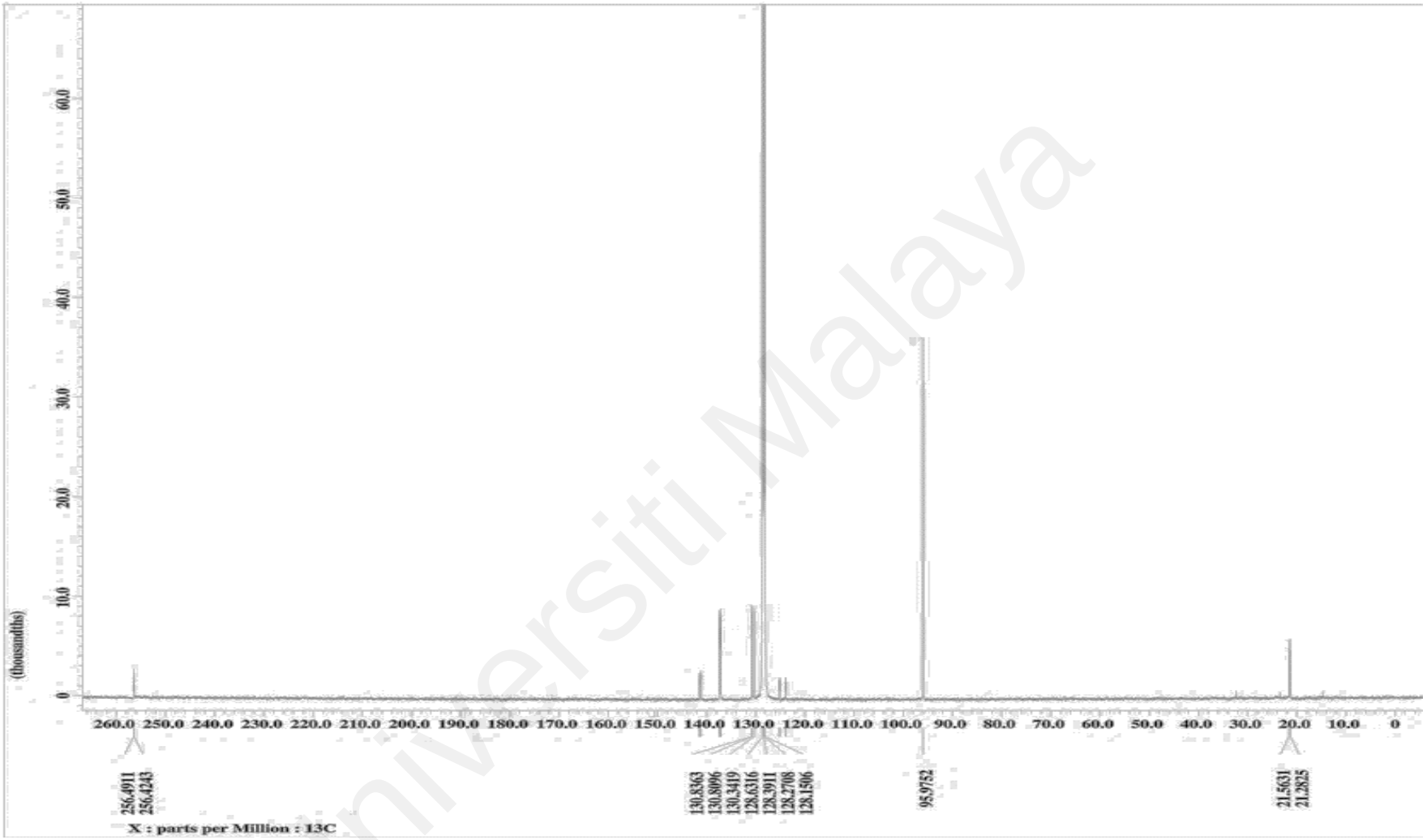

Figure 4.2: 13C-NMR spectrum of complex 1.

Universiti Malaya

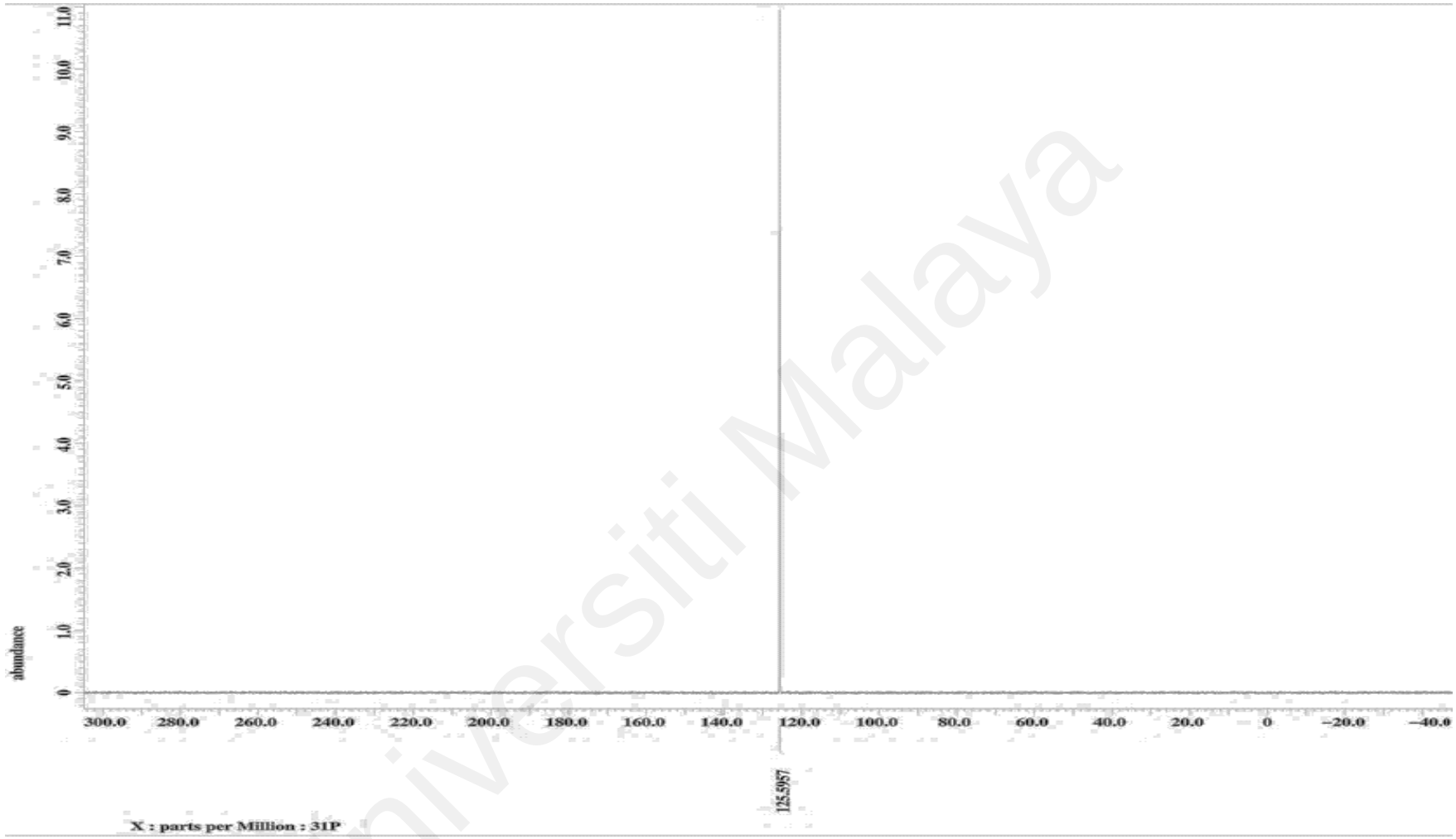

Figure 4.3: 31P-NMR spectrum of complex 1.

Universiti Malaya

4.1.2 Fourier- transform Infrared (FTIR) Analysis

The FTIR spectrum of complex 1 was displayed in Fig. 4.4 and the absorption peaks well agreed with the literature (Wong et al., 2010). The absorption peaks at 1950 and 1860 cm^{-1} (strong) were ascribed to carbonyl groups of complex 1. The peaks at 806 and 599 cm^{-1} (weak) indicated the presence of P-S bonding in complex 1. The absorption peaks for the C-H bond stretchings of the methyl groups were overlapped with the Nujol aromatic stretchings at 2854, 2923 and 2952 cm^{-1} (very strong). -CH_3 bendings were observed by the presence of absorption peaks at 1377, 1455 and 1462 cm^{-1} (medium) which were overlapped with Nujol aromatic C=C at the same region. All these observations from the FTIR analysis were agreeable with the literature indicating that complex 1 was successfully prepared and purified.

Universiti Malaya

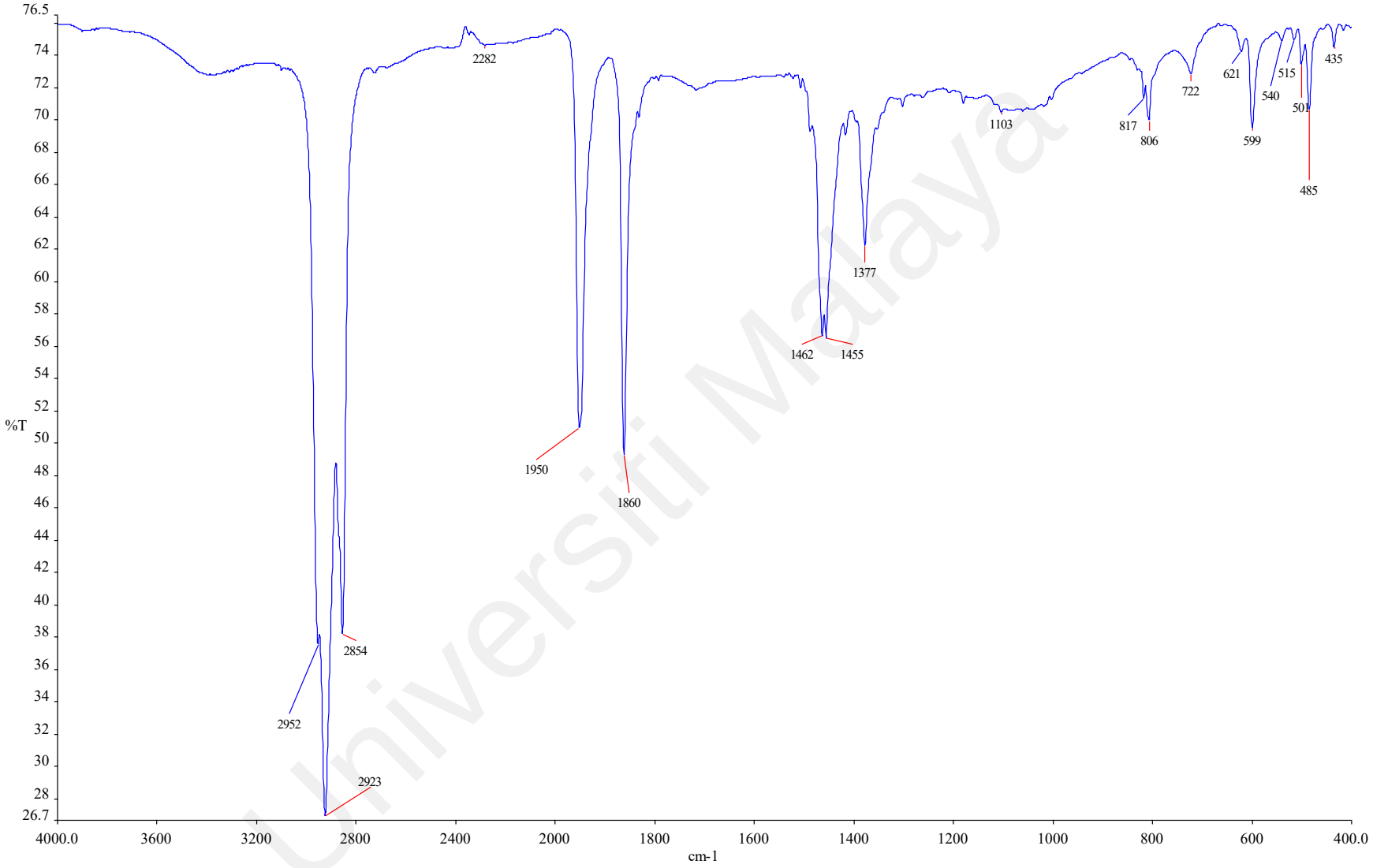

Figure 4.4: FT-IR spectrum of complex 1.

Universiti Malaya

4.2 Thermogravimetric Analysis (TGA)

Thermogravimetric analysis (TGA) was performed on complex 1 to determine the weight loss of complex 1 when subjected to thermal decomposition. The TGA curve was displayed in Fig. 4.5. From the analysis, the deposition temperature was determined for AACVD process. Complex 1 decomposed in two steps with total weight loss of 46 %. In the first step, cyclopentadienyl (Cp) ring of complex 1 which constituted 11.5 % of total mass of complex 1 was disintegrated from the complex from ~183.75 °C to ~206 °C as displayed in the TGA and derivative thermogravimetric (DTG) profiles. The second step involved the dissociation of all carbonyl groups and other organic substituents which constituted 34.4 % of total mass of complex 1 from ~206 °C to ~368 °C. Starting from 368 °C, no significant weight change was observed and based on the TGA analysis, deposition temperature of 450, 550 and 650 °C were used for AACVD process to study the effect of deposition parameter on the final morphology of the films and also in making sure that all the organic components were completely dissociated to produce inorganic films.

Universiti Malaya

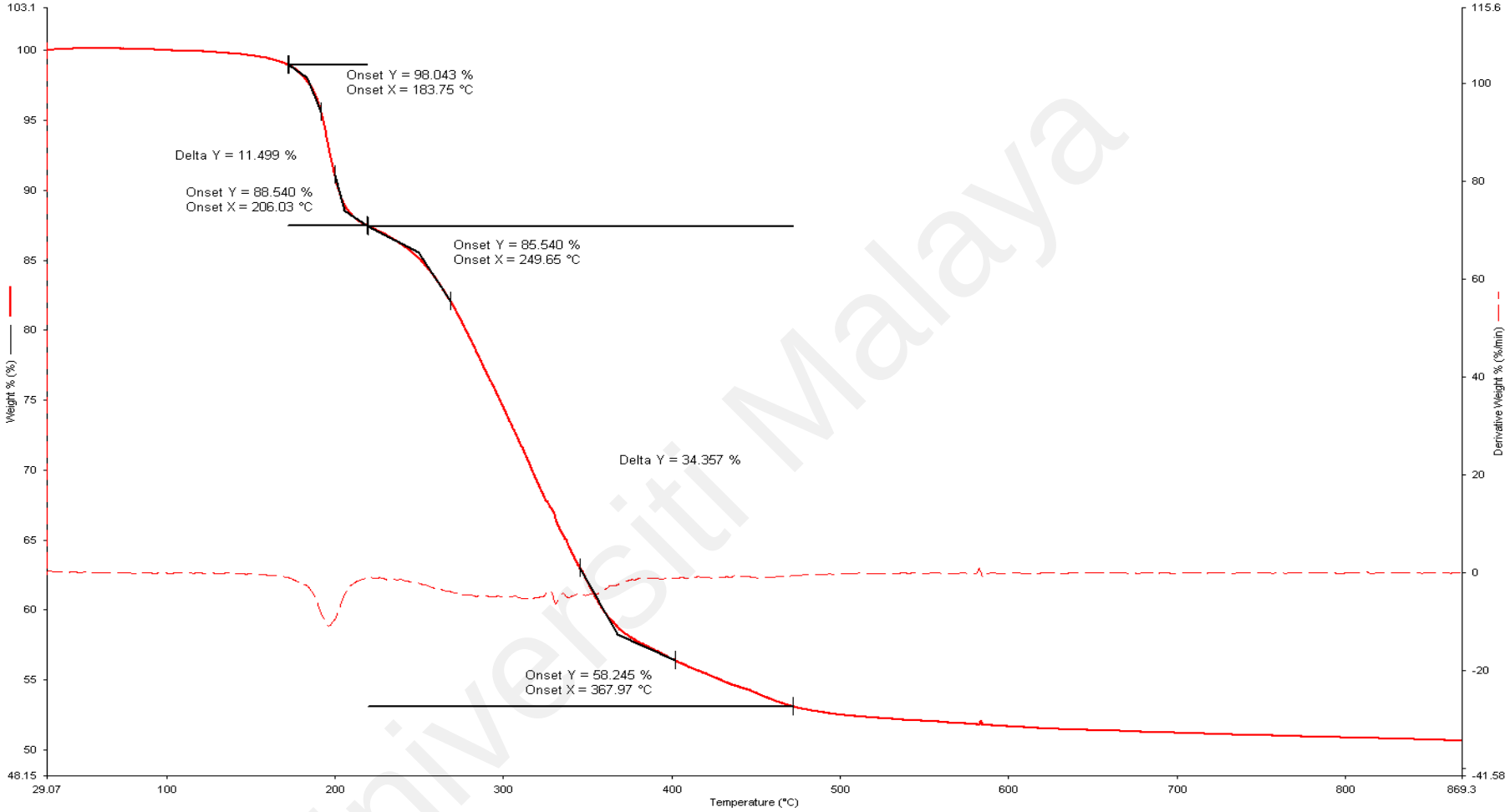

Figure 4.5: DTG and TGA curves for complex 1.

Universiti Malaya

4.3 Characterization of films fabricated with different deposition time at 550 °C

The films were fabricated at different time duration by AACVD for 20, 30 and 40 minutes at 550 °C with the carrier gas flow rate of 0.3 SCFH (SCFH: Standard cubic feet per hour). The films prepared from complex 1 (20 mL, 0.01 M in THF) were characterized with XRD, Raman spectroscopy, EDX, AFM, SEM, TEM, XPS and UV-vis spectrophotometry. The film thickness was measured by using surface profilometer. The electrochemical studies were carried out by studying the CV, LSV curve, Mott-Schottky plot, Nyquist plot and Bode plot.

4.3.1 X-ray Diffraction Analyses (XRD)

The XRD patterns of films prepared from different deposition time of 20, 30 and 40 minutes were shown in Fig. 4.5. The diffraction patterns were indexed to monoclinic Mo_2S_3 (JCPDS no. 98-006-2486) and orthorhombic MoP_2 (JCPDS no. 98-003-7222). The XRD patterns for blank FTO glass substrate were also obtained from XRD analysis.

The enlarged XRD patterns for 20-minute and 30-minute films with 2θ from 14.5° to 25° were shown in Fig. 4.6 to observe the diffraction peaks of Mo_2S_3 and MoP_2 at low intensities. The 40-minute film had the strongest diffraction peak of MoP_2 at 23.6° (021) indicating that AACVD process favoured the formation of MoP_2 in (021) reflection plane and the intensity for the peak increased significantly with longer deposition time. The observed peak list was displayed in Table 4.1 which was matched with the 2θ positions of the indexed Mo_2S_3 and MoP_2 phases.

The crystallite size, D was obtained from Debye-Scherrer equation, $D = \frac{K\lambda}{\beta\cos\theta}$, where K denotes particle shape factor of 0.9, λ denotes wavelength of X-ray, β denotes width of half maximum (in radians) and θ denotes Braggs' angle (in radians) (Kumar et al., 2020).

Universiti Malaya

The Mo_2S_3 grown in 20-minute film had an average crystallite size of 37.4 nm and MoP_2 with 22.6 nm. The Mo_2S_3 grown in 30-minute film had the average crystallite size of 38.3 nm and MoP_2 was 20 nm (Refer to Table 4.2). The Mo_2S_3 grown in 40-minute film had the average crystallite size of 82.5 nm whereas MoP_2 was 73 nm. Based on the XRD diffraction analysis, it was observed that crystallite sizes of Mo_2S_3 and MoP_2 increased with longer deposition time as the amount of Mo_2S_3 and MoP_2 deposited in the films increased during AACVD. The XRD analysis also showed that as deposition time increased, the preferable phases grown at 550 °C for Mo_2S_3 and for MoP_2 were (10-1) and (021), respectively.

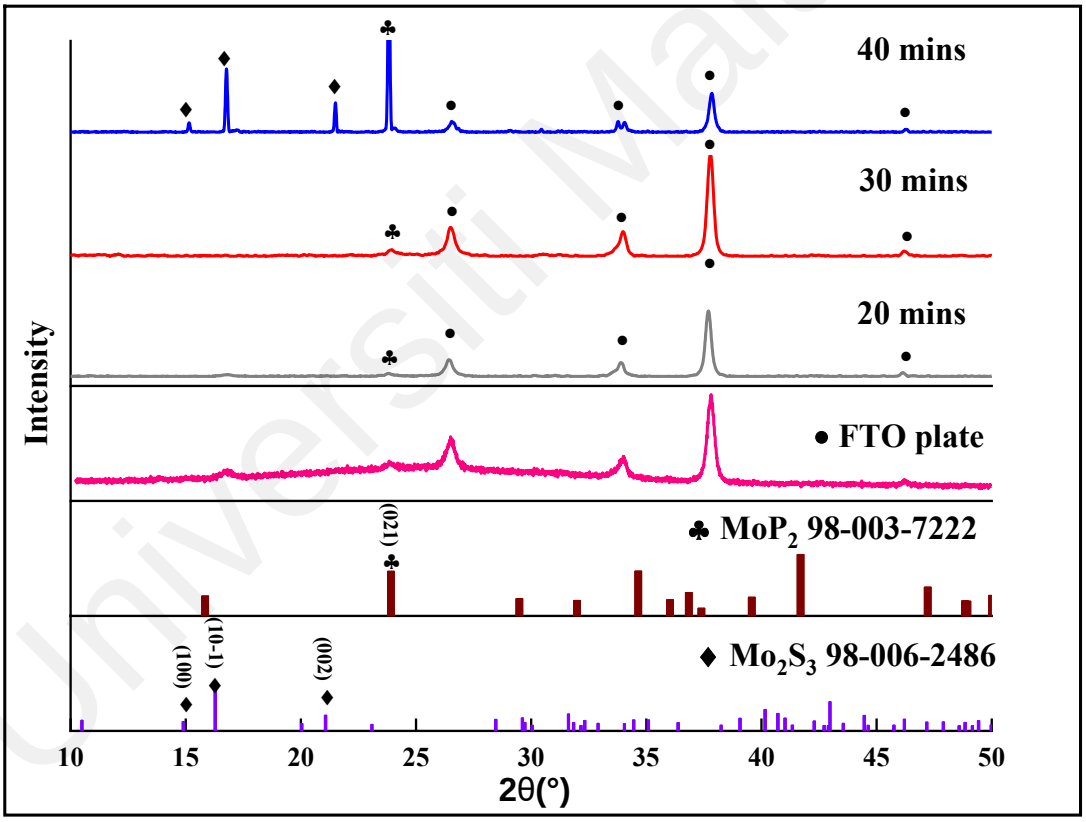

Figure 4.6: XRD diffraction patterns of the 20-, 30- and 40-minute films fabricated at 550 °C.

Universiti Malaya

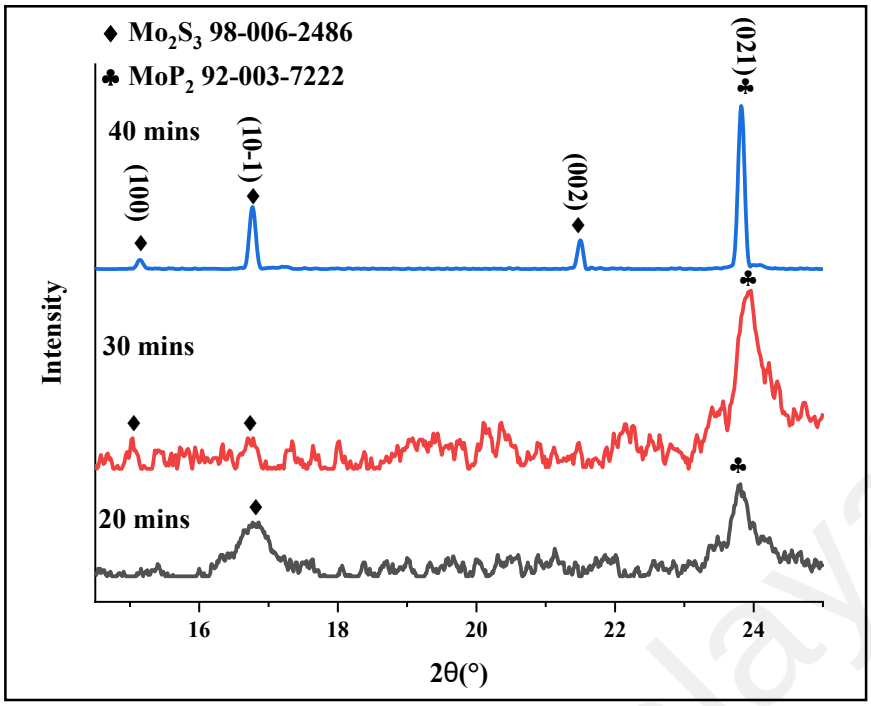

Figure 4.7: Enlarged XRD diffraction patterns of the films fabricated at 550 °C with range of 2θ from 14.5°-25°.

Table 4.1: XRD peaks of the films fabricated at different deposition times at 550 °C.

Deposition time (mins)	2θ (°)	Assigned Peaks	Reference 2θ (°)
20	16.8	Mo_2S_3 (10-1)	16.3
	23.8	MoP_2 (021)	23.9
30	15.0	Mo_2S_3 (100)	14.9
	16.7	Mo_2S_3 (10-1)	16.3
	23.9	MoP_2 (021)	23.9
40	15.0	Mo_2S_3 (100)	14.9
	16.6	Mo_2S_3 (10-1)	16.3
	21.3	Mo_2S_3 (002)	21.1
	23.6	MoP_2 (021)	23.9

Table 4.2: Average crystallite sizes of Mo_2S_3 and MoP_2 of the films fabricated at different deposition times at 550 °C.

Deposition time (mins)	Materials	Average Crystallite size (nm), $D = \frac{K\lambda}{\beta\cos\theta}$.
20	Mo_2S_3	37.4
	MoP_2	22.6

Universiti Malaya

Table 4.2, Continued.

30	Mo_2S_3	38.3
	MoP_2	20.0
40	Mo_2S_3	82.5
	MoP_2	73.0

4.3.2 Raman Spectroscopy Analyses

Raman spectroscopy for the fabricated films prepared from 20, 30 and 40 minutes of AACVD at 550 °C showed similar Raman absorption spectra (Refer to Fig. 4.8) because the materials grown in the films were similar as indicated by XRD analysis. The Raman spectrum for blank FTO substrate did not exhibit any absorption peak from 150-700 cm^{-1}. According to Zhou et al. (2018), Mo_2S_3 consists of Mo-S chains and 1T'-MoS_2. The obtained Raman shifts of the films at 156, 191 and 315 cm^{-1} were very close to the reported values of 147, 237 and 335 cm^{-1}, which corresponded to J_1, J_2 and J_3 vibrational modes, respectively for 1T'-MoS_2 of Mo_2S_3 structure. In addition, the Raman absorption peaks observed at 274, 432 and 469 cm^{-1} were assigned to the E_{1g}, C and 2LA(M) modes, respectively for 1T'-MoS_2 of the Mo_2S_3 structure, which also were very close to literature values of 283, 450 and 468 cm^{-1}, respectively (Jlidi et al., 2021; Bozheyev et al., 2014). E_{1g} is the in-plane vibration mode and 2 LA(M) is attributed to the in-plane vibrations of molybdenum- and sulphur- atoms (Bozheyev et al., 2014).

The presence of MoP_2 was indicated by the presence of A_1 Raman vibrational modes at 231, 378 and 507 cm^{-1}, which were close to the theoretical values of 224, 375 and 493 cm^{-1}, respectively (Luo et al., 2018). The presence of Raman peak at 543 cm^{-1} was ascribed to B_2 vibration mode of MoP_2 which had the theoretical value of 520 cm^{-1} (Luo et al., 2018). The Raman shift at 348 cm^{-1} was assigned to an unidentified vibrational mode of MoP_2 which had the theoretical value of 350 cm^{-1} (Luo et al., 2018).

University Malaya

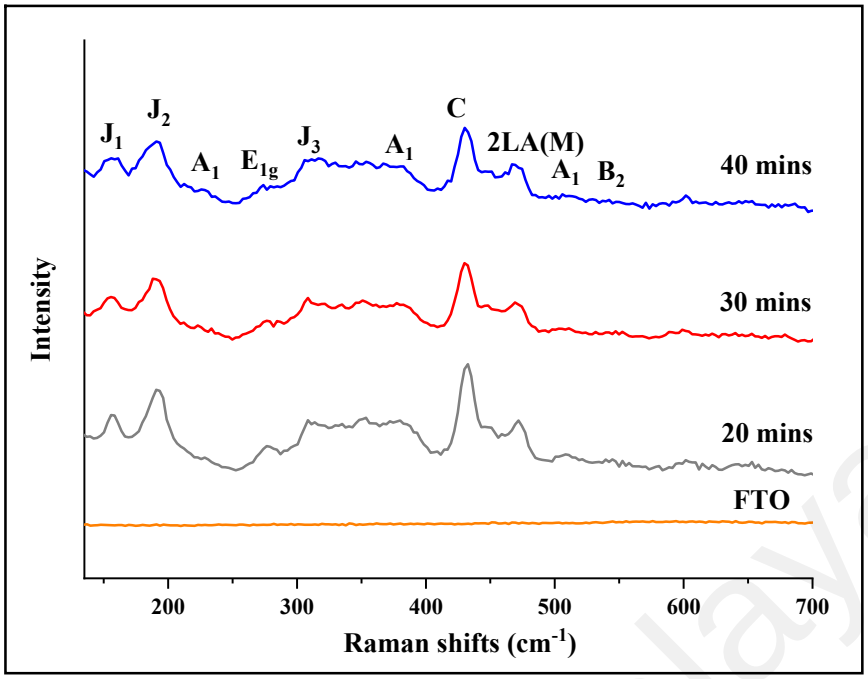

Figure 4.8: The Raman shifts of the 20-, 30- and 40-minute films fabricated at 550 °C.

4.3.3 X-ray Photoelectron Spectroscopy (XPS) Analyses

The fabricated films prepared from different deposition time of 20, 30 and 40 minutes were analysed with XPS. Fig. 4.9- 4.11 displayed the XPS spectra for Mo 3d, S 2p and P 2p of the films. From the XPS spectrum of Mo 3d, all the films had Mo^{3+} species with the binding energy values at 229.4 eV ($3d_{5/2}$) and 232.6 eV ($3d_{3/2}$). They also had Mo^{6+} species due to the appearance of XPS peaks at binding energy values of 232.8 eV ($3d_{5/2}$) and 235.9 eV ($3d_{3/2}$). The presence of Mo^{6+} indicated the formation of MoP_2 in the films in all deposition times. The presence of Mo^{3+} species showed that Mo_2S_3 was also produced in the films. The XPS spectra for S 2p were obtained to show the presence of S^{2-} species which formed the Mo_2S_3.

Universiti Malaya

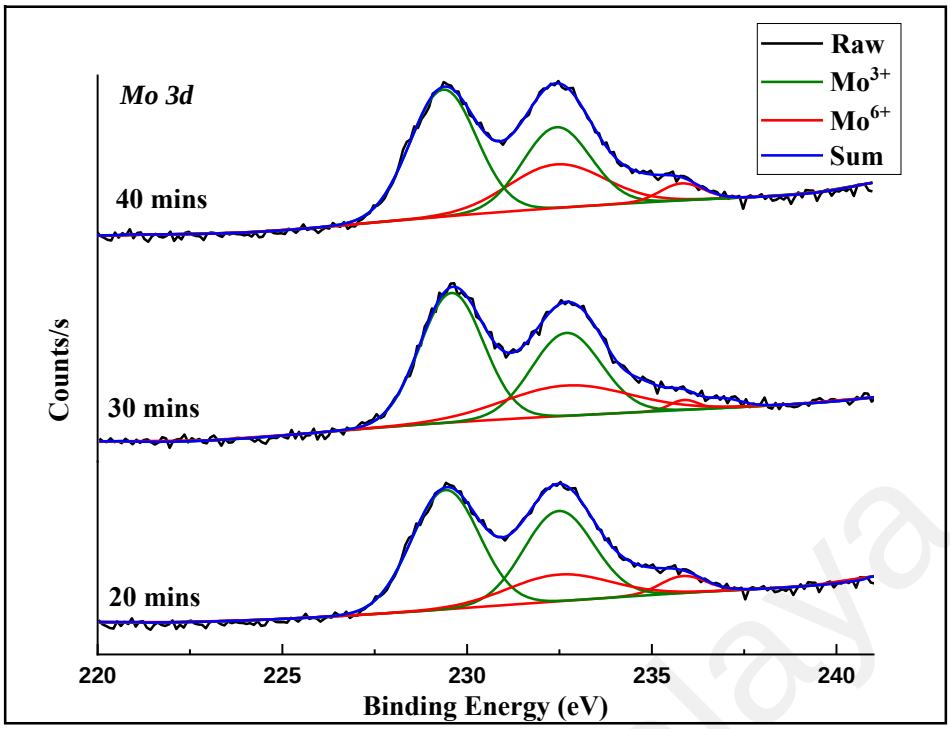

Figure 4.9: XPS spectrum of Mo 3d of the 20-, 30- and 40-minute films fabricated at 550 °C.

The XPS spectrum of S 2p in Fig. 4.10 had shown the peaks at the binding energy values of 162.2 eV ($2p_{3/2}$) and 163.3 eV ($2p_{1/2}$). The film prepared from 40 minutes of deposition time showed the surface oxidation of sulphide species as indicated by the presence of SO_3^{2-} species whose peaks were at the binding energies of 167.0 eV ($2p_{3/2}$) and 168.2 eV ($2p_{1/2}$). SO_4^{2-} species was also present alongside SO_3^{2-} in the film produced after 40 minutes of deposition time due to surface oxidation during AACVD process. The presence of SO_4^{2-} species was indicated by the presence of S 2p peaks at 167.9 eV ($2p_{3/2}$) and 169.1 eV ($2p_{1/2}$).

Universiti Malaya

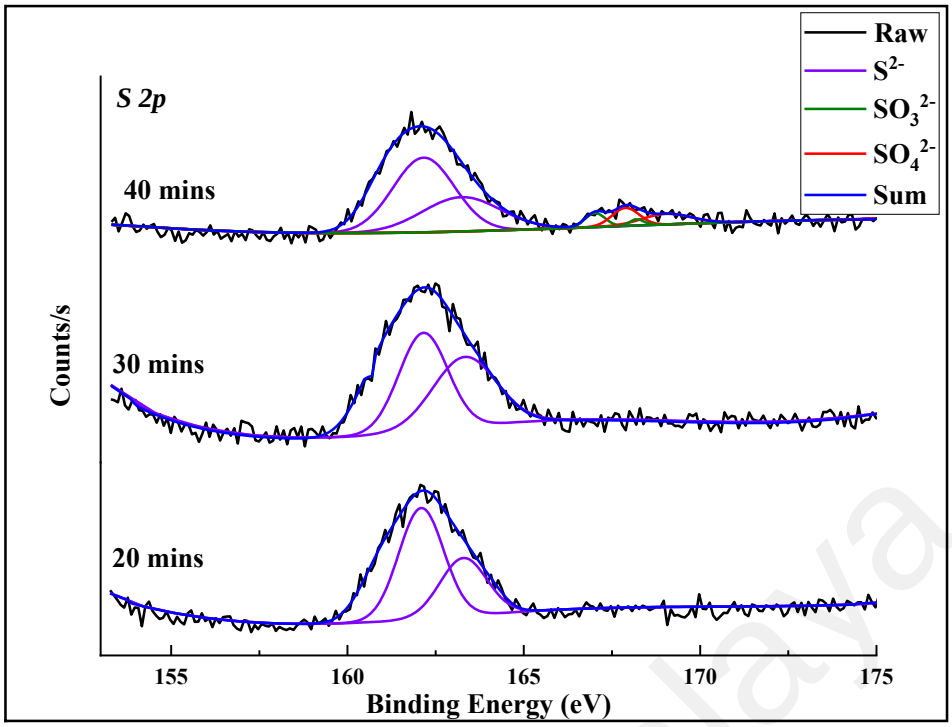

Figure 4.10: XPS of S 2p of the 20-, 30- and 40-minute films fabricated at 550 °C.

The XPS spectra for P 2p as shown in Figure 4.11 were obtained to show the presence of P^{3-} species which formed the MoP_2. The spectra showed the presence of peaks at the binding energy values of 129.5 eV ($2p_{3/2}$) and 130.3 eV ($2p_{1/2}$) in the XPS spectrum of P 2p which indicated the presence of P^{3-} in the films.

Universiti Malaya

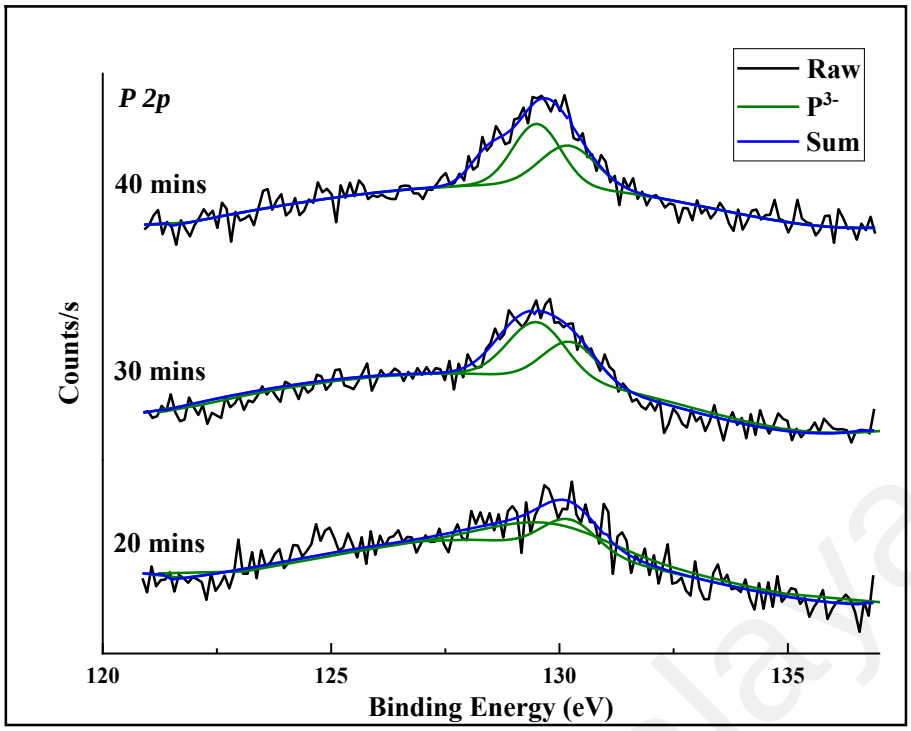

Figure 4.11: XPS of P 2p of the 20-, 30- and 40-minute films fabricated at 550 °C.

The binding energy values of Mo^{3+} species in Mo_2S_3 were reported to be 228.6 eV ($3d_{5/2}$) and 231.8 eV ($3d_{3/2}$) (Zhou et al., 2018). Whereas, the binding values of Mo^{6+} species in MoP_2 were reported to be 232.6 eV ($3d_{5/2}$) and 235.8 eV ($3d_{3/2}$) (Wu et al., 2016). The shift to higher binding energy for Mo^{3+} and Mo^{6+} in Mo_2S_3/MoP_2 composite was due the electronic interaction between Mo_2S_3 and MoP_2.

From the integration of $3d_{5/2}$ curves for Mo^{3+} and Mo^{6+}, the Mo^{6+}/Mo^{3+} ratios could be calculated to determine the composition ratios of Mo_2S_3 and MoP_2 grown in the films. The Mo^{6+}/Mo^{3+} ratios for 20, 30 and 40-minute films were found to be 0.28, 0.20 and 0.45, respectively. Therefore, the 30-minute film had the lowest MoP_2 to Mo_2S_3 composition ratio whereas the 40-minute film had the largest MoP_2 to Mo_2S_3 composition ratio.

Universiti Malaya

4.3.4 Energy Dispersive X-ray (EDX) Spectroscopy and Elemental Mapping Analyses

EDX spectroscopy was carried out on the films prepared at 20, 30 and 40 minutes of deposition time to determine the element compositions in terms of atomic percentage (%) on chosen sites on the samples' surfaces. The averaged atomic percentages of phosphorus, sulphur and molybdenum were calculated from 5 random sites on each sample. The averaged atomic percentages of the elements in the films were displayed in Table 4.3 and the EDX spectra were displayed in Fig. 4.12-4.14. Elemental mapping analyses were carried out to determine the homogeneity in distribution and composition of Mo, S and P incorporated in the fabricated films prepared from 20, 30 and 40 minutes of deposition time over the selected surface area of the films. From elemental mapping analyses as shown in Fig. 4.15- 4.17, Mo and S were distributed homogenously in the films. Phosphorus occurred dominantly in the large grains as shown in the elemental mapping. Therefore, it was suggested that the grains were consisted of MoP_2 among the Mo_2S_3 particles. It was shown that 20 and 30-minute films had wide distribution of MoP_2 grains. The 20-minute film had the observed Mo: S: P atomic percentage ratio of 1.30: 1.50: 1.00 followed by the 30-minute film with ratio of 1.75: 2.25: 1.00 and the 40-minute film with ratio of 1.75: 1.90: 1.00, respectively. Therefore, the S/P ratio for the 20, 30 and 40-minute films were 1.5, 2.25 and 1.90, respectively. It was also observed that the Mo: S: P atomic percentage ratio did not match the stoichiometric ratio of Mo_2S_3 and MoP_2. This could be due to incomplete dissociation of organometallic complex precursor during AACVD.

Universiti Malaya

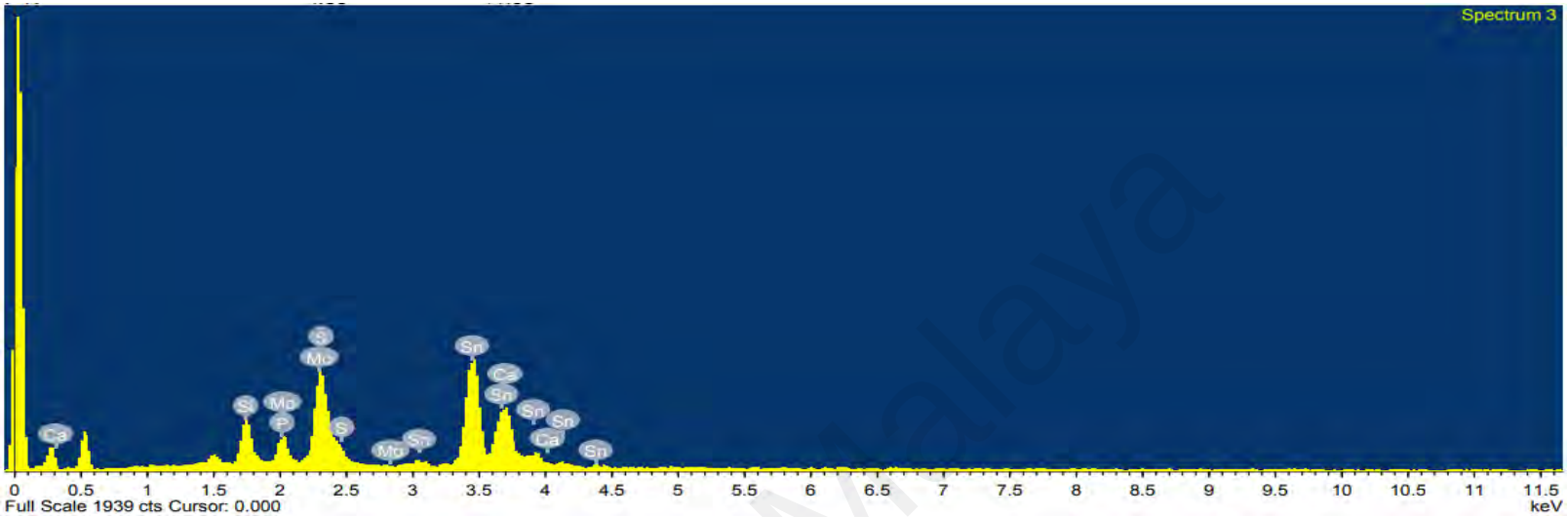

Figure 4.12: EDX spectrum for 20-minute film fabricated at 550 °C.

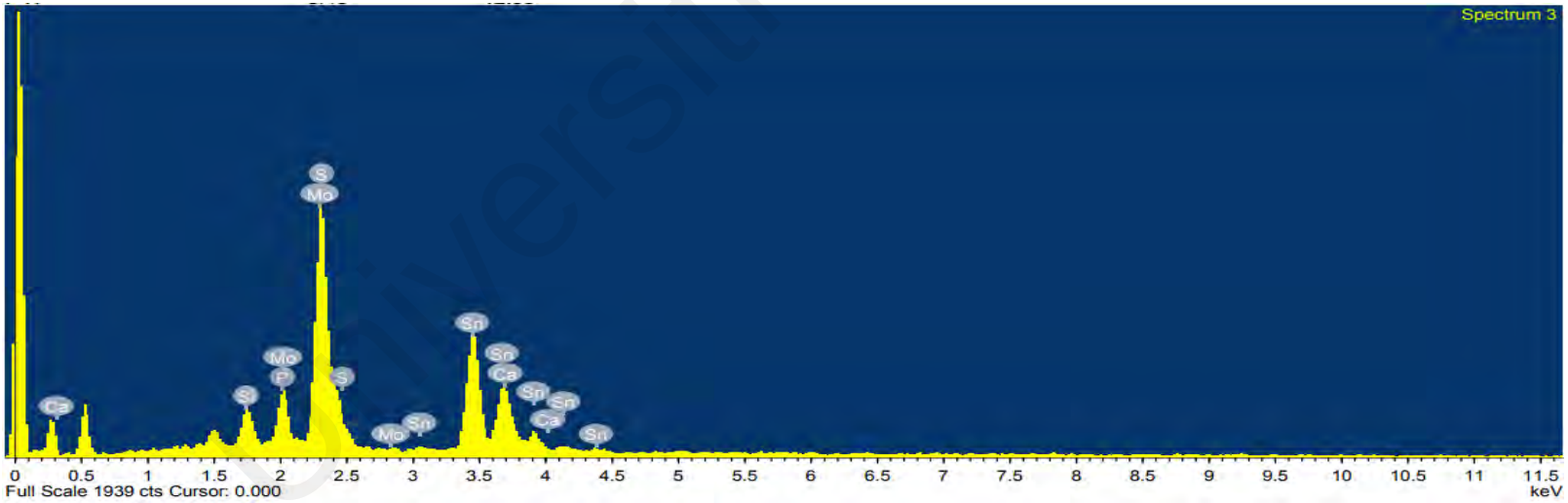

Figure 4.13: EDX spectrum for 30-minute film fabricated at 550 °C.

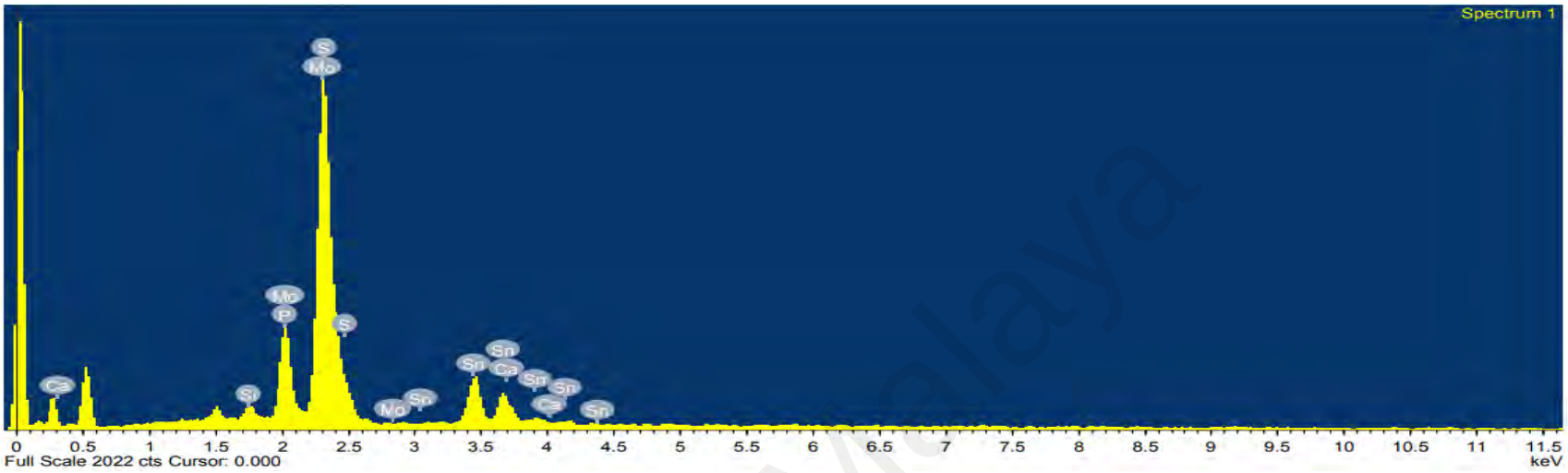

Figure 4.14: EDX spectrum for 40-minute film fabricated at 550 °C.

Universiti Malaya

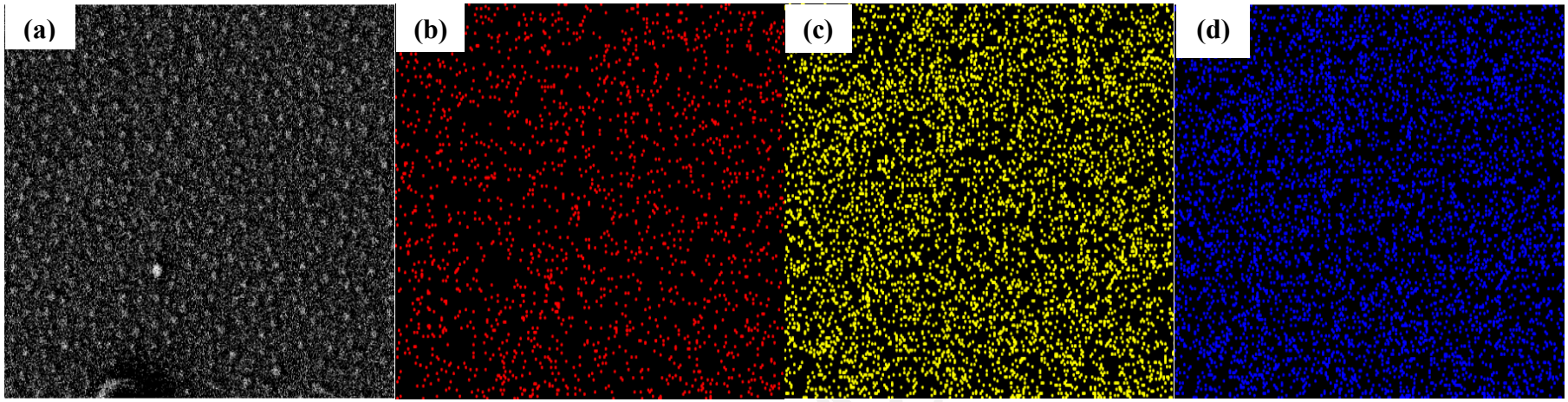

Figure 4.15: Elemental mapping of the (a) analysed area of the 20-minute film with distribution of (b) phosphorus, (c) sulphur and (d) molybdenum.

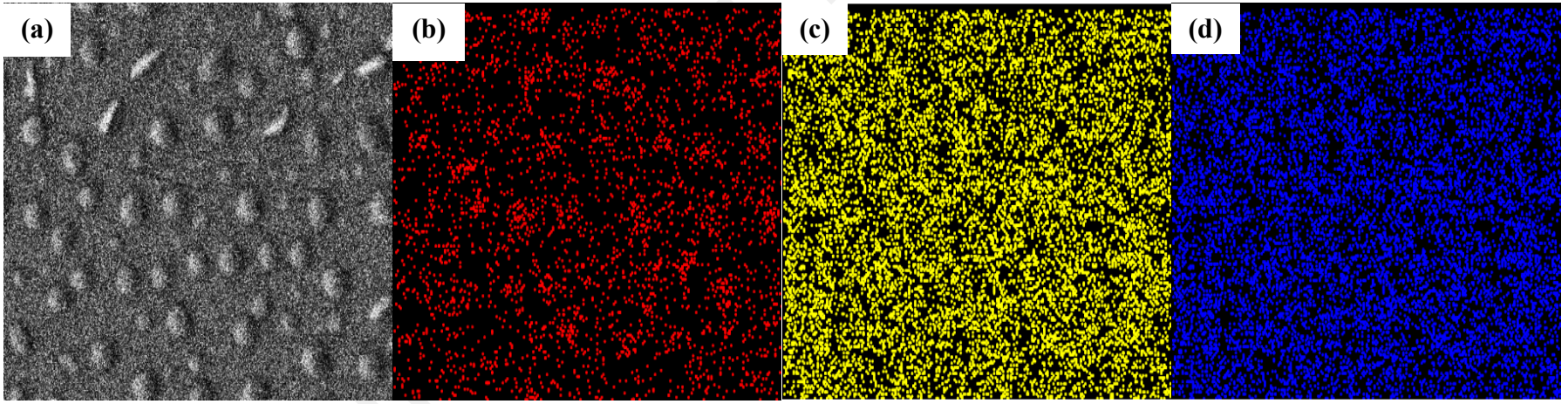

Figure 4.16: Elemental mapping of the (a) analysed area of the 30-minute film with distribution of (b) phosphorus, (c) sulphur and (d) molybdenum.

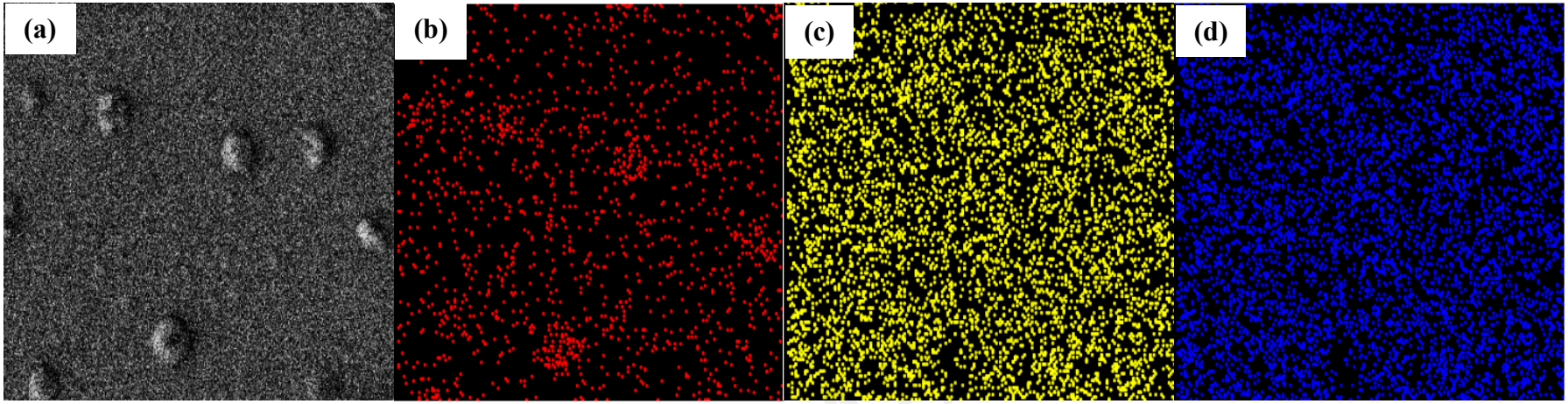

Figure 4.17: Elemental mapping of the (a) analysed area of the 40-minute film with distribution of (b) phosphorus, (c) sulphur and (d) molybdenum.

Universiti Ma

Table 4.3: Atomic percentages of Mo, S and P in the films obtained by EDX.

Deposition time (mins)	Elements	Atomic percentage (%)
20	Mo	34.40
	S	39.42
	P	26.17
30	Mo	34.99
	S	45.10
	P	19.91
40	Mo	37.92
	S	40.71
	P	21.37

4.3.5 Atomic Force Microscopy (AFM) Analyses

The morphology of the films was observed with atomic force microscopy (AFM) and FESEM. 2D and 3D AFM images are displayed in Fig. 4.18 with scan size of 10 μm × 10 μm. The corresponding line profiles are displayed in Fig. 4.18. The morphology obtained from 2D AFM showed grains scattered over the surface and was in agreement with SEM analysis which displayed the same morphology as shown in Fig. 4.20. The surface roughness parameters consisting of roughness average (R_a), root mean square (R_q), maximum profile height (R_{pv}), maximum valley depth (R_v) and maximum peak height (R_p) were displayed in Table 4.4. The root-mean-square surface roughness (R_q) of 20-minute, 30-minute and 40-minute films were 106.4 nm, 69.3 nm and 16.7 nm, respectively. The topological studies showed that the surface roughness of the films decreases with increasing deposition time.

Universiti Malaya

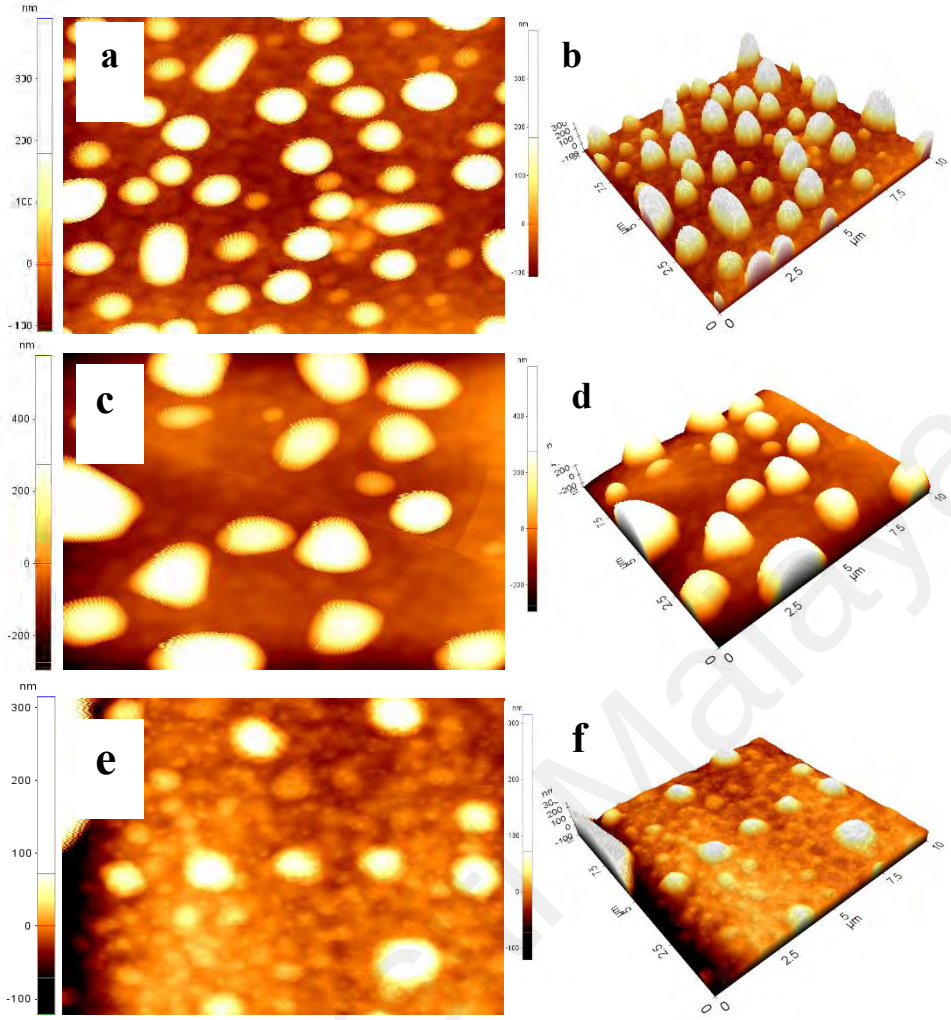

Figure 4.18: AFM of 2D and 3D images for the (a, b) 20-minute, (c, d) 30-minute and (e, f) 40-minute films fabricated at 550 °C.

University of Malaya

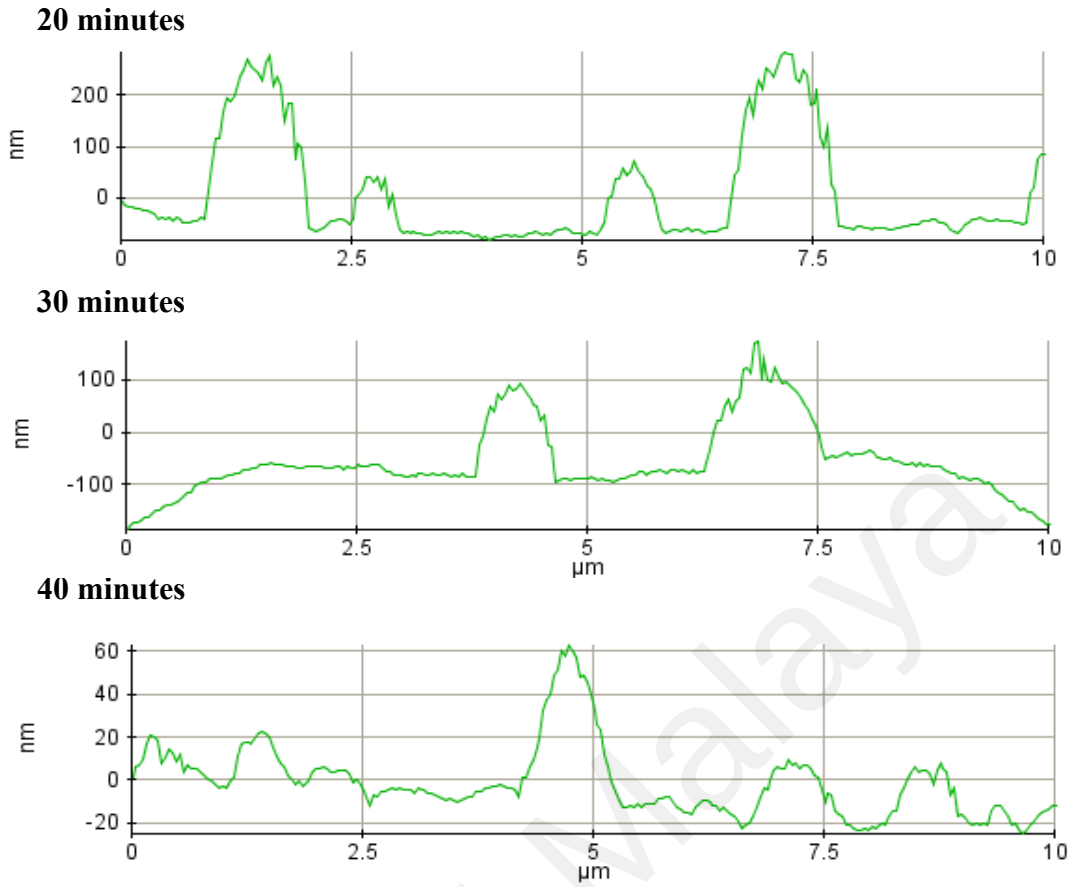

Figure 4.19: Line profiles for the 20-, 30- and 40-minute films fabricated at 550 °C.

Table 4.4: Surface roughness parameters for the 20-, 30- and 40- minute films fabricated at 550 °C.

Films	Parameters	Values (nm)
20 mL/20 mins	Roughness average, R_a	85.046
	Root mean square, R_q	106.447
	Maximum profile height, R_{pv}	367.998
	Maximum valley depth, R_v	83.869
	Maximum peak height, R_p	284.129
20 mL/30 mins	Roughness average, R_a	49.755
	Root mean square, R_q	69.321
	Maximum profile height, R_{pv}	360.726
	Maximum valley depth, R_v	186.948
	Maximum peak height, R_p	173.778
20 mL/40 mins	Roughness average, R_a	12.120
	Root mean square, R_q	16.719
	Maximum profile height, R_{pv}	88.069
	Maximum valley depth, R_v	25.263
	Maximum peak height, R_p	62.806

Universiti Malaya

4.3.6 Scanning Electron Microscopy (SEM) Analyses

The morphology obtained from FESEM (Fig. 4.20) showed grains scattered over the surface of the films. The size of the grains increased with increasing length of deposition time as displayed in the size distribution histogram as shown in Fig. 4.21 obtained from population size of 200 particles. The cracks observed in SEM images for 40-minute films were the result of long period of deposition time (Kibsgaard et al., 2014). The large distribution of adequately sized MoP_2 grains on the surface of 20-minute and 30-minute films gave them the large root-mean-square surface roughness R_q. Based on the size distribution histograms, the particle size of the grains in the range of 1000-3000 nm was dominant in 20-minute (79.5%) and 30-minute (71%) films. The particle size of less than 1000 nm was dominant in 40-minute film (60 %). It was observed that roughness decreased with increment of deposition time. This correlation corresponded with increasing distances between the agglomerated grains as shown in the AFM and SEM images. This resulted to wider surface with lower surface roughness. It was observed that 40-minute film with the largest distances between the agglomerated grains possessed the lowest R_q.

Universiti Malaya

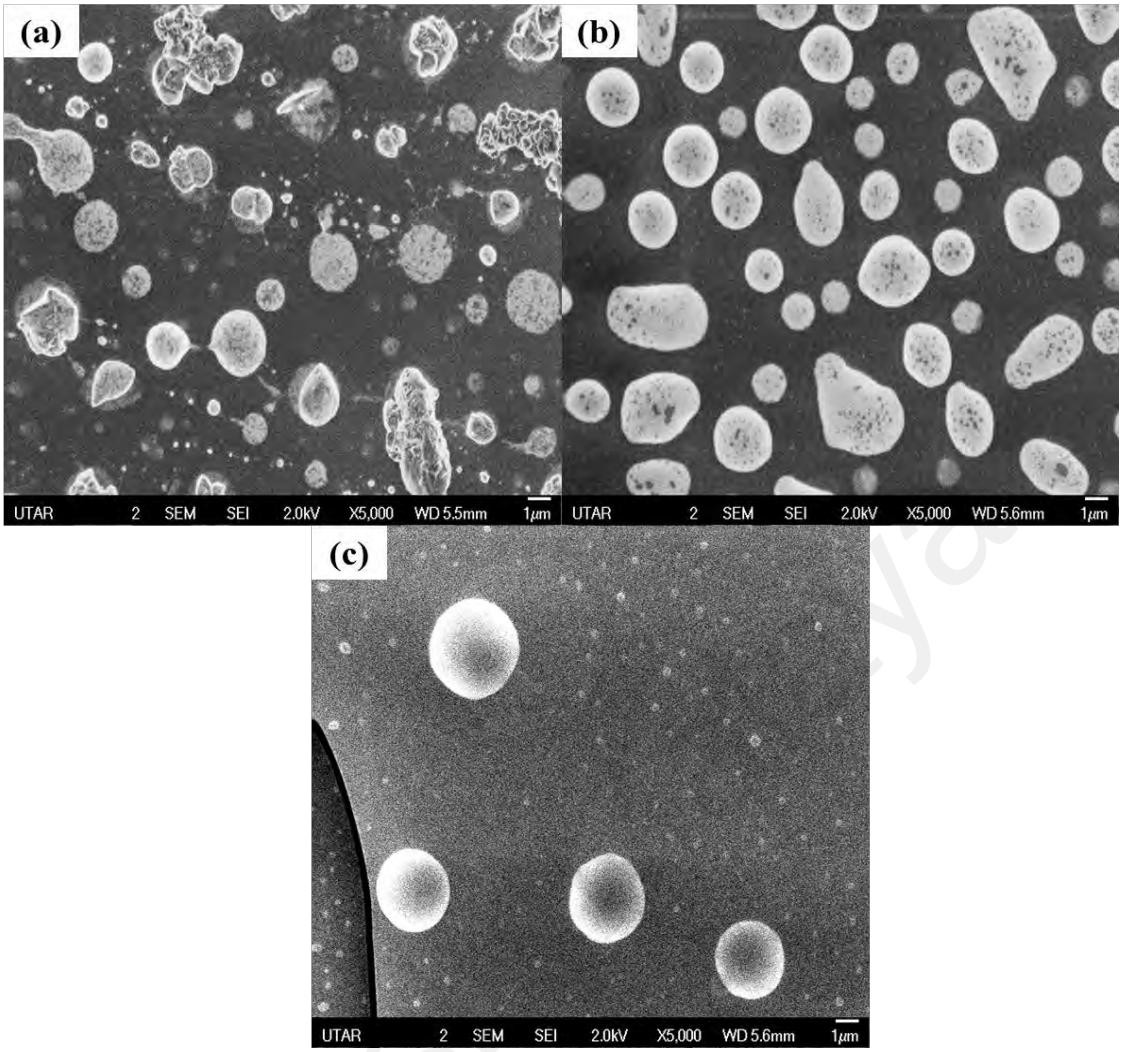

Figure 4.20: SEM images in ×5,000 magnification of the (a) 20-minute, (b) 30-minute and (c) 40-minute films fabricated at 550 °C.

Universiti

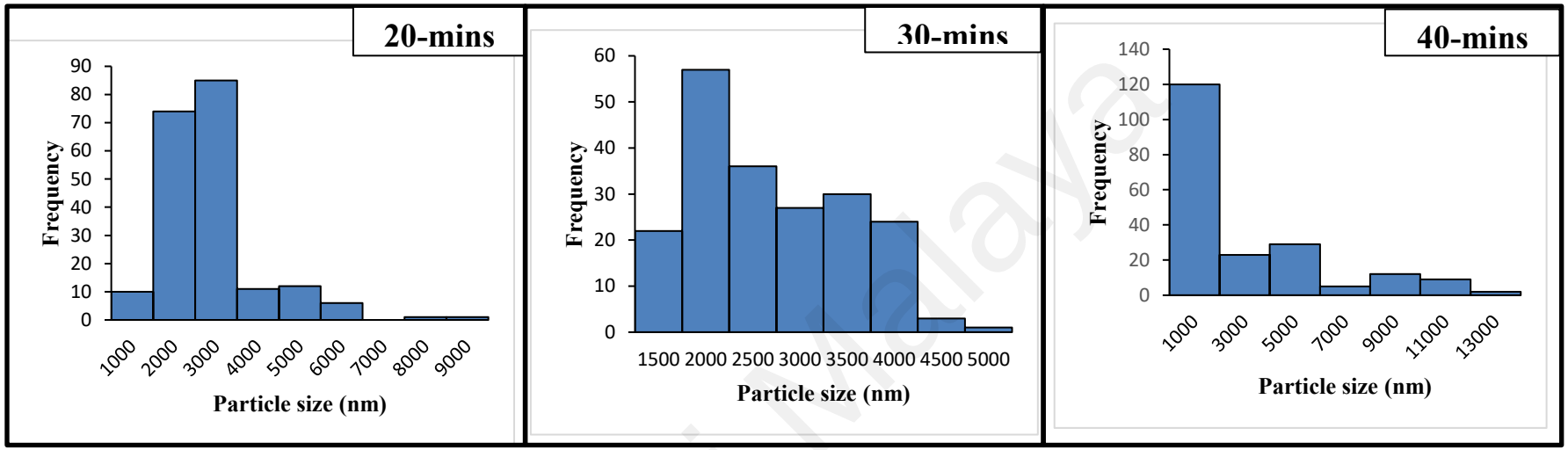

Figure 4.21: Histograms displaying size distribution of nanoparticles of the 20-, 30- and 40-minute films fabricated at 550 °C.

Universiti Malaya

4.3.7 Film Thickness Measurements

The thickness of the films was measured by using surface profilometer. the thickness had increased with increasing deposition time. The film thickness of the 20-minute, 30-minute and 40-minute films were 432 nm. 968 nm and 4062 nm respectively. The sharp increase in film thickness was observed in 40-minute film due to very large amount of precursor material that were deposited onto the FTO glass substrate during the longest period of AACVD deposition process. This observation shows that the deposition time is the determining factor on the film thickness.

4.3.8 High-Resolution Transmission Electron Microscopy (HRTEM)

High-resolution transmission electron microscopy (HRTEM) was employed to observe the structure of Mo_2S_3/MoP_2 film. The 40-minute film was chosen to be analysed and the TEM image was shown in Fig. 4.22 (a). The HRTEM image in Fig. 4.22 (b) showed the two different phases with *d*-spacings of 0.26 nm and 0.38 nm which corresponded to the (01-2) plane of Mo_2S_3 and (021) plane of MoP_2, respectively. This observation was in agreement with studies carried out by Jin et al. (2020) and Zhou et al. (2018). TEM analysis showed the formation of Mo_2S_3/MoP_2 heterostructure. Moreover, based on the FFT images obtained from the HRTEM as displayed in Fig. 4.22 (c), the Mo_2S_3 phase was indicated by the (002) and (101) reflection planes whereas MoP_2 was indicated by the reflection planes of (110) and (021).

Universiti Malaya

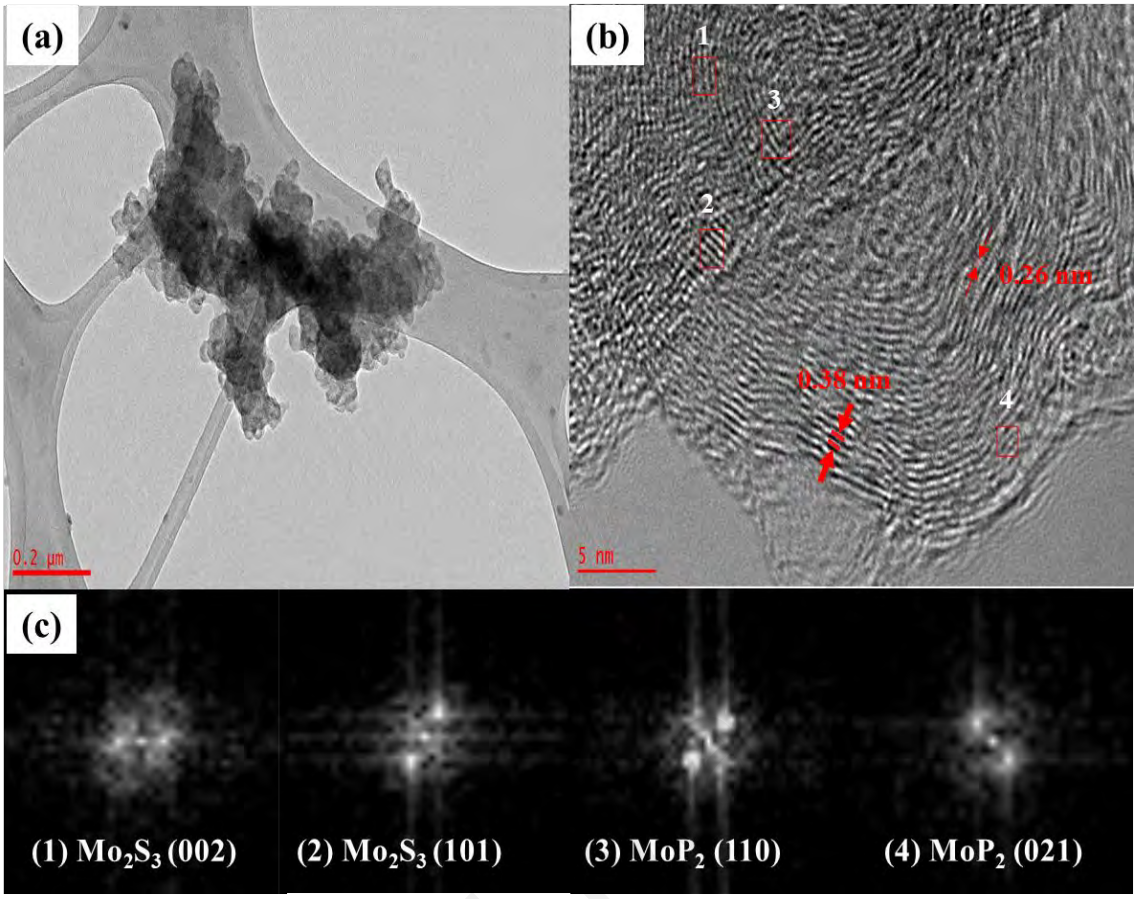

Figure 4.22: (a) TEM image of particles on 40-minute film with (b) HRTEM image showing *d*-spacings of Mo_2S_3 and MoP_2 and the (c) FFT images of the selected areas of the HRTEM image.

4.3.9 UV-vis Spectrophotometry

The optical property of the fabricated films was analysed with UV-vis spectrophotometry. From the UV-vis absorption spectra displayed in Fig. 4.23, it was shown that absorbance increased with longer deposition time where the 40-minute film exhibited the highest absorbance followed by 30-minute and 20-minute films. As the deposition time was longer, the amount of precursor material deposited on the FTO substrates increased leading to higher light absorption. The direct bandgap energy values of the Mo_2S_3/MoP_2 films prepared after 20, 30 and 40 minutes of deposition time were calculated by using the Tauc plot equation in Eq. 4.1,

$$(\alpha h\nu)^{\frac{1}{n}} = B(h\nu - E_g) \qquad (4.1)$$

where B is a proportionality constant, h is Planck's constant, ν is vibration frequency, α is absorption coefficient, E_g is the bandgap energy value and n=1/2 for direct transition (Lau et al., 2022). The absorption coefficient, α was obtained from the equation in the Eq. 4.2 (Suresh, 2013);

$$\alpha = \frac{2.303 \times A}{d} \qquad (4.2)$$

where A is absorbance determined from the UV-vis spectrum and d is the film thickness measured by using surface profilometer. To determine the bandgap energy values, the tangential lines along the curves in the Tauc plot were extrapolated until they intersected at x-axis. The values of the x-intercepts were the bandgap energy values of the films.

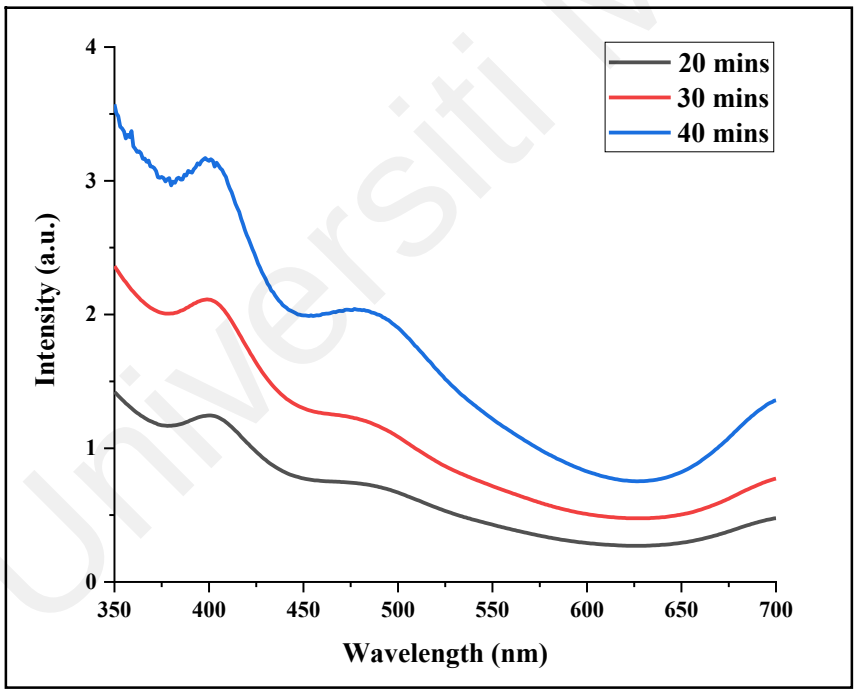

Figure 4.23: UV-vis absorbance spectra of the films prepared at 20, 30 and 40 minutes of deposition time at 550 °C.

Universiti Malaya

The two peaks observed in the absorption spectra in Fig. 4.23 suggested that two types of materials were incorporated in the films and based on the characterization results, Mo_2S_3 and MoP_2 were present in the composite material. Mo_2S_3 material had the literature bandgap energy value of ~2.3 eV and MoP_2 was reported to have the bandgap energy value of 2.8 eV in visible light region (Lim et al., 2019; Wu et al., 2015). Interestingly, the valence band (VB) and conductive band (CB) of the MoP_2 overlapped and the band gap of 2.8 eV for MoP_2 was the energy difference between VB and the band below VB rather than between VB and CB as in typical semiconductors (Wu et al., 2015). The bandgap energy values were determined from the Tauc plot displayed in Fig. 4.24 and found to be 2.1-2.2 eV and 2.7 eV, which were close to the literature values for Mo_2S_3 and MoP_2 (Lim et al., 2019; Wu et al., 2015).

Universiti Malaya

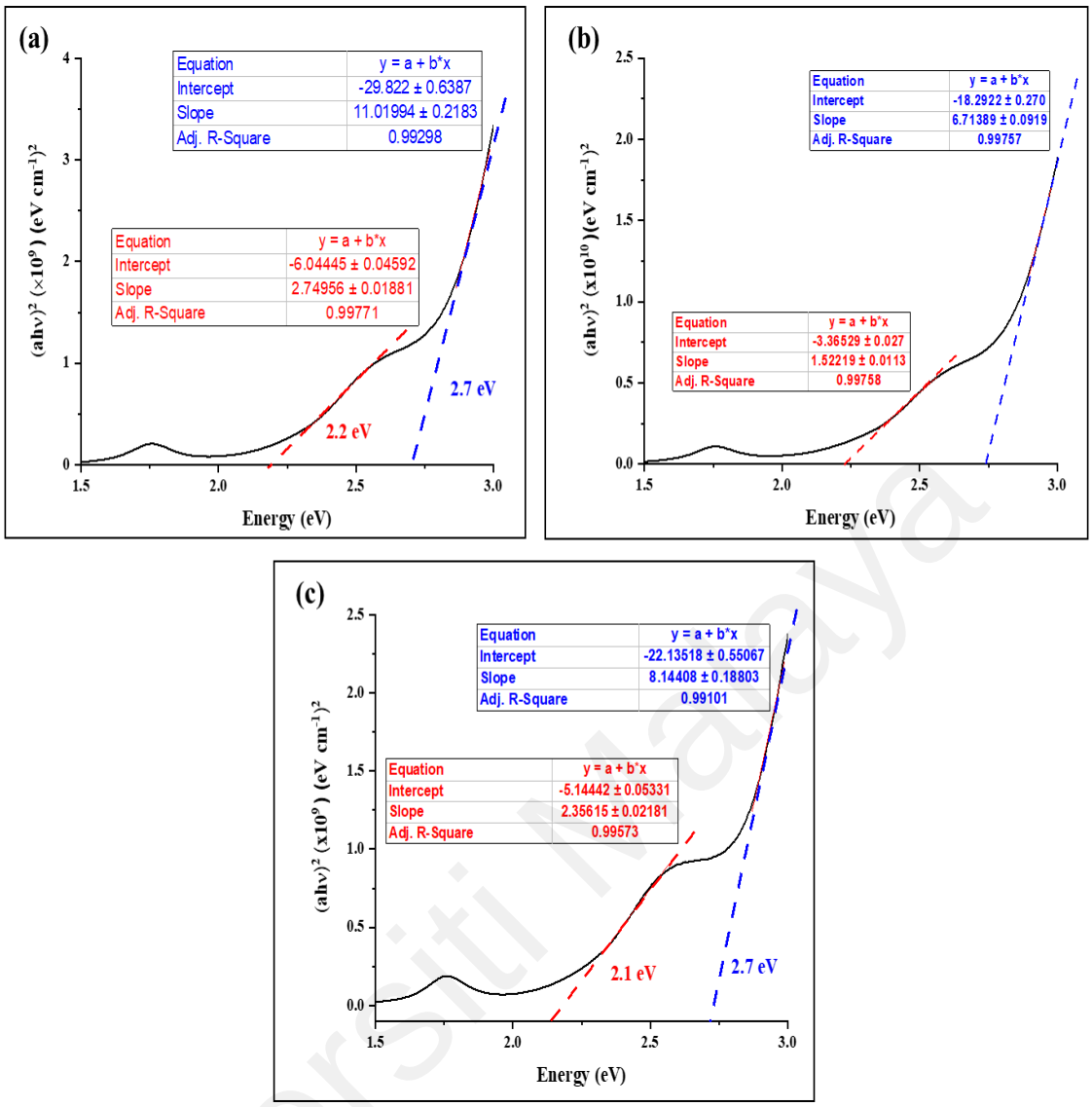

Figure 4.24: Tauc plots and bandgap values of films fabricated at (a) 20 minutes, (b) 30 minutes and (c) 40 minutes of deposition time at 550 °C.

4.3.10 Electrochemical Studies

In electrochemical studies, the three-electrode configuration was employed with Ag/AgCl used as reference electrode that was filled with 3M NaCl solution, platinum wire acted as a counter electrode and the films were the working electrodes. 0.25M of H_2SO_4 (pH 0.95 at 25 °C) was used as the electrolyte. The analyses to be performed were linear sweep voltammetry (LSV) for the analyses of the current-voltage (*J-V*) characteristics of the films, Mott-Schottky analyses for the calculation of charge carrier

Universiti Malaya

densities as well as electrochemical impedance spectroscopy (EIS) to determine the impedances of the films as well as the lifetimes of the films. $E_{Ag/AgCl}$ was calibrated to Reduction Hydrogen Electrode potential (RHE), E_{RHE} by using the Nernst equation; $E_{RHE} = E_{Ag/AgCl} + 0.059\ pH + E^{\circ}_{Ag/AgCl}$, where $E^{\circ}_{Ag/AgCl}$ = 0.1976V at 25 °C (298.15K).

CV analysis was performed for 5 cycles at the scan rate of 100 mV/s and the CV curves were displayed in Fig. 4.25. It was found that 40-minute film had the highest stability whereas 20- and 30-minute films exhibited changes of the curve after each cycle pointing to their low stability in electrocatalytic activity in acidic media. Based on the CV curves, the E_{ox} at which the anodic peak occurred for the 20-, 30- and 40-minute films were found to be 0.59, 0.42 and 0.45 V vs. RHE, respectively and the E_{red} at which the anodic peak occurred for the films were found to be 0.35, 0.18 and 0.19 V vs. RHE, respectively. The potential difference, ΔE_p between E_{ox} and E_{red} for the 20-, 30- and 40-minute films were found to be 0.24, 0.24 and 0.26 V, respectively. The numbers of electrons transferred (denoted by z) were determined by using Eq. 4.3 as shown in the following;

$$\Delta E_p = \frac{59\ mV}{z} \qquad (4.3)$$

Based on the calculations, the numbers of electrons transferred in the CV analyses for the 20-, 30- and 40-minute films in acidic media of pH 0.95 in the potential window of -0.6 V to 0.6 V vs. Ag/AgCl were obtained to be 0.246, 0.246 and 0.227, respectively.

Universiti Malaya

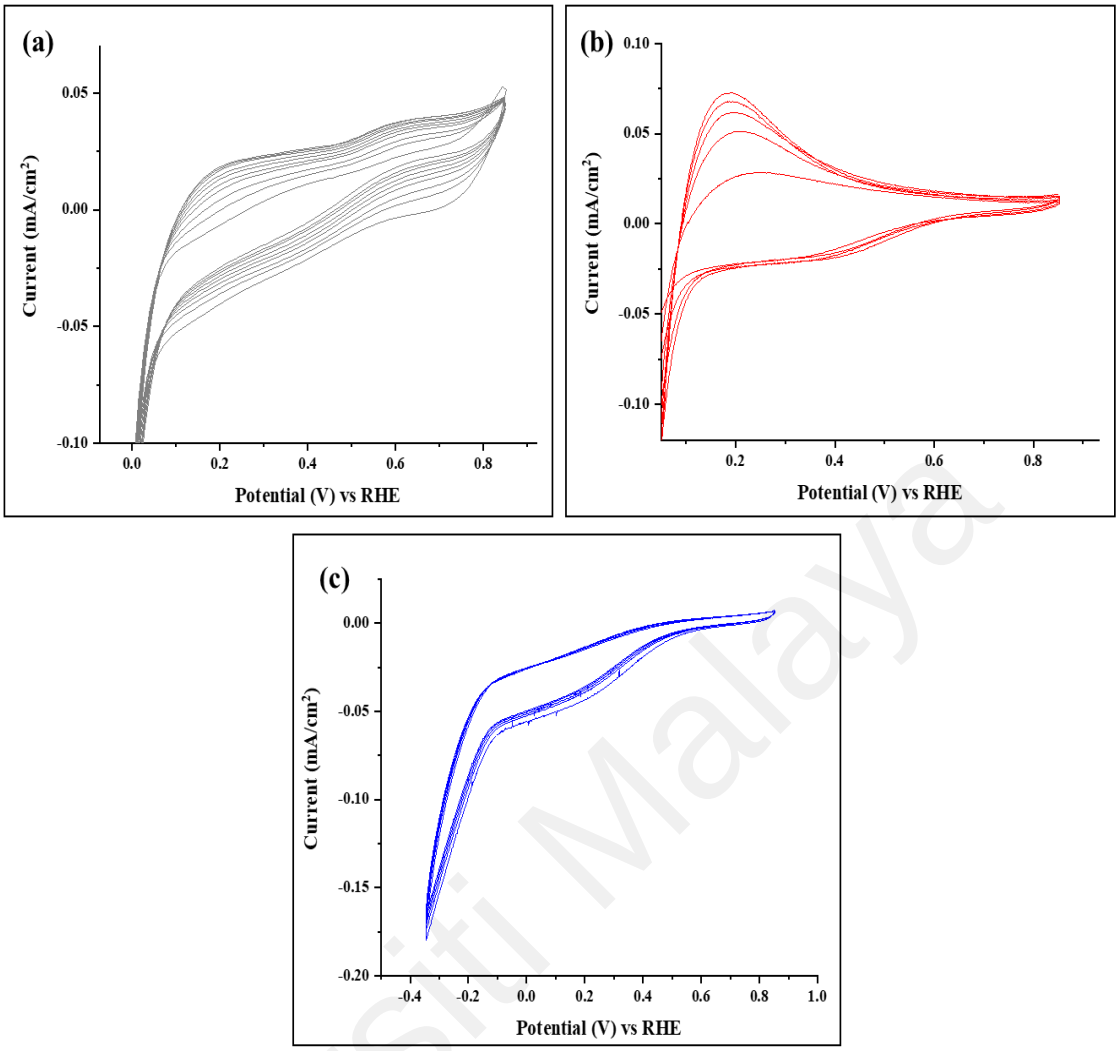

Figure 4.25: CV curves of (a) 20-minute, (b) 30-minute and (c) 40-minute films.

Theoretically, HER occurs at 0 V vs. RHE at which the system has achieved equilibrium potential (Zhang et al., 2020). Overpotential, η is the applied potential for the cathodic shift from the equilibrium potential to drive HER process. The extra potential is provided to exceed the thermodynamic demand in order to drive HER process (Zhang et al., 2020). The smaller the value of the overpotential, the better performance is exhibited by the electrocatalyst (Zhang et al., 2020). The onset potential (measured at 1 mA/cm^2 and overpotential at 10 mA/cm^2 are commonly used to evaluate the performance of electrocatalysts in HER (Feng et al., 2020). The *J-V* curves obtained from LSV analysis with the potential window of -0.35 to 0.85 mV (vs. RHE) were displayed in Fig. 4.26.

Universiti Malaya

The onset potential for 20-minute and 30-minute film were found to be 93 mV and 45 mV, respectively. The 40-minute film was found to have the largest onset potential without reaching 1 mA/cm^2 in the same potential window.

Based on LSV analyses, it was found that at overpotential vs RHE of 250 mV, 30-minute film generated current density of 10 mA/cm^{2,} more than that of 20-minute film which was 4.3 mA/cm^2. Though the 30-minute film had the lowest MoP_2 composition (Mo^{6+}/Mo^{3+} ratio of 0.20), the MoP_2 grains were widely distributed. Wide distribution of MoP_2 grains provided more heterojunctions between Mo_2S_3 and MoP_2 resulting to the best electrochemical performance for 30-minute film. 40-minute film exhibited the poorest activity with current density of 0.1 mA/cm^2 generated at 250 mV although it had the largest MoP_2 composition (Mo^{6+}/Mo^{3+} ratio of 0.45). The poorest performance was due to the poor distribution of MoP_2 grains over the Mo_2S_3 nanoparticles as displayed in SEM-elemental mapping analyses which resulted to the lack of heterojunctions which provided active sites for HER. The LSV analysis showed that the 30-minute film required lower applied potential than the reported urchin-like Mo_2S_3 (257 mV) to generate 10 mA/cm^2 of current density in acidic media (Zhou et al., 2018).

High surface roughness of the 20 and 30-minute films as indicated by the higher R_q values than 40-minute film provided the films with more assessable active sites for HER therefore exhibiting more superior performance than 40-minute film (Abdel-Karim et al., 2012). The larger overpotential exhibited by 20-minute film could be attributed to its very large surface roughness that led to higher resistivity in electron transport due to electron scattering though it could result to more exposure of active sites for HER (Tang et al., 2012). Therefore, the surface roughness should be optimised to ensure low resistivity in electron transport as well as more assessable active site for HER.

Universiti Malaya

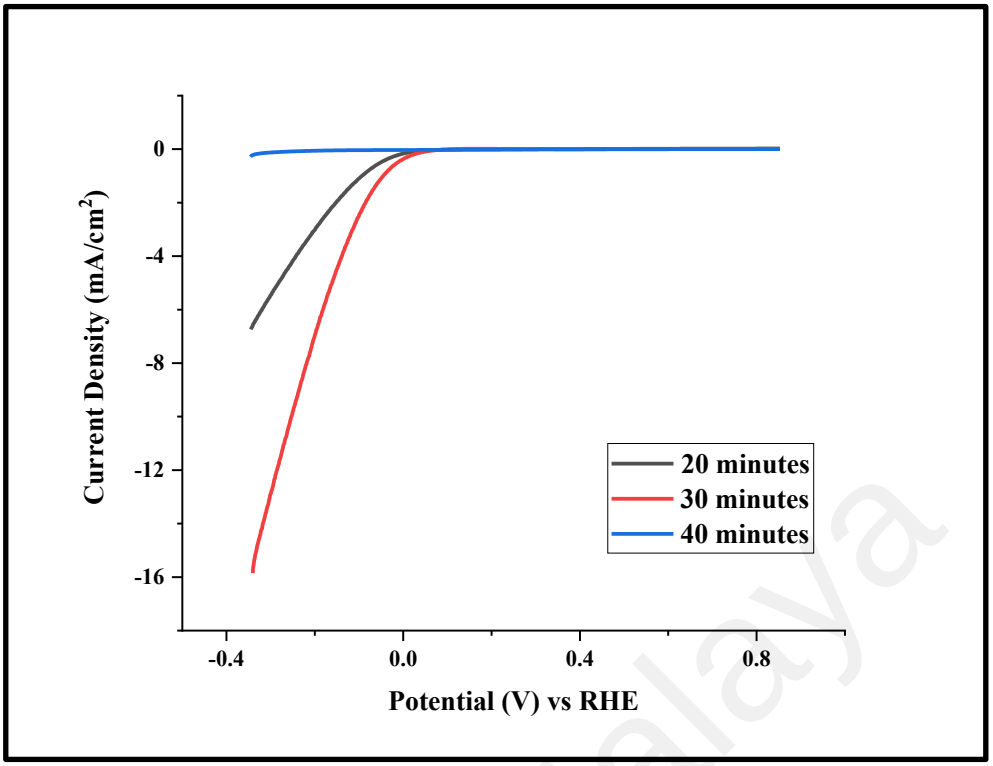

Figure 4.26: LSV curves (*J-V*) of 20-, 30- and 40-minute films.

The Mott-Schottky (MS) plots of the films were displayed in Fig. 4.27. MS plots were generated with $\frac{1}{C^2}$ against applied potential, V_p. The MS plots were obtained by Eq. 4.4 (Lau et al., 2022).

$$\frac{1}{C^2} = \frac{2}{A^2 N_d \varepsilon_r \varepsilon_\circ}[(V_p - V_{fb}) - \frac{k_B T}{q}] \qquad (4.4)$$

Where *C* is specific capacitance (in F cm^{-2}), A is surface area of electrode, N_d is donor density, $\varepsilon_\circ$ is vacuum permittivity, ε_r is the relative dielectric constant of the film, V_{fb} is flat band potential, k_b is Boltzmann's constant and T is ambient temperature (in K). Capacitance is the amount of charge per volt. Therefore, according to Eq. (4.4), as the applied voltage increases, the capacitance decreases. This relationship is inversely proportional.

Universiti Malaya

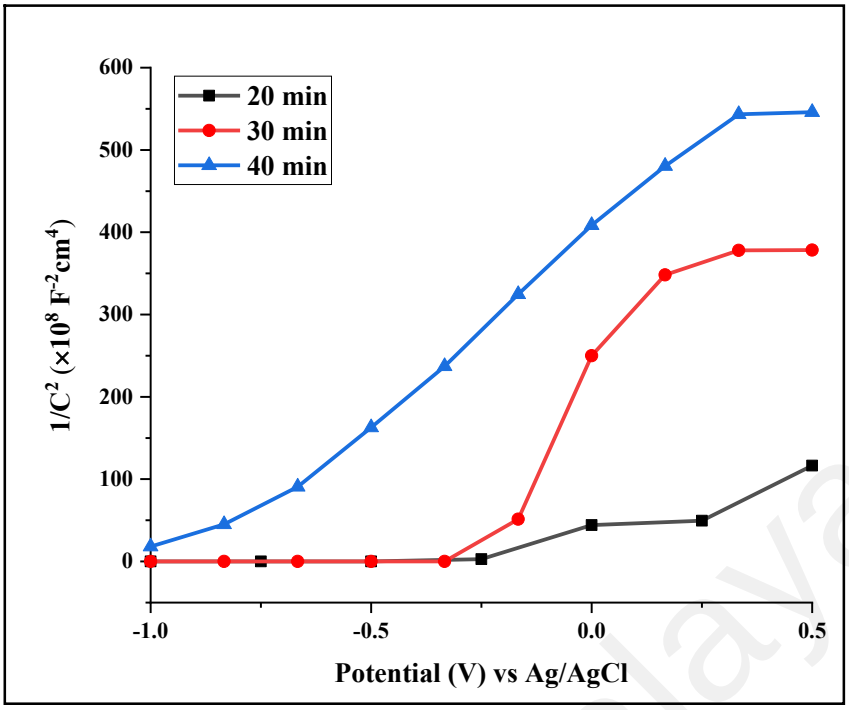

Figure 4.27: MS plots for the 20-, 30- and 40-minute films fabricated at 550 °C.

Based on the MS plots, the positive slopes were obtained for all the films indicating that the films were n-type semiconductors and electrons were the majority charge carriers. The n-type semiconductor donates electrons which catalyses HER in acidic media. The charge density was calculated based on the MS analysis of the films by using Eq. 4.5 in the following (Lau et al., 2022):

$$N_d = \left({}^{2}/_{A^2 e_o \varepsilon_o \varepsilon_r}\right)\left[\frac{d\left(\frac{1}{c^2}\right)}{dV}\right]^{-1} \qquad (4.5)$$

where $\left[\frac{d\left(\frac{1}{c^2}\right)}{dV}\right]$ is the slope of the obtained Mott-Schottky plot and e_o is charge of electron, which is 1.6×10^{-19} F/V. Eq. 4.5 could be simplified into Eq. 4.6 as shown in the following (Lau et al., 2022):

$$N_d(cm^{-3}) = \frac{1.42\times10^{32}(F^2\times V^{-1}\times cm)}{\varepsilon_r \times A^2(cm^4)\times \text{Slope } (F^2\times V^{-1})} \qquad (4.6)$$

Universiti Malaya

Relative dielectric constant, ε_r which is dimensionless is often assumed to be 10 because it is usually slightly or below this value (Chen et al., 2013). The MS slopes and electron densities for the films were tabulated in Table 4.4.

The calculated electron densities (donor densities) were displayed in Table 4.5. The 20-minute film had the highest donor density of 6.07×10^{20} cm^{-3}. Although 40-minute film had higher donor density than the 30-minute film, the electron flow was restricted by the morphology of the 40-minute film which displayed the lack of homogeneity in distribution of MoP_2 grains as well as its unfavorable film thickness. Based on the MS analysis, although the charge density was the lowest for 30-minute film, it was suggested that high electron mobility enhanced the HER kinetics in 30-minute film owing to its morphology which promoted electronic interaction between Mo_2S_3 and MoP_2. The MS analysis also revealed that high donor density is not a standalone criterion which directs excellent HER performance taking the mobility of charge carrier into consideration. The donor density of the MoS_2/Mo_2S_3 film had been reported to be 8.24×10^{17} cm^{-3} and this result suggested the introduction of P dopants increased the electron density of the Mo_2S_3 significantly (Lim et al., 2019). Therefore, low P:S ratio could be the reason that resulted in the lowest donor charge density as in the case of 30-minute film which possessed the lowest P:S ratio based on Table 4.3.

Regarding the free energy for hydrogen adsorption (ΔG_{H*}) of the materials, too large electron density may also deteriorate the HER performance. Too large electron density increases the adsorption energy of the material and subsequently impedes the desorption of hydrogen atoms to produce hydrogen gas (Wang et al., 2020). The poorer HER performance for 20-minute and 40-minute films was probably caused by too large electron density which had impeded the desorption of hydrogen atoms to produce H_2 gas in HER.

Universiti Malaya

Table 4.5: The charge densities of the 20-, 30- and 40-minute films fabricated at 550 °C.

Films	Area (cm^2)	Slope of MS plot, $\left[\frac{d\left(\frac{1}{c^2}\right)}{dV}\right]$ (F^2V^{-1})	Donor density, N_d (cm^{-3})
20-minutes	1.3	138.48×10^8	6.07×10^{20}
30-minutes	1.7	890.73×10^8	5.52×10^{19}
40-minutes	1.3	494.94×10^8	1.70×10^{20}

EIS analyses were performed on the films to obtain the Nyquist plots and the Bode plots. Nyquist plot is used to determine the electron kinetics of the analysed sample. From the Nyquist plot which depicted the semi-circular curve as displayed in Fig. 4.28 (a), the diameter of the curve was obtained to determine the charge transport resistance of the films which is denoted by R_{CT}. The R_{CT} for each film was analysed once to avoid prolonged exposure of the samples to the analysis condition which was destructive to the films during electrochemical studies. The smaller diameter of the semi-circular plot indicates smaller resistance which leads to better electron transfer. Based on the Nyquist plot displayed in Fig. 4.28 (a), 30-minute film had the lowest transport resistance, R_{CT} with the smallest diameter of the semi-circular plot of 715.14 Ω. The result well agreed with the LSV analysis that the 30-minute film showed better performance in LSV analyses than 20 and 40-minute films. The transport resistance from lowest to highest was in the order of 30 minutes < 20 minutes < 40 minutes. Due to very large film thickness, the electrons were subjected to large transport resistance causing the electron flow to be hindered in 40-minute film. With respect to the surface roughness, the larger R_q for the 20-minute film than that of 30-minute film resulted to more electronic transport resistance (Tang et al., 2012).

By referring to the Bode plots shown in Fig. 4.28 (b), the frequency at which the peaks occurred were determined to calculate the electron lifetimes of the fabricated

Universiti Malaya

semiconductor materials by using the formula, $\tau = \frac{1}{2\pi\nu}$, where ν is the frequency where the peak occurs and is inversely proportional to the electron lifetime (τ = 1/ (2πν). The frequency maxima and lifetime for the films were displayed in Table 4.6. The frequency maxima from lowest to highest was in the order of 40-minute < 20-minute < 30-minute. The higher the frequency maxima, the shorter the lifetime of the film. Therefore, the 40-minute film had the longest lifetime whereas the 30-minute film had the shortest lifetime. The film with long electron lifetime would have long electronic transport path length and minimal electron-hole recombination (Kaur et al., 2020). It is demonstrated that the R_{CT} of the electrocatalyst is directly proportional with the length of lifetime (Kaur et al., 2020). High transport resistance reduced the charge recombination in 40-minute film and hence large number of electrons were accumulated in the film which contributed to the longest electron lifetime for the 40-minute film.

Table 4.6: The Frequency maxima and lifetime of the 20-, 30- and 40-minute films fabricated at 550 °C.

Deposition time (mins)	Frequency Maxima (Hz)	Lifetime τ = 1/ (2πν) (s)
20	0.15	1.06
30	3.96	0.04
40	0.06	2.65

Universiti Malaya

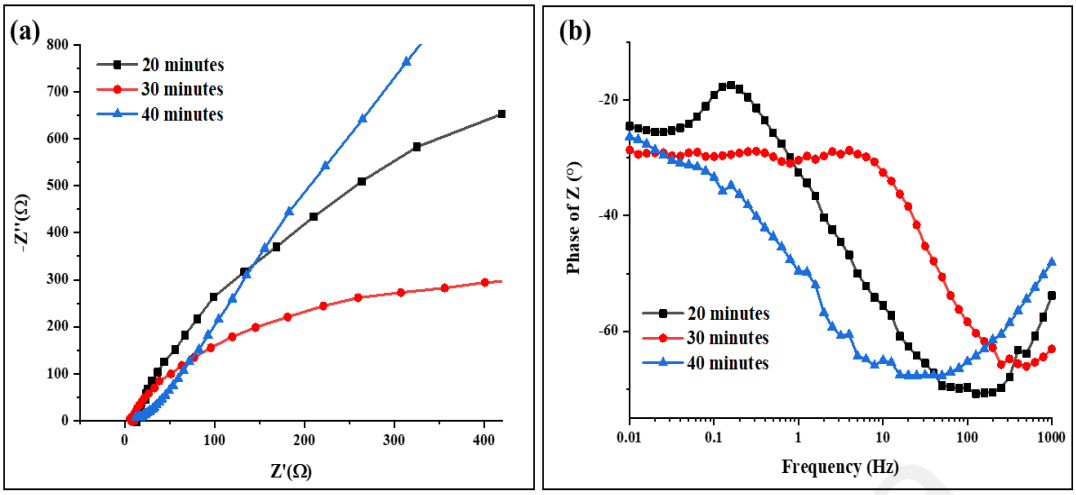

Figure 4.28: (a) Nyquist plots and (b) Bode plots of the 20-, 30- and 40-minute films fabricated at 550 °C.

4.3.11 Inherent Properties of the Films

Charge transfer resistance (R_{CT}), Tafel slope (b) and exchange current density (j_o) are some of the inherent properties of the electrocatalysts commonly used to access the efficiency of the electrocatalysts in HER. Tafel slopes were determined from plots of overpotential η vs log (current density) obtained from LSV (*J-V*) curves to illustrate the inherent properties of the films based on the Tafel equation, $\eta = b\log j + a$ (Wang et al., 2021). (b is Tafel slope and j is current density, η is overpotential). η is the difference between the electrode and standard potential and in the HER the $E_0 = 0V$ (Shinagawa et al., 2015). Tafel slope and exchange current density, j_0 are correlated to rate of electron transfer and HER kinetics. Tafel slope describes the mechanism of the electrochemical reaction and also reflects the desorption speed of adsorbed hydrogen atoms (Feng et al., 2020; Shinagawa et al., 2015). The exchange current density, j_0 was obtained by extrapolating the Tafel slope until it cut at x-axis where η =0 V vs. RHE. j_0 is the current density at equilibrium in which cathodic and anodic current are equalled (Shi et al, 2016; Wang et al., 2021). j_0 describes the electron transfer ability and feasibility of electrode

Universiti Malaya

reaction which depend on several factors such as materials of the electrode, the choice of electrolyte and temperature (Shi et al, 2016).

Tafel slopes (b) and exchange current densities (j_0) of the fabricated films were displayed in Table 4.7. The smaller the Tafel slope, the faster the rate of HER (faster charge transfer kinetic) (Wang et al., 2021). High j_o indicates smaller current density is required to perform the electrochemical reaction (Shi et al., 2016). Ideally, the electrocatalyst with high HER performance should have relatively small Tafel slope, small overpotential and high j_0 (Zhang et al, 2021; Wu et al., 2017).

There are three types of rate-limiting steps that proceed in HER process. Heyrovsky, Tafel and Volmer reactions are the rate-determining steps if the Tafel slopes are ~30, ~40 and close to or larger than 120 mV/dec, respectively (Song et al., 2016).

J-V curves obtained from LSV analyses were converted to the Tafel plots displayed in Fig. 4.29. The 20-minute and 30-minute film had similar Tafel slopes with 123.2 and 123.4 $mVdec^{-1}$, respectively. From the calculations of exchange current densities (j_o), 30-minute film had the highest value of 0.408 mA/cm^2 whereas 20-minute film had the j_o of 0.182 mA/cm^2. Both calculated values were also higher than the j_o of MoP_2 nanoparticles which was reported to be 0.038 mA/cm^2 (Luo et al., 2018). The j_o value of carbon supported MoS_2/MoP catalyst treated at 900 °C was reported to be 0.192 mA/cm^2 which demonstrated that the 30-minute film exhibited faster reaction rate per surface area than the carbon supported MoS_2/MoP and also the pristine MoP_2 due to the larger number of active sites in the 30-minute Mo_2S_3/MoP_2 film (Wu et al., 2018). The result suggested that the synergistic effect between phosphorus and sulphur that provided more active sites for the electron exchange process which enhanced the reaction rate of the HER. The poorest electrochemical performance exhibited by the 40-minute film was due to its morphology. The highly aggregated grains observed in the 40-minute film

Universiti Malaya

impeded the catalytic efficiency of the catalyst. The largest charge transfer resistance, R_{CT} of the 40-minute film indicated that the transport of electrons in the catalyst was most restricted. The inherent properties of the films were displayed in Table 4.7.

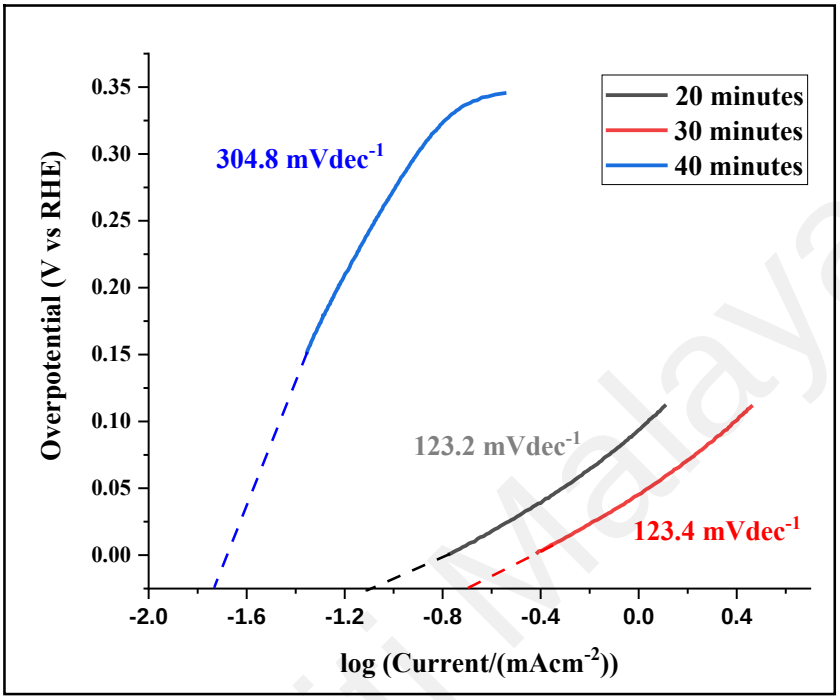

Figure 4.29: Tafel slopes for the 20-, 30- and 40-minute films fabricated at 550 °C.

Table 4.7: Inherent properties of the 20-, 30- and 40-minute films fabricated at 550 °C.

Films	Tafel slope, *b* ($mVdec^{-1}$)	Exchange current density, j_0 (mA/cm^2)	Charge transfer resistance, R_{CT} (kΩ)
20-minute	123.2	0.182	3.019
30-minute	123.4	0.408	0.715
40-minute	304.8	0.013	13.958

4.4 Characterization of Films Fabricated with different volume/deposition time at 550 °C

The films were fabricated with different volume of precursor solution and different time of deposition of 10 mL/10 mins, 15 mL/15 mins, 20 mL/20 mins and 25 mL/25 mins at the deposition temperature of 550 °C with the carrier gas flow set at higher

Universiti Malaya

rate at a 0.5 SCFH. The films were characterised with XRD, Raman spectroscopy, SEM, EDX, AFM, UV-vis spectrophotometry, and electrochemical studies.

4.4.1 X-ray Diffraction Analyses (XRD)

The XRD diffraction patterns of the films were indexed to monoclinic Mo_2S_3 (JCPDS no. 98-006-2486) and orthorhombic MoP_2 (JCPDS no. 98-003-7222) as displayed in Fig. 4.30. The peak list was shown in Table 4.8 and the 2θ positions were matched with the reference 2θ in the diffraction patterns of the indexed Mo_2S_3 and MoP_2 phases. The enlarged XRD patterns with range of 2θ from 10°-25° and 30°-31.5° were displayed in Fig. 4.31 (a) and 4.31 (b), respectively. Lower number of peaks of Mo_2S_3 planes were observed as solution volume and deposition time increased. The restricted growth of Mo_2S_3 planes was possibly caused by the increased activation energy in nucleation process to form crystals when the deposition rate increased with higher loading of Mo_2S_3 particles onto the 20 mL/20 mins and 25 mL/ 25 mins films (Khoo et al., 2016). The (021) plane of MoP_2 was present in all the films.

Universiti Malaya

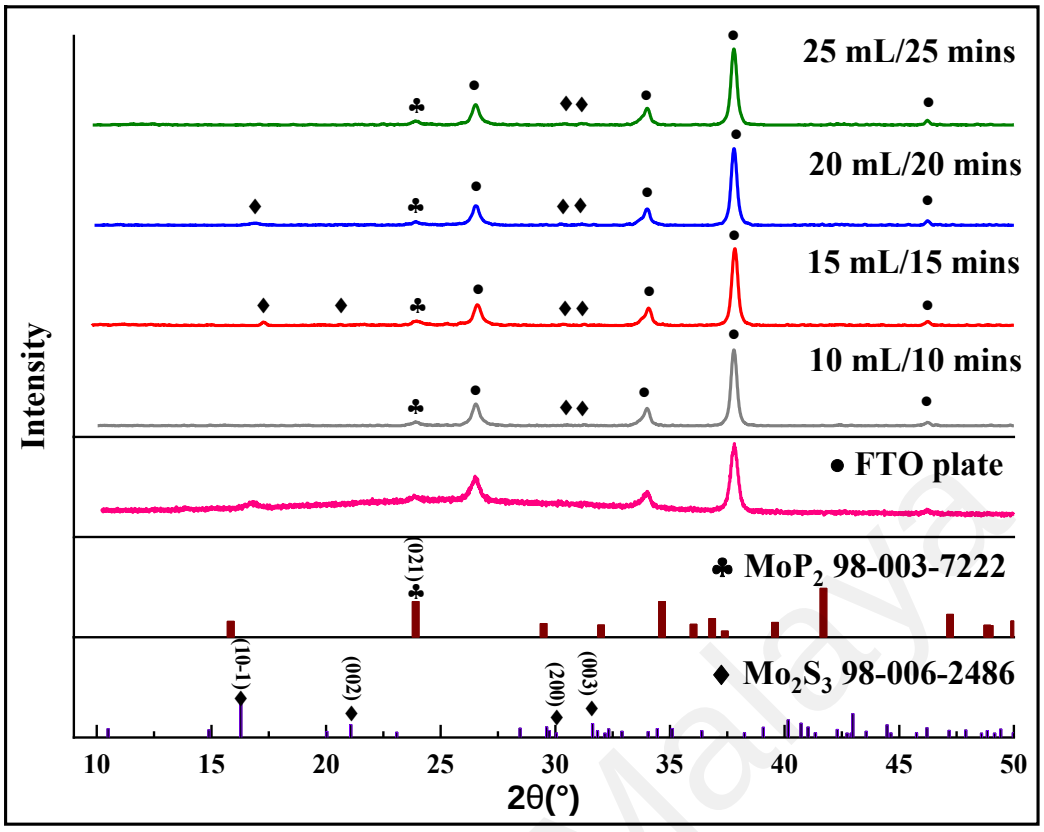

Figure 4.30: XRD patterns of 10 mL/10 mins, 15 mL/15 mins, 20 mL/20 mins and 25 mL/25 mins films fabricated at 550 °C.

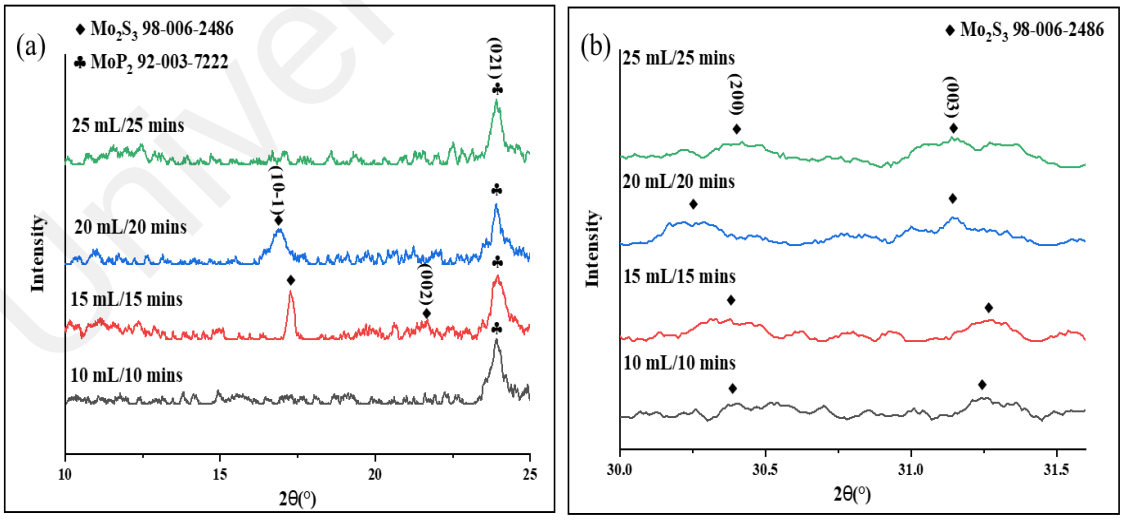

Figure 4.31: Enlarged XRD patterns of the films in 2θ range of (a) 10°-25° and (b) 30°- 31.5° fabricated at 550 °C.

Universiti Malaya

Table 4.8: XRD peak list for the 10 mL/10 mins, 15 mL/15 mins, 20 mL/20 mins and 25 mL/25 mins films fabricated at 550 °C.

Films	2θ (°)	Assigned Peaks	Reference 2θ (°)
10 mL/10 mins	24.2	MoP_2 (021)	23.9
	30.4	Mo_2S_3 (200)	30.0
	31.2	Mo_2S_3 (003)	31.6
15 mL/15 mins	17.3	Mo_2S_3 (10-1)	16.3
	21.7	Mo_2S_3 (002)	21.1
	24.2	MoP_2 (021)	23.9
	30.4	Mo_2S_3 (200)	30.0
	31.3	Mo_2S_3 (003)	31.6
20 mL/20 mins	16.9	Mo_2S_3 (10-1)	16.3
	24.1	MoP_2 (021)	23.9
	30.2	Mo_2S_3 (200)	30.0
	31.1	Mo_2S_3 (003)	31.6
25 mL/25 mins	24.2	MoP_2 (021)	23.9
	30.4	Mo_2S_3 (200)	30.0
	31.1	Mo_2S_3 (003)	31.6

The crystallite size, *D* was obtained from Debye-Scherrer equation, $D = \frac{K\lambda}{\beta\cos\theta}$ and the average crystallite sizes of Mo_2S_3 and MoP_2 of the films were displayed in Table 4.9. The average crystallite size of Mo_2S_3 grown in the 10 mL/10 mins film was 48 nm whereas its average crystallite size of MoP_2 was 25.7 nm. 15 mL/15 mins film had the average crystallite size for Mo_2S_3 of 52.8 nm and MoP_2 29.5 nm. The crystallite sizes for both phases increased as volume and deposition time increased. 20 mL/20 mins film had the average crystallite size for Mo_2S_3 of 41.2 nm and MoP_2 29.6 nm (Refer to Table 4.9). Unexpectedly, the crystallite size of Mo_2S_3 for 20 mL/20 mins had decreased from 15 mL/15 mins but the crystallite size of MoP_2 increased. 25 mL/25 mins had the average crystallite size for Mo_2S_3 of 35.5 nm and MoP_2 35.7 nm. The crystallite size of MoP_2 had shown increasing trend with increasing time of deposition and volume of precursor solution. However, the crystallite sizes of Mo_2S_3 decreased with increasing volume from 15 mL onwards suggesting that the size growth of Mo_2S_3 had reached its limit after 15 minutes of deposition time with 15 mL of precursor solution. The decrease in crystallite size of Mo_2S_3 from 15 mL/15 mins was probably caused by the increased activation

Universiti Malaya

energy for nucleation process when the deposition rate increased with increased volume of precursor solution and deposition time (Khoo et al., 2016).

Table 4.9: Average crystallite sizes of Mo_2S_3 and MoP_2 of the films fabricated with different volumes of precursor solution at different deposition times at 550 °C.

Films	Materials	Average Crystallite size (nm), $D = \frac{K\lambda}{\beta\cos\theta}$.
10 mL/10 mins	Mo_2S_3	48.0
	MoP_2	25.7
15 mL/15 mins	Mo_2S_3	52.8
	MoP_2	29.5
20 mL/20 mins	Mo_2S_3	41.2
	MoP_2	29.6
25 mL/25 mins	Mo_2S_3	35.5
	MoP_2	35.7

Based on the study from Section 4.3 in which the films were fabricated at a lower flow rate of 0.3 SCFH at the same deposition temperature of 550 °C, the crystallite sizes of Mo_2S_3 and MoP_2 (37.4 nm and 22.6 nm, respectively) of the film fabricated with 20 mL of precursor solution were smaller than the 20 mL/20 mins film which was fabricated at higher flow rate of 0.5 SCFH (Refer to Table 4.9). This had shown that increasing the flow rate increased the concentration of the precursor vapour generated to be deposited onto the substrate leading to larger crystallite sizes growth.

In addition to that, higher flow rate promoted more evaporation of solvent and the loading of Mo_2S_3 and MoP_2 onto the film became more enhanced. The agglomeration of Mo_2S_3 and MoP_2 particles to form larger crystallite size became restricted in lower flow rate. Therefore, flow rate is an important factor in controlling the crystallite size of the precursor materials.

Universiti Malaya

4.4.2 Raman Spectroscopy

The Raman spectra exhibited by the films prepared in different volumes and times at 0.5 SCFH as shown in Fig. 4.32 were similar to the spectra exhibited by the films prepared at different deposition times at fixed volume of 20 mL at 0.3 SCFH as shown in Fig. 4.8. Raman absorption peaks obtained were ascribed to Mo_2S_3 and MoP_2 phases in all the films. The increased precursor volume and deposition time had led to more formation of Mo_2S_3 and MoP_2 in the film. Therefore, higher intensities of the Raman absorption peaks for the two materials were observed. Based on the XRD analysis and similar Raman spectra obtained in this case, it was shown that Mo_2S_3 and MoP_2 composite materials were successfully grown in 10 mL/10 mins, 15 mL/15 mins, 20 mL/20 mins and 25 mL/25 mins films.

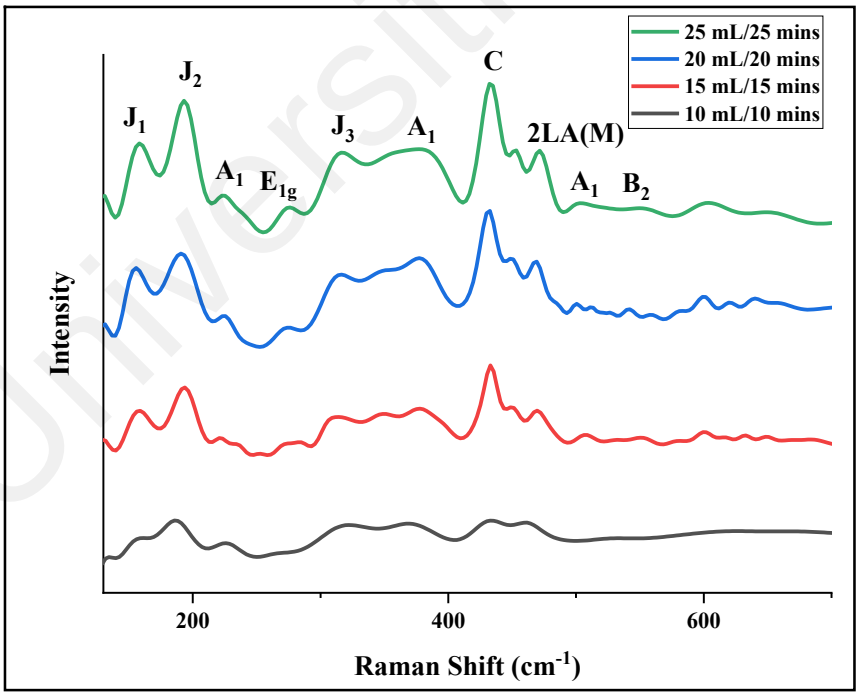

Figure 4.32: Raman shifts for 10 mL/10 mins, 15 mL/15 mins, 20 mL/20 mins and 25 mL/25 mins films fabricated at 550 °C.

Universiti Malaya

4.4.3 Energy Dispersive X-ray (EDX) Spectroscopy and Elemental Mapping Analyses

The Mo, S and P compositions and their distributions in the 10 mL/10 mins, 15 mL/15 mins, 20 mL/20 mins and 25 mL/25 mins films were analysed with EDX and elemental mapping analyses. The EDX spectra for the films were displayed in Fig. 4.33-4.36. The Mo, S and P distributions of the films displayed in the elemental mapping images in Fig. 4.37- 4.40 were found to be homogenously distributed in all the films. It was observed that P occurred dominantly in the larger grains for 15 mL/15 mins (Fig. 4.38) and 25 mL/25 mins films (Fig 4.40). As both deposition time and precursor volume increased, more agglomeration of MoP_2 grains occurred. S also covered the grains indicating the homogenous mixing of both Mo_2S_3 and MoP_2 materials after the AACVD process. Based on the atomic percentage of elements displayed in Table 4.10, 25 mL/25 mins film had the highest S/P ratio whereas 10 mL/10 mins film had the lowest S/P ratio. This indicated that the increase in S percentage was greatly influenced by the loading amount of precursor material.

Table 4.10: Atomic percentages of Mo, S and P of films fabricated at 550 °C.

Films	Element	Atomic percentage (%)
10 mL/10 minutes	Mo	34.40
	S	39.42
	P	26.17
15 mL/15 minutes	Mo	34.99
	S	45.10
	P	19.91
20 mL/20 minutes	Mo	37.92
	S	40.71
	P	21.37
25 mL/25 minutes	Mo	36.32
	S	46.22
	P	17.46

Universiti Malaya

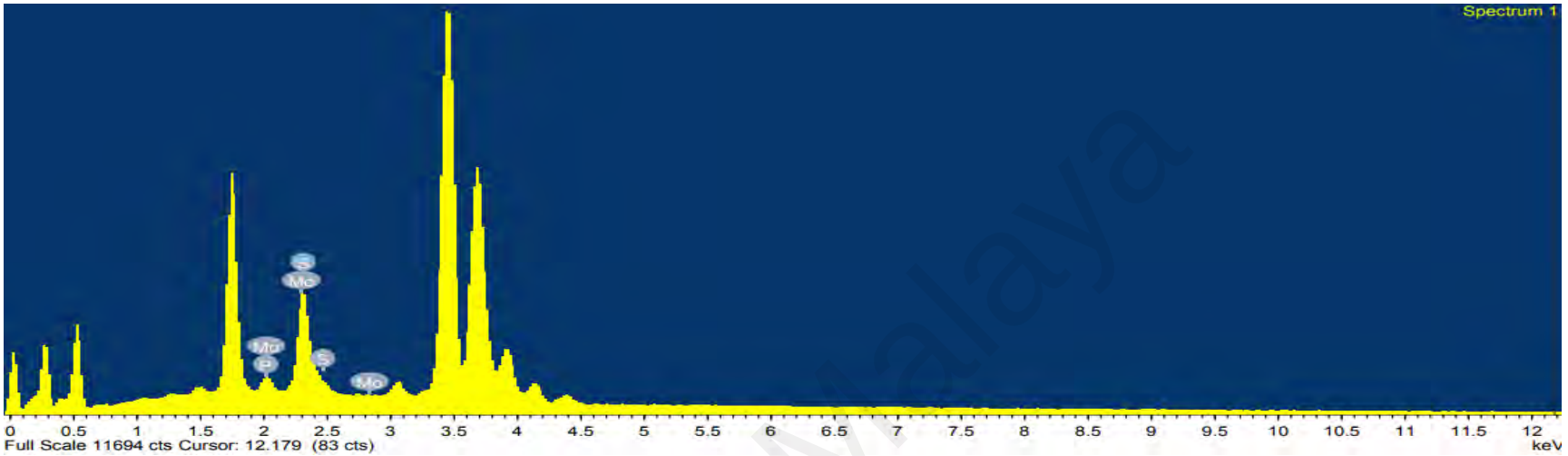

Figure 4.33: EDX spectrum for 10 mL/10 mins film fabricated at 550 °C.

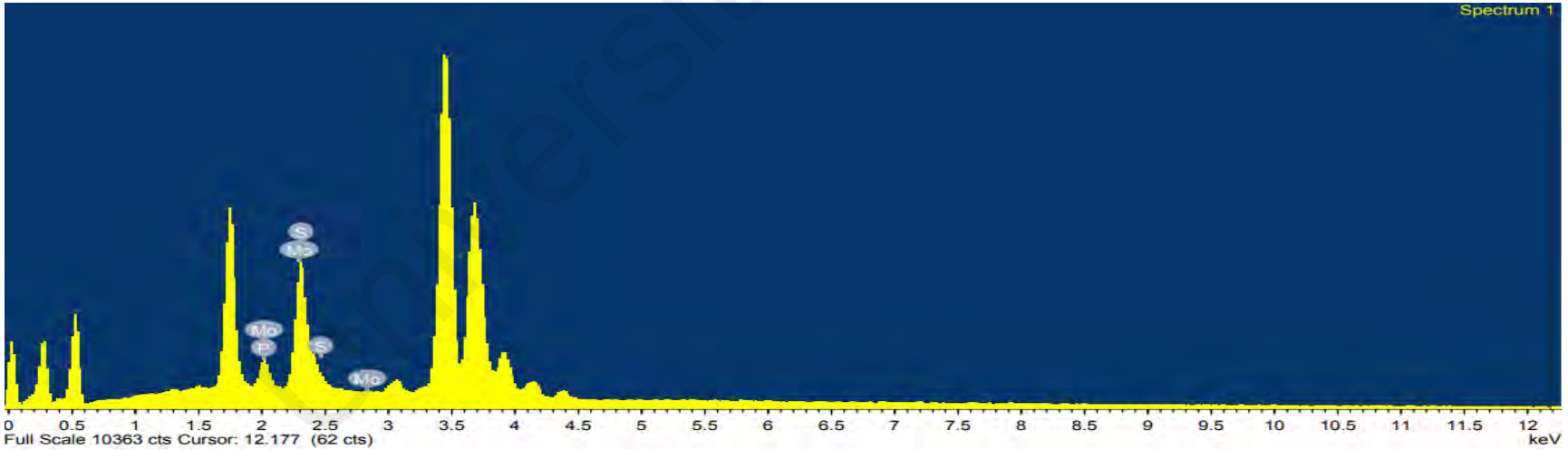

Figure 4.34: EDX spectrum for 15 mL/15 mins film fabricated at 550 °C.

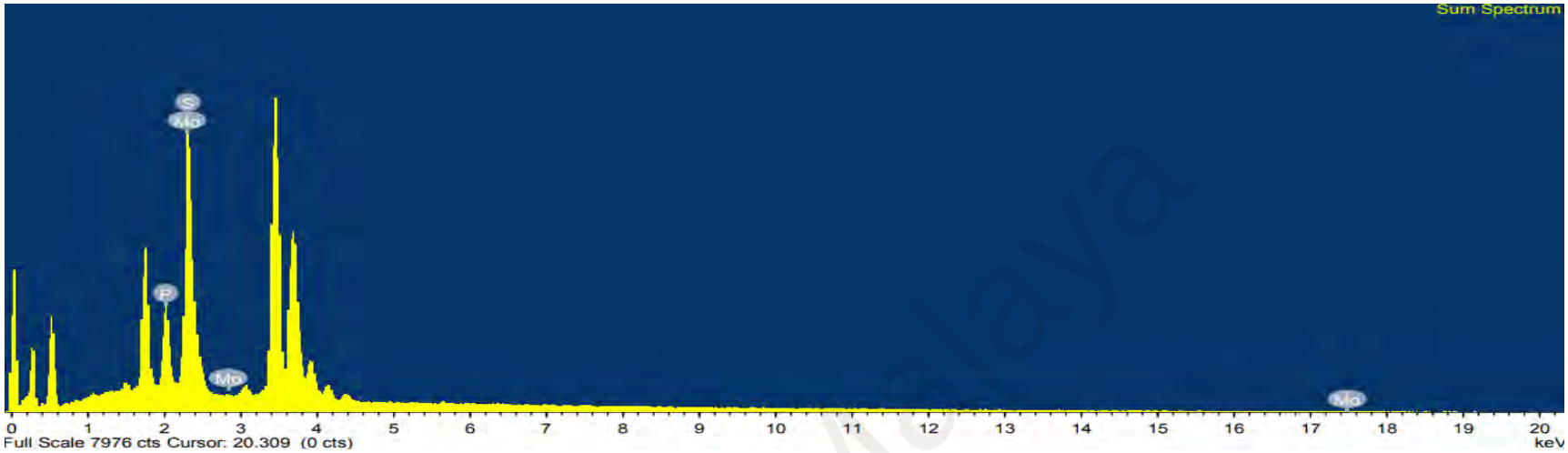

Figure 4.35: EDX spectrum for 20 mL/20 mins film fabricated at 550 °C.

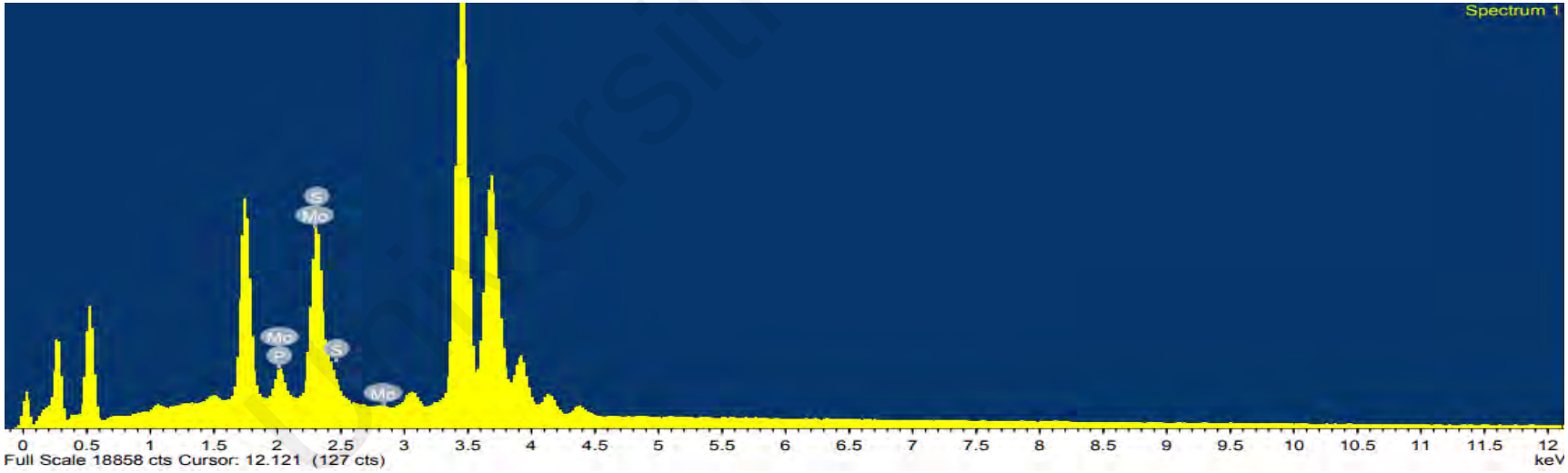

Figure 4.36: EDX spectrum for 25 mL/25 mins film fabricated at 550 °C.

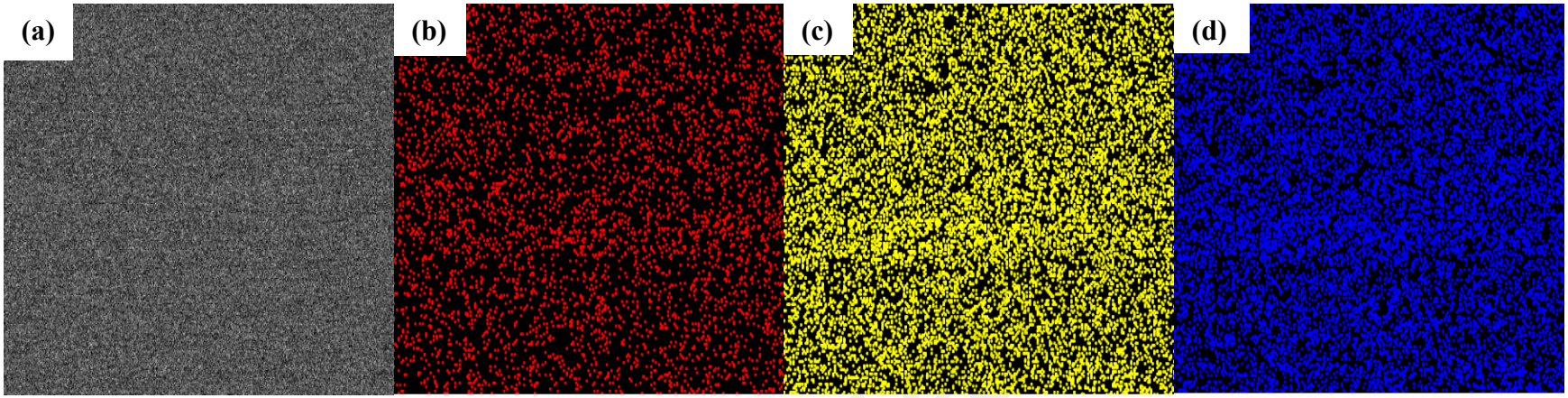

Figure 4.37: Elemental mapping of the (a) analysed area of 10 mL/10 mins film with distribution of (b) phosphorus, (c) sulphur and (d) molybdenum.

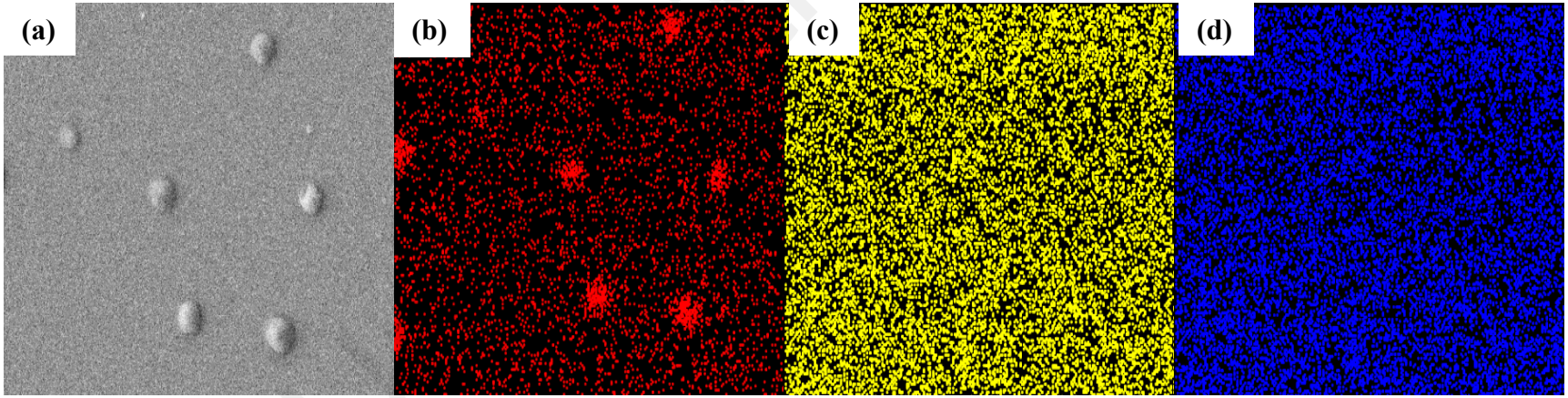

Figure 4.38: Elemental mapping of the (a) analysed area of 15 mL/15 mins film with distribution of (b) phosphorus, (c) sulphur and (d) molybdenum.

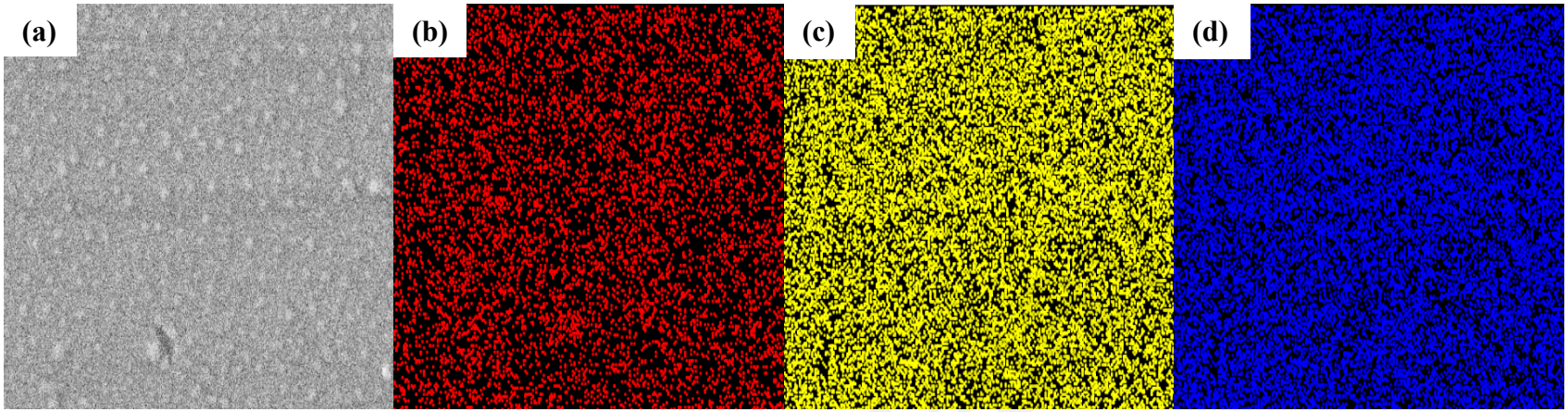

Figure 4.39: Elemental mapping of the (a) analysed area of 20 mL/20 mins film with distribution of (b) phosphorus, (c) sulphur and (d) molybdenum.

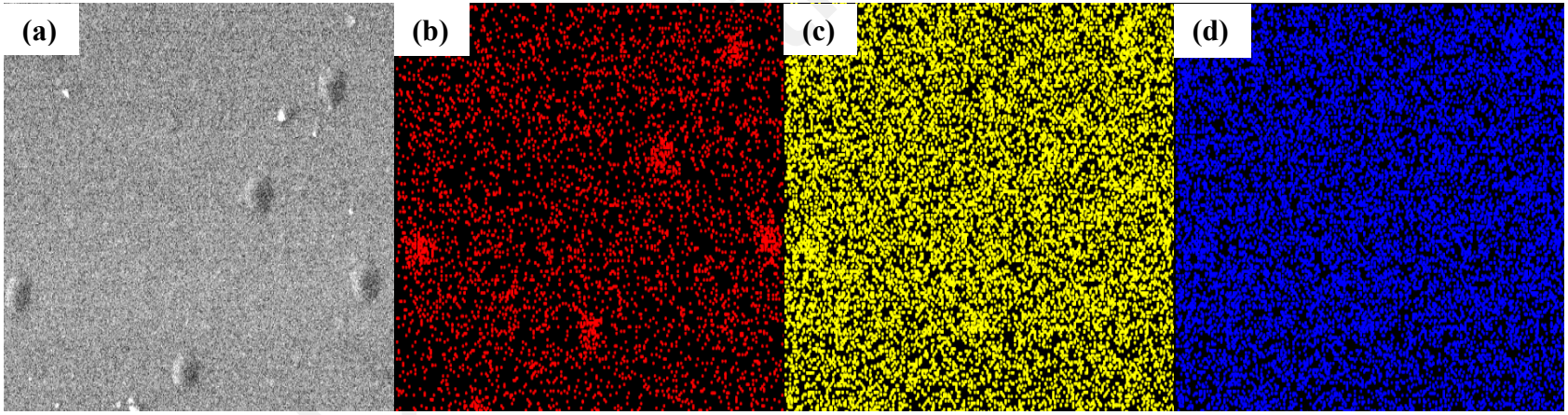

Figure 4.40: Elemental mapping of the (a) analysed area of 25 mL/25 mins film with distribution of (b) phosphorus, (c) sulphur and (d) molybdenum.

4.4.4 Atomic Force Microscopy (AFM) Analyses

Based on the surface roughness parameters of the films displayed in Table 4.11, 10 mL/10 mins film had the lowest root-mean-square roughness, R_q of 7.216 nm and 20 mL/20 mins had the highest R_q of 20.965 nm. There was an increasing trend for surface roughness of the films in the order of 10 mL/10 mins < 15 mL/15 mins < 20 mL/20 mins. There was a sharp reduction in surface roughness in 25 mL/25 mins film because the deposition of the film was most uniform. The AFM images obtained in 10 μm × 10 μm scan area as displayed in Fig. 4.41 showed that small grains were densely packed homogenously over the surface of 10 mL/10 mins film. For longer deposition time, larger grains started to grow on top of smaller sized grains as in 15 mL/15 mins film. The large grains in the 15 mL/15 mins were distanced from each other and the large grains were very isolated in 20 mL/20 mins film. Small-size grains were also observed in 25 mL/25 mins film along with irregular-shaped larger grains and the final topology was the smoothest of the films fabricated at 550 °C. The uniform topology observed in 25 mL/25 mins was the result of homogenous and consistent deposition of precursor material onto the substrate. The largest particle size difference led to the highest R_q in 20 mL/20 mins. The line profiles of the films were displayed in Fig. 4.42.

Universiti Malaya

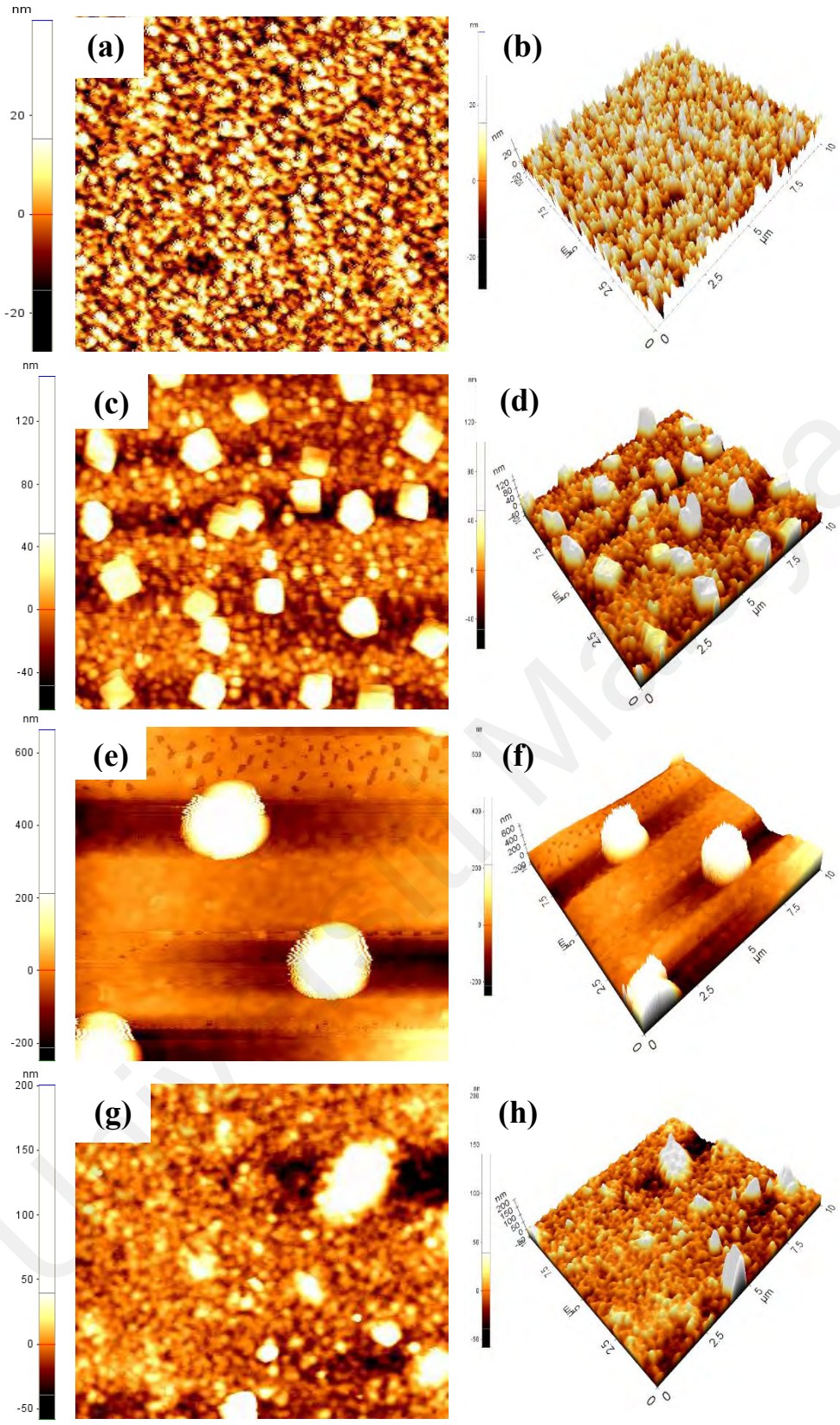

Figure 4.41: AFM of 2D and 3D images for (a, b) 10 mL/10 mins, (c, d) 15 mL/15 mins, (e, f) 20 mL/20 mins and (g, h) 25 mL/25 mins films fabricated at 550 °C.

10 mL/10 minutes

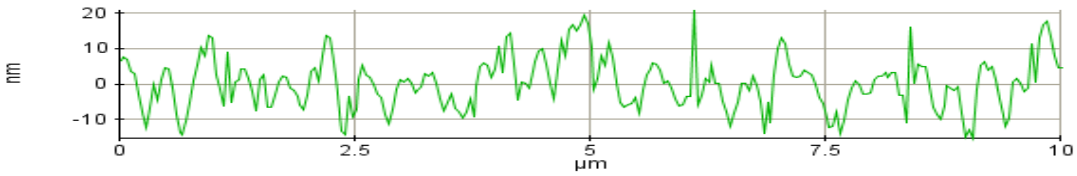

15 mL/15minutes

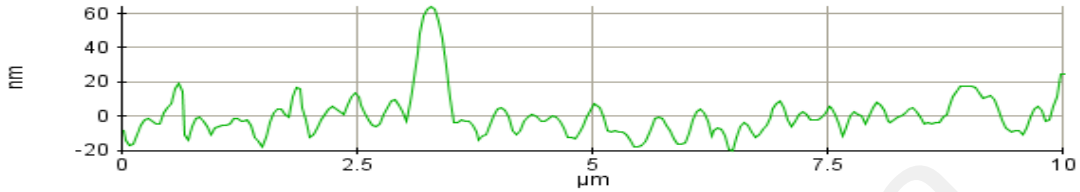

20 mL/20 minutes

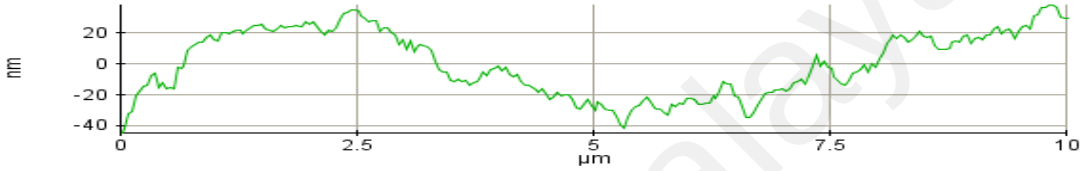

25 mL/ 25 mins

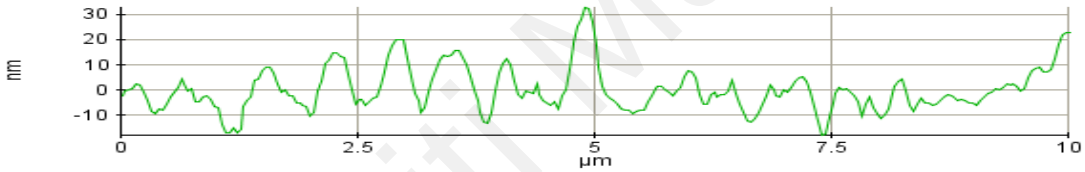

Figure 4.42: Line profiles of 10 mL/10 mins, 15 mL/15 mins, 20 mL/20 mins and 25 mL/25 mins films fabricated at 550 °C.

Table 4.11: Surface roughness parameters of films fabricated at 550 °C.

Films	Parameters	Values (nm)
10 mL/10 mins	Roughness average, R_a	5.606
	Root mean square, R_q	7.216
	Maximum profile height, R_{pv}	36.132
	Maximum valley depth, R_v	15.341
	Maximum peak height, R_p	20.790
15 mL/15 mins	Roughness average, R_a	8.317
	Root mean square, R_q	12.901
	Maximum profile height, R_{pv}	84.092
	Maximum valley depth, R_v	20.175
	Maximum peak height, R_p	63.917

University Malaya

Table 4.11, Continued.

20 mL/20 mins	Roughness average, R_a	18.852
	Root mean square, R_q	20.965
	Maximum profile height, R_{pv}	82.592
	Maximum valley depth, R_v	44.713
	Maximum peak height, R_p	37.878
25 mL/25 mins	Roughness average, R_a	6.405
	Root mean square, R_q	8.680
	Maximum profile height, R_{pv}	50.520
	Maximum valley depth, R_v	17.839
	Maximum peak height, R_p	32.682

4.4.5 Scanning Electron Microscopy (SEM) Analyses

SEM analyses were carried out on the 10 mL/10 minutes, 15 mL/15 minutes, 20 mL/20 minutes and 25 mL/25 minutes films fabricated at 0.5 SCFH. The SEM images at magnification of ×10,000 as shown in Fig. 4.43 corresponded to their respective AFM images as shown in Fig. 4.41. Based on the SEM images, the grains were densely and widely distributed over the 10 mL/10 minutes film whereas the grains were poorly dispersed in 20 mL/20 minutes films. Grains with irregular shapes were observed in 15 mL/15 minutes film on top of the layer of round nanoparticles. The grains in 25 mL/25 minutes films were less dense than the 10 mL/10 minutes film though also widely distributed. The carrier gas flow rate had very significant effect on the morphology of the films. Based on the size distribution obtained from population size of 200 particles displayed in the histograms in Fig. 4.44, the mean particle sizes were in the range of 200-400 nm (77.5 %) in 10 mL/10 mins, 400-800 nm (76.5 %) in 15 mL/15 mins, 400-700 nm (50.5 %) in 20 mL/20 mins and 150-200 nm (49.5 %) in 25 mL/25 mins. Therefore, the mean particle size was the largest in 15 mL/15 mins film and whereas the smallest was observed in 25 mL/25 mins film.

Universiti Malaya

The 20 mL/20 mins film fabricated at lower carrier gas flow rate of 0.3 SCFH had produced the mean particle size at the range of 1000-3000 nm. Similarly, at a higher gas flow rate of 0.5 SCFH, much smaller mean particle size at the range of 150-200 nm were produced. This observation agreed with Hernández-Salcedo et al., (2015) where higher carrier gas flow rate promoted higher evaporation rate of the droplets in the furnace tube during AACVD process, which resulted due to the abrupt formation of the crust on the droplet that caused it to burst into smaller sized particles due to the pressure build-up. This could be the case with 25 mL/25 mins film which had the smallest mean particle size. The study showed that the final particle size is dependent on the temperature, time and gas flow rate of the AACVD process.

Universiti Malaya

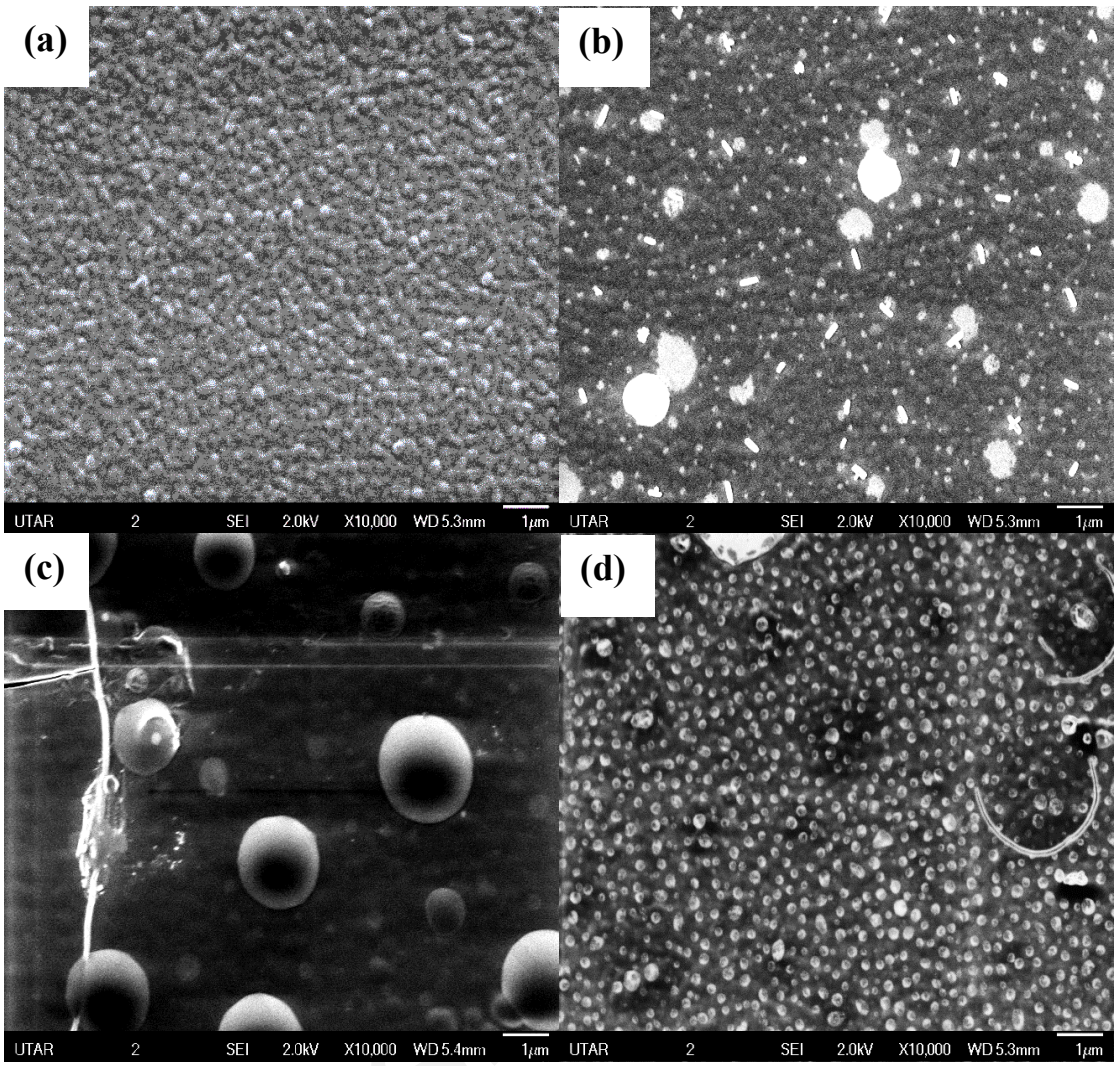

Fig. 4.43: SEM images in magnification of ×10,000 of (a) 10 mL/10 minutes, (b) 15 mL/15 minutes, (c) 20 mL/20 minutes and (d) 25 mL/25 minutes films fabricated at 550 °C.

Universi

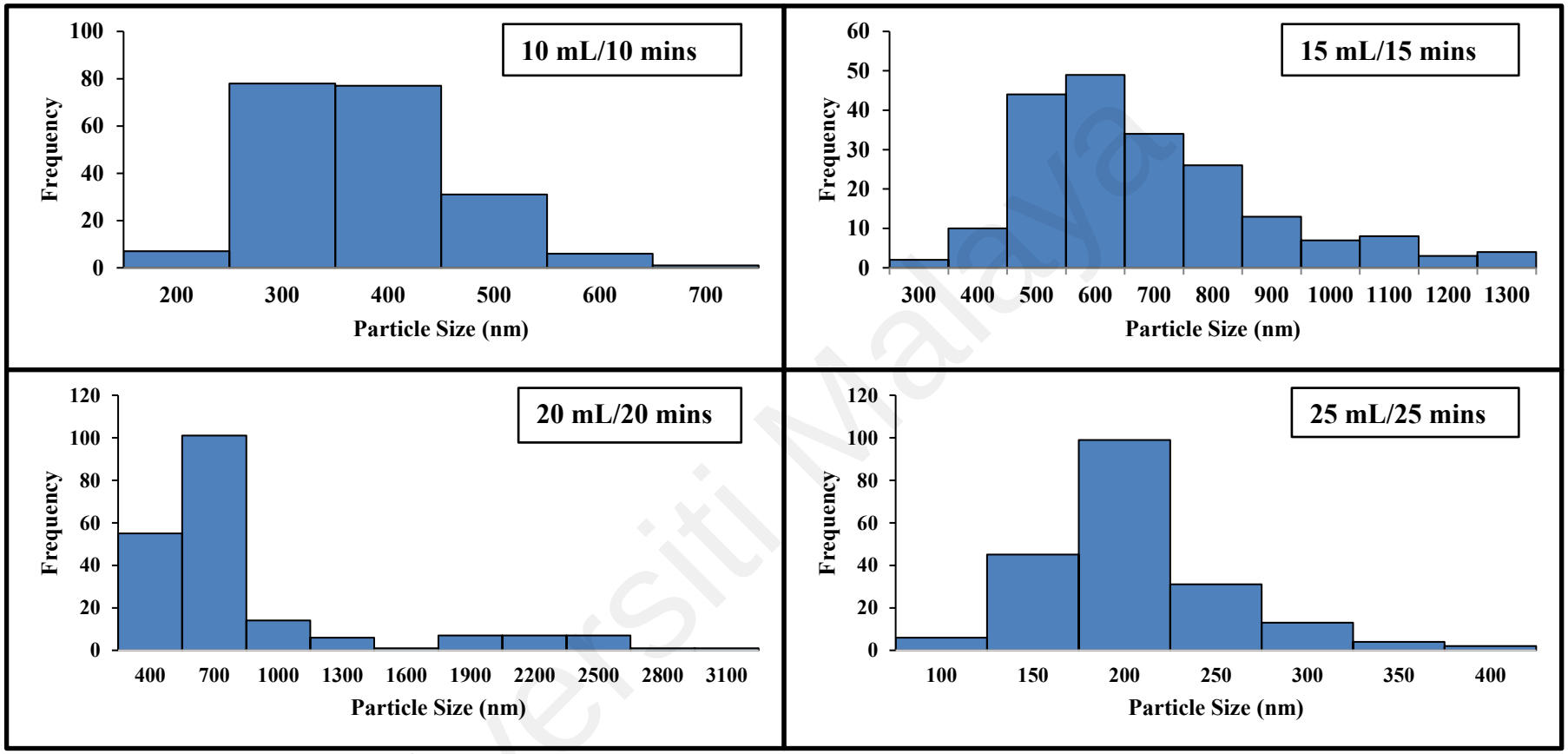

Fig. 4.44: Histograms displaying size distributions of nanoparticles of the films fabricated at 550 °C.

University Malaya

4.4.6 Film Thickness Measurements

The thickness of the films fabricated at 0.5 SCFH was measured by using surface profilometer. It was observed that the thickness had increased with longer deposition time coupled with larger volume of precursor solution. It was found that the film thickness for 10 mL/10 mins, 15 mL/15 mins, 20 mL/20 mins and 25 mL/25 mins were 152 nm, 436 nm, 618 nm and 825 nm, respectively. This had shown that the film thickness is dependent on duration of deposition time and precursor volume.

The 20mL/20mins film prepared with lower flow rate of carrier gas (0.3 SCFH) had the film thickness of 432 nm. The increase in film thickness was shown with higher carrier gas flow rate. This suggested that higher flow rate promotes thicker film as well as crystallite sizes of both the Mo_2S_3 and MoP_2. Therefore, flow rate is an important parameter in controlling the film thickness.

4.4.7 UV-vis Spectrophotometry Analyses

The optical property of the films was analysed by UV-vis spectrophotometry. From the absorption spectra in Fig. 4.45, the UV-vis absorption study showed that absorbance increased with larger volume and longer deposition time. However, the absorbance was the greatest for 20 mL/20 mins. The phenomenon could be explained based on the relationship between the surface morphology and absorbance of the film. High roughness enhances the reflection of the beam and therefore the absorption of materials can occur many times in the material and with greater success (Niu et al., 2019). The highest absorption exhibited by 20 mL/20 mins film could be explained by the highest roughness root-mean-square, R_q.

Universiti Malaya

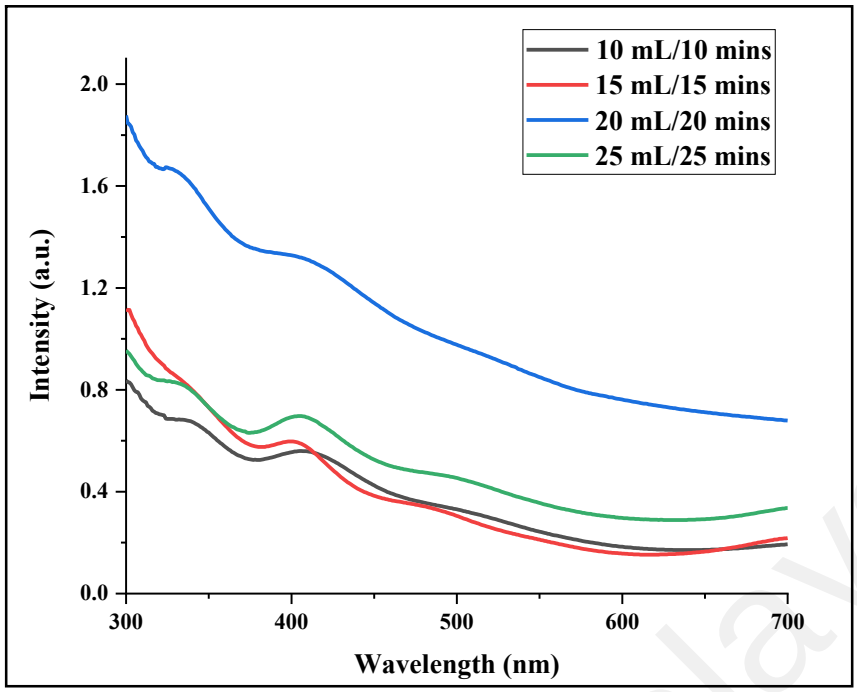

Figure 4.45: UV-vis absorbance spectra of 10 mL/10 mins, 15 mL/15 mins, 20 mL/20 mins and 25 mL/25 mins films fabricated at 550 °C.

The absorption spectra were converted to Tauc plots to determine the bandgap energy values of the films. Based on the Tauc plots shown in Fig. 4.46, two bandgap energy values were observed for all the films were very close. This pointed that the films possessed two types of materials that were Mo_2S_3 and MoP_2. It was noteworthy that 20 mL/20 mins film had the lowest bandgap energy values. Low bandgap energy value is desired because it indicates high efficiency of electrons getting excited from valence band to conduction band which promotes electron flow for HER process. The materials with large particles are found to have low band gap as in the case with 20 mL/20 mins film (Sathish et al., 2006).

Universiti Malaya

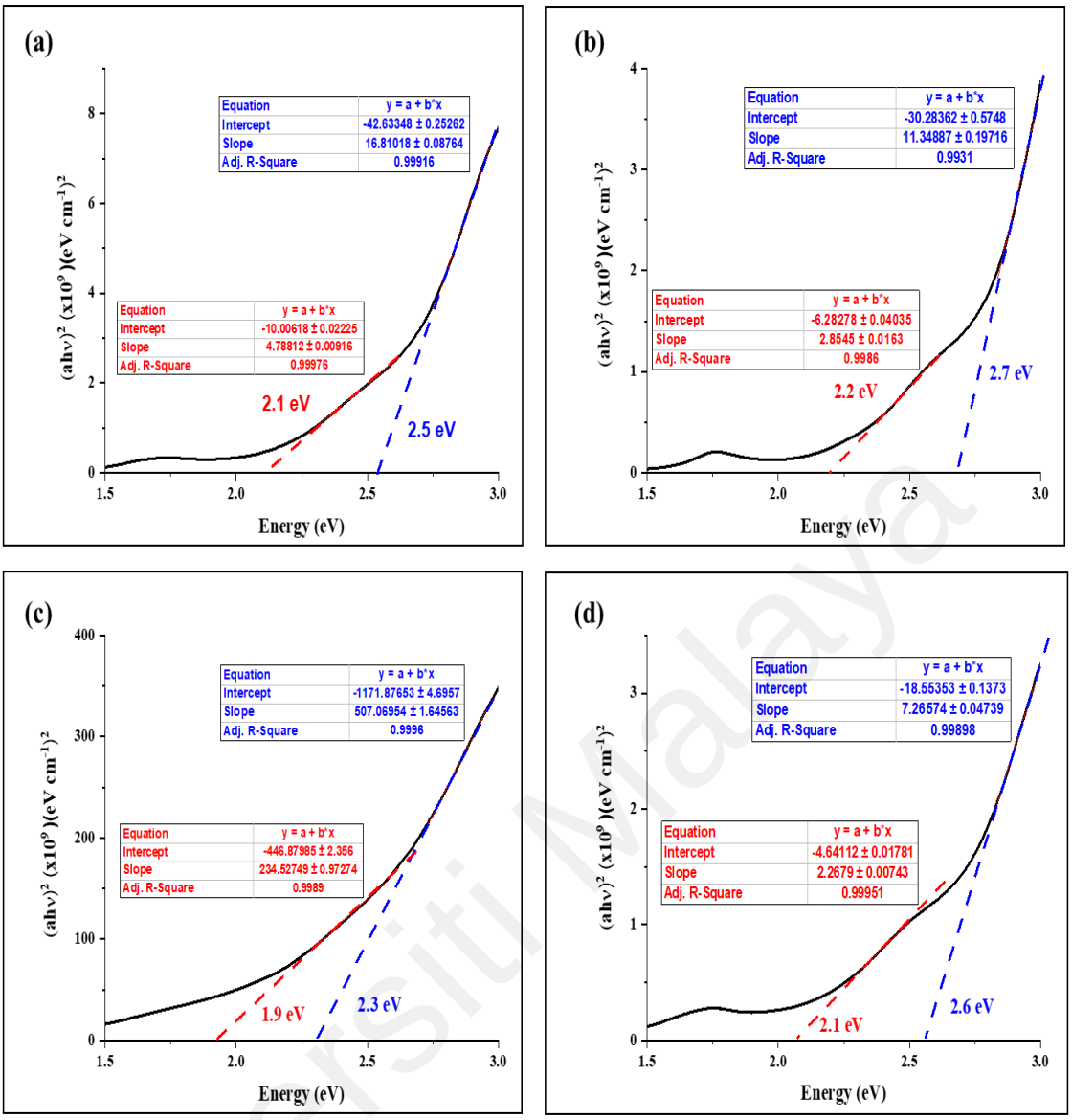

Figure 4.46: Tauc plots and bandgap values of (a) 10 mL/10 mins, (b) 15 mL/15 mins, (c) 20 mL/20 mins (c) and (d) 25 mL/25 mins films fabricated at 550 °C.

4.4.8 Electrochemical studies

The electrochemical studies were performed with acidic electrolyte (0.25 M H_2SO_4 with pH 0.95). CV curves are displayed in Fig. 4.47. Based on the CV analyses, the curves were shown to be stable after 5 cycles for 10 mL/10 mins, 15 mL/15mins and 25 mL/25 mins films with the scan rate of 0.1 V/s. 20 mL/20 mins exhibited the lowest stability after 5 cycles as shown by the changes in the positions of the curves in 5 cycles. Based on the CV curves, the E_{ox} at which the anodic peak occurred for the 10 mL/10

Universiti Malaya

mins, 15 mL/15 mins and 25 mL/25 mins films were found to be 0.69, 0.60 and 0.61 V vs. RHE, respectively and the E_{red} at which the anodic peak occurs for the films were extracted to be 0.48, 0.44 and 0.35 V vs. RHE, respectively. The CV curve for 20 mL/20 mins did not exhibit E_{ox} and E_{red} peaks indicating that redox reaction was not observed for the film. The potential difference, ΔE between E_{ox} and E_{red} for the 10 mL/10 mins, 15 mL/15 mins and 25 mL/25 mins films were 0.21, 0.16 and 0.26 V, respectively. Based on the calculation by using Eq. 4.3, the numbers of electrons transferred for 10 mL/10 mins, 15 mL/15 mins and 25 mL/25 mins films were calculated to be 0.281, 0.369 and 0.227, respectively in acidic media of pH 0.95 in the potential window of -0.6 V to 0.6 V vs. Ag/AgCl.

Universiti Malaya

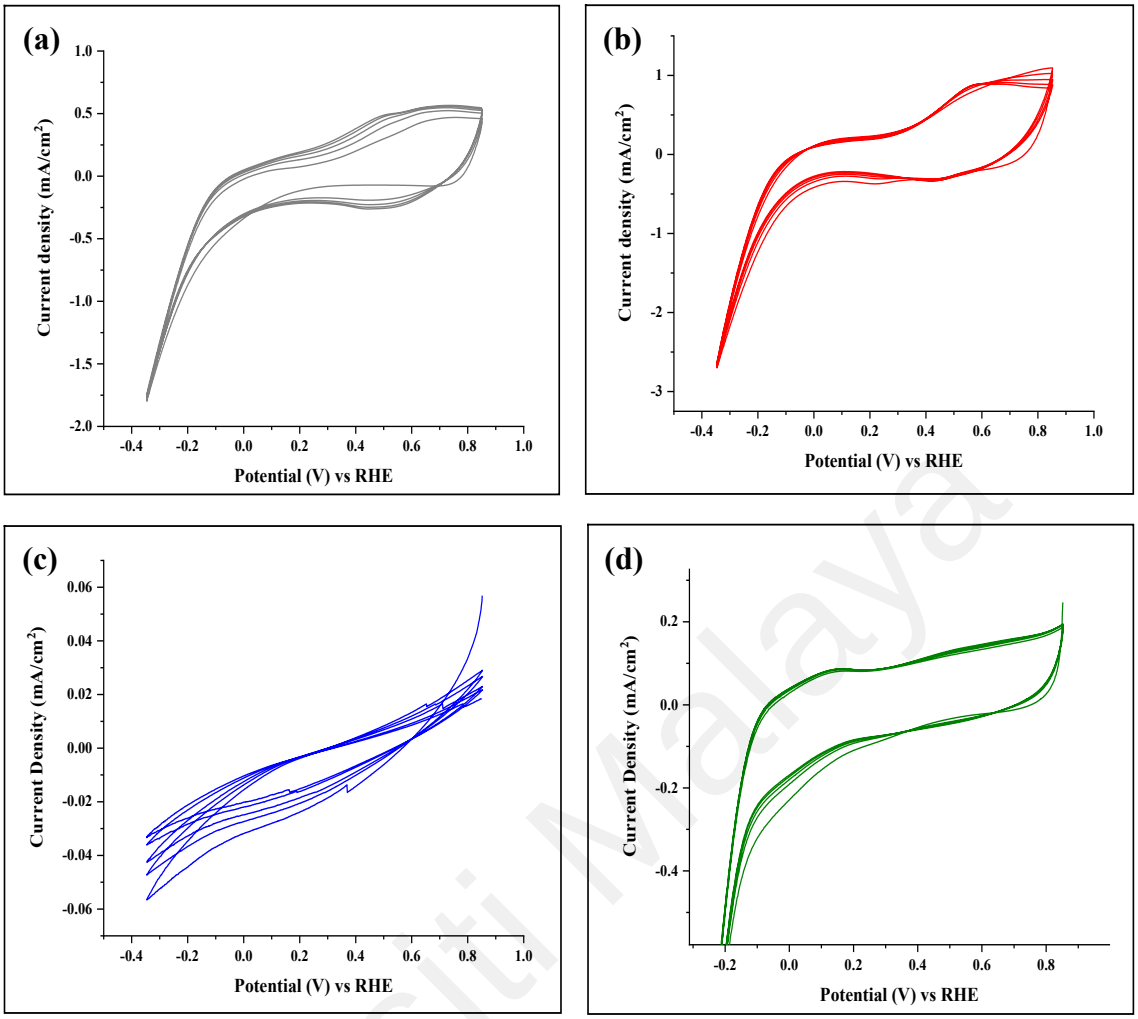

Figure 4.47: CV curves after 5 cycles for (a) 10 mL/10 mins, (b) 15 mL/15 mins, (c) 20 mL/20 mins and (d) 25 mL/25 mins films.

The *J-V* curves of the films are displayed in Fig. 4.48 with the potential window of -0.35 to 0.85 mV (vs. RHE). The onset potential was determined by taking the overpotential at which the current density was 1 mA/cm^2. The onset potential (vs. RHE) of the 10 mL/10 mins, 15 mL/15 mins and 25 mL/25 mins films were determined to be 235, 258 and 266 mV, respectively. The 20 mL/20 mins film was found to have the highest onset potential without reaching the current density of 1 mA/cm^2 in the same potential window. For comparison purpose, overpotential of 250 mV vs. RHE was used to compare the current densities of the films. Based on the *J-V* curves, 15 mL/15 mins had exhibited the best electrocatalytic performance, producing the current density of 1.2

Universiti Malaya

mA/cm^2 with overpotential of 250 mV vs. RHE whereas 20 mL/ 20 mins exhibited the poorest HER performance producing only 0.3 mA/cm^2 with the overpotential of 250 mV vs. RHE.

The 20 mL/20 mins film which was produced at slower carrier gas flow rate (0.3 SCFH) was found to produce 4.3 mA/cm^2 of current density with the overpotential of 250 mV vs. RHE compared with 0.3 mA/cm^2 exhibited by the 20 mL/20 mins film fabricated at faster flow rate (0.5 SCFH). The higher surface roughness (R_q = 106.447 nm) of 20 mL/20 mins fabricated at 0.3 SCFH compared with the 20 mL/20 mins fabricated at 0.5 SCFH (R_q = 20.965 nm) provided the film with better HER kinetics. This suggested that high roughness provided more active sites available for catalysing HER (Abdel-Karim et al., 2012). Among 10 mL/10 mins, 15 mL/15 mins and 25 mL/25 mins films, the highest electrocatalytic activity exhibited by 15 mL/15 mins film was attributed to its larger surface roughness.

In the case with 20 mL/20 mins film, although it possessed the larger surface roughness than 15 mL/15 mins film, its poor electrocatalytic performance was due to its morphology. The 20 mL/20 mins film fabricated showed the lack of homogenous distribution of grains over the surface of the catalyst as shown in SEM image in Fig. 4.43. This observation showed that the morphology of the film played important role in determining the performance of the catalyst in HER activity. The study showed that morphology with well-dispersed grains provided films with advantage in electrocatalytic performance in HER.

Universiti Malaya

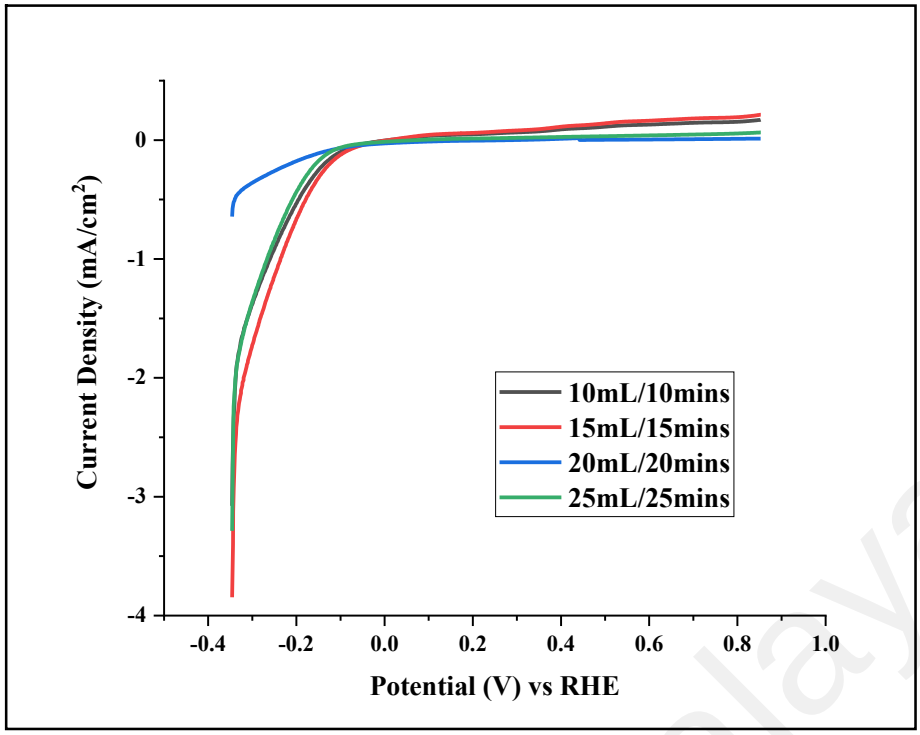

Figure 4.48: LSV curves of 10 mL/10 minutes, 15 mL/15 minutes, 20 mL/20 minutes and 25 mL/25 minutes films fabricated at 550 °C.

MS plots were obtained to determine the charge carrier densities (in cm^{-3}) as well as the conductivity of the semiconductor film (n-type or p-type). All the films exhibited n-type conductivity as indicated by the positive slopes in the MS plots as shown in Fig. 4.49. The dominant charge carriers were the electrons. Based on the MS plot in Fig. 4.49, the charge carrier densities could be compared among the films by determining the slope of the plot, $[\frac{d(\frac{1}{c^2})}{dV}]$. The slope is inversely proportional to the charge carrier densities. The slopes of the MS plot and charge carrier densities for 10 mL/10 mins, 15 mL/15 mins, 20 mL/20 mins and 25 mL/25 mins films were tabulated in Table 4.12. The charge carrier densities were calculated by using Eq. 4.6 in which the relative dielectric constant, ε_r is assumed to be 10 because it is usually slightly above or below this value (Chen et al., 2013).

Universiti Malaya

It was observed that increasing charge carrier densities increases HER performances of the films. Therefore, in this case, charge carrier density was the determining factor that contributed to the conductivity of the films. Based on the calculated charge carrier densities displayed in Table 4.12, 15 mL/15 mins film had the largest electron density whereas 20 mL/20 mins film had the lowest electron density available for HER activity. The lowest electron density could be due to the lack of homogenous deposition of MoP_2 over the surface and therefore the interaction between Mo_2S_3 and MoP_2 was minimal resulting to ineffective increase in electron concentration which was promoted by the P in the heterojunctions in the films (Liu et al., 2017).

Table 4.12: MS slopes and electron densities of the films fabricated at 550 °C.

Films	Area (cm^2)	Slope of MS plot, $\left[\frac{d\left(\frac{1}{c^2}\right)}{dV}\right]$ (F^2V^{-1})	Charge carrier density, N_d (cm^{-3})
10 mL/10 mins	1.10	12.054×10^{10}	9.14×10^{19}
15 mL/15 mins	0.90	9.742×10^{9}	1.80×10^{21}
20 mL/20 mins	1.10	0.942×10^{15}	1.25×10^{16}
25 mL/25 mins	0.98	0.934×10^{13}	1.58×10^{18}

Universiti Malaya

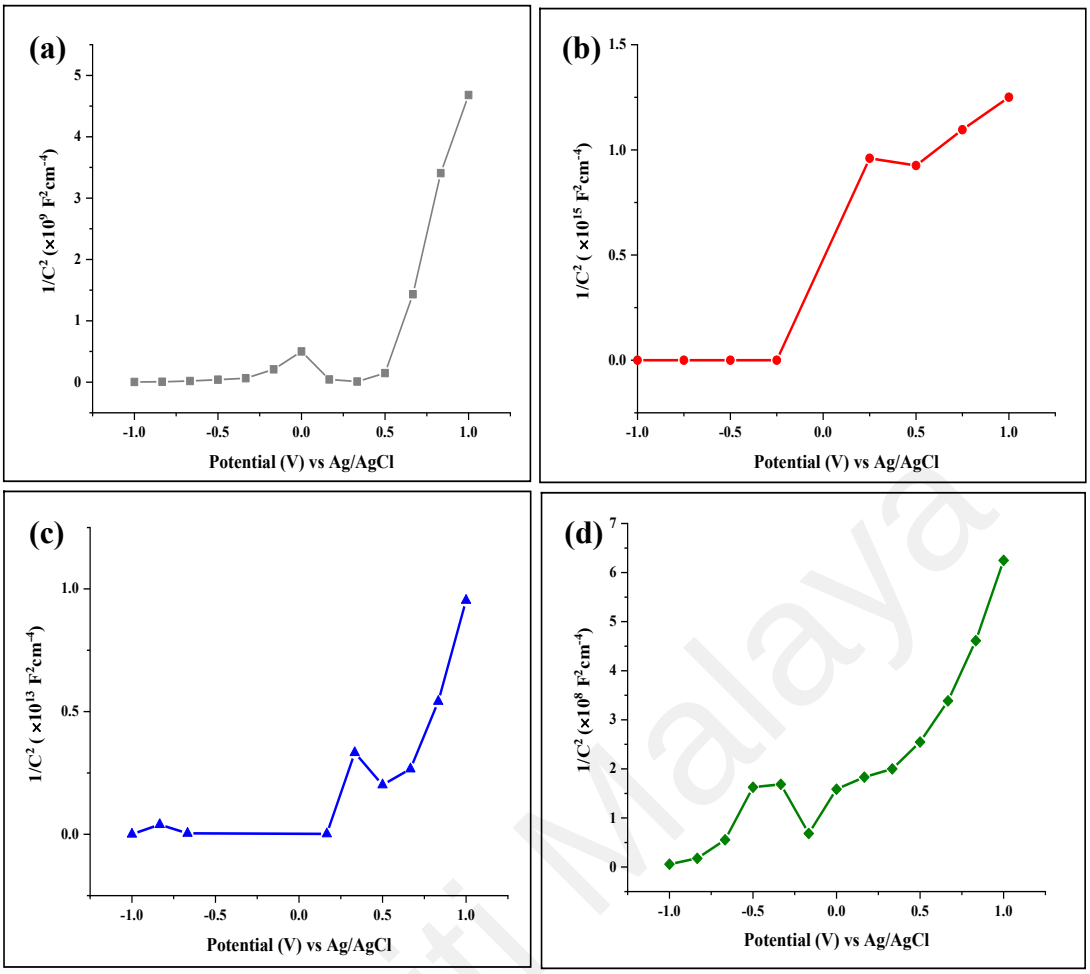

Figure 4.49: MS plots of (a) 10 mL/10 minutes, (b) 15 mL/15 minutes, (c) 20 mL/20 minutes and (d) 25 mL/25 minutes films in applied potential from -1.0 to 1.0 V vs Ag/AgCl.

The electrochemical impedance spectroscopy (EIS) of the films was analyzed in the frequency range from 0.01Hz to 100,000 Hz at a fixed potential. Nyquist plots and Bode plots are displayed in Fig. 4.50. The Nyquist plots obtained from EIS analysis displayed in Fig. 4.50 (a) showed different diameter sizes of the semicircular plots. The charge transport resistance, R_{CT} is directly proportional to diameter size of the plot. Based on the Nyquist plot, 15 mL/15 mins film had the lowest transport resistance, R_{CT} with the smallest diameter of the semicircular plot of 5.177 kΩ. The result was consistent with the LSV analysis that the 15 mL/15 mins film showed the best performance in LSV analysis than the other films. As shown in Table 4.11, the transport resistance from lowest to

Universiti Malaya

highest was in the order of 15 mL/15 mins < 10 mL/10 mins < 25 mL/25 mins <20 mL/20 mins.

Based on the Nyquist plots, the poorest performance of 20 mL/ 20 mins could be explained by its largest charge transport resistance which was found to be 35.2 kΩ. The large film thickness in 20 mL/ 20 mins and 25 mL/ 25 mins contributed to the large charge transport resistance which restricted the effective transport of electrons in the catalyst to drive HER activity. The 20 mL/20 mins film fabricated at slower carrier gas flow (0.3 SCFH) had the charge transport resistance of 3.02 kΩ. The value was much smaller than that of the 20 mL/20 mins film fabricated with larger film thickness (R_{CT} = 35.2 kΩ). This observation showed that large film thickness resulted in high R_{CT} which impeded the transport of electrons for HER process.

Based on the Bode plots shown in Fig. 4.50 (b), the frequency maxima for the films were determined for calculation of the lifetimes. The result showed that 15 mL/15 mins film had the longest lifetime as the frequency maxima peak was at the lowest frequency. The calculation of lifetime uses the formula, $\tau = \frac{1}{2\pi\nu}$. The frequency maxima, ν for the 15 mL/15 mins film was found to be 2.22 Hz and therefore, the lifetime, τ was calculated to be 71.7 ms. The frequency maxima for other films were at the high-frequency region and therefore, their lifetimes were shorter than 15 mL/15 mins film.

Universiti Malaya

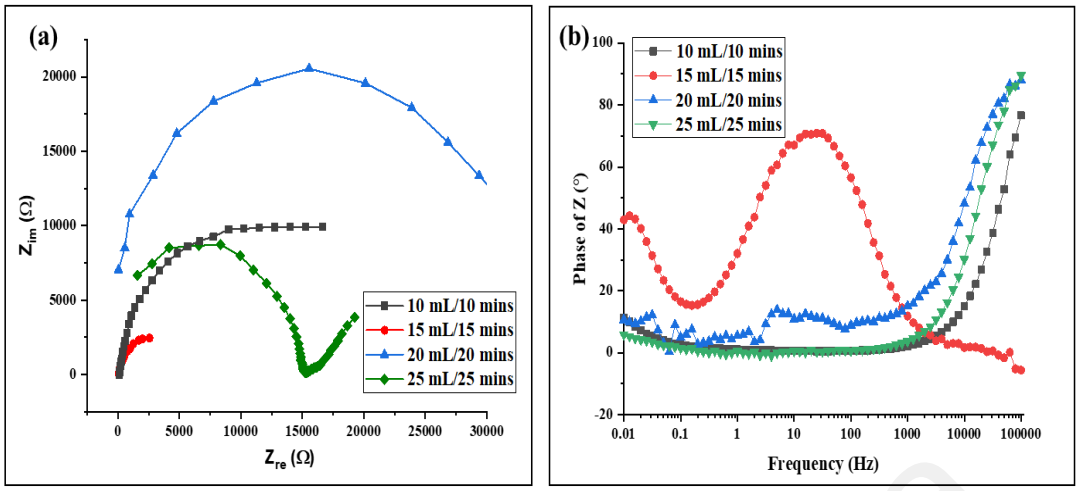

Figure 4.50: (a) Nyquist plots and (b) Bode plots of 10 mL/10 minutes, 15 mL/15 minutes, 20 mL/20 minutes and 25 mL/25 minutes films fabricated at 550 °C.

4.4.9 Inherent properties of the films

The Tafel plots were generated from *J-V* curves obtained from LSV analysis and are displayed in Fig. 4.51. From the Tafel plots, the Tafel slopes were found to be larger than 120 mV/dec which indicated that Volmer step was the rate determining step in HER activity for the films. 15 mL/15 mins film had the lowest Tafel slope of 120.7 mV/dec indicating that the film exhibited the best performance in HER. 20 mL/20 mins film had exhibited the poorest HER performance as indicated by its largest Tafel slope of 256.4 mV/dec.

Exchange current density, j_0 indicates the absolute value of anodic or cathodic density when HER is in balanced state (η = 0V vs. RHE). Based on Table 4.13, the 20 mL/20 mins film had the highest j_0 meaning that the film could generate highest electron density when HER was in the balanced state. Though the film had this advantage over the other films, it showed poorest HER performance because the desorption of hydrogen atom to produce hydrogen gas was most restricted according to the definition of large

Universiti Malaya

Tafel slope (Feng et al., 2020). The results demonstrated that low Tafel slope does not necessarily mean high j_0.

The relationship between morphology and HER performance is evident based on the results presented above. The films which possessed high roughness and homogenous distribution of particles over the catalyst's surface had better electrocatalytic property. The lack of either one of the mentioned properties may restrict the film's potential in the catalytic performance. Based on the size distribution study, smaller mean particle size of the film showed better electrocatalytic performance than the film with large mean particle size. The poorest performance exhibited by the 20 mL/20 mins film could be due to its large mean particle size (400-700 nm). Large particle size restricted the exposure of active sites for catalysing HER activity efficiently. It was also noteworthy that the 25 mL/25 mins film exhibited poorer HER performance than 10 mL/10 mins and 15 mL/15 mins though it had the lowest mean particle size. This could be explained by its large film thickness which restricted electron transport within the film. Besides mean particle size, film thickness and the film roughness also determined the electrocatalytic kinetics of the films.

Universiti Malaya

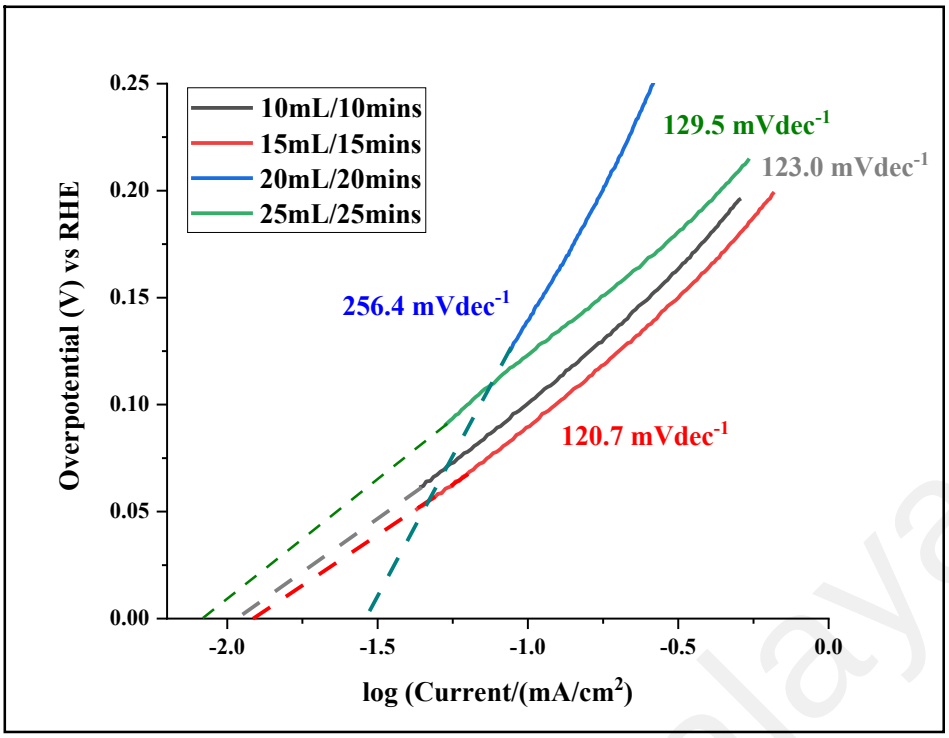

Figure 4.51: Tafel slopes for the 10 mL/10 minutes, 15 mL/15 minutes, 20 mL/20 minutes and 25 mL/25 minutes films fabricated at 550 °C.

Table 4.13: Inherent properties of the 10 mL/10 minutes, 15 mL/15 minutes, 20 mL/20 minutes and 25 mL/25 minutes films fabricated at 550 °C.

Films	Tafel slope, b ($mVdec^{-1}$)	Exchange current density, j_0 (mA/cm^2)	Charge transfer resistance, R_{CT} (kΩ)
10 mL/10 mins	123.0	0.015	17.0
15 mL/15 mins	120.7	0.018	5.18
20 mL/20 mins	256.4	0.028	35.24
25 mL/25 mins	129.5	0.012	32.57

4.5 Characterization of Films Fabricated at Different Deposition Temperatures.

For the films prepared at 0.5 SCFH gas flow rate at 550 °C, the 15 mL/15 mins film showed better electrocatalytic performance in HER. We are interested to study the effect of deposition temperatures on the 15 mL/15 mins films in the electrocatalytic performance in HER. Thus, 15 mL/15 mins films were fabricated at 450, 550 and 650 °C with the carrier gas flow rate of 0.5 SCFH. The films were also characterized with XRD,

Universiti Malaya

Raman spectroscopy, SEM, EDX, AFM, UV-vis spectrophotometry, and electrochemical studies.

4.5.1 X-ray Diffraction Analyses (XRD)

The XRD diffraction patterns were indexed to monoclinic Mo_2S_3 (JCPDS no. 98-006-2486) and orthorhombic MoP_2 (JCPDS no. 98-003-7222) and were displayed in Fig. 4.52. Based on the diffraction patterns, it was shown that more planes of Mo_2S_3 were grown at higher deposition temperature. It was also observed that the film produced at 650 °C showed very strong diffraction peak for (021) plane of MoP_2. The diffraction peaks for (200) and (003) planes for Mo_2S_3 were enlarged and were displayed in Fig. 4.53 in the 2θ range of 29.5°-31.5°. The observed peak list was displayed in Table 4.14 matched with the 2θ positions of the indexed Mo_2S_3 and MoP_2.

Universiti Malaya

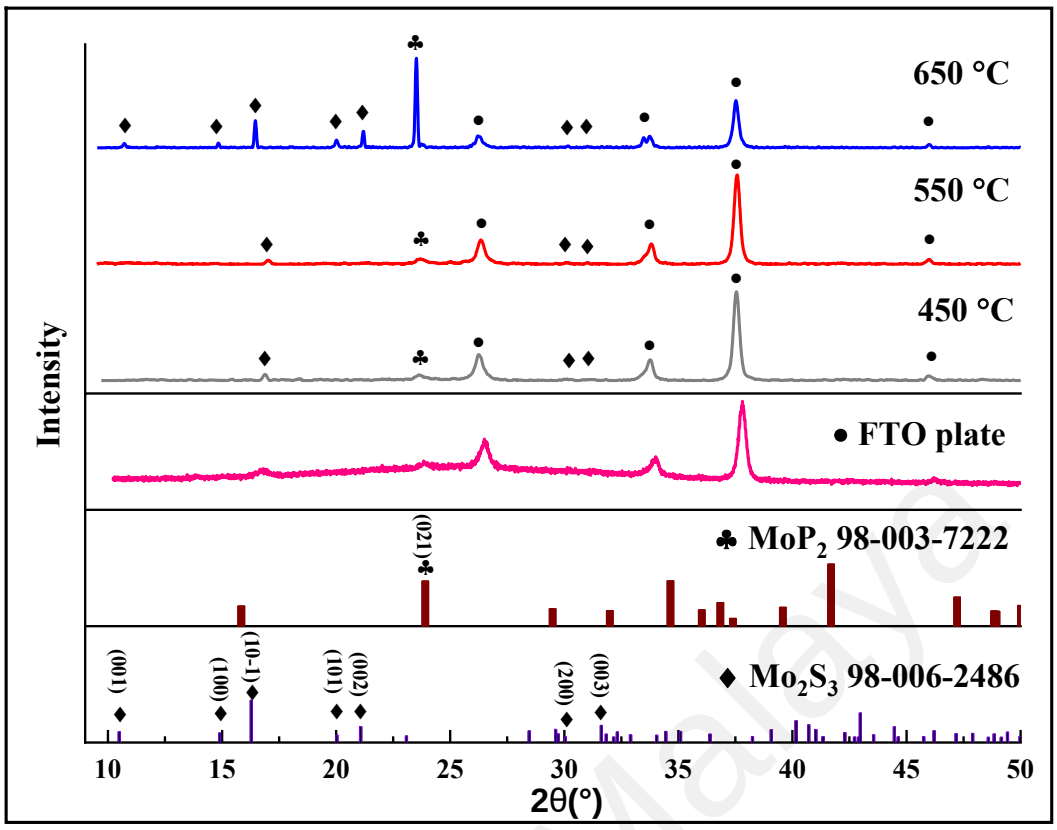

Figure 4.52: XRD patterns of the 15 mL/15 mins films fabricated at deposition temperatures of 450, 550 and 650 °C.

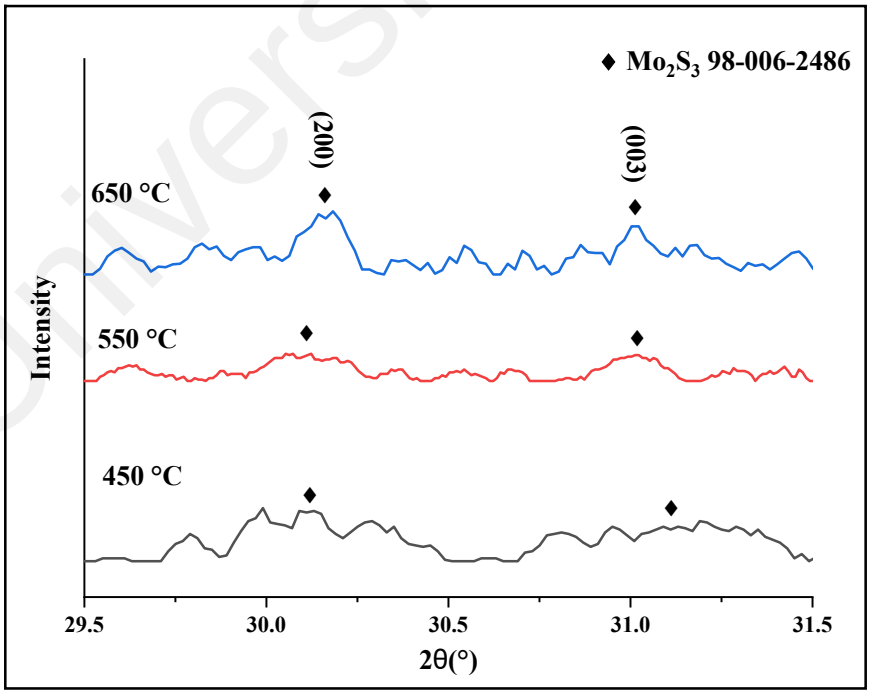

Figure 4.53: Enlarged XRD patterns of the 15 mL/15 mins films in 2θ range of 29.5°-31.5° at 450, 550 and 650 °C.

Universiti Malaya

Table 4.14: XRD peaks for the films fabricated at 450, 550 and 650 °C.

Temperature (°C)	2θ (°)	Assigned Peaks	Reference 2θ (°)
450	16.9	Mo_2S_3 (10-1)	16.3
	23.6	MoP_2 (021)	23.9
	30.1	Mo_2S_3 (200)	30.0
	31.1	Mo_2S_3 (003)	31.6
550	17.5	Mo_2S_3 (10-1)	16.3
	24.2	MoP_2 (021)	23.9
	30.1	Mo_2S_3 (200)	30.0
	31.0	Mo_2S_3 (003)	31.6
650	10.7	Mo_2S_3 (001)	10.5
	14.8	Mo_2S_3 (100)	14.9
	16.5	Mo_2S_3 (10-1)	16.3
	20.0	Mo_2S_3 (101)	20.0
	21.2	Mo_2S_3 (002)	21.1
	23.5	MoP_2 (021)	23.9
	30.2	Mo_2S_3 (200)	30.0
	31.0	Mo_2S_3 (003)	31.6

The crystallite size, *D* was obtained from Debye-Scherrer equation, $D = \frac{K\lambda}{\beta\cos\theta}$. Based on the calculation, it was found that the film fabricated at 450 ºC had the average crystallite size of 46 nm for Mo_2S_3 and 26.9 nm for MoP_2. The film fabricated at 550 ºC had the average crystallite size of 52.8 nm for Mo_2S_3 and 29.5 nm for MoP_2. The film fabricated at 650 ºC had the average crystallite size of 88.3 nm for Mo_2S_3 and 94.7 nm for MoP_2 (Refer to Table 4.15). The results showed that the average crystallite size increased with increasing deposition temperature for both Mo_2S_3 and MoP_2 phases. Higher temperature increased the rate of deposition reaction that resulted in the fast growth of crystallites leading to larger crystallite sizes of Mo_2S_3 and MoP_2.

Universiti Malaya

Table 4.15: Average crystallite sizes of Mo_2S_3 and MoP_2 of the films fabricated at 450, 550 and 650 °C.

Deposition temperature (°)	Materials	Average Crystallite size (nm), $D = \frac{K\lambda}{\beta\cos\theta}$.
450	Mo_2S_3	46.0
	MoP_2	26.9
550	Mo_2S_3	52.8
	MoP_2	29.5
650	Mo_2S_3	88.3
	MoP_2	94.7

4.5.2 Raman Spectroscopy

The Raman spectra for the films are displayed in Fig. 4.54. The Raman peaks intensities were shown to increase from 450 °C to 550 °C indicating that the increase in the amount of Mo_2S_3 and MoP_2 materials being deposited in the films. The film fabricated at 550 °C exhibited the strongest peaks for the vibrational modes for Mo_2S_3 and MoP_2. At 650 °C it was observed that these peaks were coalesced together with significant decrease in intensity. From the XRD results in Fig. 4.52 and 4.53, the vibration modes of both Mo_2S_3 and MoP_2 were also present in the Raman spectra indicating that the same composite material was fabricated at these three deposition temperatures.

Universiti Malaya

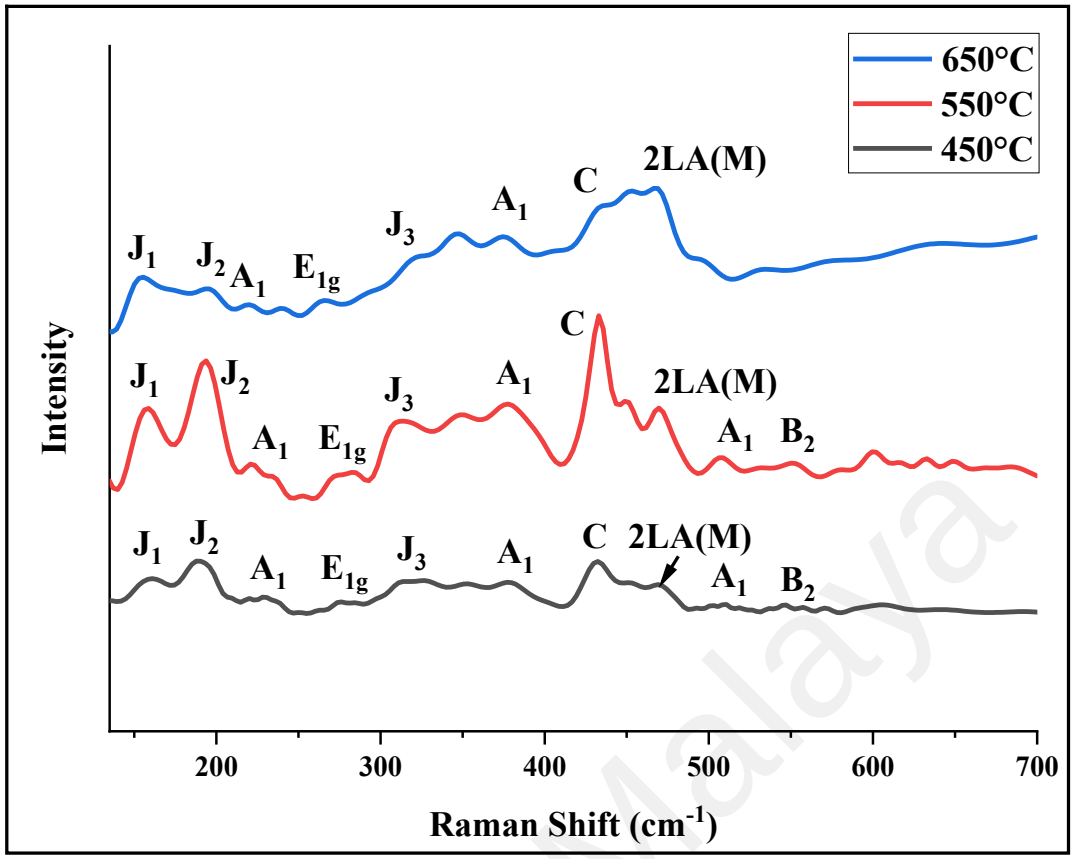

Figure 4.54: The Raman shifts of the 15 mL/15 mins films fabricated at 450, 550 and 650 °C.

4.5.3 Energy Dispersive X-ray (EDX) Spectroscopy and Elemental Mapping Analyses

The Mo, S and P compositions and their distributions in the 15 mL/15 mins films fabricated at 450, 550 and 650 °C, respectively, were analysed with EDX and elemental mapping analyses. The atomic percentages for Mo, S and P are displayed in Table 4.16. The EDX spectra of the films are shown in Fig. 4.55-4.57. The S/P ratio for the films were found to be 2.54, 2.26 and 2.81, respectively. Based on the calculated S/P ratio, higher deposition temperature promoted more growth of Mo_2S_3 than MoP_2. The Mo, S and P distributions were observed by the elemental mapping images that are displayed in Fig. 4.58-4.60. It was shown that Mo, S and P were homogenously distributed over the film and P occurred dominantly in the larger grains as exhibited by the 15 mL/15 mins film fabricated at 550 °C based on the EDX mapping for P displayed in Fig. 4.56.

Universiti Malaya

Table 4.16: Atomic percentages of Mo, S and P of the films fabricated at 450, 550 and 650 °C.

Deposition Temperature (°C)	Element	Atomic percentage (%)
450	Mo	37.74
	S	44.68
	P	17.58
550	Mo	34.99
	S	45.10
	P	19.91
650	Mo	35.58
	S	47.51
	P	16.91

Universiti Malaya

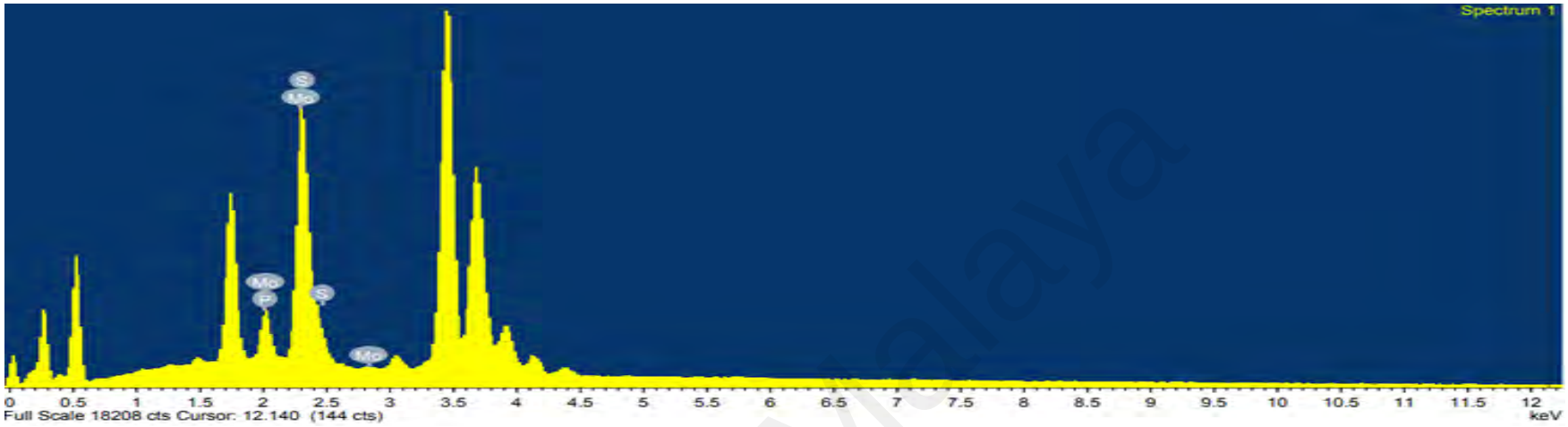

Figure 4.55: EDX spectrum for 15 mL/15 mins film fabricated at 450 °C.

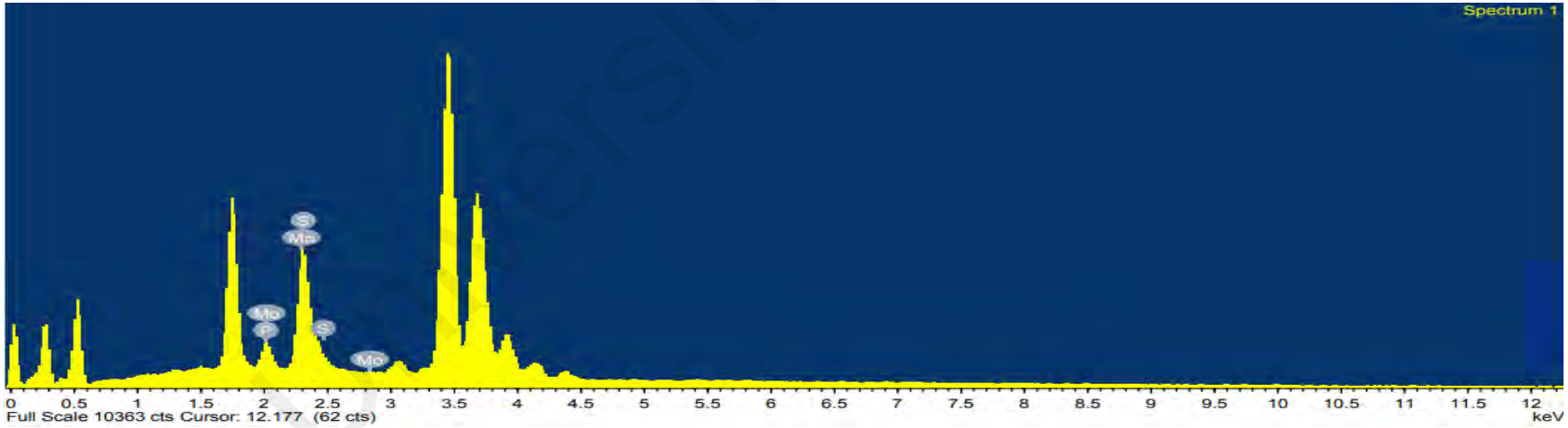

Figure 4.56: EDX spectrum for 15 mL/15 mins film fabricated at 550 °C.

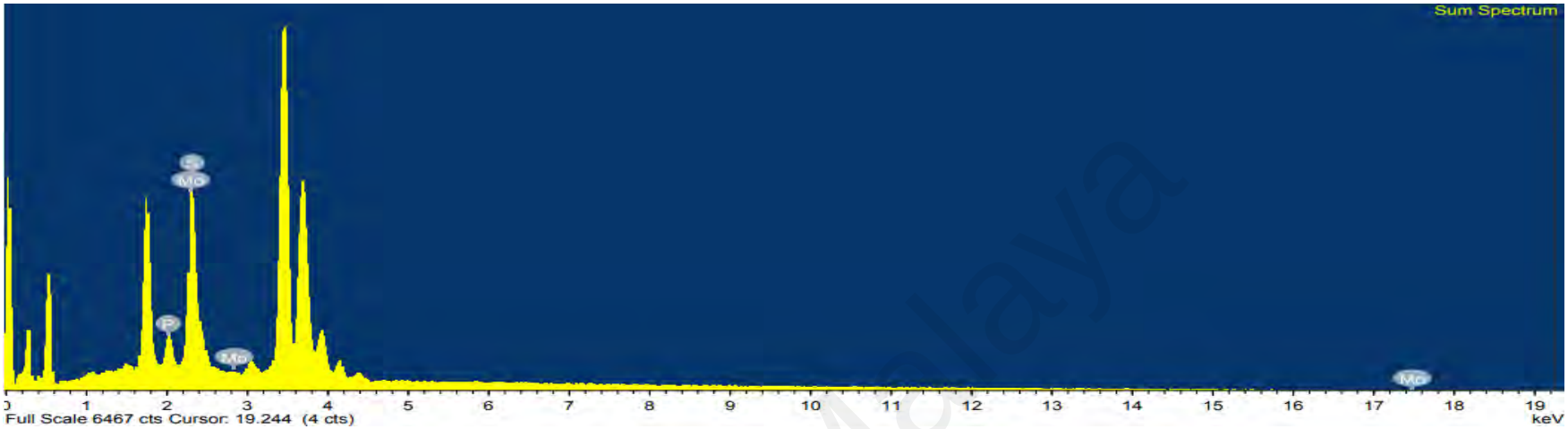

Figure 4.57: EDX spectrum for 15 mL/15 mins film fabricated at 650 °C.

Universiti Malaya

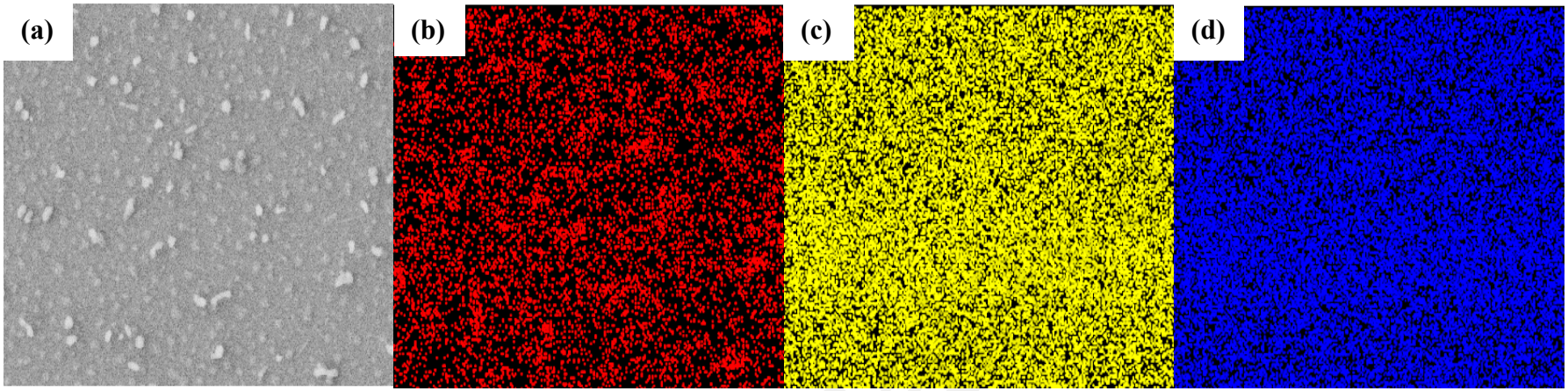

Figure 4.58: Elemental mapping of the (a) analysed area of 15 mL/ 15 mins film fabricated at 450 °C with distribution of (b) phosphorus, (c) sulphur and (d) molybdenum.

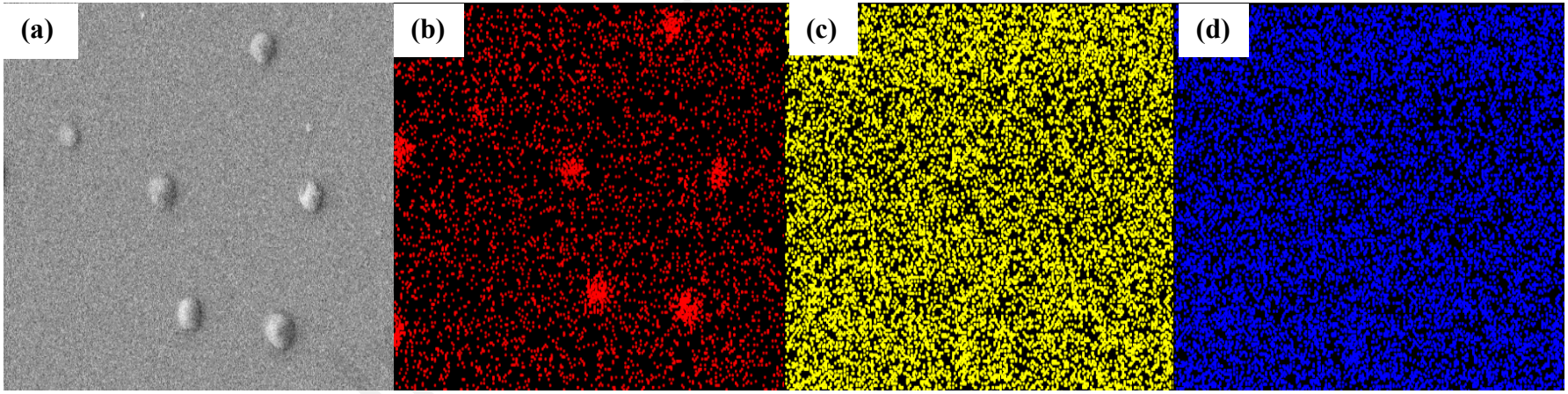

Figure 4.59: Elemental mapping of the (a) analysed area of 15 mL/ 15 mins film fabricated at 550 °C with distribution of (b) phosphorus, (c) sulphur and (d) molybdenum.

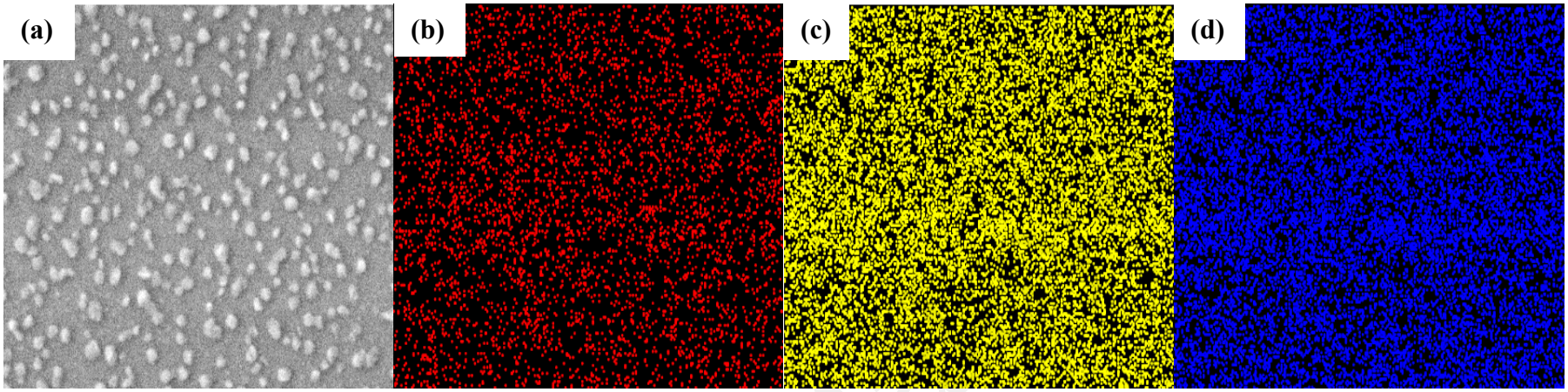

Figure 4.60: Elemental mapping of the (a) analysed area of 15 mL/ 15 mins film fabricated at 650 °C with distribution of (b) phosphorus, (c) sulphur and (d) molybdenum.

Universiti Ma

4.5.4 Atomic Force Microscopy (AFM)

The topologies of the films fabricated by AACVD process at 450, 550 and 650 °C were analysed by AFM and the following images are displayed in Fig. 4.61. The line profiles displaying the topologies of the films were shown in Fig. 4.62. Comparing the three films, 550 °C produced the lowest root-mean-square roughness, R_q of 12.9 nm to 450 °C (43.7 nm) and 650 °C (88.4 nm), respectively (Refer to Table 4.17). The increased agglomeration of the grains promoted by higher deposition temperature led to the increased surface roughness of the films.

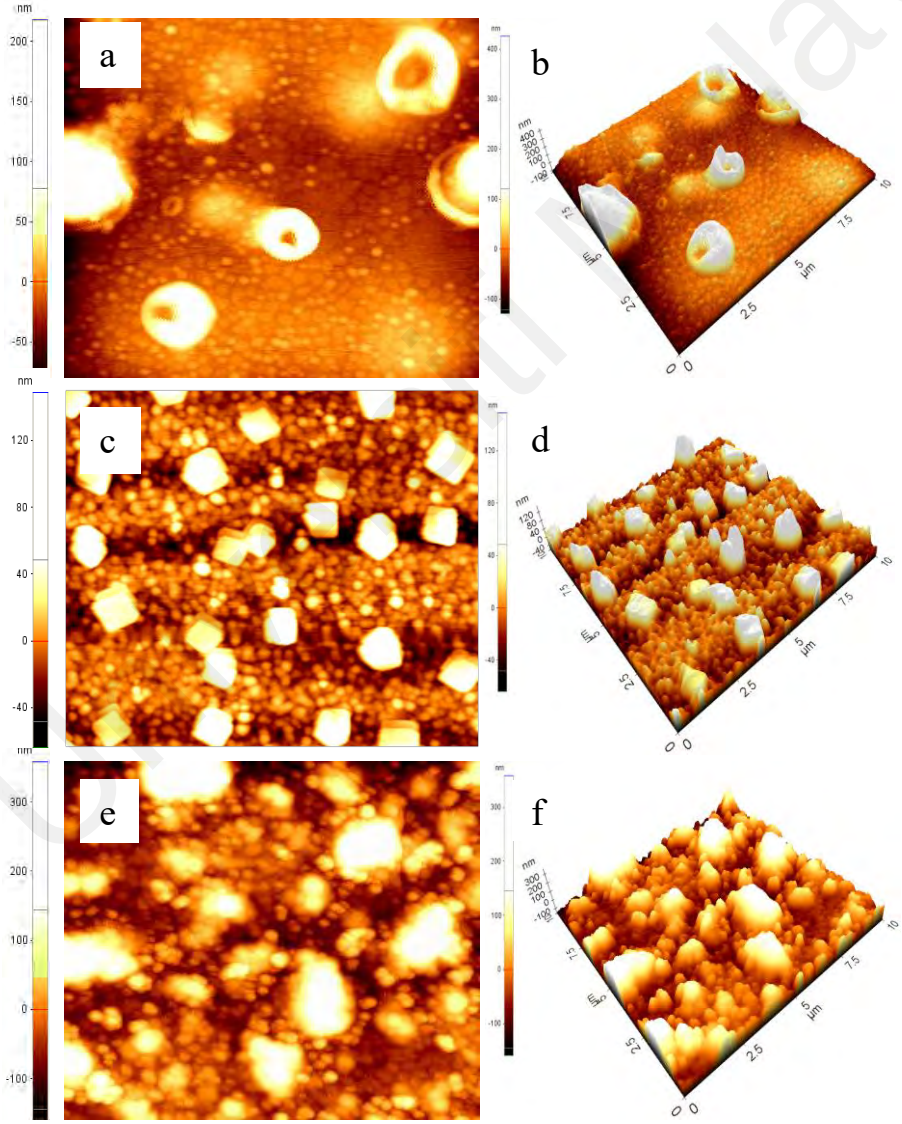

Figure 4.61: AFM images of films fabricated after 15 minutes at (a, b) 450 °C, (c, d) 550 °C and (e, f) 650 °C.

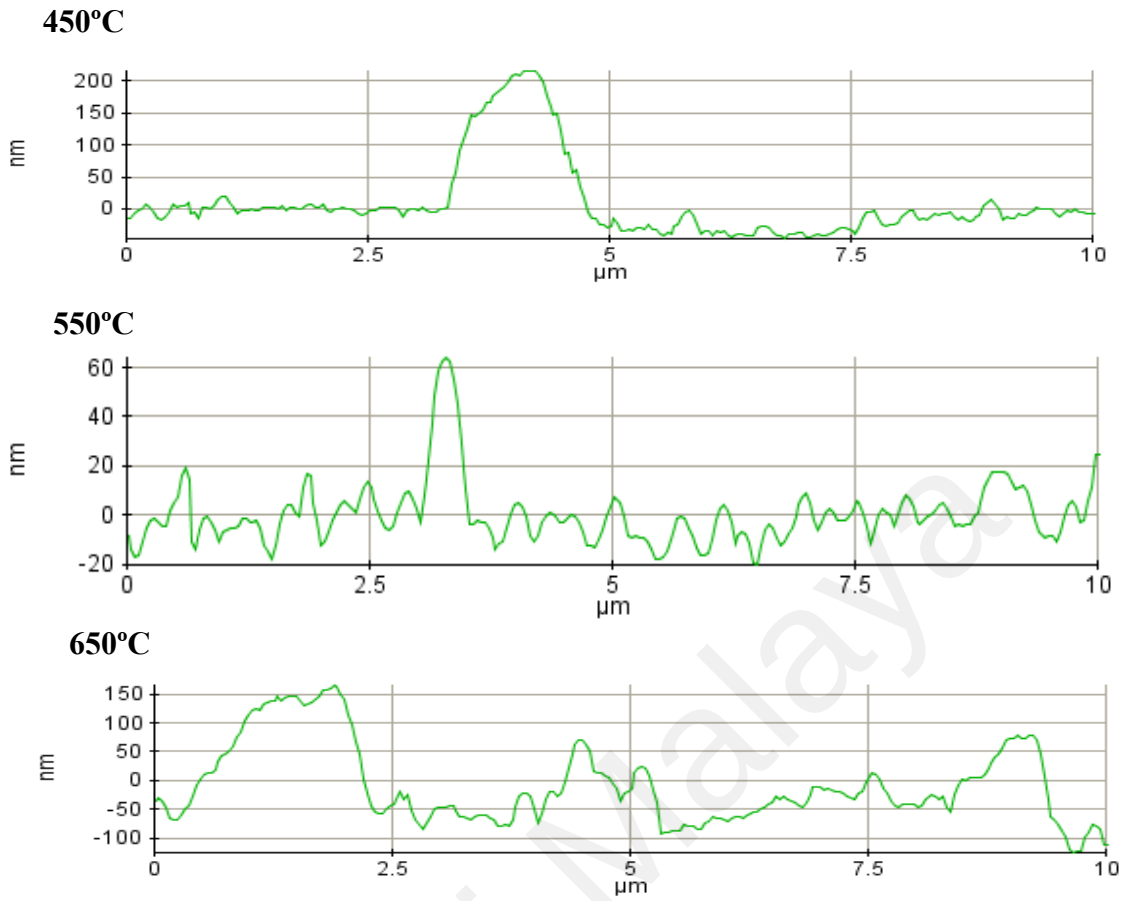

Figure 4.62: Line profiles for 15 mL/ 15 mins films fabricated at 450, 550 and 650 °C.

Table 4.17: Surface roughness parameters of the films fabricated at 450, 550 and 650 °C.

Films	Parameters	Values (nm)
15mL/ 15mins/ 450 °C	Roughness average, R_a	28.969
	Root mean square, R_q	43.738
	Maximum profile height, R_{pv}	263.144
	Maximum valley depth, R_v	50.901
	Maximum peak height, R_p	212.243
15 mL/15 mins/ 550 °C	Roughness average, R_a	8.317
	Root mean square, R_q	12.901
	Maximum profile height, R_{pv}	84.092
	Maximum valley depth, R_v	20.175
	Maximum peak height, R_p	63.917
15mL/ 15mins/ 650 °C	Roughness average, R_a	54.190
	Root mean square, R_q	88.436
	Maximum profile height, R_{pv}	289.753
	Maximum valley depth, R_v	124.679
	Maximum peak height, R_p	165.074

Universiti Malaya

4.5.5 Scanning Electron Microscopy (SEM) Analyses

The morphologies of the films prepared from deposition process at 450, 550 and 650 °C was observed by using SEM analysis. The SEM images at magnification of ×5,000 as shown in Fig. 4.63 corresponded to their respective AFM images shown in Fig. 4.61. The film from 450 °C had exhibited rough appearance in morphology with large population of small particles with a mean particle size of 101-150 nm (50.5%) that widely distributed over the surface of substrate based on the histogram displaying size distribution of 200 particles in Fig. 4.64. As compared to the 650 °C film, the morphology showed large irregularly sized grains widely distributed on the surface with a mean particle size of 501-1000 nm (42.5 %). The resultant larger grains fabricated at 650 °C as indicated in SEM analysis (Fig. 4.63) was due to the effect of high-temperature deposition condition which led to the fast evaporation process of the solvent in the furnace and consequently increased the agglomeration of the particles (Hernández-Salcedo et al., 2015). With large irregularly sized particles in the film fabricated at 650 °C, the high-roughness topology was displayed in AFM analysis. The film fabricated at 550 °C had large grains in between the densely arranged small grains. The study also showed that 550 °C was the best optimal temperature for fabrication of film with most uniform thickness and based on the particle size distribution, the film had a mean size of 501-800 nm (76.5 %).

Universiti Malaya

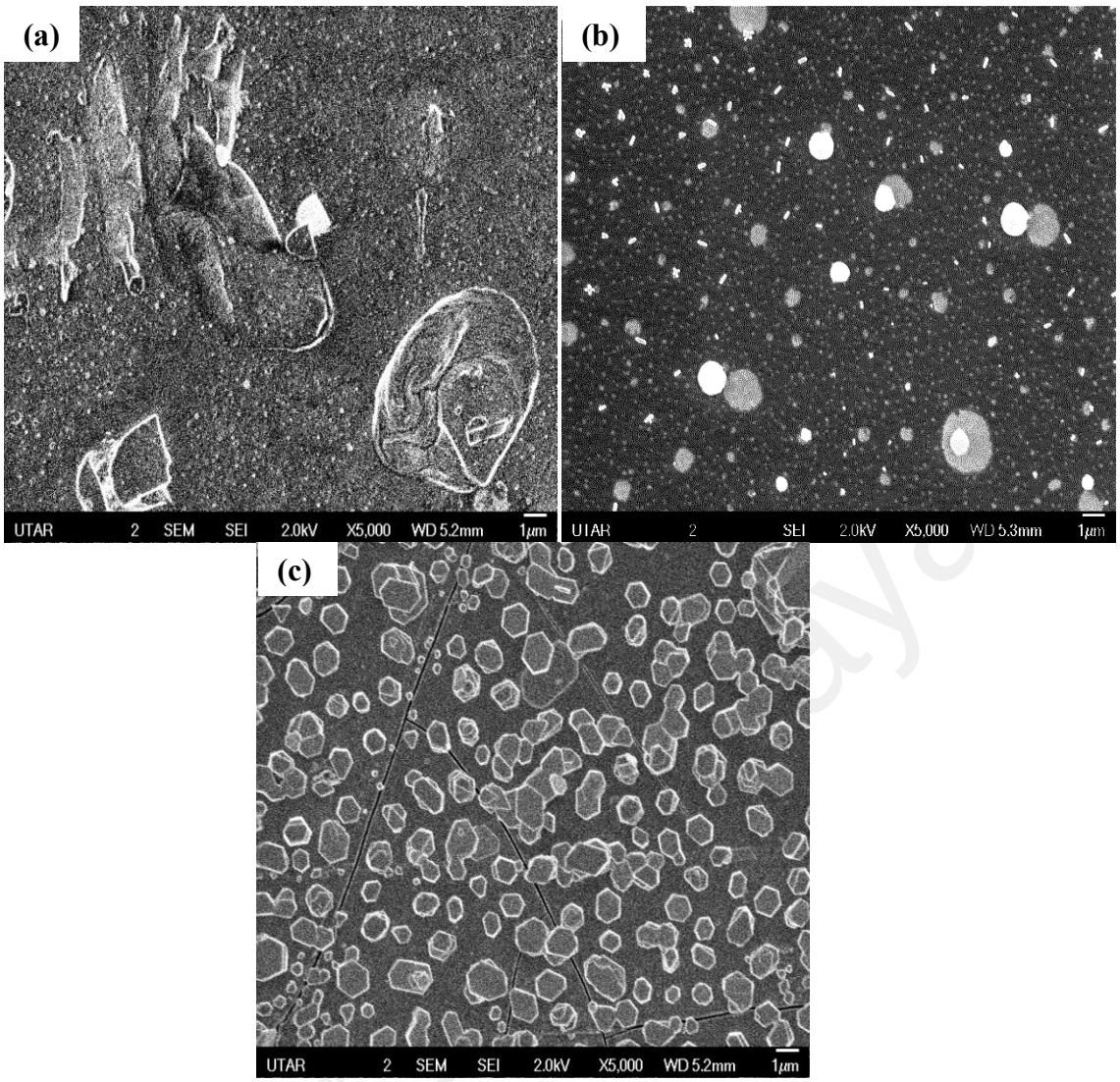

Figure 4.63: SEM images with magnification of ×5,000 for 15 mL/15 mins films fabricated at deposition temperature of (a) 450 °C, (b) 550 °C and (c) 650 °C.

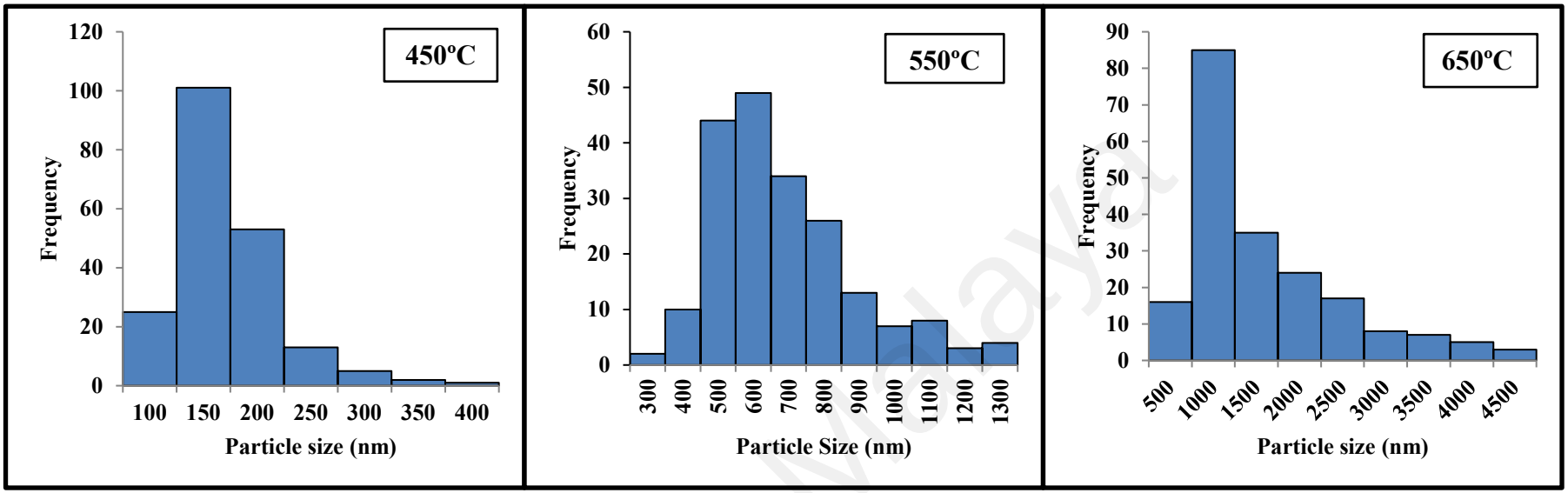

Figure 4.64: Histograms displaying size distributions of nanoparticles of the 15 mL/15 mins films at 450, 550 and 650 °C.

University Malaya

4.5.6 Film Thickness Measurements

The thickness of the 15 mL/15 mins films fabricated at 450, 550 and 650 ºC deposition temperature was measured by using surface profilometer. The measured film thickness was 438, 436 and 496 nm for 450, 550 and 650 ºC deposition temperatures, respectively. It was noted that the thickness increment for 450 and 550 °C was negligible but more pronounced increment was observed for 650 °C. The amount of precursor materials deposited in the films was same for all deposition temperatures and this led to insignificant change in film thickness for all the films. There was no notable correlation between deposition temperature and growth thickness except particle size was found to increase with deposition temperature.

4.5.7 UV-vis Spectrophotometry Analyses

The optical property of the films was studied in determination of band gap which is an important aspect in producing high-performance electrocatalysts. The UV absorption spectra of these films are displayed in Fig. 4.65. The result showed that film fabricated at 650 °C had the highest adsorption followed by films fabricated at 450 °C and 550 °C, respectively. The higher absorbance exhibited by the film fabricated at 450 ºC as compared to 550 °C could be due to its higher surface roughness which led to multi internal reflections of the beam which enhanced light absorption (Niu et al., 2019). The highest beam reflection frequency for the film fabricated at 650 °C resulted by the highest surface roughness led to the highest beam absorption as displayed in Fig. 4.65.

Universiti Malaya

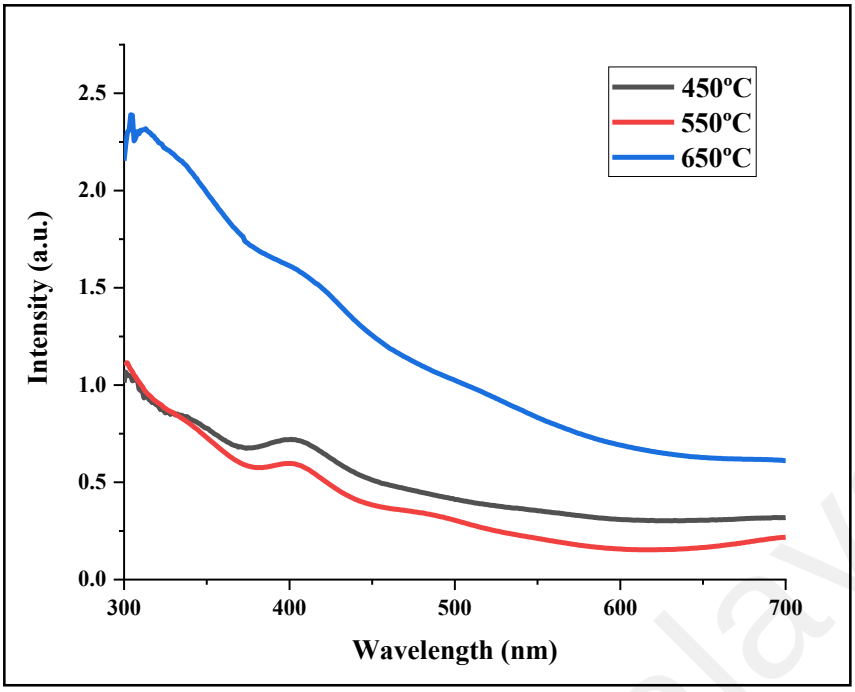

Figure 4.65: UV-vis absorbance spectra of 15 mL/15 mins films fabricated at 450, 550 and 650 °C.

The Tauc plots displayed in Fig. 4.66 showed two bandgap energy values for all the films and the values were very close to the literature bandgap energy values for Mo_2S_3 and MoP_2 (Lim et al., 2019; Wu et al., 2015). It was observed that the bandgap energy values did not show significant difference with increasing deposition temperature with the two bandgap energy values of 2.1 to 2.2 eV and 2.6 to 2.7 eV based on the Tauc plots.

Universiti Malaya

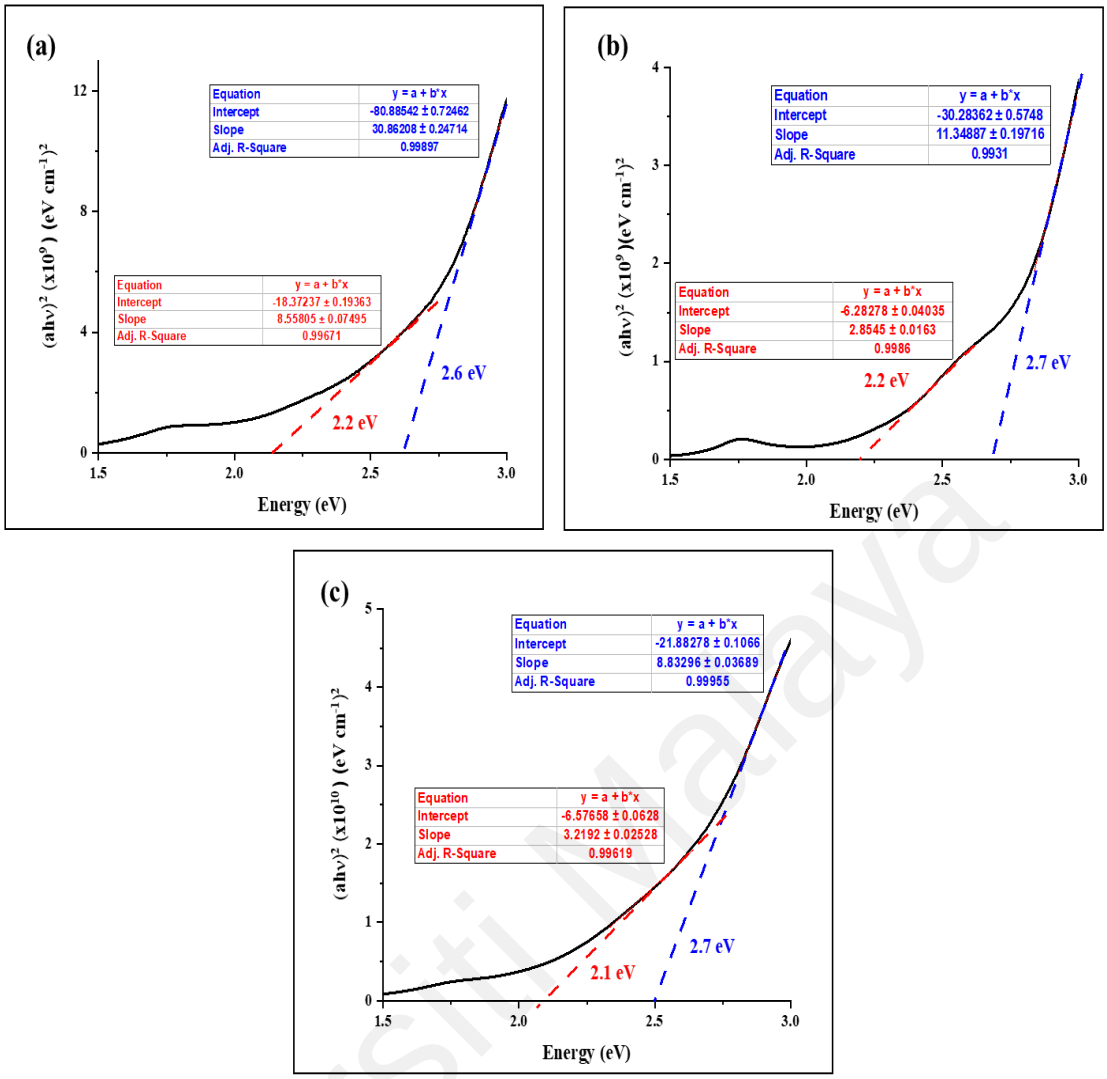

Figure 4.66: Tauc plots and bandgap values of the 15 mL/15 mins films fabricated at deposition temperature of (a) 450 ºC, (b) 550 ºC and (c) 650 ºC.

4.5.8 Electrochemical Studies

The electrochemical studies were performed with acidic electrolyte (0.25 M H_2SO_4 with pH 0.95). Based on the CV analyses, the curves displayed in Fig. 4.67 were shown to be stable after 5 cycles for the 15 mL/15mins films fabricated at 450, 550 and 650 ºC with the scan rate of 0.1 V/s. Based on the CV curves, the E_{ox} at which the anodic peak occurred for the 15 mL/15 mins films fabricated at 450, 550 and 650 ºC were found to be 0.64, 0.60 and 0.61 V vs. RHE, respectively and the E_{red} at which the cathodic peak occurred for the films were found to be 0.47, 0.44 and 0.24 vs. RHE, respectively. The potential difference, ΔE_p between E_{ox} and E_{red} for the 15 mL/15 mins films fabricated at

Universiti Malaya

450, 550 and 650 ºC were calculated to be 0.17, 0.16 and 0.37 V, respectively. Based on the calculation by using Eq. 4.3, the number of electrons transferred for 15 mL/15 mins films fabricated at 450, 550 and 650 ºC were calculated to be 0.347, 0.368 and 0.159 respectively in acidic media of pH 0.95 in the potential window of -0.6 to 0.6 V vs. Ag/AgCl.

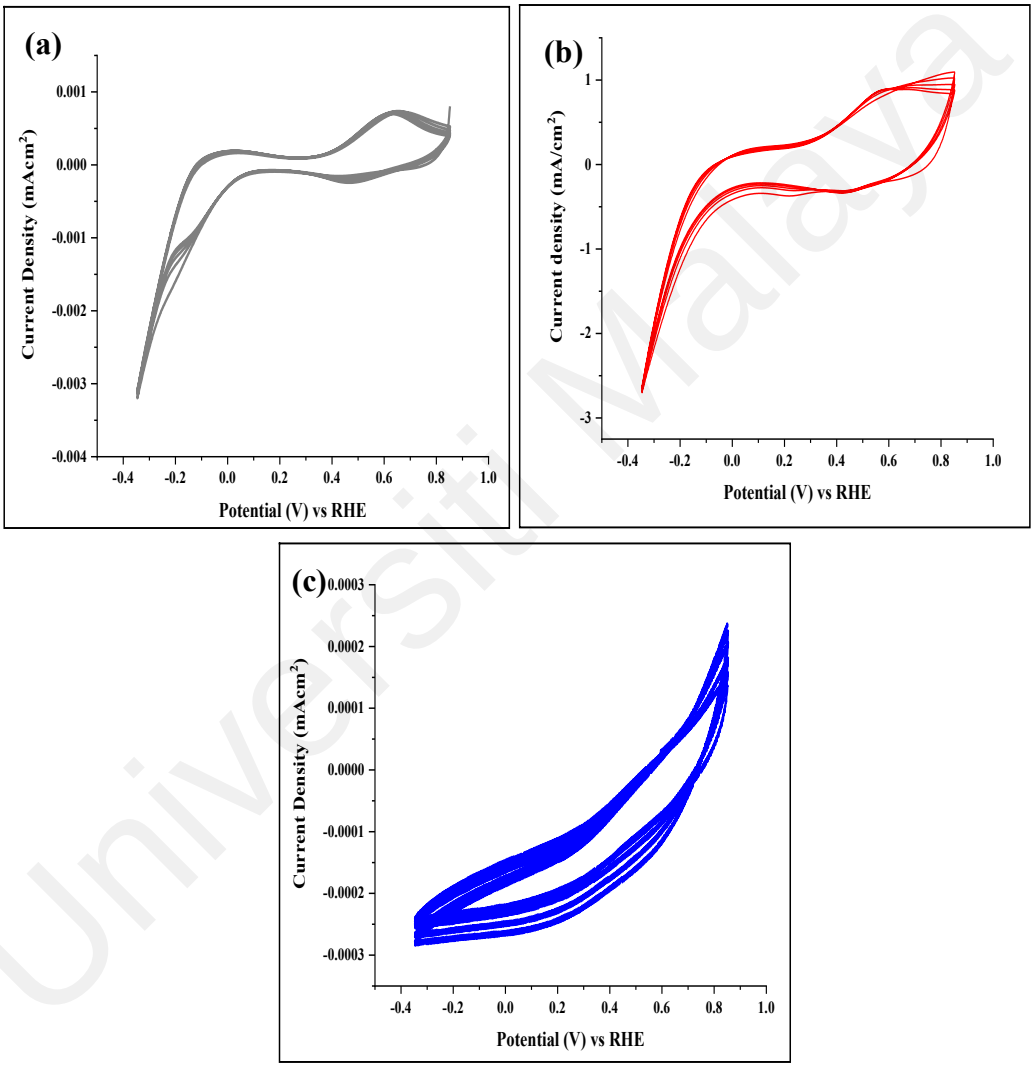

Figure 4.67: CV curves after 5 cycles for films fabricated at deposition temperature of (a) 450 ºC, (b) 550 °C and (c) 650 °C.

The *J-V* curves of the 15 mL/15 mins films obtained from LSV analysis with the potential window of -0.35 to 0.85 mV (vs. RHE) are displayed in Fig. 4.68. Onset potential was determined by taking the overpotential (vs. RHE) at which the current

density was 1 mA/cm^2 (Feng et al., 2020). The onset potential (vs. RHE) of the films fabricated at 450 and 550 ºC were found to be 223 and 236 mV, respectively. From LSV analyses, it was observed that the current densities generated by the 450 and 550 °C films were comparable. The film fabricated at 650 ºC had the highest onset potential without reaching current density of 1 mA/cm^2 in the same potential window.

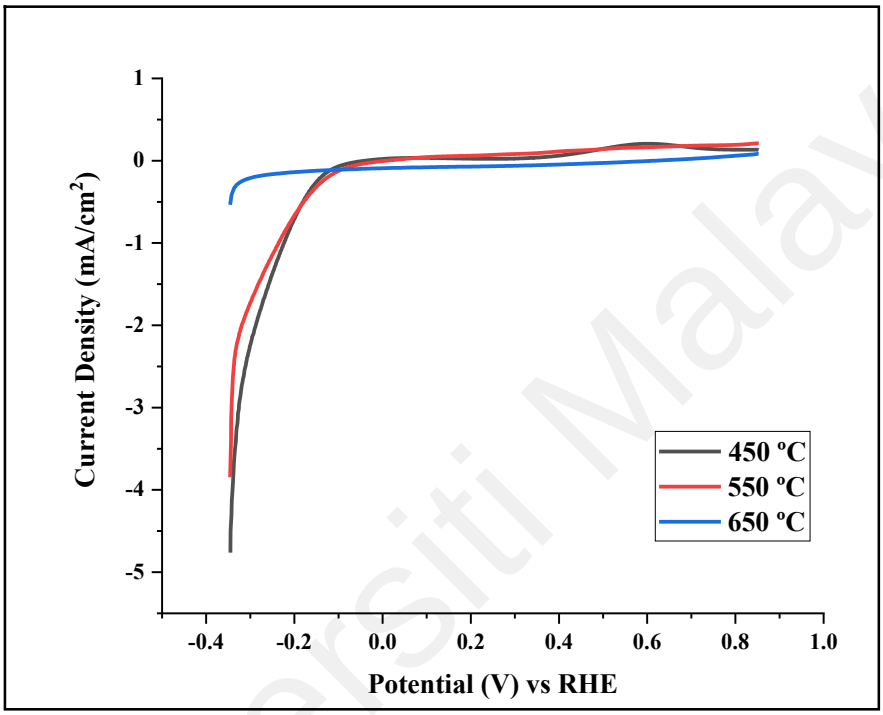

Figure 4.68: LSV curves of the 15 mL/15 mins films fabricated at 450, 550 and 650 °C.

Based on the MS plot in Fig. 4.69, the electron densities could be compared among the films by determining the slope of the plot, $[\frac{d\left(\frac{1}{c^2}\right)}{dV}]$. The slope is inversely proportional to the electron density. The slopes of the MS plots and electron densities for 15 mL/15 mins films fabricated from 450, 550 and 650 °C of deposition temperature are displayed in Table 4.18. The charge carrier densities were calculated by using Eq. 4.6 in which the relative dielectric constant, ε_r is assumed to be 10 because it is usually slightly above or below this value for semiconductors (Chen et al., 2013). Based on the MS plots that are

Universiti Malaya

displayed in Fig. 4.69, the film fabricated at 450 and 550 °C exhibited n-type conductivity but film fabricated at 650 °C exhibited both n- and p-type semiconductor properties in different applied potential windows. The n-type property was exhibited from -1 to -0.5 V vs Ag/ AgCl followed by the p-type property exhibited from -0.5 to 1 V vs Ag/ AgCl for the film fabricated at 650 °C. The positive slopes observed in MS plots indicated n-type property in which electrons were the dominant charge carriers. The p-type property exhibited by 650 °C film in the potential window from -0.5 to 1 V vs. RHE indicated that holes were the dominant positively charged carriers.

The charge density for the holes within the film fabricated at 650 ºC was calculated independently from the electron density which was determined by the positive slope of the MS plot. Based on the electron densities of the films, the film fabricated at 650 °C had the lowest electron density. The poorest HER performance exhibited by the film fabricated at 650 ºC as shown in the *J-V* curves displayed in Fig. 4.68 was due to the lowest charge carrier density. The charge carrier density must be adequate in order to contribute to the desired overall conductivity of the semiconductor. The extra holes indicated by the negative MS slope for the film fabricated at 650 °C caused the ΔG_{H*} value to be more positive which rendered the hydrogen adsorption step to be less favourable because electrons tended to fill the holes instead of participating in HER process (Wang et al., 2020).

Universiti Malaya

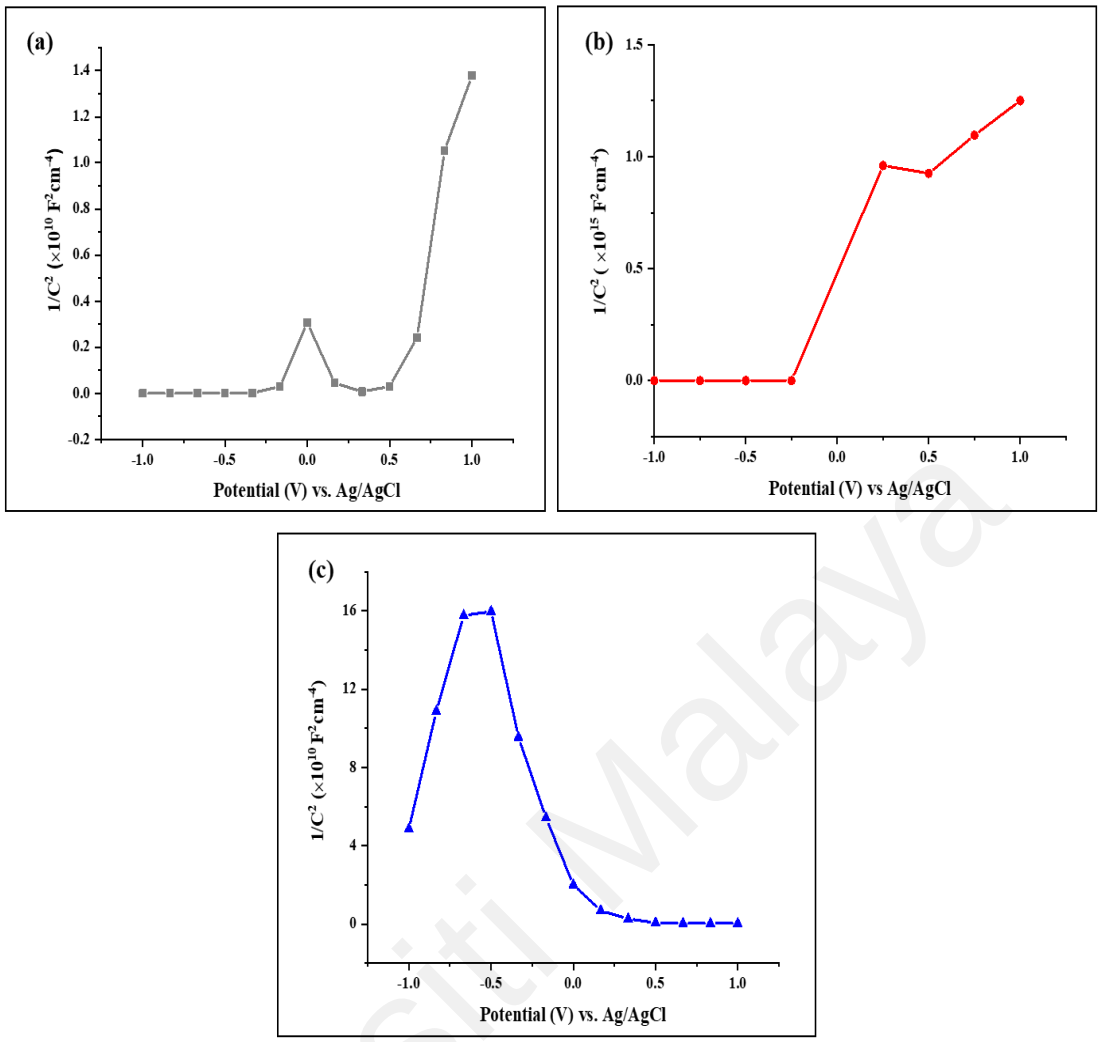

Figure 4.69: MS plots of films fabricated at deposition temperature of (a) 450 °C, (b) 550 °C and (c) 650 °C in applied potential from -1.0 to 1.0 vs Ag/AgCl.

Table 4.18: MS slopes and electron densities of the 15 mL/15 min films fabricated at 450, 550 and 650 °C.

Deposition Temperature (ºC)	Area (cm^2)	Slope of MS plot, $\left[\frac{d\left(\frac{1}{C^2}\right)}{dV}\right]$ (F^2V^{-1})	Donor density, N_d (cm^{-3})
450	0.90	3.407×10^{10}	5.14×10^{20}
550	0.90	9.742×10^{9}	1.80×10^{21}
650	0.90	n-type: 32.721×10^{10}	5.36×10^{19}
		p-type: 22.881×10^{10}	7.66×10^{19}

The electrochemical impedance spectroscopy (EIS) of the 15 mL/15 mins films fabricated at 450, 550 and 650 ºC was analyzed in the frequency range from 0.01 Hz to 100,000 Hz at a fixed potential. Nyquist plots and Bode plots are displayed in Fig. 4.70.

Universiti Malaya

Based on the Nyquist plot as shown in Fig. 4.70 (a), the 15 mL/15 mins film fabricated at 550 ºC had the lowest charge transfer resistance of 5.18 kΩ whereas the film fabricated at 650 ºC had the largest charge transfer resistance of 27.4 kΩ. The largest mean particle size of 501-1000 nm of film fabricated at 650 °C limited the exposure of active sites to participate in the HER activity and this was demonstrated by the poor performance observed in LSV analyses. The presence of the extra holes as shown in MS analysis rendered the film fabricated at 650 °C with more restriction in HER performance.

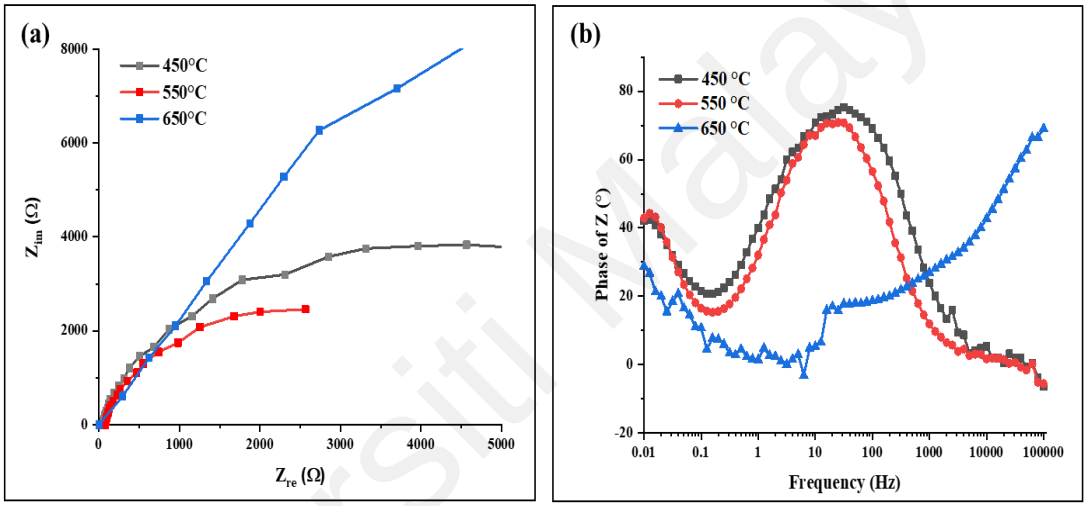

Figure 4.70: (a) Nyquist plots and (b) Bode plots of the 15 mL/15 mins films fabricated at 450, 550 and 650 °C.

Based on the Bode plots displayed in Fig. 4.70 (b), the frequency maxima at which the peaks occurred were determined for the calculation of the lifetimes, τ of the films by using the formula, $\tau = 1/(2\pi\nu)$. The frequency maxima and the calculated lifetime are displayed in Table 4.16. The frequency maxima for the film fabricated at 650 °C occurred at the high-frequency region and hence the film had the shortest lifetime. The frequency maxima for the film fabricated at 450 and 550 °C were found to be 3.22 and 2.22 Hz, respectively from the Bode plots which resulted in having the lifetimes of 49.4 and 71.7 ms, respectively. It was observed that for other films fabricated from different AACVD

Universiti Malaya

conditions, the films with high electrocatalytic performance would have short lifetime. But in this case, the film from 650 ºC of deposition temperature had the shortest lifetime even though it exhibited the poorest electrocatalytic performance. This could be due to the presence the extra holes which recombine with electrons.

4.5.9 Inherent properties of the films

The Tafel plots were generated from the *J-V* curves obtained from LSV analysis and are displayed in Fig. 4.71. Exchange current density, j_o is the current at overpotential of 0 V and it reflects the rates of electron transport between electrolyte and the working electrode. Surface roughness is an important factor for exchange current density. Higher exchange current density indicates more active surface of the electrode. It was found that small Tafel slopes do not necessarily possess high exchange current density, j_0. The LSV results showed that j_0 increased with increasing Tafel slope.

The 15 mL/15 mins film fabricated at 450 °C had the lowest Tafel slope therefore exhibited the fastest HER kinetics. The Tafel slope of 83.7 mV/dec was closer to 120 mV/dec for Volmer reaction than ~40 mV/dec for Tafel reaction. Therefore, the film underwent Volmer reaction as rate determining step for HER process. Though the j_0 of the 15 mL/15 mins film fabricated at 650 °C was the highest, with excellent current flow at equilibrium state, the presence of extra holes and high resistance in electron flow resulted in the very poor performance of the film. The inherent properties of the films are displayed in Table 4.19.

Universiti Malaya

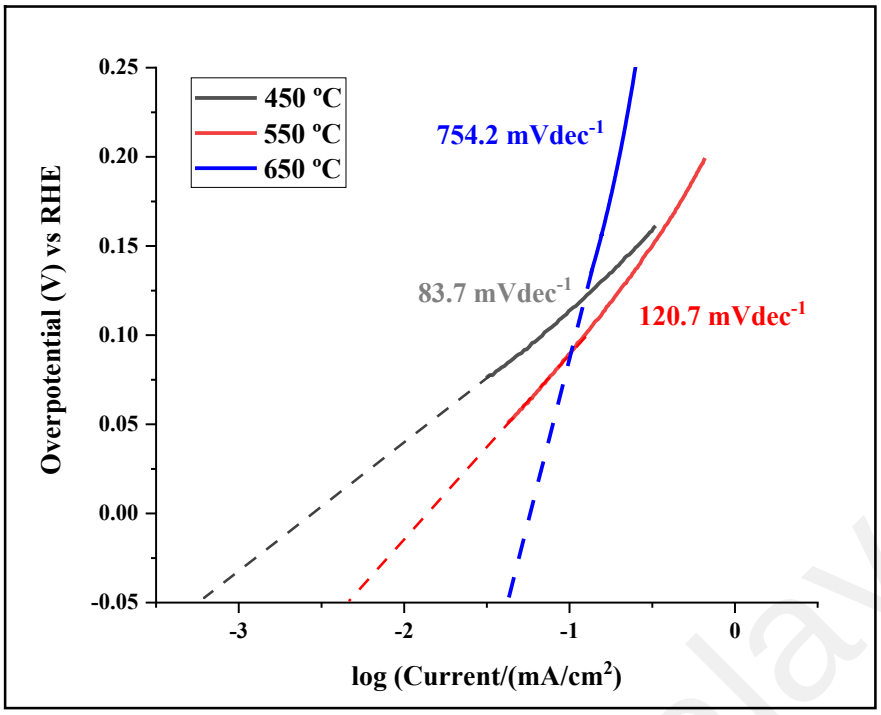

Figure 4.71: Tafel slopes for the 15 mL/15 mins films fabricated at 450, 550 and 650 °C.

Table 4.19: Inherent properties of the films fabricated at 450, 550 and 650 °C.

Temperature (°C)	Tafel slope, b (mVdec^{-1})	Exchange current density, j_0 (mA/cm^2)	Charge transfer resistance, R_{CT} (kΩ)
450	83.7	0.004	8.35
550	120.7	0.018	5.18
650	754.2	0.118	27.4

4.6 Characterization of Films Fabricated with different volume/deposition time at 450 °C

Since film fabricated at 450 °C showed favourable HER kinetics in acidic media as indicated by its low Tafel slope (Refer to Table 4.19). To further investigate electrocatalytic performance of the films at this temperature in alkaline media. The films were fabricated from different volumes of precursor solution with 10, 15 and 20 mL at the carrier gas flow rate of 0.5 SCFH at 450 °C. The time of deposition was also varied according to the volume with 10 mL for 10 minutes, 15 mL for 15 minutes and 20 mL for

Universiti Malaya

20 minutes. The films were characterised with XRD, Raman spectroscopy, EDX, AFM, SEM, UV-vis spectrophotometry, and electrochemical studies. The electrochemical studies were repeated to study the electrolyte's pH effect on the electrocatalytic performance of the films in the alkali media (Refer to Section 4.6.8).

4.6.1 X-ray Diffraction Analyses (XRD)

The XRD diffraction patterns of the 10 mL/10 mins, 15 mL/15 mins and 20 mL/20 mins films fabricated at 450 °C were indexed to monoclinic Mo_2S_3 (JCPDS no. 98-006-2486) and orthorhombic MoP_2 (JCPDS no. 98-003-7222) and the diffraction patterns are displayed in Fig. 4.72. The diffraction peaks for (200) and (003) planes for Mo_2S_3 were enlarged with the 2θ range of 29.8°-31.5° shown in Fig. 4.73. It was observed that Mo_2S_3 (200) and (003) were not formed in 20 mL/20 mins. It had been shown in Section 4.4.1 that fewer Mo_2S_3 planes were observed as solution volume and deposition time increased. The restricted growth of Mo_2S_3 planes was possibly caused by the increased activation energy in nucleation process to form crystals when the deposition rate increased with higher loading of Mo_2S_3 particles onto the 20 mL/20 mins (Khoo et al., 2016). The observed peak list is displayed in Table 4.20 which was matched with the 2θ positions of the indexed Mo_2S_3 and MoP_2 phases.

Universiti Malaya

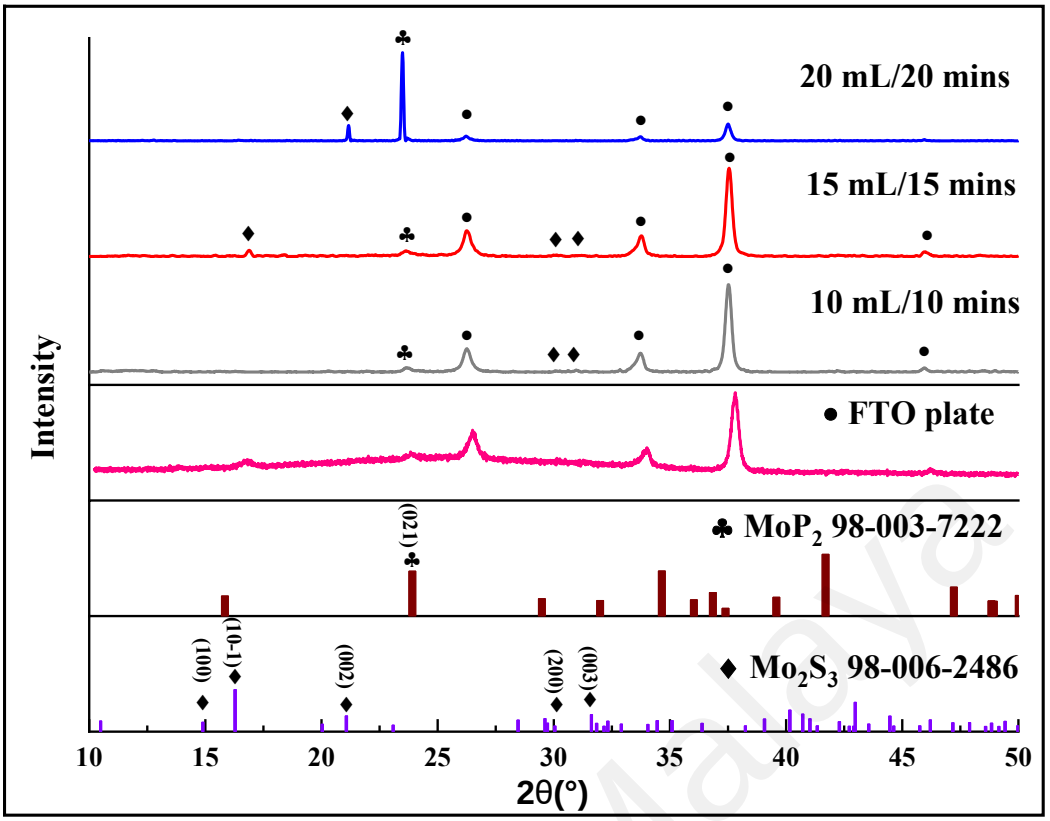

Figure 4.72: XRD diffraction patterns of 10 mL/10 mins, 15 mL/15 mins and 20 mL/20 mins films fabricated at 450 °C.

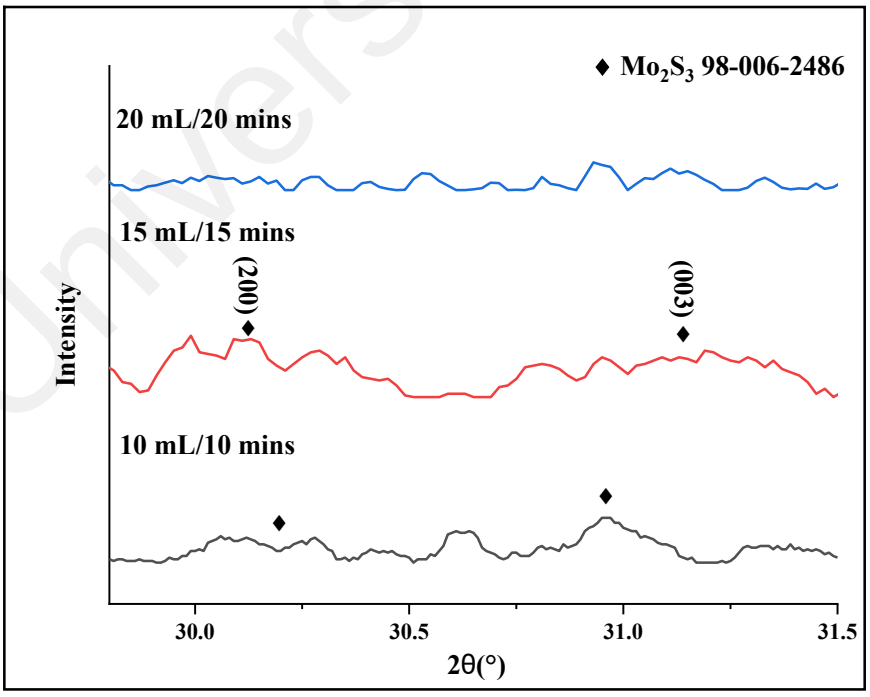

Figure 4.73: Enlarged XRD patterns of the films fabricated at 450 °C in 2θ range of 29.8°-31.5°.

Universiti Malaya

Table 4.20: XRD peaks for the fabricated films fabricated at 450 °C.

Films	2θ (°)	Assigned Peaks	Reference 2θ (°)
10 mL/10 mins	23.6	MoP_2 (021)	23.9
	30.2	Mo_2S_3 (200)	30.0
	31.0	Mo_2S_3 (003)	31.6
15 mL/15 mins	16.9	Mo_2S_3 (10-1)	16.3
	23.6	MoP_2 (021)	23.9
	30.1	Mo_2S_3 (200)	30.0
	31.2	Mo_2S_3 (003)	31.6
20 mL/20 mins	21.2	Mo_2S_3 (002)	21.1
	23.5	MoP_2 (021)	23.9

The crystallite size, D for the films fabricated at 450 °C was obtained from Debye-Scherrer equation, $D = \frac{K\lambda}{\beta\cos\theta}$. Based on the calculation, it was found that 10 mL/10 mins film had the average crystallite size of 14.5 nm for Mo_2S_3 and 22.6 nm for MoP_2. The 15 mL/15 mins film had the average crystallite size of 46 nm for Mo_2S_3 and 26.9 nm for MoP_2 (Refer to Table 4.21). The results showed that the average crystallite size increased with increasing deposition temperature for both Mo_2S_3 and MoP_2 phases. Based on the XRD diffraction patterns for the films fabricated at 450 °C as shown in Fig. 4.68, the growth of MoP_2 phase in (021) plane was most favoured in 20 mL/20 mins film and the peak intensity for MoP_2 increased with larger precursor amount. For Mo_2S_3, only (002) reflection plane was observed in 20 mL/20 mins film suggesting this was the favourable phase of the Mo_2S_3 at this deposition temperature.

Table 4.21: Average crystallite sizes of Mo_2S_3 and MoP_2 of the films fabricated at 450 °C.

Films	Materials	Average Crystallite size (nm), $D = \frac{K\lambda}{\beta\cos\theta}$.
10 mL/10 mins	Mo_2S_3	14.5
	MoP_2	22.6
15 mL/ 15 mins	Mo_2S_3	46.0
	MoP_2	26.9
20 mL/20 mins	Mo_2S_3	114.1
	MoP_2	110.9

Universiti Malaya

4.6.2 Raman Spectroscopy

The Raman spectra exhibited in Fig. 4.74 for the 10 mL/10 mins, 15 mL/15 mins and 20 mL/20 mins films fabricated at 450 °C showed similar patterns with difference in the peak intensities. 20 mL/20 mins film showed the strongest intensities for the Raman peaks due to the largest amount of precursor material being deposited on the substrate. Based on the observation that the Raman shifts were the same with other films prepared in other AACVD conditions and hence the films fabricated at 450 °C were also consisted of Mo_2S_3 and MoP_2.

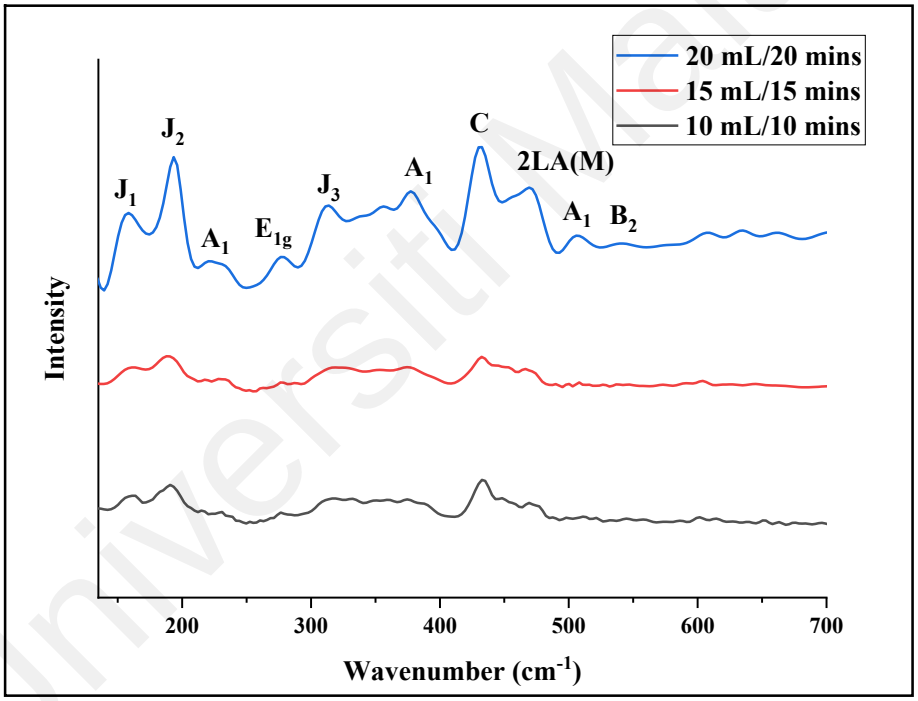

Figure 4.74: Raman shifts for 10 mL/10 mins, 15 mL/15 mins and 20 mL/20 mins films fabricated at 450 °C.

Universiti Malaya

4.6.3 Energy Dispersive X-ray (EDX) Spectroscopy and Elemental Mapping Analyses

The Mo, S and P composition and their distribution in the 10 mL/10 mins, 15 mL/15 mins and 20 mL/20 mins films fabricated at 450 °C were analysed with EDX and elemental mapping analysis. The atomic percentages for Mo, S and P are displayed in Table 4.22. The EDX spectra of the films are shown in Fig. 4.75-4.77 in which the highest peak in each of the spectra was ascribed to the tin (Sn) element from the substrate. The S/P ratio for the 10 mL/10 mins, 15 mL/15 mins and 20 mL/20 mins films were obtained to be 1.3, 2.5 and 1.9, respectively. The result showed that 15 mL/15 mins film fabricated at 450 °C had the highest S/P ratio. Based on the elemental mapping images displayed in Fig. 4.78- 4.80, the Mo, S and P were homogenously distributed. It was observed that the 20 mL/20 mins film had the largest P distribution while the 10 mL/10 mins film had the least P distribution.

Table 4.22: Atomic percentages of Mo, S and P of the films fabricated at 450 °C.

Films	Element	Atomic percentage (%)
10 mL/10 minutes	Mo	28.88
	S	40.14
	P	30.98
15 mL/15 minutes	Mo	37.74
	S	44.68
	P	17.58
20 mL/20 minutes	Mo	37.92
	S	40.71
	P	21.37

Universiti Malaya

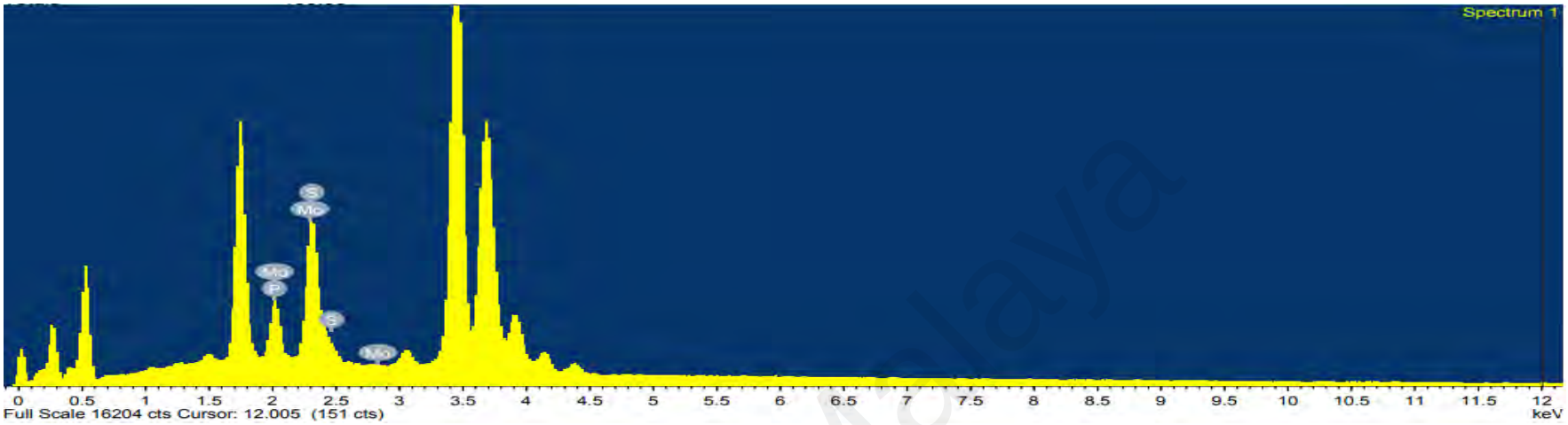

Figure 4.75: EDX spectrum for 10 mL/10 mins film fabricated at 450 °C.

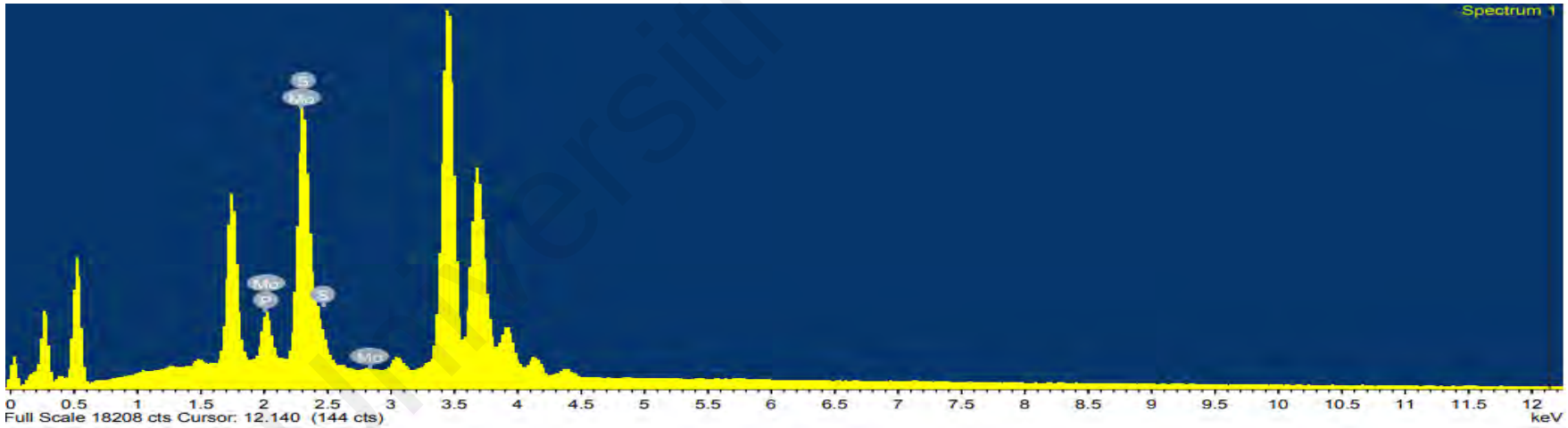

Figure 4.76: EDX spectrum for 15 mL/15 mins film fabricated at 450 °C.

Universiti Malaya

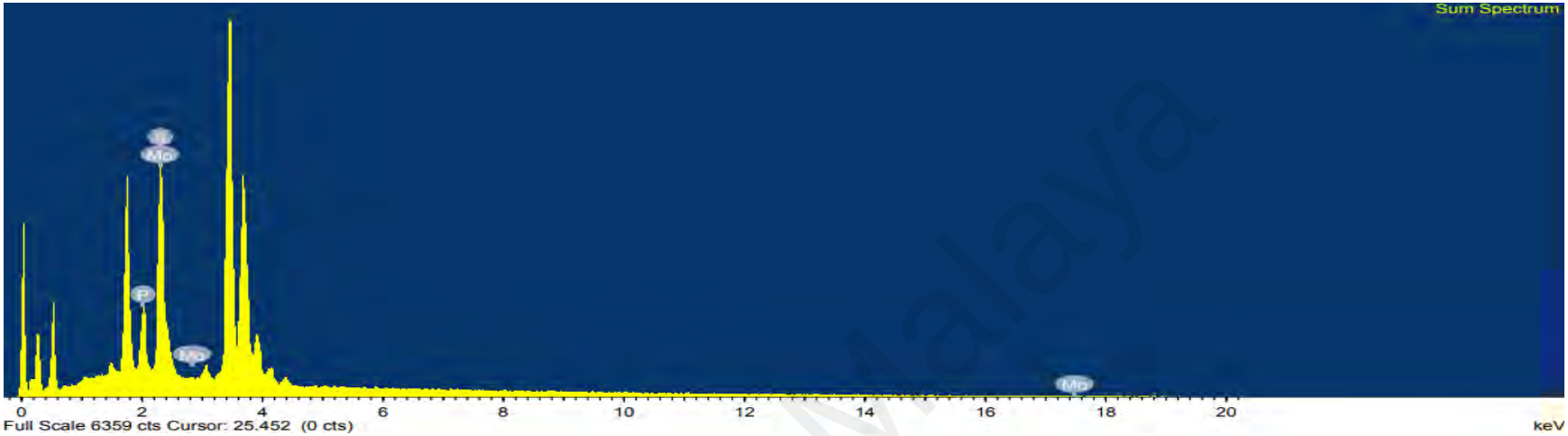

Figure 4.77: EDX spectrum for 20 mL/20 mins film fabricated at 450 °C.

Universiti Malaya

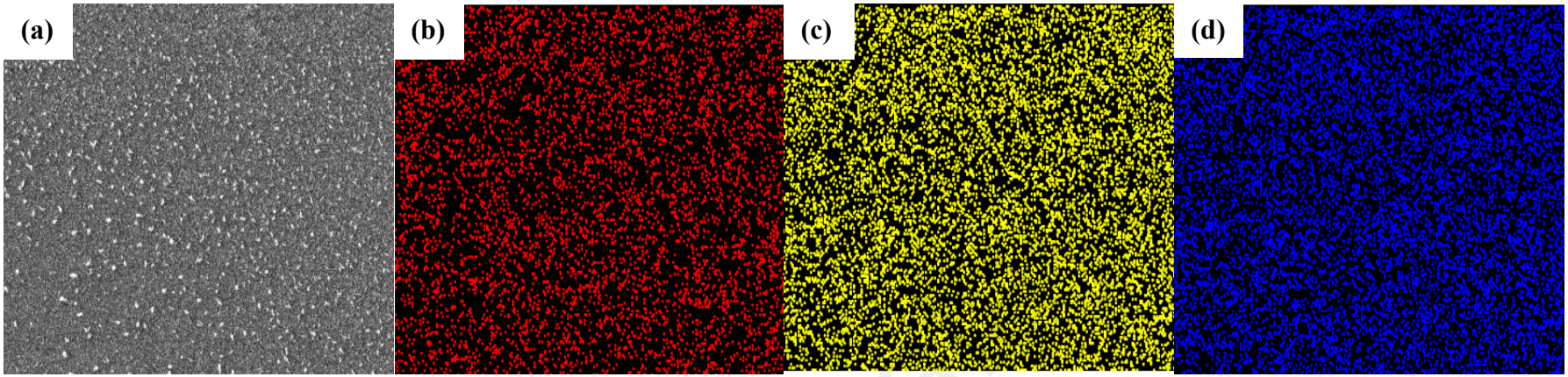

Figure 4.78: Elemental mapping of the (a) analysed area of 10 mL/10 mins film fabricated at 450 °C with distribution of (b) phosphorus, (c) sulphur and (d) molybdenum.

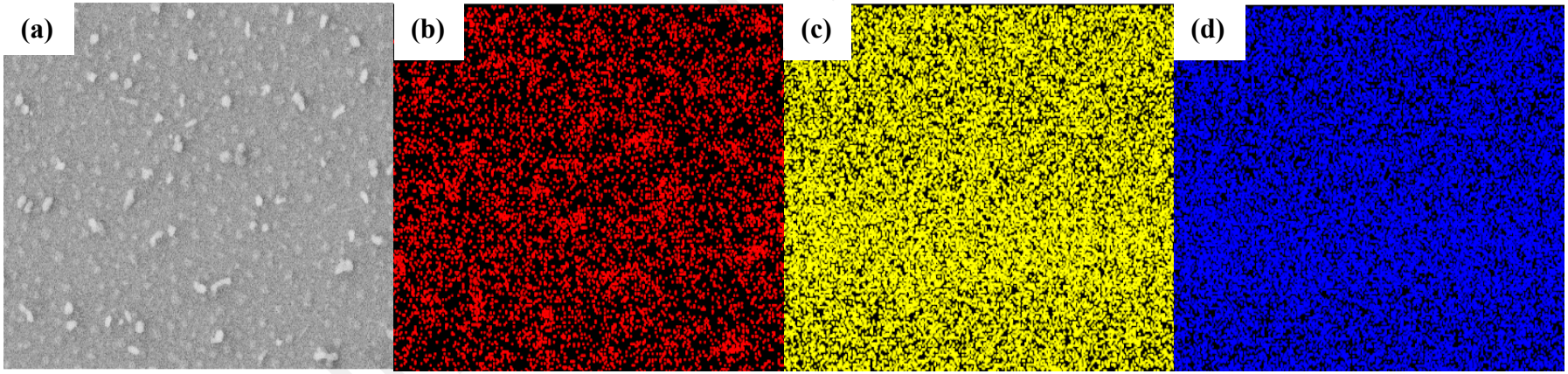

Figure 4.79: Elemental mapping of the (a) analysed area of 15 mL/15 mins film fabricated at 450 °C with distribution of (b) phosphorus, (c) sulphur and (d) molybdenum.

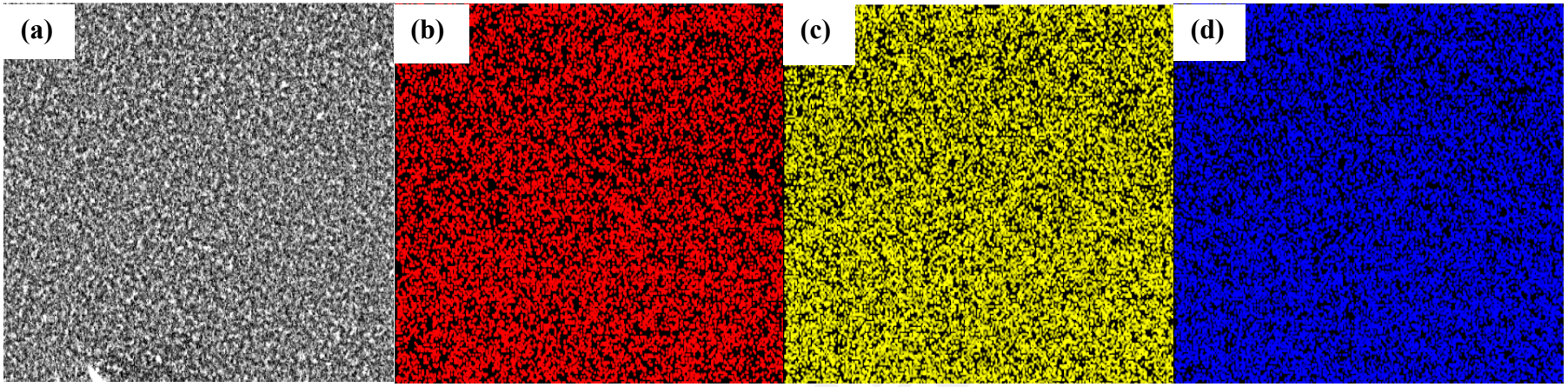

Figure 4.80: Elemental mapping of the (a) analysed area of 20 mL/20 mins film fabricated at 450 °C with distribution of (b) phosphorus, (c) sulphur and (d) molybdenum.

Universiti M

4.6.4 Atomic Force Microscopy Analyses (AFM)

The topologies of the films fabricated by AACVD process at 450 °C were analysed by using AFM and the images are displayed in Fig. 4.81. The line profiles for the films are displayed in Fig. 4.82. Based on the surface roughness parameters of the films fabricated at 450 ºC as displayed in Table 4.23, the 15 mL/15 mins had the largest root-mean square roughness, R_q of 43.7 nm whereas the 10 mL/10 mins film had the lowest R_q value of 23.4 nm. The larger surface roughness in 15 mL/15 mins and 20 mL/20 mins films (R_q= 36.4 nm) promoted more exposed active sites for electrocatalytic performance (Refer to section 4.6.8) as compared to 10 mL/10 mins with lowest surface roughness. However, if the surface roughness is too large, it could have a negative effect on the films' activity due to increased scattering of electrons which led to high resistivity to electron transport (Tang et al., 2012; Niu et al., 2019). High electron scattering frequency may impede the effectiveness of electron transport for electrocatalytic process.

Universiti Malaya

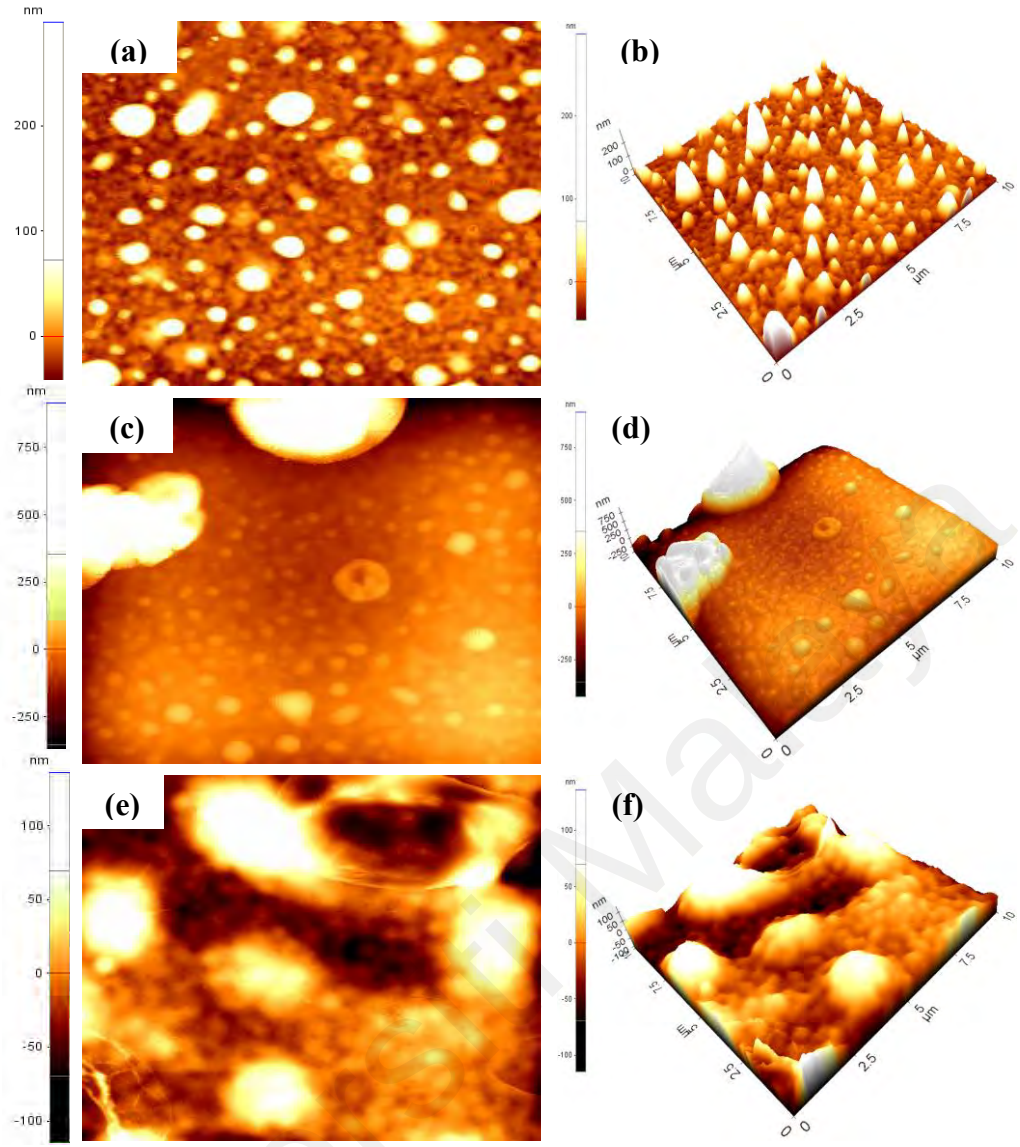

Figure 4.81: 2D and 3D AFM images of (a, b) 10 mL/10 mins, (c, d) 15 mL/15 mins and (e, f) 20 mL/20 mins films fabricated at 450 °C.

University of Malaya

10 mL/10 mins

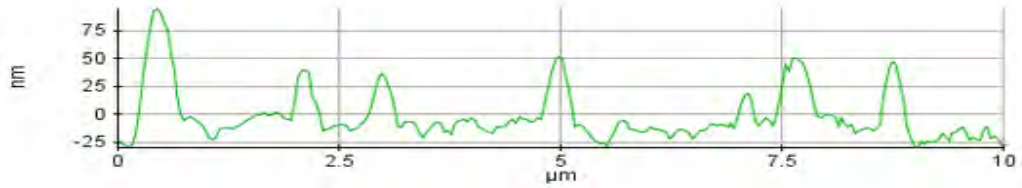

15 mL/15 mins

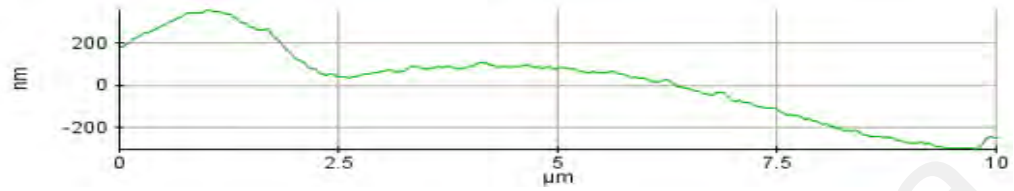

20 mL/20 mins

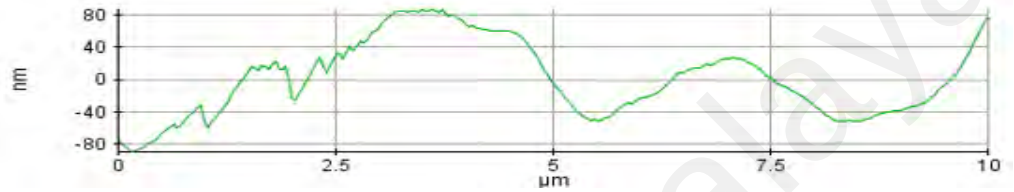

Figure 4.82: Line profile of the films fabricated at 450 °C.

Table 4.23: Surface roughness parameters of the films fabricated at 450 ºC.

Films	Parameters	Values (nm)
10 mL/10mins	Roughness average, R_a	16.719
	Root mean square, R_q	23.390
	Maximum profile height, R_{pv}	124.353
	Maximum valley depth, R_v	29.880
	Maximum peak height, R_p	94.474
15 mL/15 mins	Roughness average, R_a	28.969
	Root mean square, R_q	43.738
	Maximum profile height, R_{pv}	263.144
	Maximum valley depth, R_v	50.901
	Maximum peak height, R_p	212.243
20 mL/ 20 mins	Roughness average, R_a	30.232
	Root mean square, R_q	36.438
	Maximum profile height, R_{pv}	140.397
	Maximum valley depth, R_v	66.606
	Maximum peak height, R_p	73.791

University Malaya

4.6.5 Scanning Electron Microscopy (SEM) Analyses

The morphologies of the films fabricated at 450 °C were analysed by SEM. The SEM images are displayed in Fig. 4.83. The SEM images at magnification of ×5,000 as shown in Fig. 4.83 corresponded to their respective AFM images shown in Fig. 4.81. Based on the SEM images, the grainy morphology was observed in the 10 mL/10 mins film. The larger grains were observed on the surface of the 15 mL/15 mins film while large flakes were observed above the closely packed grains in 20 mL/20 mins film. The size distribution of 200 particles are displayed as histograms in Fig 4.84. The mean particle size for 10 mL/10 mins film was 180-340 nm (80.5 %), for 15 mL/15 mins film was 200-500 nm (76.5 %) and for 20 mL/20 mins was 500-1500 nm (70 %). From this observation, it was found that the mean particle size increased with longer deposition time and higher volume of precursor solution at the same deposition temperature. The similar trend was also observed for films fabricated at 550 °C.

In comparison with 20 mL/20 mins film that was prepared at 550 °C under the same carrier gas flow rate of 0.5 SCFH, film fabricated at 450 °C had larger mean particle size than film fabricated at 550 °C (400-700 nm). From the study with 15 mL/15 mins film fabricated at three different deposition temperatures (450, 550 and 650 °C), it is shown that increasing temperature promotes the agglomeration of particles, but it seemed that it was not the case for 20 mL/20 mins films fabricated at 450 and 550 °C. This showed that the growth in particle size was not obvious after transition from 450 to 550 °C for volume of precursor solution at 20 mL, because the droplets formed were less concentrated which required longer time for the droplets to reach saturation point for the growth of particles in the film. Therefore, there was a discrepancy in the change of particle size of 20 mL/20 mins from deposition temperature of 450 to 550 °C. The results showed that the volume of precursor solution had significant effect on the mean particle size of

Universiti Malaya

the fabricated films by taking into account of the amount of time needed to reach the saturation point.

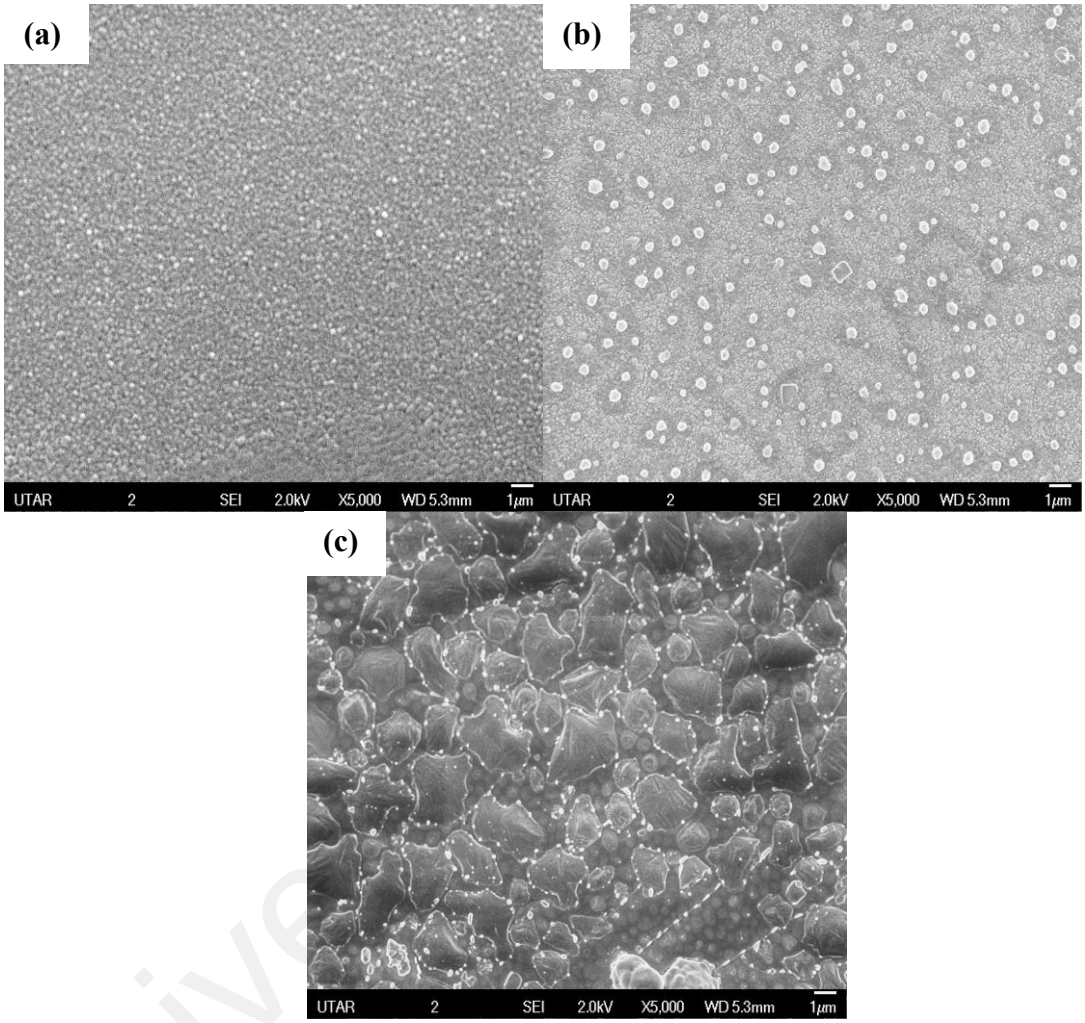

Figure 4.83: SEM images in ×5,000 magnification of (a) 10 mL/10 mins, (b) 15 mL/15 mins, and (c) 20 mL/20 mins films prepared at 450 °C.

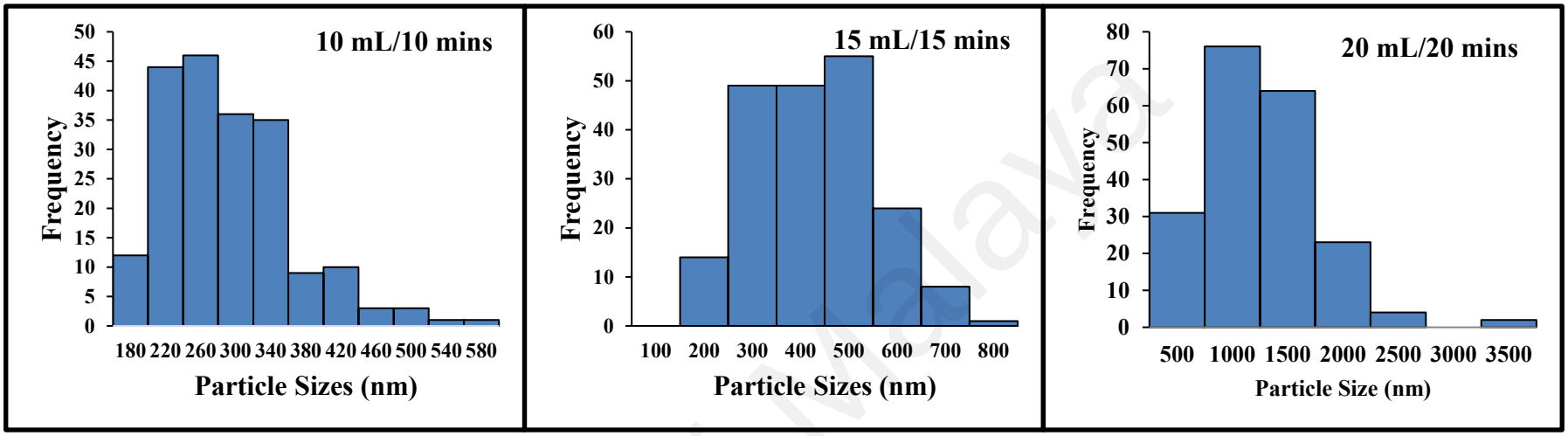

Figure 4.84: Histograms displaying size distributions of nanoparticles of the films fabricated at 450 °C.

University Malaya

4.6.6 Film thickness measurements

The film thickness of the films fabricated at 450 °C was measured using surface profilometer. The thickness for 10 mL/10 mins, 15 mL/15 mins and 20 mL/20 mins films were 285, 438 and 317 nm, respectively. The thickness showed decreasing trend from 15 mL/15 mins to 20 mL/20 mins films. This could be due to the formation of more dilute droplets generated at 450 °C of deposition temperature for producing 20 mL/20 mins film. When the concentration of the droplets is lower, the droplets will be subjected to a lower rate of evaporation which results in the droplets taking longer time to reach nucleation point for particle growth (Ma, 2021). As a result, less solute particles led to the reduction of film thickness from 15 mL/15 mins film to 20 mL/20 mins film prepared at 450 °C. Compared with the film thickness of the films fabricated under 0.5 SCFH flow rate at 550 °C, increasing trend was observed (618 nm for 20 mL/20 mins) at higher deposition temperature. This observation suggested that thickness of the film depended greatly on the rate of evaporation.

4.6.7 UV-vis Spectrophotometry Analyses

The optical properties of the 10 mL/10 mins, 15 mL/15 mins and 20 mL/20 mins films were analysed by using UV-vis spectrophotometry analyses. Based on the absorption spectra displayed in Fig. 4.85, the absorbance increased with higher volume of precursor solution and longer deposition time. As the amount of precursor materials deposited on the substrate was higher, higher beam absorption was exhibited.

Universiti Malaya

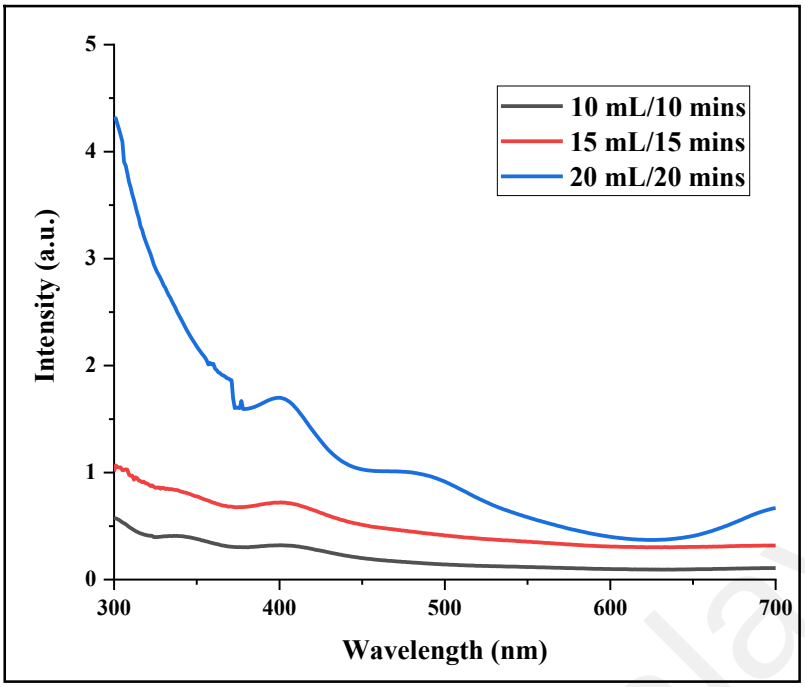

Figure 4.85: UV-vis absorption spectra of the films fabricated at 450 °C.

The UV-vis absorption spectra were converted to Tauc plots which are displayed in Fig 4.86 to determine the band gaps of the Mo_2S_3/MoP_2 composite material grown in the films. Based on the Tauc plots, two band gaps were observed to be in the range from 1.9 to 2.2 eV which was ascribed to the Mo_2S_3 phase and the range from 2.6 to 2.7 eV which was ascribed to the MoP_2 phase (Lim et al., 2019; Wu et al., 2015). The band gap and absorption spectra were found to be similar for all the films fabricated in different synthesis conditions.

Universiti Malaya

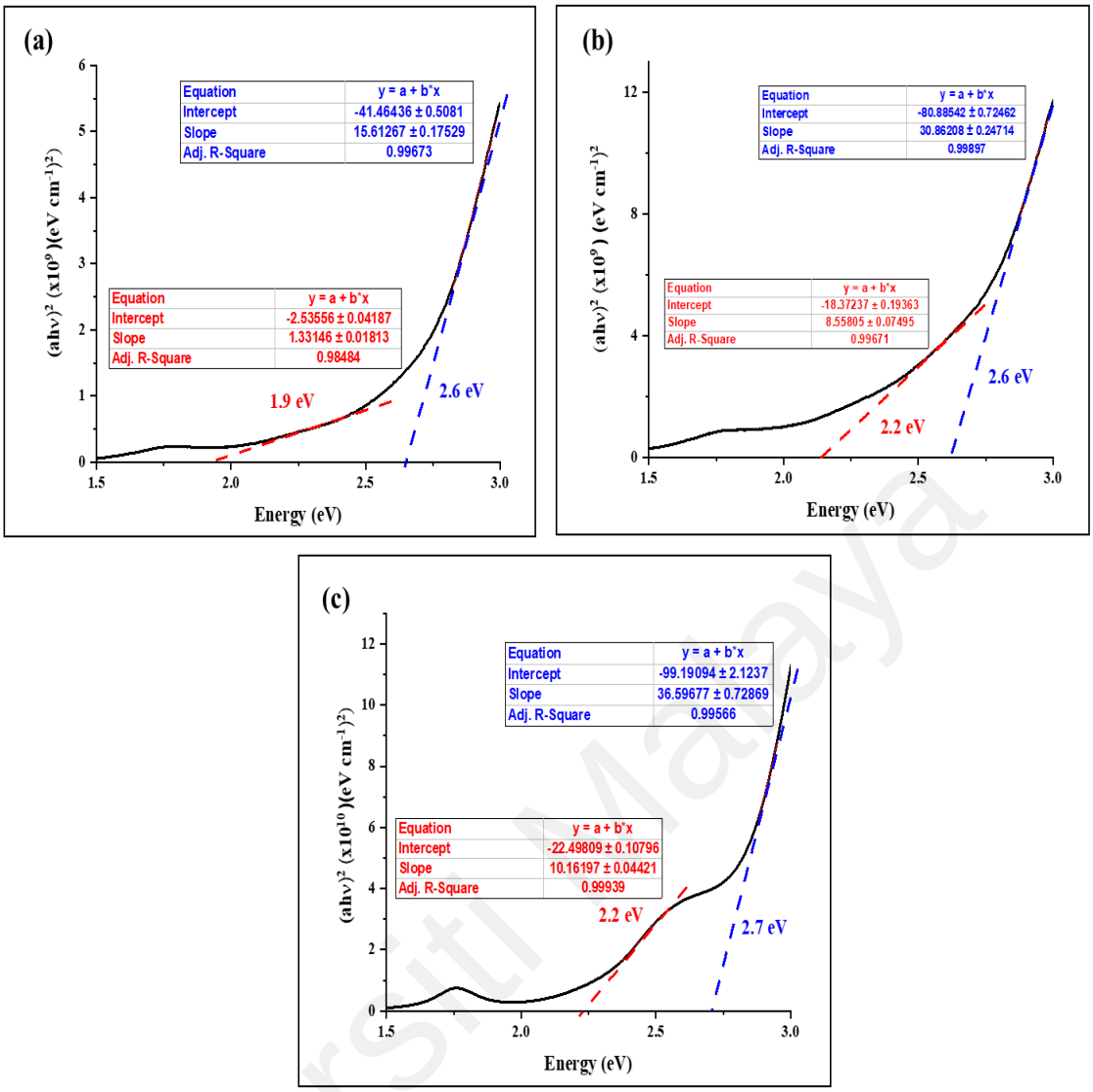

Figure 4.86: The Tauc plots for the (a) 10 mL/10 mins, (b) 15 mL/15 mins and (c) 20 mL/20 mins films fabricated at 450 °C.

4.6.8 Electrochemical Studies

The electrochemical studies were performed on the 10 mL/10 mins, 15 mL/15 mins and 20 mL/20 mins films fabricated at 450 °C in the alkaline media prepared by mixing 4.878 g (0.25M) of Na_2S and 11.03 g (0.35M) of Na_2SO_3 (pH 11.71) in deionised water. Before analysis, the electrolyte was purged with nitrogen gas for 15 minutes and stirred to eliminate the oxygen effects. CV curves are shown in Fig. 4.87. 5 cycles of CV scans were performed on the films at the scan rate of 0.1 V/s and changes in the curve position were observed for the films in alkaline media. There were no E_{ox} and E_{red}

Universiti Malaya

observed in the CV curves indicating that redox reaction was not observed for the films under the potential window of -0.6 to 0.6 V vs. Ag/AgCl.

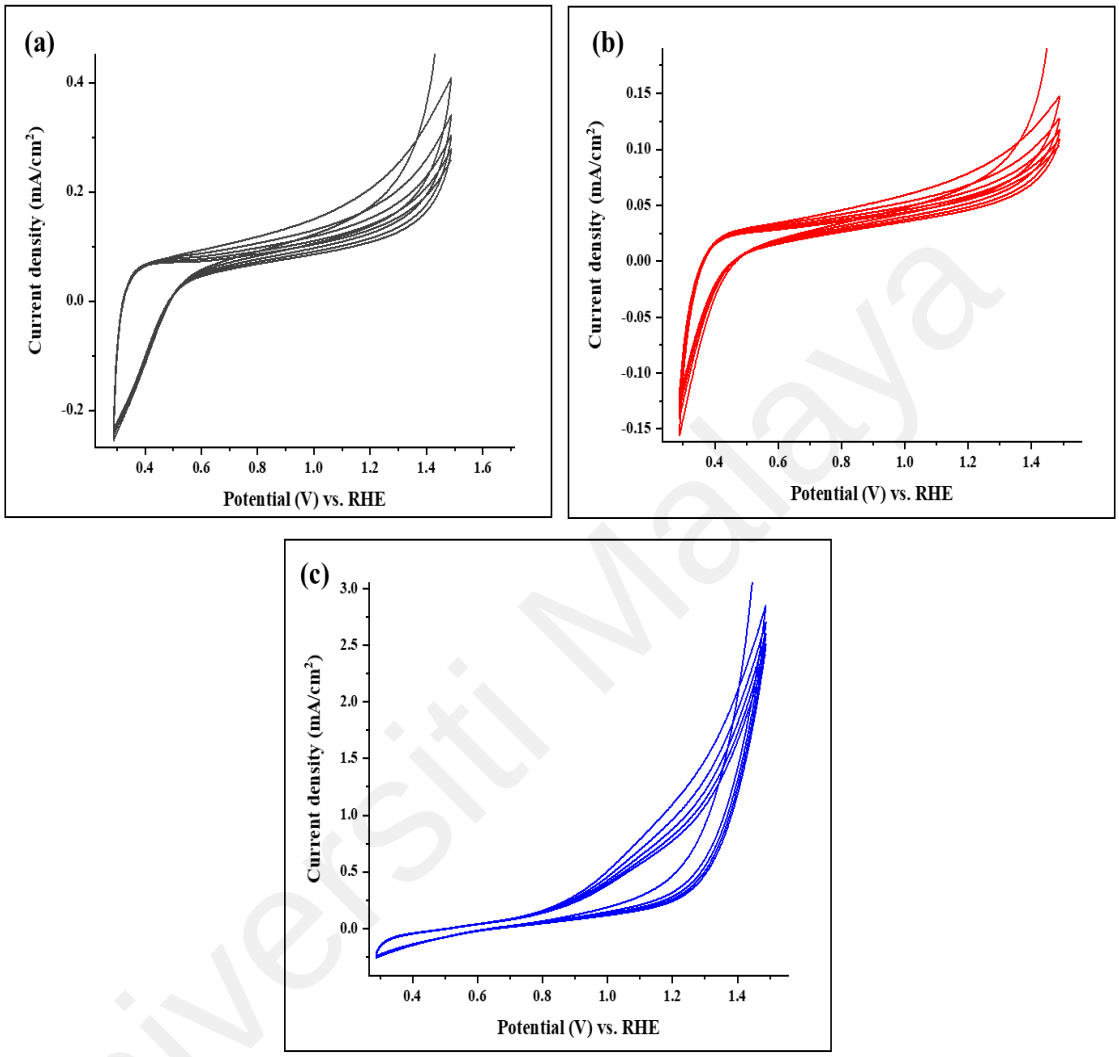

Figure 4.87: CV curves for the (a) 10 mL/10 mins, (b) 15 mL/15 mins and (c) 20 mL/ 20 mins films fabricated at 450 °C.

Based on the LSV analyses with the potential window from 0.4 to 1.5 V vs. RHE, the oxygen evolution reaction (OER) was the more prominent water splitting reaction in alkaline media just as HER was very prominent in acidic media for the films. Based on the *J-V* curves shown in Fig. 4.88 (a), the 20 mL/20 mins film fabricated at 450 °C exhibited the best performance with overpotential of 1.14 V vs. RHE to generate the current density of 1 mA/cm^2. The Tafel plots were generated from the *J-V* plots obtained

Universiti Malaya

from LSV analysis and are displayed in Fig. 4.88 (b). The Tafel slopes were determined for the OER reaction, and it was found that 20 mL/20 mins had the smallest Tafel slope of 190 mV/dec compared with 10 mL/10 mins and 15 mL/15 mins films. 20 mL/20 mins film had exhibited the fastest rate in OER process in alkaline condition.

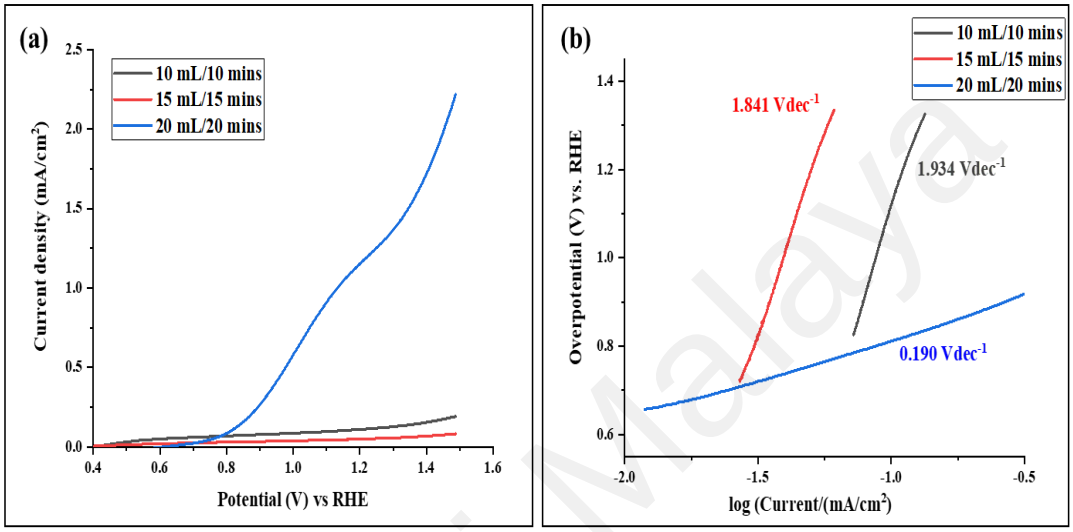

Figure 4.88: (a) LSV curves for the films fabricated at 450 °C and the (b) respective Tafel plots for the films.

Based on the MS plots displayed in Fig. 4.89, the slopes $[\frac{d(\frac{1}{c^2})}{dV}]$ for the films were determined and electron densities were calculated by using Eq. 4.6 and are displayed in Table 4.24. For the calculations of electron densities, the relative dielectric constant, ε_r was assumed to be 10 because it is usually slightly above or below this value (Chen et al., 2013). The films exhibited positive slopes indicating n-type conductivity which showed that the electrons were the majority charge carriers. The calculations indicated that 20 mL/20 mins film had the highest electron density, with the value of 9.75×10^{21} cm^{-3}.

Universiti Malaya

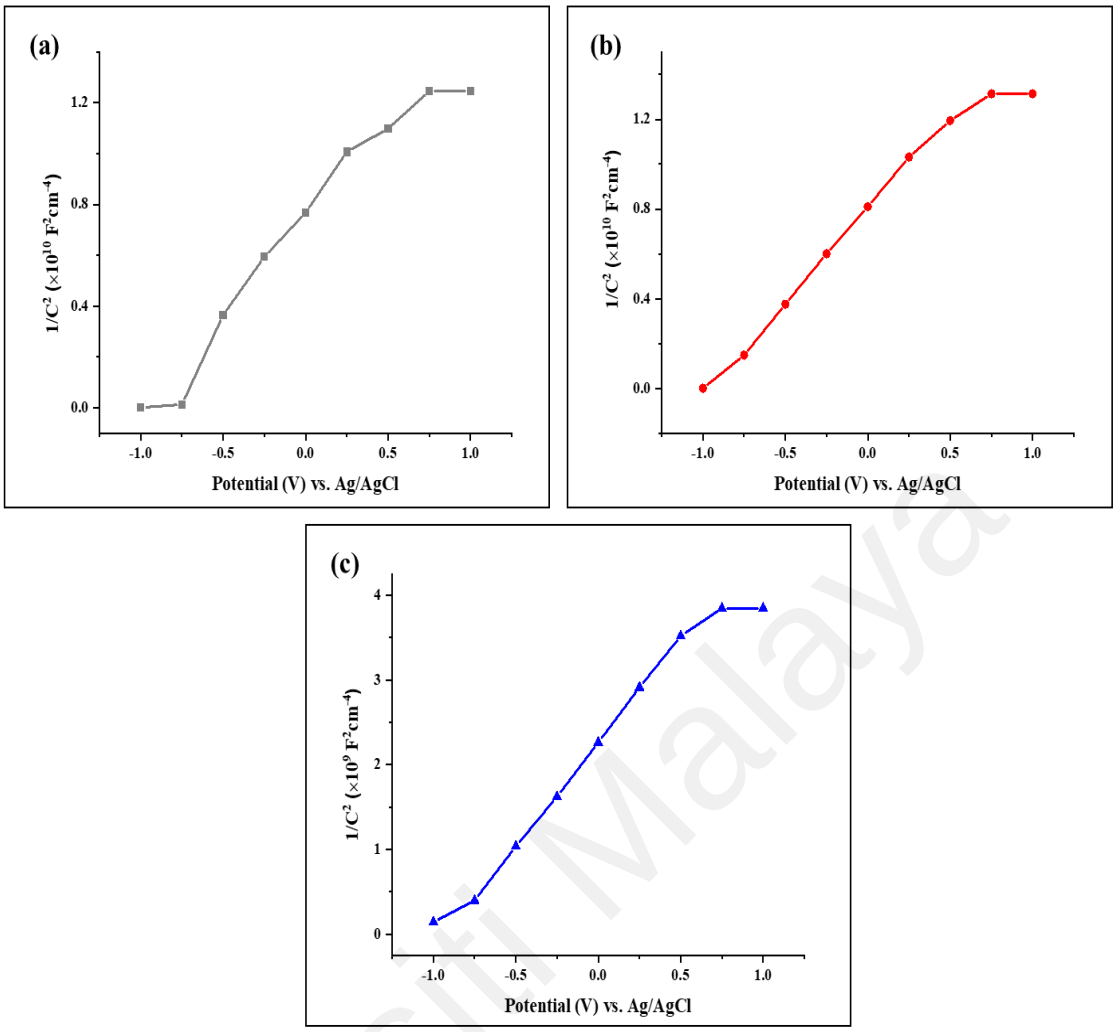

Figure 4.89: MS plots of 10 mL/10 mins (a), 15 mL/15 mins (b) and 20 mL/20 mins (c) films fabricated at 450 °C in applied potential from -1.0 to 1.0 vs Ag/AgCl reference electrode.

Table 4.24 MS slopes and electron densities of the films fabricated at 450 °C.

Films	Area (cm^2)	Slope of MS plot, $\left[\frac{d\left(\frac{1}{C^2}\right)}{dV}\right]$ (F^2V^{-1})	Donor density, N_d (cm^{-3})
10 mL/10 mins	1.10	0.797×10^{10}	1.47×10^{21}
15 mL/15 mins	1.10	0.790×10^{10}	1.48×10^{21}
20 mL/20 mins	0.80	2.276×10^{9}	9.75×10^{21}

The electrochemical impedance spectroscopy (EIS) of the films fabricated at 450 ºC deposition temperature was analyzed in the frequency range from 0.01 Hz to 100,000 Hz at a fixed potential. Nyquist plots and Bode plots are displayed in Fig. 4.90. Based on

Universiti Malaya

the diameters of the semicircular curves for the films in the Nyquist plot in Fig. 4.90 (a), the increasing charge transport resistance R_{CT} was arranged in the order of 10 mL/10 mins < 15 mL/15 mins < 20 mL/20 mins. Interestingly, the increasing trend in donor density of the films was observed with increasing R_{CT}. The increasing R_{CT} was resulted from the decrease in charge mobility. Therefore, it could be qualitatively determined that the charge mobility was the lowest in 20 mL/20 mins film due to the largest mean particle size compared with other films. However, the film exhibited the best OER performance whereas the other films which had lower charge transport resistance exhibited poorer OER activity. It was suggested that holes were most available in 20 mL/20 mins films for OER process. The low electron mobility possibly caused the hole-electron recombination to be hindered and hence more holes were available to catalyse OER.

Bode plots as displayed in Fig. 4.90 (b) were obtained to determine the lifetimes, τ of the films by using the formula, $\tau = 1/ (2\pi\nu)$. The frequency maxima and the lifetimes of the films fabricated at 450 °C are displayed in Table 4.25. The lifetimes from shortest to longest was in the order of 10 mL/10 mins < 15 mL/15 mins < 20 mL/20 mins. 20 mL/20 mins film had the longest lifetime because the electron-hole recombination was minimal. The shorter lifetime for 10 mL/10 mins and 15 mL/15 mins films was due to higher electron mobility (low transport resistance) which increased the probability for electron-hole recombination. The inherent properties (Tafel slope and R_{CT}) of the films are displayed in Table 4.26.

Universiti Malaya

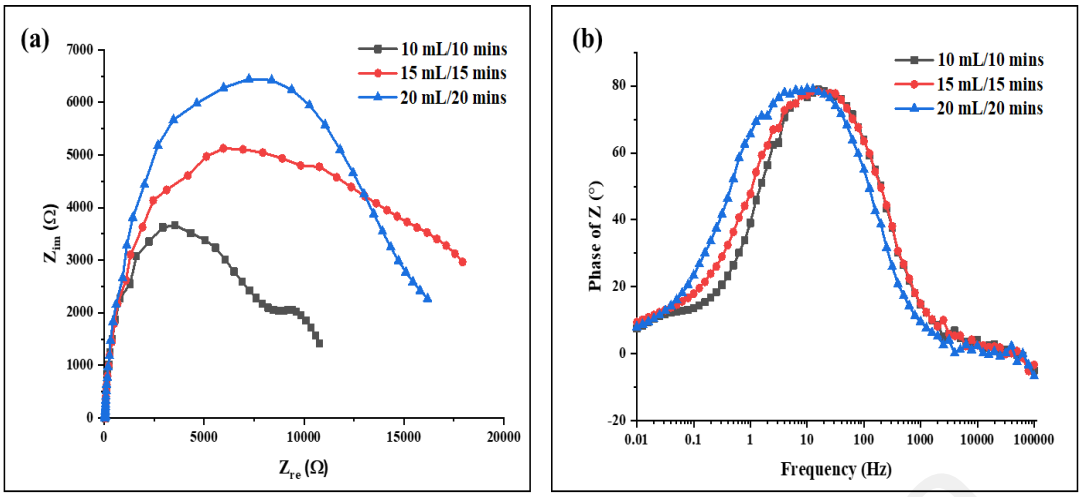

Figure 4.90: Nyquist plots (a) and Bode plots (b) of the films fabricated at 450 °C.

Table 4.25: The Frequency maxima and lifetime of the fabricated films.

Films	Frequency Maxima (Hz)	Lifetime $\tau = 1/(2\pi\nu)$ (ms)
10 mL/10 mins	1.74	91.5
15 mL/15 mins	1.52	104.7
20 mL/20 mins	1.00	159.2

Table 4.26: Inherent properties of the films fabricated at 450 °C.

Films	Tafel slope, b (mVdec^{-1})	Charge transfer resistance, R_{CT} (kΩ)
10 mL/10 mins	1934	6.97
15 mL/15 mins	1841	9.35
20 mL/20 mins	190	11.9

4.7 Mechanism of HER Process in Acidic Media

HER can be described in two ways, hydroxonium ion reduction and water reduction as shown in the following (Shinagawa et al., 2015);

$$2H_3O^+ + 2e^- \rightleftharpoons H_2 + 2H_2O \text{ (Hydroxonium ion reduction)}$$

$$2H_2O + 2e^- \rightleftharpoons H_2 + 2OH^- \text{ (Water reduction)}$$

Universiti Malaya

Tafel slopes were used to determine the reaction mechanism for HER and compare the performance of the electrocatalysts. The hydronium ion reduction reaction involves three steps, Volmer, Heyrovsky and Tafel step as described in the following (Shinagawa et al., 2015);

$$H_3O^+ + e^- \rightarrow H_{ad} + H_2O \text{ (Volmer step)}$$

$$H_3O^+ + e^- + H_{ad} \rightarrow H_2 + H_2O \text{ (Heyrovsky step)}$$

$$2H_{ad} \rightarrow H_2 \text{ (Tafel step)}$$

The Tafel slopes for all the films were found to be more than or close to 120 mV/dec indicating that the rate determining step in HER catalysed by the Mo_2S_3/MoP_2 films was Volmer step which is the hydrogen atom adsorption step in the acidic media. It is widely accepted that the minimum Tafel slopes for Volmer, Heyrovsky and Tafel reactions are 120, 40 and 30 mV/dec^{-1}, respectively (Shinagawa et al., 2015).

Hydrogen desorption process occurs at the catalyst surface as described by either the Heyrovsky or Tafel steps. In the acidic media, electrons flow from the electrocatalyst to the counter electrode which is a platinum wire and subsequently reduce hydroxonium ions to form hydrogen atoms which were adsorbed onto the surface of the electrocatalyst. The adsorbed hydrogen atoms would then be released as hydrogen gas following the processes known as the Heyrovsky reaction and Tafel reaction which happened in parallel (Wu et al., 2016).

The Mo_2S_3/MoP_2 provide active sites for hydrogen adsorption and desorption in HER. The interaction between Mo_2S_3 and MoP_2 renders both adsorption and desorption steps feasible in HER. The high electron mobility in Mo_2S_3 structure enables the effective reduction of hydroxonium ions to form hydrogen atoms which were then adsorbed onto the catalyst surface. The altered ΔG_{H*} as a result of interaction between sulphur and

Universiti Malaya

phosphorus in Mo_2S_3/MoP_2 composite had leads to desorption of hydrogen atoms to produce H_2 (Wu et al., 2018). From the study linking morphology and electrochemical analysis, the wide distribution of MoP_2 grains and high contact of the grain with Mo_2S_3 nanoparticles provide the films with favourable synergistic effect for efficient catalytic performance in HER based on the mechanism described above.

4.8 Mechanism of OER Process in Alkali Media

Water splitting can also occur in alkaline media. Besides HER, oxygen evolution reaction (OER) also occurs at the electrocatalyst**.** In OER, the electrocatalyst exhibits excellent performance for generation of oxygen in alkaline media (Wu et al., 2017). Compared to acidic media, the alkaline media can include a more broadened range of earth-abundant materials as OER electrocatalysts (Hu et al., 2019). In this study, we attempted to study the OER performance by the fabricated Mo_2S_3/MoP_2 films in alkaline media.

For the n-type semiconductor like the Mo_2S_3/MoP_2, electrons and holes are the majority and minority charge carriers, respectively. Holes are formed when external voltage is applied to excite the electrons from valence band (VB) to the conduction band (CB). Electrons are the key charge carriers for HER and holes participate in OER reaction by accepting the electrons from the electrolyte after the excitation of electrons for HER. This process in alkaline media is described in the in the following equation.

$$2OH^- \rightarrow \frac{1}{2}O_2 + H_2O + 2e^- \qquad (4.7)$$

Based on the MS analyses for the films fabricated at 450 °C (Refer to Fig. 4.89), electrons were the main charge carriers, but the HER reaction became less prominent in alkaline media. The hydroxonium ions have weaker coordinate bond than the covalent bond of water molecules. Therefore, the HER kinetics are more feasible in acidic than in

Universiti Malaya

alkaline and neutral media (Feng et al., 2019). In alkaline media, the strong adsorption of OH^- species may lead to higher overpotential for HER reaction and hence OER becomes more favourable (Hu et al., 2019). Based on the LSV analyses (Refer to Fig. 4.88 (a)), OER was more prominent in alkaline media.

4.9 Mechanism of Electron Transfer

The mechanism of the electron transfer was also studied. The band position was calculated based on the reported studies carried out by Dong et al. (Dong et al., 2014). The theoretical valence band edge potential (E_{VB}) and conduction band edge potential (E_{CB}) of a semiconductor was calculated by using equations shown as Eq. 4.8 and 4.9.

$$E_{CB} = X - E_C - 0.5E_g \quad (4.8)$$

$$E_{VB} = E_{CB} + E_g \quad (4.9)$$

In Eq. 4.8, X is the electronegativity of the semiconductor and E_C is the energy of free electron in hydrogen scale which is 4.5 eV. E_g is the band gap of the semiconductor. The electronegativity of the individual element was calculated by using the equation shown in Eq. 4.10.

$$X_{element} = 0.5(E_{EA} + E_{ion}) \quad (4.10)$$

From Eq. 4.9, both E_{EA} and E_{ion} are the electron affinities and first ionization energies of the individual elements of the materials e.g., Mo and S as in Mo_2S_3 and Mo and P as in MoP_2, respectively. The calculations for the electronegativity of individual elements are shown in Table 4.27.

Universiti Malaya

Table 4.27: Calculations for the electronegativity of Mo_2S_3 and MoP_2.

Materials	Mo_2S_3	MoP_2
E_{EA} (eV)	0.747 (Mo) 2.073 (S)	0.747 (Mo) 0.746 (P)
E_{ion} (eV)	7.092 (Mo) 10.360 (S)	7.092 (Mo) 10.487 (P)
$X_{element}$ (eV)	3.920 (Mo) 6.217 (S)	3.920 (Mo) 5.616 (P)

With the calculated electronegativity of individual elements, the electronegativity of the overall materials can be determined. The calculation showed that Mo_2S_3 has larger electronegativity than MoP_2. It had been reported that the valence band (VB) and conductive band (CB) of the MoP_2 overlapped and the bandgap was actually the energy difference between VB and the band below VB rather than between VB and CB as in typical semiconductors (Wu et al., 2015). The band below the valence band for MoP_2 was taken as normal valence band in constructing the energy diagram for HER. The overall electronegativity of the Mo_2S_3 and MoP_2 were calculated by using Eq. 4.11 and 4.12, which takes into account the electronegativity of each element.

$$X_{Mo_2S_3} = (X_{Mo} \times X_{Mo} \times X_S \times X_S \times X_S)^{\frac{1}{n}} \qquad (4.11)$$

$$X_{Mo_2S_3} = (3.920^2 \times 6.217^3)^{\frac{1}{5}} = 5.17 \text{ eV}$$

$$X_{MoP_2} = (X_{Mo} \times X_P \times X_P)^{\frac{1}{n}} \qquad (4.12)$$

$$X_{MoP_2} = (3.920 \times 5.616^2)^{\frac{1}{3}} = 4.98 \text{ eV}$$

By using Eq. 4.8 and Eq. 4.9, both the conduction, E_{CB}, and valence, E_{VB} bands were calculated as shown in the following.

$$E_{CB} = X - E_C - 0.5E_g$$

$$E_{CB(Mo_2S_3)} = 5.17 \text{ eV} - 4.5 \text{ eV} - 0.5(2.3) \text{ eV} = -0.48 \text{ eV}$$

Universiti Malaya

$$E_{CB(MoP_2)} = 4.98\ eV - 4.5\ eV - 0.5(2.8)\ eV = -0.92\ eV$$

$$E_{VB} = E_{CB} + E_g$$

$$E_{VB(Mo_2S_3)} = -0.48\ eV + 2.3\ eV = 1.82\ eV$$

$$E_{VB(MoP_2)} = -0.92\ eV + 2.8\ eV = 1.88\ eV$$

The calculated E_{CB} and E_{VB} were used to construct the electron transfer process of the Mo_2S_3/MoP_2 heterostructure material as shown in Fig. 4.91. The E_{CB} and E_{VB} of FTO glass substrate at room temperature reported to be -0.54 and 2.89 eV, respectively and the band gap was very large ($E_g = 3.43$ eV) (Carrera-Crespo et al., 2021). The band gaps of Mo_2S_3 and MoP_2 were 2.3 and 2.8 eV, respectively and the resulting heterostructure provides both the valence and conduction bands within the band position of FTO glass substrate to enhance electron transport as illustrated in Fig. 4.91.

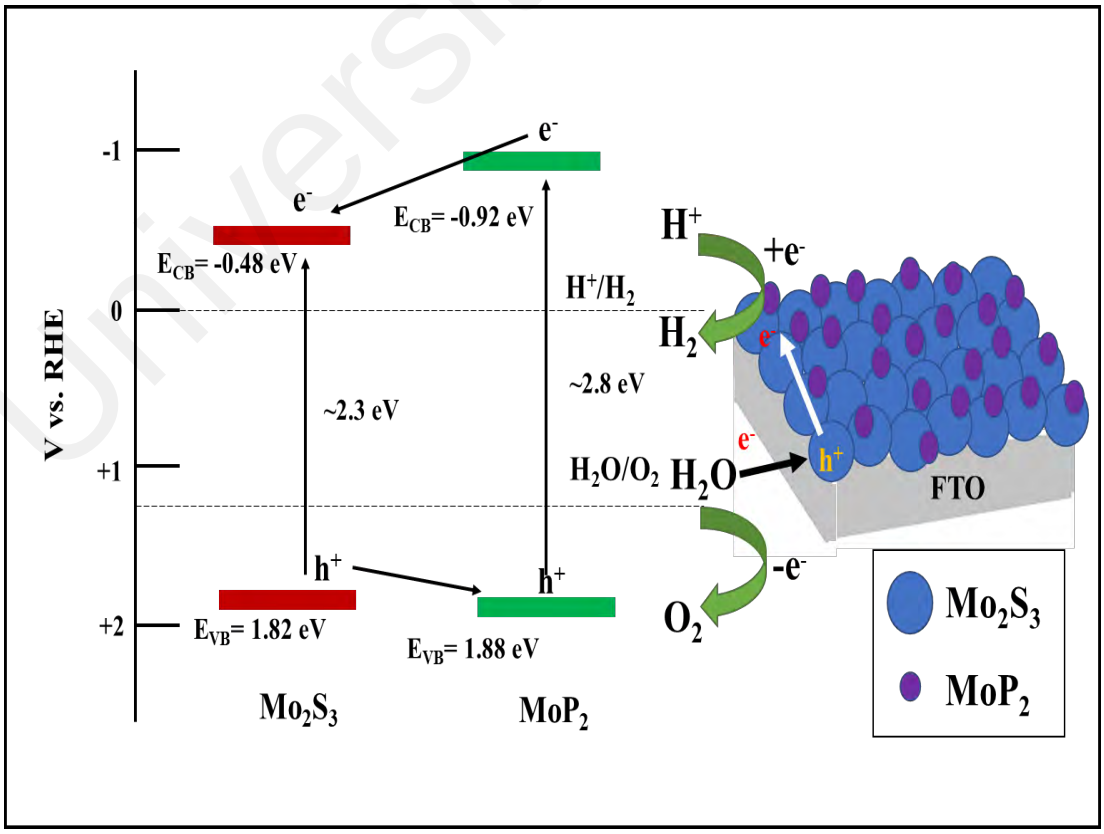

Figure 4.91: Electron transfer process in Mo_2S_3/MoP_2 heterostructure for overall water splitting process.

Universiti Malaya

In acidic media, the Mo_2S_3/MoP_2 provides the lower conduction bands which accepts electrons to reduce the protons into hydrogen atoms. The heterostructure provides favourable band positions which enables the electron flow to occur in tandem between the two materials, which leads to enhanced electrocatalytic performance. In alkaline media, the creation of holes after the excitation of electrons by external voltage can receive electrons from the OH^- species and the species become oxidised to generate oxygen. Finally, the synergistic effect caused by the electronic interaction between Mo_2S_3 and MoP_2 provides larger number of excited electrons which will enhance electrocatalytic water-splitting mechanism of the final heterostructure.

Universiti Malaya

CHAPTER 5: CONCLUSION

5.1 Conclusion

The new composite material, Mo_2S_3/MoP_2 was fabricated by AACVD using a single precursor solution prepared by dissolving the as-synthesized complex **1** in THF. The electrocatalytic performance of the Mo_2S_3/MoP_2 composite materials had not been studied. In this study, it was found that the key factor towards producing the desirable films was modulation of fabrication parameters such as the carrier gas flow rate, deposition time, temperature, and volume of the precursor solution, respectively. The changes in these parameters could result in different compositions (Mo_2S_3 and MoP_2), as well as morphological and topological characteristics such as particle size, film thickness and overall distribution of particles on the film's surface which are crucial for efficient electron transport that determines the overall electrocatalytic performance. This work possessed significant novelty as the fabrication method and the electrochemical studies of the new Mo_2S_3/MoP_2 composite material were the hallmarks of the studies. From the electrochemical studies in acidic media with pH 0.95, all the Tafel slopes were found to be more than and close to 120 mV/dec. Therefore, Volmer reaction or the reduction of protons and adsorption of hydrogen atoms on the catalytic surface was the rate determining step for HER process. From the study involving alkaline media with pH 11.71, OER was more prominent than HER and the film with rich numbers of holes exhibited high OER performance. This study provided insights on the resultant morphology of the films obtained from various synthesis conditions leading to their intrinsic properties of the films such as onset potential, charge transport resistance, exchange current density, charge donor density as well as the electron lifetime. The

Universiti Malaya

overall physical properties and intrinsic parameters of the highest performing films from each of the studied synthesis conditions are displayed in Table 5.1 and 5.2, respectively.

Table 5.1: Physical properties of the highest performing films from each AACVD condition.

Volume/Time	Flow rate (SCFH)	Temperature (°C)	Mean particle size (nm)	R_q (nm)	Thickness (nm)
20 mL/30 mins	0.3	550	1000-3000	106.4	968
15 mL/15 mins	0.5	550	400-800	12.9	436
15 mL/15 mins	0.5	450	101-150	43.7	438
20 mL/20 mins	0.5	450	500-1500	36.4	317

Table 5.2: Inherent properties of the highest performing films from each AACVD condition.

Films	pH	Onset potential (mV)	N_d (cm^{-3})	Tafel slope (mV/dec)	j_o (mA/cm^2)	R_{CT} (kΩ)	τ (ms)
20 mL/30 mins	0.95	93	5.52×10^{19}	123.4	0.408	0.715	40
15 mL/15 mins (550 °C)	0.95	258	1.80×10^{21}	120.7	0.018	5.18	71
15 mL/15 mins (450 °C)	0.95	223	5.14×10^{20}	83.7	0.004	8.35	49
20 mL/20 mins	11.71	1140	9.75×10^{21}	190.0	0.099	11.9	159

Based on Table 5.1, it is shown that larger volume of precursor solution as well as higher deposition temperature encouraged the growth of larger particles. Although too large surface roughness and film thickness may result in high transport resistance of the charge carriers but a balance between the two parameters can be achieved to enhance electrocatalytic performance of the films. For instance, 20 mL/30 mins film had the largest particle size compared with other films as shown in Table 5.1. However, the larger film thickness seemed to have mitigated the negative effect of the large particle size in

Universiti Malaya

electrocatalytic performance. The large surface roughness of the 20 mL/30 mins film had led to enhanced exposure of active sites for catalysing HER. 20 mL/30 mins film fabricated at 550 °C which generated the most current density for catalysing HER reaction as indicated by the lowest onset potential and the highest exchange current density, j_o. The highest conductivity of the film as indicated by the lowest charge transport resistance, R_{CT} was the key property of electron transport for generation of high current density. 15 mL/15 mins film prepared at 450 °C exhibited the fastest rate of reaction in HER process as indicated by its smallest Tafel slope in acidic media. It was also shown that the films which exhibited high performance in water splitting process had short lifetime which was the setback for the Mo_2S_3/MoP_2 composite materials that were fabricated in our study.

Based on Table 5.2, large donor density led to the long lifetime because the amount of charge carriers available for water splitting process was large. Therefore, the most suitable AACVD condition has to be determined to produce the films with desired performance for water splitting application as well as having a favorably long lifetime. The very high onset potential and Tafel slope exhibited by 20 mL/20 mins fabricated at 450 °C showed that the Mo_2S_3/MoP_2 composite material may not be a suitable electrocatalyst for OER process but the electrocatalytic performance in alkaline media of films fabricated from other AACVD conditions had not been studied yet. It was demonstrated that the good distribution of grains over the film surface promote enhanced interaction between Mo_2S_3 and MoP_2 which was the desired advantage for efficient charge carrier transport resulting from the synergistic effect between the two materials as illustrated in Fig. 4.91 for water splitting application. The inherent properties of the film are the important determining factors that influence the efficiency of the electrocatalyst.

Universiti Malaya

5.2 Future works

In this study, we have demonstrated the electrocatalytic performance of Mo_2S_3/MoP_2 composite material fabricated from different synthesis conditions. For future study, we will continue to explore the electrocatalytic water-splitting performance of molybdenum sulphides doped with other Group V elements such as antimony (Sb). The aim is to synthesize an antimony incorporated molybdenum organometallic complex to be applied as a precursor material for AACVD. The antimony-based compound such as antimony triselenide (Sb_2Se_3) has promising optoelectrical properties (e.g., the ability to absorb sunlight) (Tan et al., 2018). Therefore, it is of our interest to explore the photoelectrochemical properties of the antimony doped molybdenum sulphide materials in future.

Universiti Malaya

REFERENCES

Abdel-Karim, R., Halim, J., El-Raghy, S., Nabil, M., & Waheed, A. (2012). Surface morphology and electrochemical characterization of electrodeposited Ni–Mo nanocomposites as cathodes for hydrogen evolution. *Journal of Alloys and Compounds, 530*, 85-90.

Ahmad, H., Kamarudin, S., Minggu, L., & Kassim, M. (2015). Hydrogen from photo-catalytic water splitting process: A review. *Renewable and Sustainable Energy Reviews, 43*, 599-610.

Al-Dulaimi, N., Lewis, E. A., Savjani, N., McNaughter, P. D., Haigh, S. J., Malik, M. A., . . . O'Brien, P. (2017). The influence of precursor on rhenium incorporation into Re-doped MoS_2 ($Mo_{1-x}Re_xS_2$) thin films by aerosol-assisted chemical vapour deposition (AACVD). *Journal of Materials Chemistry C, 5*(35), 9044-9052.

Anantharaj, S., Karthik, P. E., Subramanian, B., & Kundu, S. (2016). Pt nanoparticle anchored molecular self-assemblies of DNA: an extremely stable and efficient HER electrocatalyst with ultralow Pt content. *ACS Catalysis, 6*(7), 4660-4672.

Ariffin, S., Lim, H., Talib, Z., Pandikumar, A., & Huang, N. (2015). Aerosol-assisted chemical vapor deposition of metal oxide thin films for photoelectrochemical water splitting. *International journal of hydrogen energy, 40*(5), 2115-2131.

Ayal, A. K., Zainal, Z., Lim, H.-N., Talib, Z. A., Lim, Y.-C., Chang, S.-K., . . . Amin, W. N. M. (2016). Electrochemical deposition of CdSe-sensitized TiO_2 nanotube arrays with enhanced photoelectrochemical performance for solar cell application. *Journal of Materials Science: Materials in Electronics, 27*(5), 5204-5210.

Bo, L., Pu, L., Hu, Y., Nian, F., Zhang, Z., Li, P., & Tong, J. (2022). Hydrangea like composite catalysts of ultrathin Mo_2S_3 nanosheets assembled on N, S-dual-doped graphitic biocarbon spheres with highly electrocatalytic activity for HER. *International Journal of Hydrogen Energy, 47*(10), 6700-6709.

Bozheyev, F., An, V. V., & Irtegov, Y. (2014). Properties of copper and molybdenum sulfide powders produced by self-propagating high-temperature synthesis. *Advanced Materials Research, 872*, 191-196.

Bradlyn, B., Elcoro, L., Cano, J., Vergniory, M. G., Wang, Z., Felser, C., Aroyo, M. I., & Bernevig, B. A. (2017). Topological quantum chemistry. *Nature, 547*(7663), 298-305.

Carrera-Crespo, J., Fuentes-Camargo, I., Palma-Goyes, R., García-Pérez, U., Vazquez-Arenas, J., Chairez, I., & Poznyak, T. (2021). Unrevealing the effect of transparent

fluorine-doped tin oxide (FTO) substrate and irradiance configuration to unmask the activity of FTO-$BiVO_4$ heterojunction. *Materials Science in Semiconductor Processing, 128*, Article#105717.

Che, R., Bai, N., & Peng, L.-M. (2003). Structure and growth of monoclinic Mo_2S_3 nanorods. *Applied Physics Letters, 83*(17), 3561-3563.

Chen, Z., Deutsch, T. G., Dinh, H. N., Domen, K., Emery, K., Forman, A. J., . . . Jaramillo, T. F. (2013). Flat-Band Potential Techniques. In *Photoelectrochemical Water Splitting* (pp. 63-85): Springer.

Chen, Z., Jaramillo, T. F., Deutsch, T. G., Kleiman-Shwarsctein, A., Forman, A. J., Gaillard, N., . . . Sunkara, M. (2010). Accelerating materials development for photoelectrochemical hydrogen production: Standards for methods, definitions, and reporting protocols. *Journal of Materials Research, 25*(1), 3-16.

Curtis, M. D., & Klingler, R. J. (1978). Metal-metal multiple bonds: IV. The chemistry of bis (cyclopentadienyldicarbonyl-molybdenum)(Mo-Mo). *Journal of Organometallic Chemistry, 161*(1), 23-37.

Dai, C., Tian, X., Nie, Y., Tian, C., Yang, C., Zhou, Z., . . . Gao, X. (2017). Successful synthesis of 3D $CoSe_2$ hollow microspheres with high surface roughness and its excellent performance in catalytic hydrogen evolution reaction. *Chemical Engineering Journal, 321*, 105-112.

Deng, J., Li, H., Xiao, J., Tu, Y., Deng, D., Yang, H., . . . Bao, X. (2015). Triggering the electrocatalytic hydrogen evolution activity of the inert two-dimensional MoS_2 surface via single-atom metal doping. *Energy & Environmental Science, 8*(5), 1594-1601.

Dong, H., Chen, G., Sun, J., Feng, Y., Li, C., & Lv, C. (2014). Stability, durability and regeneration ability of a novel Ag-based photocatalyst, $Ag_2Nb_4O_{11}$. *Chemical Communications, 50*(50), 6596-6599.

Downes, C. A., Clough, A. J., Chen, K., Yoo, J. W., & Marinescu, S. C. (2018). Evaluation of the H2 evolving activity of benzenehexathiolate coordination frameworks and the effect of film thickness on H_2 production. *ACS Applied Materials & Interfaces, 10*(2), 1719-1727.

Edusi, C., Sankar, G., & Parkin, I. P. (2012). The effect of solvent on the phase of titanium dioxide deposited by aerosol-assisted CVD. *Chemical Vapor Deposition, 18*(4-6), 126-132.

Universiti Malaya

Ehsan, M. A., Ming, H. N., Misran, M., Arifin, Z., Tiekink, E. R., Safwan, A. P., . . . Mazhar, M. (2012). Effect of AACVD processing parameters on the growth of greenockite (CdS) thin films using a single-source cadmium precursor. *Chemical Vapor Deposition, 18*(7-9), 191-200.

Fan, L., Tu, Z., & Chan, S. H. (2021). Recent development of hydrogen and fuel cell technologies: A review. *Energy Reports, 7*, 8421-8446.

Feng, W., Pang, W., Xu, Y., Guo, A., Gao, X., Qiu, X., & Chen, W. (2020). Transition metal selenides for electrocatalytic hydrogen evolution reaction. *ChemElectroChem, 7*(1), 31-54.

Fereja, S. L., Li, P., Guo, J., Fang, Z., Zhang, Z., Zhuang, Z., . . . Chen, W. (2021). W-doped MoP nanospheres as electrocatalysts for pH-universal hydrogen evolution reaction. *ACS Applied Nano Materials, 4*(6), 5992-6001.

Frey, G. L., Tenne, R., Matthews, M. J., Dresselhaus, M., & Dresselhaus, G. (1999). Raman and resonance Raman investigation of MoS_2 nanoparticles. *Physical Review B, 60*(4), Article#2883.

Fronzi, M., Assadi, M. H. N., & Ford, M. J. (2018). Ab initio investigation of water adsorption and hydrogen evolution on Co_9S_8 and Co_3S_4 low-index surfaces. *ACS Omega, 3*(9), 12215-12228.

Guruprasad, K., Maiyalagan, T., & Shanmugam, S. (2019). Phosphorus doped MoS_2 nanosheet promoted with nitrogen, sulfur dual doped reduced graphene oxide as an effective electrocatalyst for hydrogen evolution reaction. *ACS Applied Energy Materials, 2*(9), 6184-6194.

Hamid, M., Tahir, A. A., Mazhar, M., Ahmad, F., Molloy, K. C., & Kociok-Kohn, G. (2008). Deposition and characterization of ZnO thin films from a novel hexanuclear zinc precursor. *Inorganica Chimica Acta, 361*(1), 188-194.

Hankare, P., Manikshete, A., Sathe, D., Chate, P., Patil, A., & Gardkar, K. (2009). A novel route of synthesis of WS_2 thin film and its characterization. *Journal of Crystal Growth, 311*(13), 3386-3388.

Hernández-Salcedo, P., Amézaga-Madrid, P., Monárrez-Cordero, B., Antúnez-Flores, W., Pizá-Ruiz, P., Leyva-Porras, C., . . . Miki-Yoshida, M. (2015). Theoretical and experimental influence of aerosol assisted CVD parameters on the microstructural properties of magnetite nanoparticles and their response on the removal efficiency of arsenic. *Journal of Alloys and Compounds, 643*, S287-S296.

Universiti Malaya

Higgins, E. P., Papaderakis, A. A., Byrne, C., Walton, A. S., Lewis, D. J., & Dryfe, R. A. (2021). Intrinsic effects of thickness, surface chemistry and electroactive area on nanostructured MoS_2 electrodes with superior stability for hydrogen evolution. *Electrochimica Acta, 382*, Article#138257.

Hu, C., Zhang, L., & Gong, J. (2019). Recent progress made in the mechanism comprehension and design of electrocatalysts for alkaline water splitting. *Energy & Environmental Science, 12*(9), 2620-2645.

Jaramillo, T. F., Jørgensen, K. P., Bonde, J., Nielsen, J. H., Horch, S., & Chorkendorff, I. (2007). Identification of active edge sites for electrochemical H_2 evolution from MoS_2 nanocatalysts. *Science, 317*(5834), 100-102.

Jin, X., Tian, R., Wu, A., Xiao, Y., Dong, X., Hu, F., & Huang, H. (2020). Lithium-ion storage in molybdenum phosphides with different crystal structures. *Dalton Transactions, 49*(7), 2225-2233.

Jirkovský, J., Makarova, M., & Krtil, P. (2006). Particle size dependence of oxygen evolution reaction on nanocrystalline RuO_2 and $Ru_{0.8}Co_{0.2}O_{2-x}$. *Electrochemistry Communications, 8*(9), 1417-1422.

Jlidi, Z., Baachaoui, S., Raouafi, N., & Ridene, S. (2021). Temperature effect on structural, morphological and optical properties of 2D-MoS_2 layers: An experimental and theoretical study. *Optik, 228*, Article#166166.

Joy, J., Mathew, J., & George, S. C. (2018). Nanomaterials for photoelectrochemical water splitting–review. *International Journal of Hydrogen Energy, 43*(10), 4804-4817.

Jun, S. E., Choi, S., Choi, S., Lee, T. H., Kim, C., Yang, J. W., . . . Jang, H. W. (2021). Direct synthesis of molybdenum phosphide nanorods on silicon using graphene at the heterointerface for efficient photoelectrochemical water reduction. *Nano-micro Letters, 13*(1), 1-16.

Kaur, N., Bhullar, V., Singh, D. P., & Mahajan, A. (2020). Bimetallic implanted plasmonic photoanodes for TiO_2 sensitized third generation solar cells. *Scientific Reports, 10*(1), 1-15.

Ketchemen, K. I., Mlowe, S., Nyamen, L. D., Ndifon, P. T., Revaprasadu, N., & O'Brien, P. (2018). CdS thin films deposition by AACVD: effect of precursor type, decomposition temperature and solvent. *Journal of Materials Science: Materials in Electronics, 29*(17), 14462-14470.

Universiti Malaya

Khoo, C. Y., Liu, H., Sasangka, W. A., Made, R. I., Tamura, N., Kunz, M., . . . Thompson, C. V. (2016). Impact of deposition conditions on the crystallization kinetics of amorphous GeTe films. *Journal of Materials Science, 51*(4), 1864-1872.

Kibler, L. A. (2008). Dependence of electrocatalytic activity on film thickness for the hydrogen evolution reaction of Pd overlayers on Au (1 1 1). *Electrochimica Acta, 53*(23), 6824-6828.

Kibsgaard, J., & Jaramillo, T. F. (2014). Molybdenum phosphosulfide: an active, acid-stable, earth-abundant catalyst for the hydrogen evolution reaction. *Angewandte Chemie International Edition, 53*(52), 14433-14437.

Kim, E., Kim, S., Choi, Y. M., Park, J. H., & Shin, H. (2020). Ultrathin hematite on mesoporous WO3 from atomic layer deposition for minimal charge recombination. *ACS Sustainable Chemistry & Engineering, 8*(30), 11358-11367.

Kochuveedu, S. T. (2016). Photocatalytic and photoelectrochemical water splitting on TiO_2 via photosensitization. *Journal of Nanomaterials, 2016*, 1-12.

Kudo, A., & Kato, H. (2000). Effect of lanthanide-doping into $NaTaO_3$ photocatalysts for efficient water splitting. *Chemical Physics Letters, 331*(5-6), 373-377.

Kumar, P., & Rao, G. K. (2020). The effect of precursor concentration and post-deposition annealing on the optical and micro-structural properties of SILAR deposited SnO_2 films. *Materials Research Express, 7*(1), Article#016428.

Kun, W. N., Mlowe, S., Nyamen, L. D., Akerman, M. P., O'brien, P., Ndifon, P. T., & Revaprasadu, N. (2018). Deposition of Bi_2S_3 thin films from heterocyclic bismuth (III) dithiocarbamato complexes. *Polyhedron, 154*, 173-181.

Lamb, J. J., & Austbø, B. (2020). Current use of bioenergy and hydrogen. In *Hydrogen, Biomass and Bioenergy* (pp. 9-20): Elsevier.

Lau, K. C., Ooi, M. L., Ooi, Z. X., Wong, R., Choong, Z. L., Mazhar, M., & Goh, B. T. (2022). Fabrication of Fe-doped molybdenum multisulfide MoS_2/Mo_2S_3 thin film via aerosol-assisted chemical vapor deposition (AACVD) for photoelectrochemical (PEC) water splitting. *Electrocatalysis, 13*(2), 182-194.

Universiti Malaya

Li, J., Li, M., & Jin, Z. (2022). ZIF-67 derived hierarchical hollow Co_3S_4@ Mo_2S_3 dodecahedron S-scheme surface heterostructure for efficient photocatalytic hydrogen evolution. *Catalysis Science & Technology, 12*, 1144-1158.

Li, J., Zhang, C., Ma, H., Wang, T., Guo, Z., Yang, Y., . . . Ma, H. (2021). Modulating interfacial charge distribution of single atoms confined in molybdenum phosphosulfide heterostructures for high efficiency hydrogen evolution. *Chemical Engineering Journal, 414*, Article#128834.

Li, W., Wang, C., & Lu, X. (2021). Integrated transition metal and compounds with carbon nanomaterials for electrochemical water splitting. *Journal of Materials Chemistry A, 9*(7), 3786-3827.

Liang, K., Pakhira, S., Yang, Z., Nijamudheen, A., Ju, L., Wang, M., . . . Feng, Z. (2018). S-doped MoP nanoporous layer toward high-efficiency hydrogen evolution in pH-universal electrolyte. *ACS Catalysis, 9*(1), 651-659.

Lim, C. E., Ooi, M. L., Wong, R., Neo, K. E., Mumtaz, A., Mazhar, M., . . . Saheed, M. S. M. (2019). Facile synthesis of molybdenum multisulfide composite nanorod arrays from single-source precursor for photoelectrochemical hydrogen generation. *Applied Nanoscience, 9*(6), 1281-1292.

Lin, Y.-K., Chen, R.-S., Chou, T.-C., Lee, Y.-H., Chen, Y.-F., Chen, K.-H., & Chen, L.-C. (2016). Thickness-dependent binding energy shift in few-layer MoS_2 grown by chemical vapor deposition. *ACS Applied Materials & Interfaces, 8*(34), 22637-22646.

Liu, P., Zhu, J., Zhang, J., Xi, P., Tao, K., Gao, D., & Xue, D. (2017). P dopants triggered new basal plane active sites and enlarged interlayer spacing in MoS_2 nanosheets toward electrocatalytic hydrogen evolution. *ACS Energy Letters, 2*(4), 745-752.

Luo, Y., Luo, N., Kong, W., Wu, H., Wang, K., Fan, S., . . . Wang, J. (2018). Multifunctional interlayer based on molybdenum diphosphide catalyst and carbon nanotube film for lithium–sulfur batteries. *Small, 14*(8), Article#1702853.

Ma, T. (2021). Effect of precursor concentration and sintering on functional properties of ZnO thin films deposited by aerosol-assisted chemical vapour deposition (AACVD). *Materials Science in Semiconductor Processing, 121*, Article#105413.

Merki, D., Vrubel, H., Rovelli, L., Fierro, S., & Hu, X. (2012). Fe, Co, and Ni ions promote the catalytic activity of amorphous molybdenum sulfide films for hydrogen evolution. *Chemical Science, 3*(8), 2515-2525.

Universiti Malaya

Minggu, L.J., Daud, W.R.W., & Kassim, M.B. (2010). An overview of photocells and photoreactors for photoelectrochemical water splitting. *International Journal of Hydrogen Energy*, *35*(11), 5233-5244.

Momose, T., Nakamura, A., Daniel, M., & Shimomura, M. (2018). Phosphorous doped p-type MoS_2 polycrystalline thin films via direct sulfurization of Mo film. *Aip Advances, 8*(2), Article#025009.

Nguyen, V. H., Nguyen, T. P., Le, T. H., Vo, D. V. N., Nguyen, D. L., Trinh, Q. T., . . . Le, Q. V. (2020). Recent advances in two-dimensional transition metal dichalcogenides as photoelectrocatalyst for hydrogen evolution reaction. *Journal of Chemical Technology & Biotechnology, 95*(10), 2597-2607.

Nishanthi, S., Yadav, K. K., Baruah, A., Ganguli, A. K., & Jha, M. (2019). New sustainable and environmental friendly process of synthesis of highly porous Mo_2S_3 nanoflowers in cooking oil and their electrochemical properties. *Electrochimica Acta, 300*, 177-185.

Niu, C., Zhu, T., & Lv, Y. (2019). Influence of surface morphology on absorptivity of light-absorbing materials. *International Journal of Photoenergy, 2019* (2), 1-9

Niu, X., Yu, Y., Yao, J., Li, M., Sha, J., & Wang, Y. (2021). Preparation of black phosphorus quantum dots and the surface decoration effect on the monolayer MoS_2 photodetectors. *Chemical Physics Letters, 772*, Article#138571.

Ouyang, C., Wang, X., & Wang, S. (2015). Phosphorus-doped CoS_2 nanosheet arrays as ultra-efficient electrocatalysts for the hydrogen evolution reaction. *Chemical Communications, 51*(75), 14160-14163.

Palgrave, R. G., & Parkin, I. P. (2007). Aerosol assisted chemical vapor deposition of gold and nanocomposite thin films from hydrogen tetrachloroaurate (III). *Chemistry of Materials, 19*(19), 4639-4647.

Pan, Y., Liu, Y., Zhao, J., Yang, K., Liang, J., Liu, D., . . . Liu, C. (2015). Monodispersed nickel phosphide nanocrystals with different phases: synthesis, characterization and electrocatalytic properties for hydrogen evolution. *Journal of Materials Chemistry A, 3*(4), 1656-1665.

Pareek, A., Dom, R., Gupta, J., Chandran, J., Adepu, V., & Borse, P. H. (2020). Insights into renewable hydrogen energy: Recent advances and prospects. *Materials Science for Energy Technologies, 3*, 319-327.

Universiti Malaya

Patil, V., Shahane, G., & Deshmukh, L. (2003). Studies on photoelectrochemical (PEC) cells: A correlation between electrochemical and material properties. *Materials Chemistry and Physics, 80*(3), 625-631.

Rabi, O., Pervaiz, E., Zahra, R., Ali, M., & Niazi, M. B. K. (2020). An inclusive review on the synthesis of molybdenum carbide and its hybrids as catalyst for electrochemical water splitting. *Molecular Catalysis, 494*, Article#111116.

Rajamathi, C. R., Gupta, U., Kumar, N., Yang, H., Sun, Y., Süß, V., . . . Werner, P. (2017). Weyl semimetals as hydrogen evolution catalysts. *Advanced Materials, 29*(19), Article#1606202.

Saha, S., Kumar, J. S., Murmu, N. C., Samanta, P., & Kuila, T. (2018). Controlled electrodeposition of iron oxide/nickel oxide@ Ni for the investigation of the effects of stoichiometry and particle size on energy storage and water splitting applications. *Journal of Materials Chemistry A, 6*(20), 9657-9664.

Sathish, M., Viswanathan, B., & Viswanath, R. (2006). Alternate synthetic strategy for the preparation of CdS nanoparticles and its exploitation for water splitting. *International Journal of Hydrogen Energy, 31*(7), 891-898.

Seger, B., Herbst, K., Pedersen, T., Abrams, B., Vesborg, P. C., Hansen, O., & Chorkendorff, I. (2014). Mo_3S_4 clusters as an effective H_2 evolution catalyst on protected Si photocathodes. *Journal of The Electrochemical Society, 161*(12), Article#H722.

Seo, B., Jung, G. Y., Sa, Y. J., Jeong, H. Y., Cheon, J. Y., Lee, J. H., . . . Kwak, S. K. (2015). Monolayer-precision synthesis of molybdenum sulfide nanoparticles and their nanoscale size effects in the hydrogen evolution reaction. *ACS Nano, 9*(4), 3728-3739.

Shahid, M., Hamid, M., Tahir, A. A., Mazhar, M., Malik, M. A., & Helliwell, M. (2012). Nanostructured ZnO thin films for optical, electrical, and photoelectrochemical applications from a new Zn complex. *Industrial & Engineering Chemistry Research, 51*(50), 16361-16368.

Shi, Y., & Zhang, B. (2016). Recent advances in transition metal phosphide nanomaterials: synthesis and applications in hydrogen evolution reaction. *Chemical Society Reviews, 45*(6), 1529-1541.

Universiti Malaya

Shinagawa, T., Garcia-Esparza, A. T., & Takanabe, K. (2015). Insight on Tafel slopes from a microkinetic analysis of aqueous electrocatalysis for energy conversion. *Scientific Reports, 5*(1), 1-21.

Song, L., Wang, X., Wen, F., Niu, L., Shi, X., & Yan, J. (2016). Hydrogen evolution reaction performance of the molybdenum disulfide/nickel–phosphorus composites in alkaline solution. *International Journal of Hydrogen Energy, 41*(42), 18942-18952.

Su, H., Song, S., Li, S., Gao, Y., Ge, L., Song, W., . . . Liu, J. (2021). High-valent bimetal Ni_3S_2/Co_3S_4 induced by Cu doping for bifunctional electrocatalytic water splitting. *Applied Catalysis B: Environmental, 293*, Article#120225.

Su, P., Pei, W., Wang, X., Ma, Y., Jiang, Q., Liang, J., . . . Lu, G. Q. (2021). Exceptional electrochemical HER performance with enhanced electron transfer between Ru nanoparticles and single atoms dispersed on a carbon substrate. *Angewandte Chemie, 133*(29), 16180-16186.

Suresh, S. (2013). Investigation of the optical and dielectric properties of the urea L-malic acid NLO single crystal. *American Chemical Science Journal, 3*(3), 325-337.

Swathi, S., Rani, B. J., Ravi, G., & Yuvakkumar, R. (2019). Dopant influence on phase and electrochemical performance of molybdenum sulfide nanostructures. *AIP Conference Proceedings, 2162*, Article#020110.

Tan, J., Yang, W., Oh, Y., Lee, H., Park, J., & Moon, J. (2018). Controlled electrodeposition of photoelectrochemically active amorphous MoS_x cocatalyst on Sb_2Se_3 photocathode. *ACS Applied Materials & Interfaces, 10*(13), 10898-10908.

Tang, W., Chao, Y., Weng, X., Deng, L., & Xu, K. (2012). Optical property and the relationship between resistivity and surface roughness of indium tin oxide thin films. *Physics Procedia, 32*, 680-686.

Tang, Y.-J., Zhang, A.-M., Zhu, H.-J., Dong, L.-Z., Wang, X.-L., Li, S.-L., . . . Lan, Y.-Q. (2018). Polyoxometalate precursors for precisely controlled synthesis of bimetallic sulfide heterostructure through nucleation-doping competition. *Nanoscale, 10*(18), 8404-8412.

Taylor, L. S., & Zografi, G. (1998). The quantitative analysis of crystallinity using FT-Raman spectroscopy. *Pharmaceutical Research,* 15(5), 755-761.

Universiti Malaya

Tedstone, A. A., Lewis, E. A., Savjani, N., Zhong, X. L., Haigh, S. J., O'Brien, P., & Lewis, D. J. (2017). Single-source precursor for tungsten dichalcogenide thin films: $Mo_{1-x}W_xS_2$ ($0 \leq x \leq 1$) alloys by aerosol-assisted chemical vapor deposition. *Chemistry of Materials, 29*(9), 3858-3862.

Vergniory, M., Elcoro, L., Felser, C., Regnault, N., Bernevig, B. A., & Wang, Z. (2019). A complete catalogue of high-quality topological materials. *Nature, 566*(7745), 480-485.

Vergniory, M. G., Wieder, B. J., Elcoro, L., Parkin, S. S., Felser, C., Bernevig, B. A., & Regnault, N. (2022). All topological bands of all nonmagnetic stoichiometric materials. *Science, 376*(6595), Article#eabg9094.

Walters, G., & Parkin, I. (2009). Aerosol assisted chemical vapour deposition of ZnO films on glass with noble metal and p-type dopants; use of dopants to influence preferred orientation. *Applied Surface Science, 255*(13-14), 6555-6560.

Wang, F., Shifa, T. A., Zhan, X., Huang, Y., Liu, K., Cheng, Z., . . . He, J. (2015). Recent advances in transition-metal dichalcogenide based nanomaterials for water splitting. *Nanoscale, 7*(47), 19764-19788.

Wang, L., Lu, L., Zhang, L., Wang, X., & Qin, X. (2017). Effects of carrier gas transport on the structure and performance of Al-doped ZnO films grown by aerosol-assisted chemical vapour deposition method. *Current Nanoscience, 13*(5), 442-448.

Wang, P., Wang, X., Diao, R., Guo, Y., Wang, Y., Zhou, C., . . . Zhang, Y.-H. (2021). Hierarchical tubular MoP/MoS_2 composite with enhanced electrochemical hydrogen evolution activity. *Journal of Materials Science: Materials in Electronics, 32*(10), 14047-14056.

Wang, Y., Nie, Y., Ding, W., Chen, S., Xiong, K., Qi, X., . . . Wei, Z. (2015). Unification of catalytic oxygen reduction and hydrogen evolution reactions: highly dispersive Co nanoparticles encapsulated inside Co and nitrogen co-doped carbon. *Chemical Communications, 51*(43), 8942-8945.

Wang, Y., & Zhang, J. (2018). Structural engineering of transition metal-based nanostructured electrocatalysts for efficient water splitting. *Frontiers of Chemical Science and Engineering, 12*(4), 838-854.

Universiti Malaya

Wang, Z., Wu, H. H., Li, Q., Besenbacher, F., Li, Y., Zeng, X. C., & Dong, M. (2020). Reversing interfacial catalysis of ambipolar WSe_2 single crystal. *Advanced Science, 7*(3), Article#1901382.

Wong, R. C., Ooi, M. L., Ng, S. W., & Thomas, N. F. (2010). The first report of the reaction of Davy's reagent with $[CpMo(CO)_n]_2$ (n= 2, 3) via a phosphorus–sulfur bond cleavage process. Isolation and characterization of $CpMo(CO)_2$(S2P (SPhMe) $_2$), $Cp_2Mo_2(CO)_5(S_2P$ (SPhMe)) and Cp_2Mo_2(μ-S)(μ-S2)(μ-SPhMe)(Cp=(η5-C_5H_5)). *Inorganica Chimica Acta, 363*(10), 2307-2312.

Wu, A., Gu, Y., Xie, Y., Tian, C., Yan, H., Wang, D., . . . Fu, H. (2019). Effective electrocatalytic hydrogen evolution in neutral medium based on 2D MoP/MoS_2 heterostructure nanosheets. *ACS Applied Materials & Interfaces, 11*(29), 25986-25995.

Wu, A., Tian, C., Yan, H., Jiao, Y., Yan, Q., Yang, G., & Fu, H. (2016). Hierarchical MoS_2@ MoP core–shell heterojunction electrocatalysts for efficient hydrogen evolution reaction over a broad pH range. *Nanoscale, 8*(21), 11052-11059.

Wu, S., Yang, X., Cui, T., Feng, Q., Zhou, S., Xu, X., . . . Yang, Q. (2021). Tubular-like NiS/Mo_2S_3 microspheres as electrode material for high-energy and long-life asymmetric supercapacitors. *Colloids and Surfaces A: Physicochemical and Engineering Aspects, 628*, Article#127332.

Wu, T., Chen, S., Zhang, D., & Hou, J. (2015). Facile preparation of semimetallic MoP_2 as a novel visible light driven photocatalyst with high photocatalytic activity. *Journal of Materials Chemistry A, 3*(19), 10360-10367.

Wu, T., Pi, M., Zhang, D., & Chen, S. (2016). Three-dimensional porous structural MoP_2 nanoparticles as a novel and superior catalyst for electrochemical hydrogen evolution. *Journal of Power Sources, 328*, 551-557.

Wu, Z., Wang, J., Liu, R., Xia, K., Xuan, C., Guo, J., . . . Wang, D. (2017). Facile preparation of carbon sphere supported molybdenum compounds (P, C and S) as hydrogen evolution electrocatalysts in acid and alkaline electrolytes. *Nano Energy, 32*, 511-519.

Wu, Z., Wang, J., Xia, K., Lei, W., Liu, X., & Wang, D. (2018). MoS_2–MoP heterostructured nanosheets on polymer-derived carbon as an electrocatalyst for hydrogen evolution reaction. *Journal of Materials Chemistry A, 6*(2), 616-622.

Universiti Malaya

Xiao, P., Sk, M., Thia, L., Ge, X., Lim, R., Wang, J., . . . Wang, X. (2014). Molybdenum phosphide as an efficient electrocatalyst for the hydrogen evolution reaction. *Angewandte Chemie International Edition, 53*, 14433-14437.

Xiao, W., Li, X., Fu, C., Zhao, X., Cheng, Y., & Zhang, J. (2021). Morphology and distribution of in-situ grown MoP nanoparticles on carbon nanotubes to enhance hydrogen evolution reaction. *Journal of Alloys and Compounds, 877*, Article#160214.

Xu, Y., Wang, R., Wang, J., Li, J., Jiao, T., & Liu, Z. (2021). Facile fabrication of molybdenum compounds (Mo_2C, MoP and MoS_2) nanoclusters supported on N-doped reduced graphene oxide for highly efficient hydrogen evolution reaction over broad pH range. *Chemical Engineering Journal, 417*, Article#129233.

Yan, Y., Xia, B. Y., Zhao, B., & Wang, X. (2016). A review on noble-metal-free bifunctional heterogeneous catalysts for overall electrochemical water splitting. *Journal of Materials Chemistry A, 4*(45), 17587-17603.

Yang, L., Hong, H., Fu, Q., Huang, Y., Zhang, J., Cui, X., . . . Xiang, B. (2015). Single-crystal atomic-layered molybdenum disulfide nanobelts with high surface activity. *ACS Nano, 9*(6), 6478-6483.

Ye, R., del Angel-Vicente, P., Liu, Y., Arellano-Jimenez, M. J., Peng, Z., Wang, T., . . . Yacaman, M. J. (2016). High-performance hydrogen evolution from $MoS_{2(1-x)}P_x$ solid solution. *Advanced Materials, 28*(7), 1427-1432.

Yu, Y., Li, C., Liu, Y., Su, L., Zhang, Y., & Cao, L. (2013). Controlled scalable synthesis of uniform, high-quality monolayer and few-layer MoS_2 films. *Scientific Reports, 3*(1), 1-6.

Zhang, H., Maijenburg, A. W., Li, X., Schweizer, S. L., & Wehrspohn, R. B. (2020). Bifunctional heterostructured transition metal phosphides for efficient electrochemical water splitting. *Advanced Functional Materials, 30*(34), Article#2003261.

Zhang, X., Jia, F., & Song, S. (2021). Recent advances in structural engineering of molybdenum disulfide for electrocatalytic hydrogen evolution reaction. *Chemical Engineering Journal, 405*, Article#127013.

Zhang, X., Yu, X., Zhang, L., Zhou, F., Liang, Y., & Wang, R. (2018). Molybdenum phosphide/carbon nanotube hybrids as pH-universal electrocatalysts for hydrogen evolution reaction. *Advanced Functional Materials, 28*(16), Article#1706523.

Universiti Malaya

Zhang, Y., Ligthart, D. M., Quek, X.-Y., Gao, L., & Hensen, E. J. (2014). Influence of Rh nanoparticle size and composition on the photocatalytic water splitting performance of Rh/graphitic carbon nitride. *International Journal of Hydrogen Energy, 39*(22), 11537-11546.

Zhang, Y., Yang, J., Dong, Q., Geng, H., Zheng, Y., Liu, Y., . . . Dong, X. (2018). Highly dispersive MoP nanoparticles anchored on reduced graphene oxide nanosheets for an efficient hydrogen evolution reaction electrocatalyst. *ACS Applied Materials & Interfaces, 10*(31), 26258-26263.

Zhong, Y., Zhang, Y., Zhang, G., Li, R., & Sun, X. (2012). Site-controlled synthesis and mechanism of three-dimensional Mo_2S_3 flowers. *Applied Surface Science, 263*, 410-415.

Zhou, X., Zhao, W., Pan, J., Fang, Y., Wang, F., & Huang, F. (2018). Urchin-like Mo_2S_3 prepared via a molten salt assisted method for efficient hydrogen evolution. *Chemical Communications, 54*(90), 12714-12717.

Zhu, W., Tang, C., Liu, D., Wang, J., Asiri, A. M., & Sun, X. (2016). A self-standing nanoporous MoP_2 nanosheet array: an advanced pH-universal catalytic electrode for the hydrogen evolution reaction. *Journal of Materials Chemistry A, 4*(19), 7169-7173.

Universiti Malaya